

# **Surface functionalised and nanostructured Transparent Conductive Oxides - towards a platform for (bio)electrocatalysis**

vorgelegt von

Master of Research (M.Res) in Molecular Modelling and  
Materials Science

Tomos Gwilym Ab Alun Harris

ORCID: 0000-0003-2989-4127

von der Fakultät II - Mathematik und Naturwissenschaften  
der Technischen Universität Berlin  
zur Erlangung des akademischen Grades

Doktor der Naturwissenschaften

- Dr. rer. nat. -

genehmigte Dissertation

Promotionsausschuss:

Vorsitzender: Prof. Dr. Roel van der Krol

Gutachterin: Prof. Dr. Anna Fischer

Gutachter: Prof. Dr. Peter Hildebrandt

Gutachterin: Prof. Dr. Ulla Wollenberger

Tag der wissenschaftlichen Aussprache: 23. November 2018

Berlin 2019



## ABSTRACT

Storage of (renewable) energy in the form of chemical bonds in electrofuels, their later conversion back to electricity, or the generation of renewable chemical feedstocks from CO<sub>2</sub>, N<sub>2</sub> etc. all require the use of stable and efficient catalysts. In particular, there is urgent need for the development of efficient, precious-metal free catalysts. Enzymes and inorganic (e.g. biomimetic) molecular catalysts can provide the necessary high turnover frequencies and selectivities, as well as low overpotentials. The immobilisation, or heterogenisation, of enzymatic and molecular catalysts on electrode surfaces is imperative, thereby increasing the number of addressable active sites and facilitating electron transfer, especially when using hydrophobic catalysts in aqueous conditions. Immobilisation can be carried out on conductive metal oxides, thus allowing the combination of catalytic properties with certain electrode properties e.g. high surface areas due to nanostructuring, transparency in the case of transparent conductive oxides (TCOs), or photoadsorption in the case of narrow band semiconductors, which can drive reactions with light.

Current strategies for immobilising electrocatalysts on metal oxide surfaces use anchoring groups such as phosphonic acids, carboxylic acids, silanes and their derivatives. While each approach has its own merit e.g. high stability or good charge transfer properties, one usually comes at the expense of the other. Development of new approaches is hence required to build chemically and electrochemically robust interfaces which allow efficient and fast charge transfer rates. In this context, the development of *in situ* spectroscopic techniques will provide real-time monitoring of interface formation, catalyst binding and system evolution under reaction conditions, thus allowing for a rational design of immobilisation strategies, far beyond a simple trial-and-error approach.

In this work, electrografting of diazonium salts on nanostructured gold, indium tin oxide (ITO) and mesoporous antimony-doped tin oxide (me-ATO) thin film electrodes was successfully used to immobilise (bio)electrocatalysts. *In situ* surface enhanced infrared absorption (SEIRA) spectroelectrochemistry demonstrates the remarkably broad electrochemical stability window of 3.0 V for the electrografted interfaces on gold in acetonitrile (ranging from -2.2 to +0.8 V (vs Fc/Fc<sup>+</sup>)). Using the same *in situ* technique, a radical scavenger is shown to moderate interface formation on gold, reducing heterogeneous charge transfer resistance enough to enhance direct electron transfer between an immobilised redox active protein, namely an oxygen-tolerant [NiFe] hydrogenase, and the electrode. This moderation approach is further employed successfully on ITO. Furthermore, diazonium salts are used to immobilise a precious-metal free Mn-bipyridyl CO<sub>2</sub> reduction molecular catalyst on gold, and a Cu-bipyridyl oxygen evolution reaction (OER) molecular catalyst on ITO.

Precious-metal free oxygen reduction reaction (ORR) and OER ‘Hangman’ molecular catalysts are also immobilised on me-ATO using electrografting. *In situ* attenuated total reflection-IR spectroscopy, as well as IR spectroelectrochemistry, demonstrates the wide hydrolytic stability window (in a pH range of ca. 2.5 - 12), and the broad electrochemical stability window of at least 3.0 V in aqueous media (ranging from -0.73 to 2.23 V (vs RHE)), and 2.9 V in organic media (ranging from -1.3 V to 1.6 V (vs Fc/Fc<sup>+</sup>)) of the electrografted interfaces. *In situ* resonance Raman spectroelectrochemistry was further used to determine the co-ordination of the immobilised species and to demonstrate their excellent electrochemical accessibility. These techniques were complemented by electrochemical, UV-vis and XPS measurements, as well as applied theoretical calculations.

The work culminated in functioning precious-metal free electrocatalytic devices and the demonstration that *in situ* spectroscopy and spectroelectrochemistry are powerful tools for researchers working on oxide-based electrochemical devices. Furthermore, it was shown that electrografting of diazonium salts results in highly stable interfaces suitable for catalyst immobilisation on both gold *and* TCO materials.

# ZUSAMMENFASSUNG

Das Speichern von (erneuerbarer) Energie in Form von chemischen Bindungen in Elektrotreibstoffen, sowie deren spätere Umwandlung zurück in Elektrizität oder in die Erzeugung von erneuerbaren, chemischen Rohstoffen aus  $\text{CO}_2$ ,  $\text{N}_2$ , usw., erfordern die Anwendung von stabilen und effizienten Elektrokatalysatoren. Insbesondere besteht allein schon aus Kostengründen ein dringender Bedarf für die Entwicklung von effizienten und auch edelmetallfreien Katalysatoren. Enzyme und anorganische (z. B. biomimetische) molekulare Katalysatoren können die erforderlichen hohen Umsatzfrequenzen und Selektivitäten wie auch niedrige Überpotentiale vorweisen. Daher ist eine Immobilisierung oder ‚Heterogenisierung‘ von enzymatischen und molekularen Katalysatoren auf Elektrodenoberflächen zwingend erforderlich, wodurch die Anzahl der adressierbaren aktiven Zentren erhöht wird, und der elektronische Kontakt erleichtert wird, insbesondere wenn hydrophobe Katalysatoren unter wässrigen Bedingungen verwendet werden sollen. Die Immobilisierung kann auf leitfähigen Metalloxiden durchgeführt werden, wodurch die katalytischen Eigenschaften mit bestimmten Elektroden-eigenschaften kombiniert werden können, z.B. hohe Oberflächen durch Nanostrukturierung, Transparenz im Fall von transparenten leitfähigen Oxiden (TCO), sowie Photoabsorption bei schmalbandigen Halbleitern, die entsprechenden Reaktionen dann auch mit Licht steuern können.

Aktuelle Strategien zur Immobilisierung von Elektrokatalysatoren auf Metalloxidoberflächen verwenden Ankergruppen wie Phosphonsäuren, Carbonsäuren, Silane und ihre Derivate. Während jeder dieser Immobilisierungsansätze spezifische Vorteile mit sich bringt, z.B. in Bezug auf hohe Stabilität oder gute Ladungsübertragungseigenschaften, geht die Optimierung einer dieser Eigenschaften meist zu Lasten einer anderen. So ist zum Aufbau chemisch und elektrochemisch robuster Grenzflächen, die effiziente und schnelle Ladungsübertragungsraten ermöglichen sollen, auch die Entwicklung neuer Immobilisierungstechniken erforderlich. In diesem Zusammenhang ermöglichen *in situ* spektroskopische Techniken durch eine Echtzeitüberwachung der Grenzflächenbildung, der Katalysatoranbindung und der Systementwicklung unter Reaktionsbedingungen ein rationales Design von Immobilisierungsstrategien, welche weit über einen einfachen empirischer Ansatz hinaus gehen.

In dieser Arbeit wurde das sogenannte „Elektrografting“, ein elektrisch gesteuertes „Aufbringen“ von Diazoniumsalzen an nanostrukturierten Gold-, Indiumzinnoxid- (ITO) und mesoporösen Antimon-dotierten Zinnoxid (me-ATO) -Dünnschichtfilm-Elektroden erfolgreich zur Immobilisierung von BioElektrokatalysatoren verwendet. Durch *in situ* oberflächenverstärkte Infrarot- Absorptions-Spektroskopie (SEIRA) konnte ein bemerkenswert breites elektrochemisches Stabilitätsfenster von 3.0 V für solche „elektrogegrafte“ Grenzflächen an Gold in Acetonitril (von -2.2 bis +0.8 V vs  $\text{Fc}/\text{Fc}^+$ ) gezeigt werden. Unter Verwendung derselben *in situ*-Technik wurde gezeigt, dass ein Radikalfänger die Grenzflächenbildung auf Gold einschränkt, wodurch der heterogene Ladungsübertragungswiderstand ausreichend verringert wird, um den direkten Elektronentransfer zwischen einem immobilisierten redox-aktiven Protein und der Elektrode zu verbessern, nämlich einer sauerstofftoleranten [NiFe]-Hydrogenase. Dieser Ansatz wurde erfolgreich für die Oberflächenfunktionalisierung an ITO angewandt. Darüber hinaus werden Diazoniumsalze zur Immobilisierung von einem edelmetallfreien, molekularen Mn-Bipyridyl- $\text{CO}_2$ -Reduktionskatalysator und einem Cu-Bipyridyl-Sauerstoffproduktionsreaktion (OER) - Katalysator auf Gold und ITO verwendet.

Edelmetallfreie, molekulare Sauerstoffreduktionsreaktion (ORR) und OER "Hangman"-Katalysatoren werden ebenfalls auf me-ATO mittels Elektrografting immobilisiert. *In situ*-IR-Spektroskopie im Einsatzmodus der abgeschwächten Totalreflexion sowie IR-Spektroelektrochemie zeigen ein breites hydrolytisches Stabilitätsfenster dieser Grenzflächen (in einem Bereich von ca. 2,5 bis 12 pH-Einheiten) auf, wie auch ein breites elektrochemisches Stabilitätsfenster von mindestens 3,0 V in wässrigen Medien (von -0,73 bis 2,23 V vs RHE) und

2,9 V in organischen Medien (von -1,3 bis 1.6 V vs Fc/Fc<sup>+</sup>) der Grenzflächen. Weiterhin wurde *in situ*-Resonanz-Raman-Spektroelektrochemie verwendet um den Koordinationszustand der immobilisierten Spezies zu bestimmen und ihre ausgezeichnete, elektrochemische Zugänglichkeit zu demonstrieren. Diese Techniken wurden durch elektrochemische, UV-Vis- und XPS-Messungen sowie durch theoretische Berechnungen ergänzt.

Die Arbeit gipfelte so in funktionierenden, edelmetallfreien elektrokatalytischen Geräten und dem Nachweis, dass *In situ*-Spektroskopie und Spektroelektrochemie leistungsfähige Techniken für Forscher sind, die an oxid-basierten elektrochemischen Aufbauten arbeiten. Darüber hinaus wurde gezeigt, dass das „Elektrografting“, das sogenannte elektrisch-gesteuerte „Aufbringen“ von Diazoniumsalzen zu sehr stabilen Grenzflächen führt, die sich sowohl für Gold- als auch für TCO-Materialien zur Immobilisierung von Katalysatoren eignen.

## PUBLICATIONS

### Parts of this work are published in the following articles

**T. G. A. A. Harris**, R. Götz, P. Wrzolek, V. Davis, P. Hildebrandt, M. Schwalbe, I. Weidinger, I. Zebger, A. Fischer.

Title: "Robust electrografted interfaces on metal oxides for electrocatalysis – an in situ spectroelectrochemical study". *J. Mater. Chem. A*, **2018**, 6 (31), 15200–15212.

**T. G. A. A. Harris**, N. Heidary, J. Kozuch, S. Freilingsdorf, O. Lenz, P. Hildebrandt, I. Zebger, A. Fischer.

Title: "In-situ spectroelectrochemical studies into formation and stability of robust diazonium-derived interfaces on gold electrodes for the immobilization of an oxygen-tolerant hydrogenase". *ACS Appl. Mater. Interfaces*, **2018**, 10 (27), 23380-23391.

**T. G. A. A. Harris**, S. Rauwerdink, A. Tahraoui, S. Freilingsdorf, O. Lenz, P. Hildebrandt, I. Zebger, A. Fischer. Title: "Electrografted interfaces on metal oxides for enzyme immobilisation and bioelectrocatalysis". *Manuscript in preparation*

### Other publications

H. Gatemala, T. G. A. A. Harris, L. Pardo-Perez, C. Querebillo, S. Freilingsdorf, O. Lenz, A. Fischer, I. Weidinger, S. Ekgasit, N. Heidary, H. K. Ly, I. Zebger. "A Graphene Oxide Modified Hybrid Surface as an Alternative Platform for SEIRA Spectro-electrochemical Studies". *Manuscript in preparation*

## SELECTED TALKS

“*In situ* spectroelectrochemical approaches to study molecular interfaces on conductive oxides – Immobilisation of electrocatalysts using diazonium chemistry“, 4th International Symposium on Chemistry for Energy Conversion & Storage, Berlin, January 28 – 31 2018.

“*In situ* spectroelectrochemical approaches to study molecular interfaces on conductive oxides – Immobilisation of electrocatalysts using diazonium chemistry“, 2017 Fall Meeting – Materials Research Society (MRS), Boston, USA, November 26 – December 1 2017.

“Spectroelectrochemical Insights into the Formation of Robust Interfaces for the Immobilization of Biological and Molecular Electrocatalysts“, Electrochemistry 2016 - Gesellschaft Deutscher Chemiker (GDCh), Goslar, September 26 – 28 2016.

“Spectroelectrochemical Insights into the Formation of Robust Interfaces for the Immobilization of Biological and Molecular Electrocatalysts“, 229th Spring Meeting - Electrochemical Society (ECS), San Diego, USA, May 29 – June 3 2016.

## SELECTED POSTERS

“Diazonium salts for attaching molecular catalysts to metal oxide surfaces – an *in situ* spectroelectrochemical study“, GDCh-Wissenschaftsforum Chemie 2017, Berlin, September 10 – 14, 2017.

“Highly stable interfaces for the immobilisation of molecular catalysts on metal oxide materials – an *in situ* spectroelectrochemical study“, 5th International Conference on Multifunctional, Hybrid and Nanomaterials, Lisbon, Portugal, March 6 – 10, 2017

## ABBREVIATIONS

4-BABD – 4-benzamidobenzenediazonium tetrafluoroborate

4-NBD – 4-nitrobenzenediazonium tetrafluoroborate

Ag/AgCl – silver/silver chloride electrode

ATO – antimony-doped tin oxide

ATR – attenuated total reflection

BE – binding energy

bpy-diazo – 4-([2,2'-Bipyridine]-4-carboxamido)benzenediazonium tetrafluoroborate

CME – chemically modified electrode

CNT – carbon nanotubes

CPE – constant potential electrolysis

CV – cyclic voltammetry

DFT – density functional theory

DI – deionised

DPPH – 2,2-diphenyl-1-picrylhydrazyl

EFC – enzymatic fuel cell

EISA – evaporation induced self-assembly

ESI-MS – electrospray ionisation mass spectroscopy

ET – electron transfer

Fc/Fc<sup>+</sup> – ferrocene/ferrocenium

FTO – fluorine-doped tin oxide

GC – glassy carbon

HER – hydrogen evolution reaction

HOR – hydrogen oxidation reaction

HSM – high surface area nanomaterial

Im-diazo – 4-(1H-imidazol-1-yl)benzenediazonium tetrafluoroborate

IR – infrared

ITO – indium tin oxide

MBH – membrane-bound hydrogenase

me-ATO – mesoporous antimony-doped tin oxide

MWCNT – multi-walled carbon nanotubes

OER – oxygen evolution reaction

ORR – oxygen reduction reaction

PB – phosphate buffer

PFV – protein film voltammetry

pl-ITO – planar indium tin oxide

RCT – charge transfer resistance

RDE – rotating disc electrode

*Re* – *Ralstonia eutropha*

RHE – reversible hydrogen electrode

rR – resonance Raman

SAM – self-assembled monolayer

sc-ITO – spin-coated indium tin oxide

SEIRA – surface enhanced infrared absorption

SEM – scanning electron microscopy

TBAF – tert-butylammonium hexafluorophosphate

TBAP – tert-butylammonium perchlorate

TCO – transparent conductive oxide

TOF – turnover frequency

UV-Vis – ultraviolet visible

XPS – X-ray photoelectron spectroscopy

$\Delta E_p$  – peak separation

# TABLE OF CONTENTS

<b>1</b>	<b>Introduction and motivation</b> .....	<b>1</b>
<b>Theory</b>		
<b>2.1</b>	<b>Transparent conductive oxides (TCOs)</b> .....	<b>4</b>
2.1.1	Conductivity in semiconductors .....	4
2.1.2	The band structure of semiconductors and the Fermi energy .....	5
<b>2.2</b>	<b>Electrode processes</b> .....	<b>8</b>
2.2.1	Fermi energy and electrochemical potential .....	8
2.2.2	The electrode-electrolyte interface .....	10
2.2.3	The relation between current and potential .....	14
<b>2.3</b>	<b>Surface modification of electrode materials</b> .....	<b>17</b>
2.3.1	Chemically modified electrodes .....	17
2.3.2	Langmuir-Blodgett assembly .....	18
2.3.3	Self-assembly .....	19
2.3.4	Modification of TCO's .....	20
2.3.5	Electrochemical modification .....	23
2.3.6	Modification using diazonium salts .....	24
2.3.7	Electrochemical grafting using diazonium salts .....	26
2.3.8	Electrochemical response of adsorbed monolayers .....	27
2.3.9	Immobilisation of electrocatalysts on electrode surfaces.....	29
<b>2.4</b>	<b>Spectroscopic methods</b> .....	<b>33</b>
2.4.1	Spectroelectrochemistry .....	33
2.4.2	UV-Vis spectroscopy .....	33
2.4.3	Vibrational spectroscopy.....	35
2.4.4	Infrared spectroscopy .....	36
2.4.5	Surface Enhanced Infrared Absorption (SEIRA) spectroscopy .....	38
2.4.6	Raman spectroscopy .....	39
2.4.7	X-ray photoelectron spectroscopy .....	41
<b>2.5</b>	<b>Hydrogenases</b> .....	<b>42</b>
<b>2.6</b>	<b>Molecular catalysts</b> .....	<b>48</b>
2.6.1	Oxygen reduction reaction at metal macrocycles .....	48
2.6.2	Water oxidation molecular catalysts .....	50
<b>3</b>	<b>Materials, instruments and methods</b> .....	<b>51</b>
<b>3.1</b>	<b>Electrode synthesis</b> .....	<b>51</b>
3.1.1	Gold SEIRA film preparation.....	51
3.1.2	Indium tin oxide electrode preparation.....	51
3.1.3	Antimony-doped tin oxide electrode preparation .....	52
<b>3.2</b>	<b>Precursor synthesis</b> .....	<b>53</b>
3.2.1	Diazonium salts .....	53
<b>3.3</b>	<b>Protein purification and catalyst preparation</b> .....	<b>54</b>
3.3.1	Membrane-Bound Hydrogenase (MBH) from <i>Ralstonia eutropha</i> .....	54
3.3.2	Hangman complexes .....	55
<b>3.4</b>	<b>Electrochemistry</b> .....	<b>55</b>
<b>3.5</b>	<b>Electrode modification</b> .....	<b>56</b>
3.5.1	Functionalisation of gold .....	56
3.5.2	Functionalisation of ITO .....	57
3.5.3	Functionalisation of ATO .....	58
3.5.4	Enzyme immobilisation .....	58
<b>3.6</b>	<b>Spectroscopic characterisation</b> .....	<b>59</b>
3.6.1	ATR-IR and SEIRA .....	59

3.6.2	Density functional theory .....	60
3.6.3	X-ray photoelectron spectroscopy .....	60
3.6.4	Resonance Raman .....	61
3.6.5	UV-Vis.....	61
<b>4</b>	<b>Spectroelectrochemical investigation into the electrochemical grafting of diazonium salts on electrodes for the immobilisation of biological and molecular catalysts.....</b>	<b>62</b>
4.1	Introduction.....	62
4.2	Electrochemical reduction of diazonium salts on gold .....	66
4.3	Electrochemical stability of electrografted diazonium interfaces on gold .....	68
4.4	Effect of radical scavenger on interface formation .....	71
4.5	Spontaneous adsorption of diazonium salts on gold .....	75
4.6	Immobilisation of hydrogenase on electrografted diazonium interfaces .....	77
4.7	Immobilisation of molecular catalysts on gold using electrografting of diazonium salts .....	80
4.8	Conclusions .....	87
<b>5</b>	<b>Electrochemical grafting of diazonium salts on transparent conductive oxide (TCO) electrodes for the immobilisation of enzymes.....</b>	<b>88</b>
5.1	Introduction.....	88
5.2	Effect of radical scavenger on interface formation and immobilisation of hydrogenase.....	89
5.3	Conclusions .....	106
<b>6</b>	<b>Electrochemical grafting of diazonium salts on transparent conductive oxide (TCO) electrodes for the immobilisation of molecular catalysts.....</b>	<b>108</b>
6.1	Introduction.....	108
6.2	Immobilisation of a molecular oxygen evolution reaction catalyst on indium tin oxide (ITO) using the electrografting of a diazonium salt.....	112
6.3	Chemical and electrochemical stability of electrografted diazonium interfaces on mesoporous antimony-doped tin oxide (me-ATO).....	118
6.4	Fe-Hangman complexes immobilised on planar and porous TCOs using the electrografting of a diazonium salt for oxygen reduction reaction.....	128
6.5	Co Hangman complex immobilised on me-ATO using the electrografting of a diazonium salt for the oxygen evolution reaction .....	149
6.6	Conclusions .....	161
<b>7</b>	<b>Appendices.....</b>	<b>164</b>
7.1	Appendix to chapter 4.1 .....	164
7.2	Appendix to chapter 4.2.....	167
7.3	Appendix to chapter 4.3.....	168
<b>8</b>	<b>Bibliography</b>	<b>171</b>

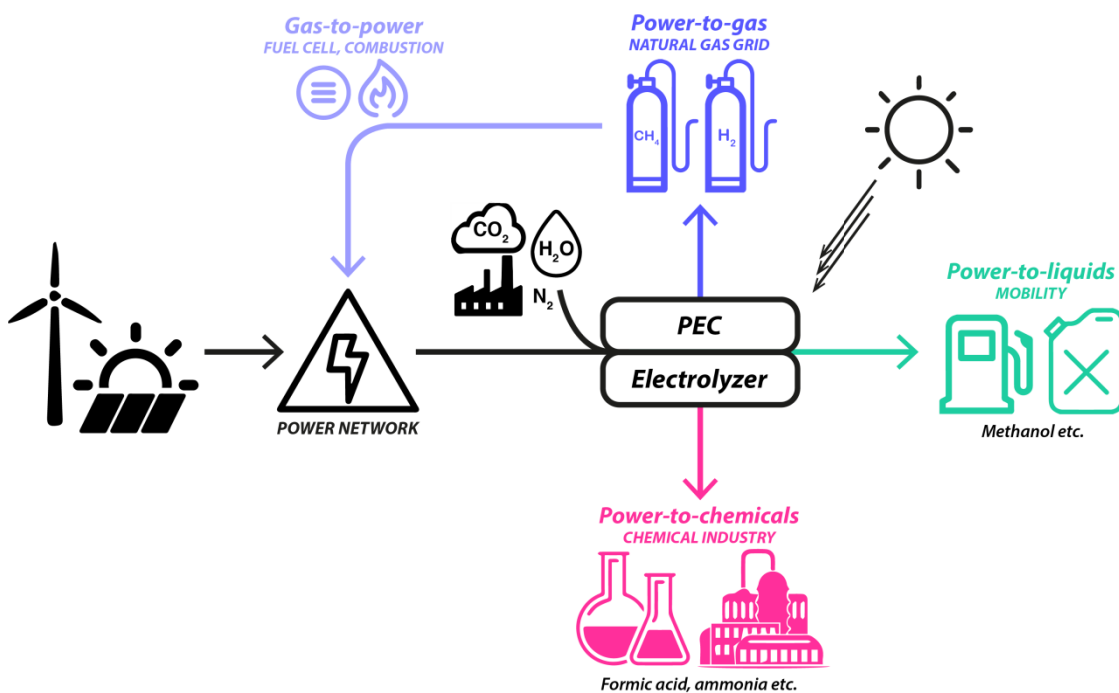




# Chapter 1

## Introduction and motivation

As societies begin to decarbonise their energy systems there is an increasing focus on methods for storing and concentrating renewable energy, or lack thereof. While the cost of solar and wind energy has plummeted to such an extent that they have become more competitive than natural gas in some areas<sup>1</sup>, they are still intermittent in supply (often resulting in oversupply) and located far from demand. One solution is to store electrical or solar energy in the form of chemical bonds in electrofuels for later conversion into power or heat in fuel cells or through combustion. Electrofuels are generally compatible with current industrial infrastructure and supply chains and can therefore be decoupled from the electricity grid e.g. in the form of liquid fuels or for use as chemical feedstocks in industry. Even if currently more costly than storing energy in batteries, electrofuels are a complementary approach, especially in situations where high energy densities are required (e.g. in aviation fuels), or in the conversion of CO<sub>2</sub> captured from unavoidable sources (e.g. cement kilns or steel plants).<sup>2</sup>



### Scheme 1

An overview of the different pathways available for the generation of electrofuels and chemical feedstocks from renewable energy via electrolyzers or photoelectrochemical cells (PECs), and their potential deployment in the economy, within existing industrial infrastructure and supply chains.

Scheme 1 gives an overview of how energy can be stored in the form of chemical energy using electrolyzers or photoelectrochemical cells (PECs) and how these chemicals can be used for

different purposes. Typical reactions include the cleavage of water *via* the so called “oxygen evolution reaction” (OER), yielding molecular oxygen O<sub>2</sub>, protons and electrons. The protons can be further reduced *via* the corresponding “hydrogen evolution reaction” (HER), yielding molecular hydrogen H<sub>2</sub>, a clean and efficient energy carrier, or can alternatively participate in the reduction of CO<sub>2</sub>, yielding various energy carriers such as methane, methanol, or chemical feedstocks such as formic acid, carbon monoxide or ethylene.<sup>3</sup> Such reactions, as well as the respective “oxygen reduction reaction” (ORR) and “hydrogen oxidation reaction” (HOR) that convert the chemical energy back into useable electrical energy (i.e. in fuel cells), require the use and development of efficient electrocatalysts, which allow them to proceed at high rates (turnover frequencies, TOF’s) with low driving forces (overpotentials), thus making them more economically viable. Many of the most efficient catalysts available today for the aforementioned reactions are based on prohibitively expensive precious metals, giving an impetus for the development of efficient, precious-metal free catalysts.

Enzymes, as possible blueprints from nature, and inorganic (e.g. biomimetic) molecular catalysts can exhibit the high TOF’s and selectivities, as well as low overpotentials. Furthermore, these properties can be easily fine-tuned chemically by modification of the 1<sup>st</sup> or the 2<sup>nd</sup> coordination sphere. Many spectroscopic methods can easily be deployed with such catalysts, providing in-depth analysis of reaction mechanisms, which is otherwise much more difficult with heterogeneous catalysts, and thus facilitating rational catalyst design. The immobilisation, or heterogenisation of enzymatic and molecular catalysts on electrode surfaces is imperative, thereby increasing the number of addressable active sites and facilitating charge transfer between the catalyst and the electrode. This is especially important for reactions in water using hydrophobic catalysts. Immobilisation can be carried out on conductive metal oxides or other electrode substrates, thus allowing the combination of catalytic properties with certain electrode properties e.g. high surface areas due to nanostructuring, and transparency in the case of transparent conductive oxides (TCOs), or photoabsorption in the case of narrow band semiconductors, which can drive reactions with light. In particular, TCOs such as antimony-doped tin oxide (ATO) are low-cost and highly stable<sup>4</sup>, and therefore of interest in prototype devices. Current strategies for attaching electrocatalysts to oxide surfaces employ anchoring groups such as phosphonic acids, carboxylic acids, silanes and their derivatives.<sup>5,6</sup> While each approach has its own merit in terms of stability or charge transfer properties, one usually comes at the expense of the other, or may require complex synthetic chemical approaches or additional stabilisation steps. Development of new approaches is hence required to build chemically and electrochemically robust interfaces that allow efficient and fast charge transfer rates.<sup>6,7</sup> In this context, the development of *in situ* spectroscopic techniques providing real-time monitoring of interface formation, stability and evolution under reaction conditions will allow for a rational design of immobilisation strategies, far beyond simple trial and error approaches.

Of particular interest are *in situ* surface sensitive infrared (IR) spectroscopic and spectroelectrochemical methods, which can provide the aforementioned real-time monitoring of the interface, as well as monitoring of catalyst immobilisation and mechanistic insights into the catalytic processes occurring at the interface. Such detailed information cannot be obtained through conventional characterisation approaches used with oxide electrodes, such as UV-vis spectroelectrochemistry or *ex situ* x-ray photoelectron spectroscopy (XPS).

In this work, diazonium electrografting was successfully used to immobilise a number of precious-metal free catalysts on gold and indium tin oxide (ITO) and ATO conductive oxide electrodes, including catalysts active for the OER and ORR, as well as a hydrogenase enzyme active for the HOR. *In situ* surface sensitive IR methods were used to characterise the electrografted interfaces and demonstrate their high electrochemical and chemical stabilities. *In situ* resonance Raman was further used on mesoporous ATO to characterise the immobilised species and demonstrate their excellent electrochemical accessibility. Both of these techniques are complemented by electrochemical, UV-vis and XPS measurements, as well as theoretical calculations. This culminated in functioning precious-metal free electrocatalytic devices and the demonstration that *in situ* IR spectroscopy is a powerful tool for researchers working on oxide-based electrochemical devices, including electrolyzers, sensors, or dye-sensitized solar cells and photocatalytic cells i.e. anywhere inorganic-molecular or inorganic-biological interfaces play an important role in a device's performance.

# Chapter 2

## Theory

### 2.1 Transparent conductive oxides (TCOs)

#### 2.1.1 Conductivity in semiconductors

When a potential difference is applied across a material, an electric field exerts a force on the charge carriers causing them to accelerate and gain momentum. As the charge carriers move through the crystal lattice they will encounter phonons, lattice impurities and defects, all of which will alter their momentum. Assuming momentum is completely lost after each collision, the average carrier velocity, or drift velocity  $v_d$ , can be written as:

$$v_d = \frac{qE\tau}{m} \quad (1)$$

where  $E$  is the applied electric field,  $q$  the carrier charge,  $m$  the charge carrier mass, and  $\tau$  the mean free time, or scattering time, between collisions, which is in turn related to the mean free path  $l$ . This can also be written in terms of carrier mobility  $\mu_q$  such that:

$$\mu_q = \frac{q\tau}{m} \quad (2)$$

Assuming all carriers move with their drift velocity, the current density  $J_x$  (in  $\text{Am}^{-2}$ ) of the carriers moving in the  $x$  direction can be written as the product of the density of electrons  $n$  and the drift velocity:

$$J_x = nqv_d \quad (3)$$

Combining equations (1) and (3) gives the relationship between current density and applied electric field:

$$J_x = \frac{nq^2\tau}{m} E_x \quad (4)$$

which gives a linear relationship, which is in fact Ohms law  $J = \sigma E$ . Conductivity  $\sigma$  can thus be written as<sup>8,9</sup>:

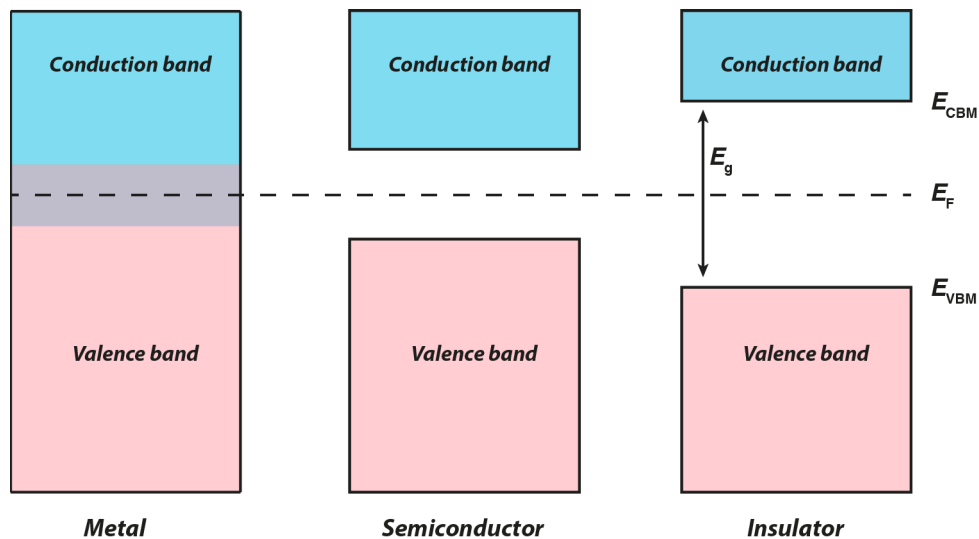
$$\sigma = \frac{q\tau}{m} nE_x = \mu_q(nE_x) \quad (5)$$

### 2.1.2 The band structure of semiconductors and the Fermi energy

Free atoms have well defined energy levels. When  $n$  identical atoms come together and interact, the Pauli principle dictates that they form  $n$  degenerate energy levels. On bringing a very large number of identical atoms together in a solid, the energy difference between the degenerate energy levels becomes so small that they can essentially be considered as continuous energy bands with forbidden energy gaps between them. In general, when considering a solid, only two bands need to be considered: the highest occupied band, known as the valence band (VB), and the next highest band, which is the lowest unoccupied band, and known as the conduction band (CB). Between the valence band maximum (VBM) and the conduction band minimum (CBM) exists a region with no electronic states that is known as the band gap. The Fermi level describes the electrochemical potential of electrons in a solid, or the energy required to add or remove an electron from that solid. The probability of an electronic state with energy  $E$  being occupied is given by the Fermi-Dirac distribution:

$$F(E) = \frac{1}{1 + \exp\left(\frac{E - E_F}{k_B T}\right)} \quad (6)$$

where  $k_B$  is the Boltzmann constant,  $T$  is the temperature and  $E_F$  is the Fermi energy level. At  $T = 0$  K,  $F(E)$  is a step function equal to 1, meaning that all the electronic states up to  $E_F$  are occupied and, therefore,  $E_F$  describes the maximum energy level occupied by an electron.<sup>9</sup>



**Scheme 2**

Energy band diagram for a metal, a semiconductor and an insulator, indicating the position of the Fermi level  $E_F$  relative to the band edges (the valence band maximum  $E_{VBM}$  and the conduction band minimum  $E_{CBM}$  and the band gap  $E_g$  of the material).

In order for a material to conduct electricity, electrons must be able to gain momentum on application of an electric field and move to higher unoccupied energy states. In the case of metals,  $E_F$  lies within an energy band meaning unoccupied states exist above  $E_F$ , therefore allowing electrical conductivity. In an insulator,  $E_F$  lies within the band gap so that at 0 K all of the

valence band states are occupied and all of the conduction band states are unoccupied, meaning the material cannot conduct electricity. At finite temperatures, electrons can be thermally excited into states above the Fermi level. Now  $E_F$  gives the energy level at which there is a 50% probability of being occupied. The Fermi-Dirac function (equation 6) varies exponentially away from  $E_F$ , therefore the degree of conductivity depends on the band gap  $E_g$  of the material.<sup>8,9</sup> Semiconductors are said to have a bandgap values of  $0 < E_g < 4$  eV and insulators  $E_g \geq 4$  eV.<sup>10</sup> TCOs exhibit high electrical conductivity while maintaining transparency in the visible range, and therefore must have an optical band gap greater than 3.2 eV. Energy band diagrams for a metal, a semiconductor and an insulator are illustrated in Scheme 2.

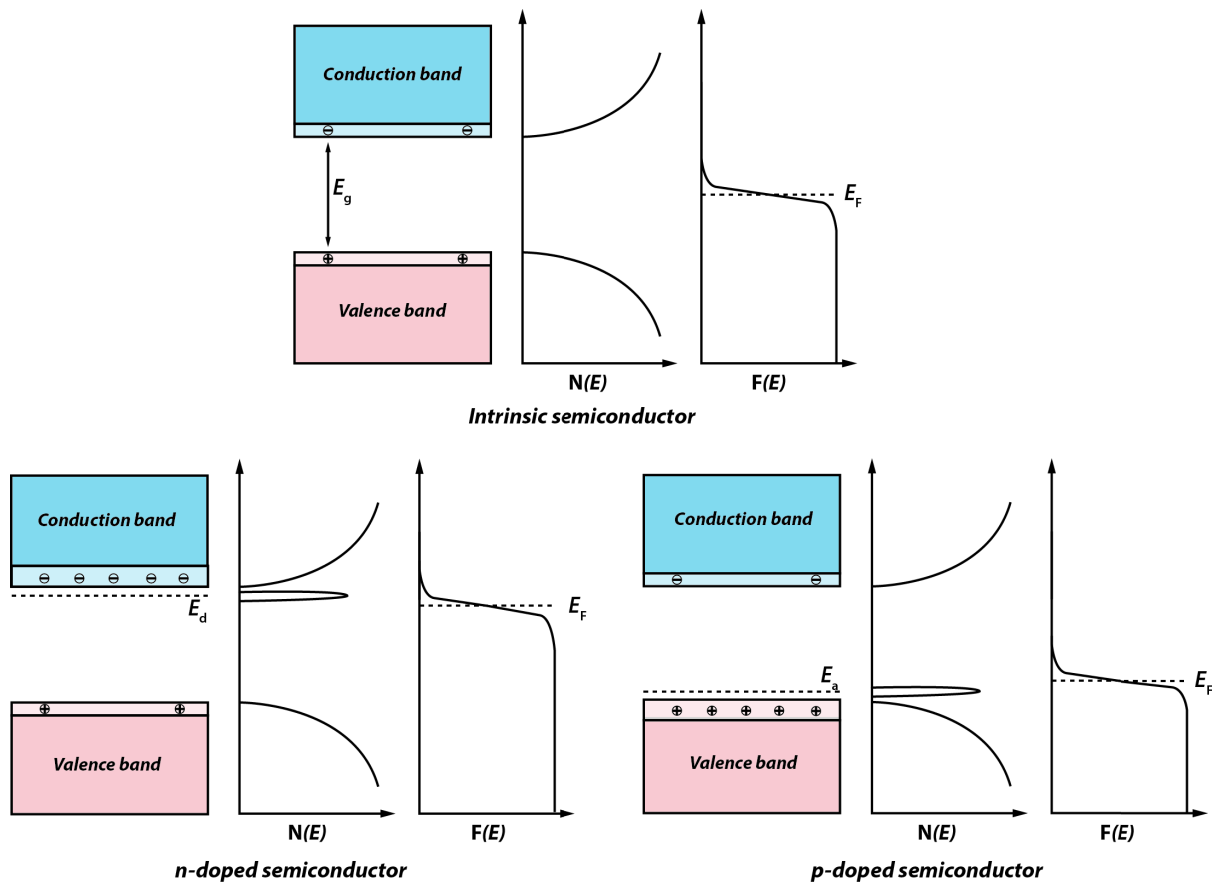
Charge neutrality requires the number of electrons  $n$  occupying states above  $E_F$  to be equal to the number of unoccupied states, or holes, beneath  $E_F$ . If the density of states at the CBM and the VBM in a material are identical, as illustrated in the simplified model in Scheme 2, then  $E_F$  will sit exactly in the middle of the bandgap i.e.  $E_F = \frac{E_{CBM} - E_{VBM}}{2}$ . The charge carrier density in the conduction band can be obtained by approximating the Fermi-Dirac integral using a Boltzmann distribution, where the density is an exponential function of the distance between  $E_F$  and  $E_{CBM}$ :

$$n \approx N_{CBM} \exp\left(-\frac{E_{CBM} - E_F}{k_B T}\right) \quad (6)$$

Similarly, the number of holes occupying the valence band is given by:

$$p \approx N_{VBM} \exp\left(-\frac{E_F - E_{VBM}}{k_B T}\right) \quad (7)$$

where  $N_{CBM}$  and  $N_{VBM}$  are the effective density of states at the conduction band minimum and valence band maximum, respectively. This approximation breaks down when  $E_F$  becomes too close to either the conduction band minimum and valence band maximum, as is often the case for doped semiconductors.



### Scheme 3

The band structure, density of states  $N(E)$  and Fermi Dirac distribution  $F(E)$  for an intrinsic semiconductor, an n-type doped extrinsic semiconductor, and a p-type doped extrinsic semiconductor. The additional donor and acceptor states introduced through doping are indicated by  $E_d$  and  $E_a$ , respectively.

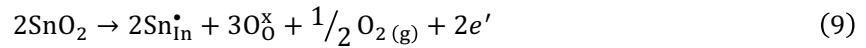
There are two cases in which  $E_F$  can deviate from the middle of the band gap: either when the density of states at the band edges are not equal to one another, or when electronic states exist somewhere inside the formally forbidden band gap. While the former case only leads to a small deviation from  $E_F = \frac{E_{CBM} - E_{VBM}}{2}$ , the latter case can push  $E_F$  closer to either band edge. These states can be introduced through doping, i.e. through introducing electron donor or acceptor impurities into the materials lattice (n-type or p-type doping), to give *extrinsic* semiconductors. In the case where there is no significant doping of the semiconductor, it is called an *intrinsic* semiconductor. The additional donor or acceptor states introduced by dopant species do not sit in the valence or conduction bands. If the distance between e.g. the donor state and the conduction band minimum is in the order of  $k_B T$ , then electrons can be thermally excited from the donor state and into the delocalised conduction band, and therefore participate in charge transport. If the donor densities become large enough, the electronic states introduced inside the band gap can interact forming their own electronic band, where electrons can be ionised to or from.

Metal oxide semiconductors differ to conventional semiconductors, such as Si, in that the electronegativity of the oxygen results in a total or partial transfer of the valence electrons from the metal ion to the oxygen giving rise to their ionic bonding character. Conductivity in oxides

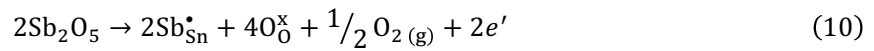
therefore arises from cationic or anionic dopants, or intrinsic point defects such as oxygen vacancies. When doping an oxide with aliovalent dopant atoms (i.e. atoms having a different valency), there must either be an ionic or an electronic compensation mechanism that preserves charge and lattice stoichiometry.<sup>11,12</sup> *n*-type conductivity can be induced in undoped indium oxide (In<sub>2</sub>O<sub>3</sub>) through the introduction of oxygen vacancies, as described using the Kröger-Vink notation shown below (for further information on these notations see<sup>13</sup>):



The oxygen anions leave doubly ionised vacancy sites and two free electron charge carriers upon their removal from the crystal structure. Alternatively, doping with aliovalent cations can also induce compensation mechanisms in semiconductors. *n*-type conductivity can be induced in this way in indium oxide through the introduction of tin oxide (SnO<sub>2</sub>), yielding indium tin oxide (ITO)<sup>14</sup>:



*n*-type conductivity can also be induced in undoped tin oxide SnO<sub>2</sub> through the introduction of oxygen vacancies, like in In<sub>2</sub>O<sub>3</sub>, or through the introduction of antimony, yielding antimony-doped tin oxide (ATO):



## 2.2 Electrode processes

### 2.2.1 Fermi energy and electrochemical potential

The electrochemical potential of a charged species *i* measures the partial molar Gibbs free energy of that species in a phase with an inner potential  $\varphi$ :

$$\bar{\mu}_i = \left( \frac{\partial \bar{G}}{\partial n_i} \right)_{T,p,n,\varphi} \quad (11)$$

The electrochemical potential can also be expressed as the components associated with the chemical species and its charge:

$$\bar{\mu}_i = \mu_i + z_i F \varphi \quad (12)$$

where  $\mu_i$  is the chemical potential, and the second term represents the electrical work done in transferring one mole of charge  $z_i F$ , where  $z_i$  is the charge of the species *i*, and  $\varphi$  is the local electrostatic potential, and  $F$  is the Faraday constant.<sup>15</sup> The chemical and electrochemical potential of an uncharged species is the same. For a metal at  $T = 0$  K, the highest occupied state

is the Fermi level  $E_F$ , and therefore  $\bar{\mu}_i = E_F$ , since any electron added must occupy the Fermi level. At finite temperatures, the values of  $\bar{\mu}_i$  and  $E_F$  will differ by an amount in the order of  $(kT)^2$ , which is negligible in most cases. The work function  $\phi$  is defined as the minimum work required to remove an electron from inside the metal to a state just outside the surface of the metal, therefore  $E_F = -\phi$ . If the reference point is taken as the vacuum level, then  $E_F = -\phi - e_0\psi$ , with the second term representing the extra work required to take the electron from the vacuum level to the surface of the metal.<sup>16</sup>

As for all chemical equilibria, the chemical potential  $\mu$  for two phases in contact with each other must be equal i.e.  $\mu_A = \mu_B$ . When two metals are brought into contact with each other, electrons will flow from one to another to achieve equilibrium, resulting in excess charge at the interface on the surface of the metals. The difference in potential is known as the contact potential.

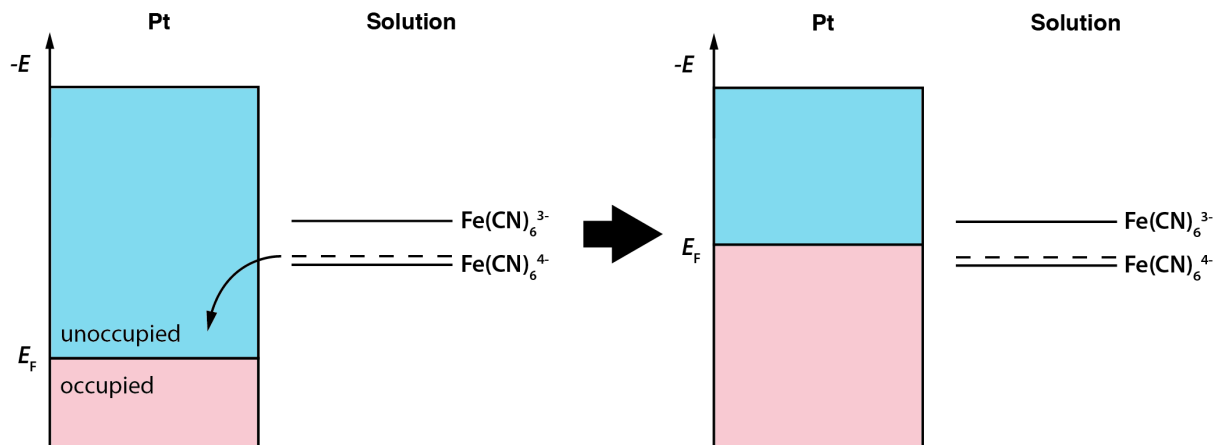
The electrochemical potential of electrons in a redox electrolyte is given by the Nernst equation

$$E_{\text{redox}} = E^{\circ}_{\text{redox}} + \frac{RT}{nF} \ln \left( \frac{[O]}{[R]} \right) \quad (13)$$

where  $n$  is the number of electrons transferred in the half-cell reaction,  $E^{\circ}$  is the standard potential, and  $[O]$  and  $[R]$  are the concentrations of the oxidised and reduced redox species.  $E_{\text{redox}} = \bar{\mu}_{\text{redox}}$  and can be considered as the Fermi level of the redox couple, provided the same energetic reference point is used. The energy of an electron in a solid-state material is measured with respect to the vacuum level, whereas the electrochemical potential of a redox species is usually measured against the standard hydrogen electrode (SHE), which lies at -4.5 eV with respect to the vacuum level. The Fermi level of a redox species can therefore be given by

$$E_{F, \text{redox}} = -4.5 \text{ eV} - qE^{\circ}_{\text{redox}} \quad (14)$$

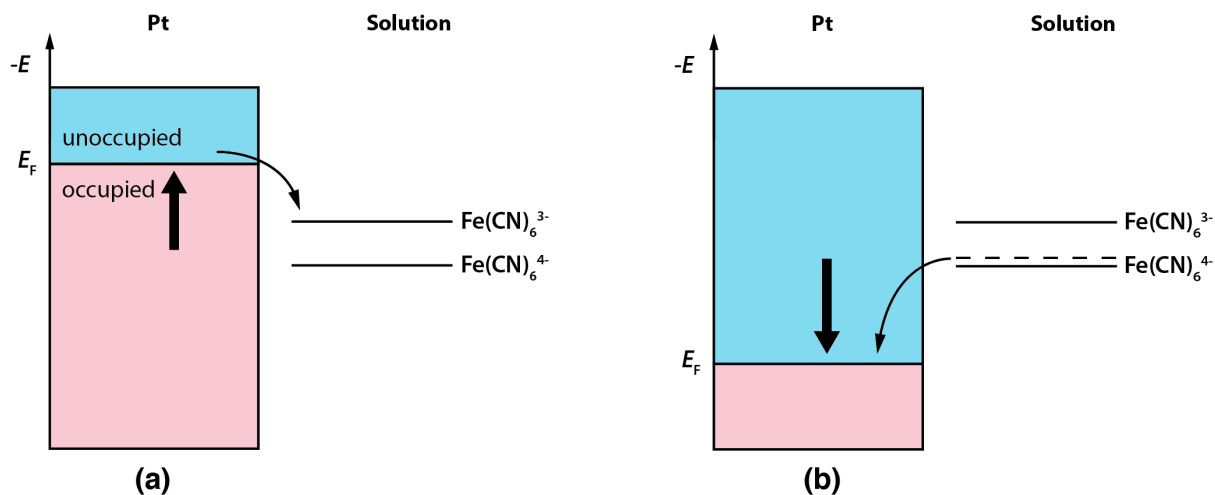
where  $q$  is the elementary charge of an electron.



**Scheme 4**

The equilibration of potential for a platinum electrode in contact with the iron ferricyanide/ferrocyanide redox couple in solution.

When a metal is in contact with a redox electrolyte, electrons will also flow from one phase to another until an equilibrium in electrochemical potential is reached. Take the example of the iron ferricyanide/ferrocyanide redox couple that is in contact with a platinum electrode, as illustrated in Scheme 4. Electrons will be transferred from the highest occupied molecular orbital (HOMO) of the ferrocyanide species to the metal electrode. This electrostatic charging will raise the Fermi level of the electrode to reflect the electrochemical potential of the electrolyte redox species.

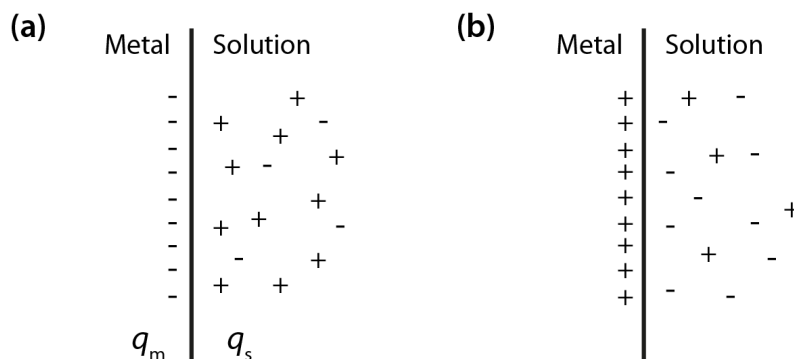


**Scheme 5**

The application of (a) a negative overpotential (bias) to the platinum electrode, which allows electron transfer from the metal to the electrolyte LUMO, or (b) a positive overpotential (bias), which allows electron transfer from the electrolyte HOMO to the metal.

At equilibrium, there is no net flow of electrons between the electrode and the electrolyte redox species. If a negative potential is applied to the metal electrode, the Fermi level will increase above the electrochemical potential of the lowest unoccupied molecular orbital (LUMO) of the ferricyanide species and electrons will be transferred from the platinum to the LUMO, resulting in the flow of reduction current, as illustrated in Scheme 5a. Similarly, if a positive potential is applied, the Fermi level will move below the HOMO of the ferrocyanide and electrons will be transferred from the HOMO to the platinum, resulting in the flow of oxidation current, as illustrated in Scheme 5b.

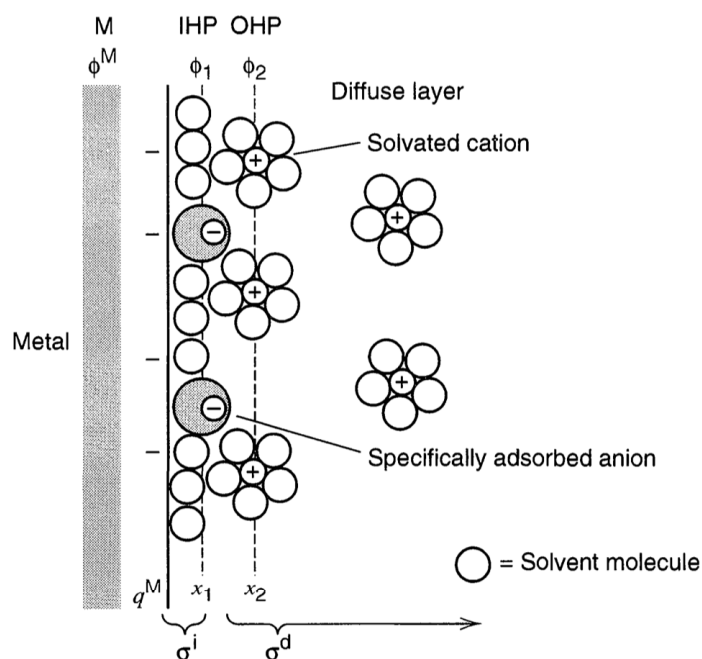
### 2.2.2 The electrode-electrolyte interface



**Scheme 6**

The metal-solution interface represented as a capacitor with a (a) negative and a (b) positive charge  $q_m$  on the metal surface.

When a metal is brought in contact with a solution, an excess charge  $q_m$  will develop at the metal surface, and an equivalent but opposite charge  $q_s$  (i.e.  $q_m = -q_s$ ) will develop at the electrolyte interface due to the equilibration of potential between the two phases, similar to when two metals are brought in contact. The charge on the metal represents an excess or depletion of electrons and will reside in a very shallow region at the surface ( $< 0.1 \text{ \AA}$ ), while the charge in solution is comprised of an excess of anions or cations within the vicinity of the electrode surface. The charged species and the corresponding dipoles present at the metal-electrolyte interface are called the electrical double layer, and can be regarded somewhat as a capacitor. The charges  $q_m$  and  $q_s$  are often given as charge densities  $\sigma$  in  $\mu\text{C}/\text{cm}^2$ , and the related double-layer capacitance  $C_d$  at a given potential is given in  $\mu\text{F}/\text{cm}^2$ . Scheme 7 shows a schematic representation of the double layer model at the metal-electrolyte interface.



#### Scheme 7

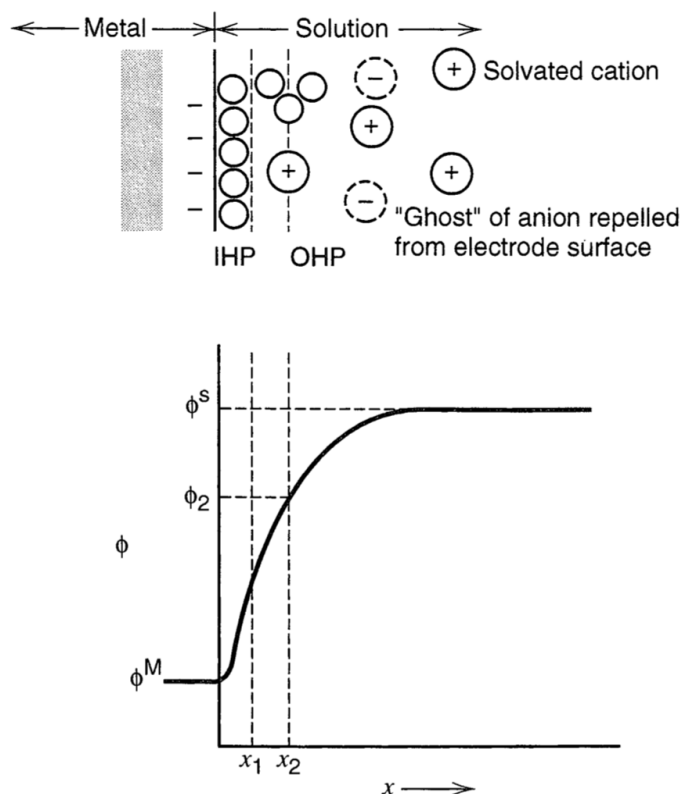
Schematic representation of the double layer model at the metal-electrolyte interface showing the inner Helmholtz plane (IHP), which contains solvent molecules and specifically adsorbed ionic and molecular species, and the outer Helmholtz plane (OHP), which contains solvated ions. The charge density of these layers is indicated by  $\sigma$ . Reproduced with permission from <sup>17</sup>, copyright John Wiley and Sons 2001.

The solution side of the double layer is itself comprised of different layers, including the inner Helmholtz layer closest to the interface, which contains solvent molecules or ionic species that are specifically adsorbed, and is defined by the inner Helmholtz plane (IHP) at a distance  $x_1$  from the interface. The total charge density associated with the species located within this layer is  $\sigma^i$  ( $\mu\text{C}/\text{cm}^2$ ). Solvated ions can approach the metal surface up to a distance of  $x_2$  from the interface, which is known as the outer Helmholtz plane (OHP), and these non-specifically adsorbed solvated ions make up the diffuse layer that extends to the bulk of the solution where there are no longer any perturbations in the ionic structure. The total charge density associated

with the species located within the diffuse layer is  $\sigma^d$ , and the total excess charge density of the solution components of the double layer  $\sigma^s$  is given by:

$$\sigma^s = \sigma^i + \sigma^d = -\sigma^m \quad (15)$$

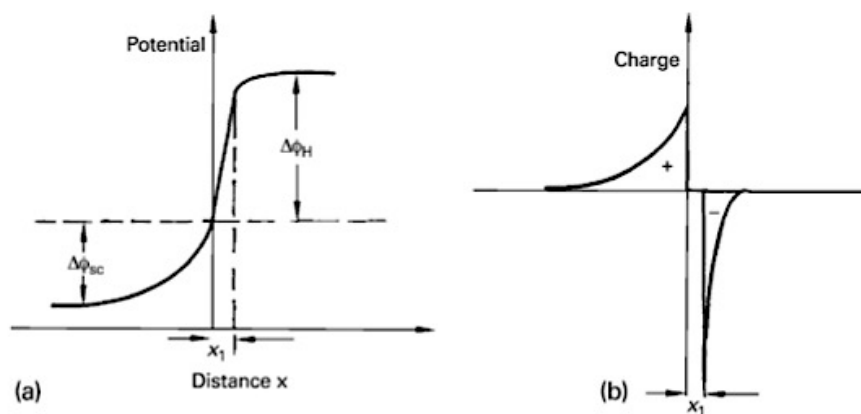
The thickness of the diffuse layer depends on the total ionic concentration in the solution. Concentrations of greater than 10 mM result in a diffuse layer of less than  $\sim 100 \text{ \AA}$ .



**Scheme 8**

The potential ( $\phi$ ) distribution at the metal-electrolyte interface in the absence of specifically adsorbed ions. Reproduced with permission from <sup>17</sup>, copyright John Wiley and Sons 2001.

Scheme 8 displays the potential distribution at the metal-electrolyte interface. As electroactive species can only approach the OHP, the potential drop across the double layer (known as the barrier height  $\Delta\phi$ ) can reduce the potential that this species will experience, and can, thus, influence the rate of redox processes that happen between non-specifically adsorbed electroactive species and the electrode. Furthermore, when a potential is applied to the metal, the change in the Fermi level of the metal will change the potential distribution and thus induce a reconstruction of the double layer, maintaining a neutral charge. The charging current can often be significant, with currents greater than the faradaic current for redox processes taking place.<sup>17</sup>

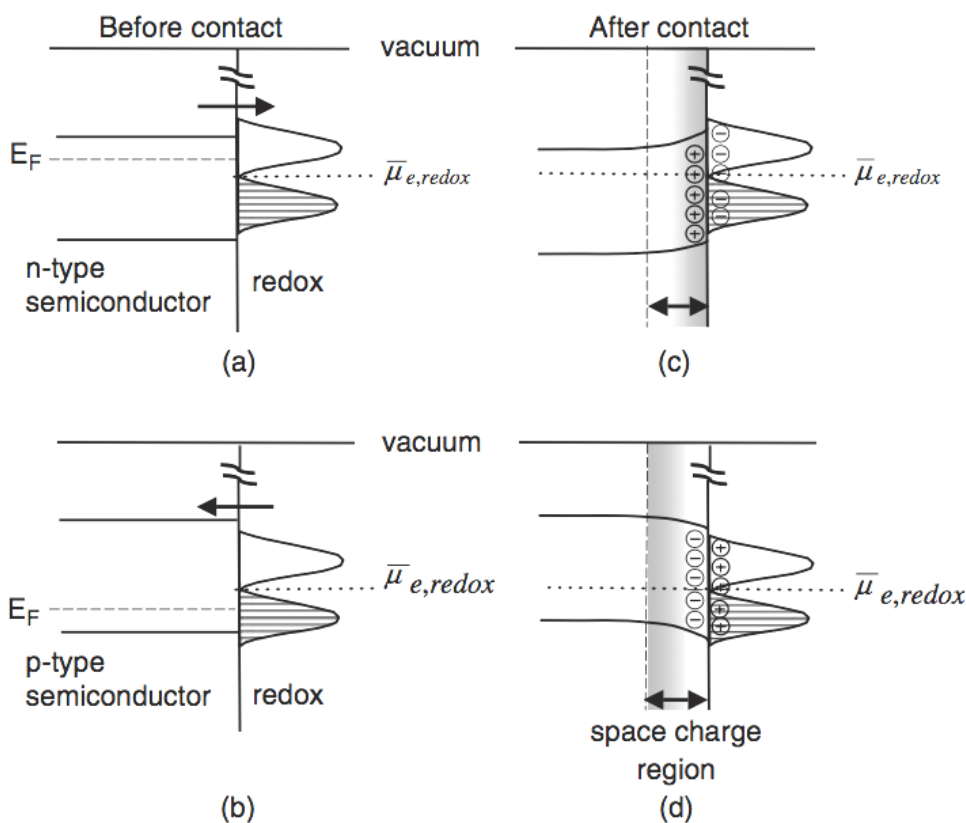


### Scheme 9

The (a) potential and (b) charge distribution at the semiconductor-electrolyte interface. Reproduced with permission from <sup>18</sup>, copyright John Wiley and Sons 2015.

The charge carrier density in semiconductors is much less than in metals, meaning that when a semiconductor is brought in contact with a solution, the excess charge induced by the equilibrium of potential between the two phases will be distributed over a greater distance than in a metal. For a moderately doped semiconductor, this so-called *space charge region* can extend 10-1000 nm inside the semiconductor region. The electrochemical potential of electrons near this region is different than those in the semiconductor bulk, and this phenomenon is similar to the diffuse double layer formed on the solution side of an electrode in solution. An example of the potential and charge distribution in the space charge region and diffuse layer is shown in Scheme 9.

As most of the potential drop occurs in the space charge region, rather than at the semiconductor solution interface (i.e. in the Helmholtz layer), the position of the band at the interface does not change. Consider when the electrochemical potential of a solution is within the bandgap and lies below the Fermi level of the semiconductor resulting in electrons being transferred to the solution phase; the positive charge at the semiconductor surface causes the band energies to become more negative with increasing distance inside the bulk, where it then remains flat without the influence of any charges or fields. This phenomenon is known as *band bending* and is illustrated for both a n- and p-type semiconductor in Scheme 10. As a result, in the given example, any excess electron in the space charge region would move towards the bulk of the semiconductor in the direction that is consistent with the existing electric field, while an excess hole in the bulk would move towards to the interface. The potential at which no excess charge exists in the semiconductor is the potential of zero charge. As there are no fields and no space-charge region under such conditions, the bands themselves are not bent, and this potential is known as the *flat-band potential*.<sup>17</sup>



#### Scheme 10

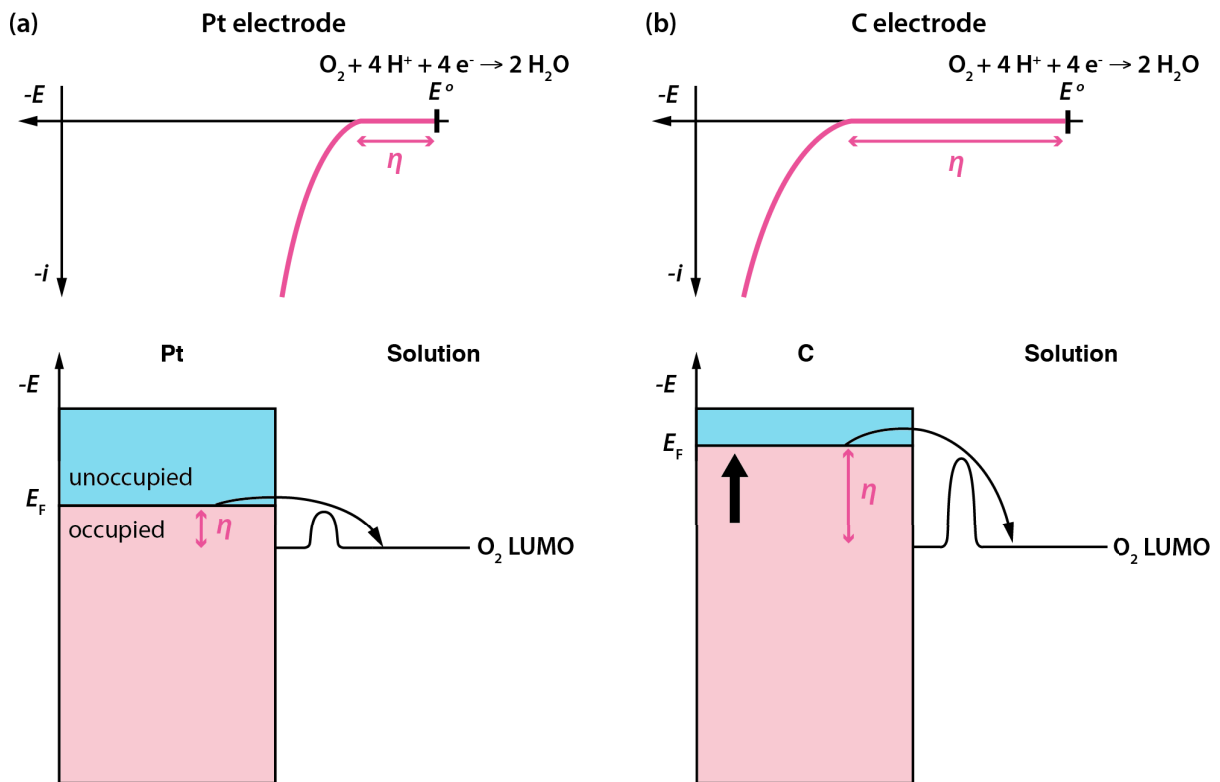
Band bending taking place at the semiconductor-electrolyte interface for a semiconductor with a Fermi energy  $E_F$  in contact with a redox species with an electrochemical potential of  $\mu_e$  lying in-between the semiconductor bandgaps. The situation before and after contact is shown for an n-type semiconductor in (a) and (c), respectively, and for a p-type semiconductor in (b) and (d). The arrows represent the direction of the electron flow. Reproduced with permission from <sup>19</sup>, copyright Elsevier 2007.

### 2.2.3 The relation between current and potential

For a non-spontaneous cell-reaction to take place, an overpotential  $\eta$  must be applied, which is the magnitude of potential applied over the equilibrium potential  $E_0$  i.e.

$$|\eta| = |E - E_0| \quad (16)$$

Take the example of the oxygen reduction reaction (ORR) at platinum or carbon; the overpotential  $\eta$  for ORR obtained at carbon is significantly greater than at platinum, despite having a similar  $E_F$ , the identical oxygen LUMO and, thus, the identical thermodynamic energy requirement. The extra potential is required to overcome the greater kinetic barrier for ORR at carbon compared to that at platinum, as illustrated in Scheme 11.



**Scheme 11**

Current-potential curves for the oxygen reduction reaction (ORR) at (a) platinum and (b) carbon electrodes, as well as band diagrams, illustrating the difference in activation energy required to overcome the kinetic barrier for ORR at each electrode.

The overall current  $i$  for a reaction  $O + e^- \rightleftharpoons R$  is the difference between the cathodic and anodic currents,  $i_{\text{red}}$  and  $i_{\text{ox}}$ , respectively:

$$i = i_{\text{red}} - i_{\text{ox}} \quad (17)$$

Each current is proportional to its corresponding heterogeneous rate constant  $k_{\text{red}}$  and  $k_{\text{ox}}$ , respectively, such that:

$$i_{\text{red}} = F A k_{\text{red}} [O] \quad (18)$$

and

$$i_{\text{ox}} = F A k_{\text{ox}} [R] \quad (19)$$

where  $A$  is the surface area of the electrode,  $[O]$  and  $[R]$  are the concentrations of the oxidised or reduced species at the surface of the electrode, and  $F$  is the Faraday constant. The rate constants  $k_{\text{red}}$  and  $k_{\text{ox}}$  can be written as a function of the standard heterogeneous rate constant  $k^0$ :

$$k_{\text{red}} = k^0 e^{\frac{-\alpha F(E-E^0)}{RT}} \quad (20)$$

and

$$k_{\text{ox}} = k^0 e^{\frac{(1-\alpha)F(E-E^0)}{RT}} \quad (21)$$

where  $\alpha$  is a dimensionless parameter that is a measure of the symmetry of the energetic barrier for electron transfer. The overall current is thus given by:

$$i = F A k^0 \left( [O] e^{\frac{-\alpha F(E-E^0)}{RT}} - [R] e^{\frac{(1-\alpha)F(E-E^0)}{RT}} \right) \quad (22)$$

At equilibrium, there is no net flow of current due to the cathodic and anodic currents being equal and opposite in value such that:

$$i_0 = i_{\text{red}} = i_{\text{ox}} \quad (23)$$

$i_0$  is known as the *exchange current* and can be written in terms of the bulk concentrations of the oxidised and reduced species:

$$i_0 = F A k^0 [O]_{\text{bulk}}^{(1-\alpha)} [R]_{\text{bulk}}^{\alpha} \quad (24)$$

From the equations 22 and 24, the current-potential equation can be described in terms of overpotential  $\eta$  rather than equilibrium potential:

$$i = i_0 \left[ \frac{[O]}{[O]_{\text{bulk}}} e^{\frac{-\alpha F \eta}{RT}} - \frac{[R]}{[R]_{\text{bulk}}} e^{\frac{(1-\alpha)F \eta}{RT}} \right] \quad (25)$$

where  $\eta = E - E_0$ . The first term in the brackets describes the cathodic component of the current at a given potential, while the second term similarly describes the anodic component. If there are no mass-transfer limitations (i.e. the solution is stirred well, or the currents are low), the concentration of the oxidised and reduced species at the surface and in the bulk will be similar, such that  $[O]/[O]_{\text{bulk}}$  and  $[R]/[R]_{\text{bulk}}$  will be approximately 1 and equation 25 will reduce to the *Butler-Volmer equation*:

$$i = i_0 \left[ e^{\frac{-\alpha F \eta}{RT}} - e^{\frac{(1-\alpha)F \eta}{RT}} \right] \quad (26)$$

For large values of  $|\eta|$ , either the cathodic or the anodic component in equation 26 will become significantly greater than the other back reaction, such that:

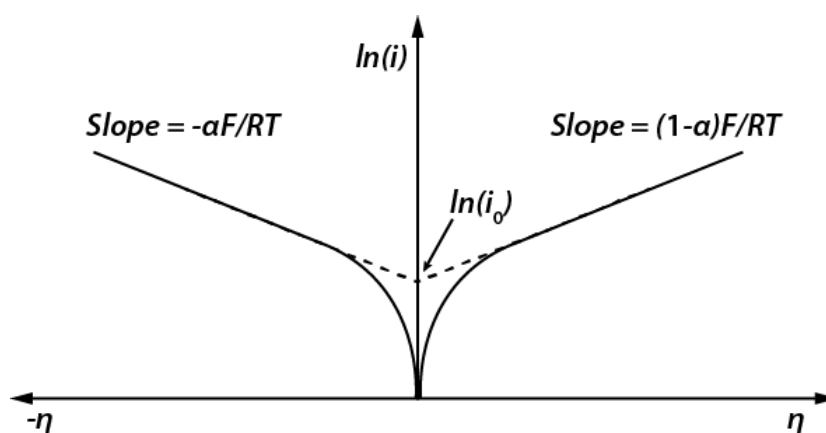
$$i_{\text{ox}} = i_0 e^{\frac{-\alpha F \eta}{RT}} \quad (27)$$

$$i_{\text{red}} = -i_0 e^{\frac{(1-\alpha)F \eta}{RT}} \quad (28)$$

or

$$\eta = \frac{RT}{\alpha F} \ln i_0 - \frac{RT}{\alpha F} \ln i_{ox} \quad (29)$$

$$\eta = -\frac{RT}{(1-\alpha)F} \ln i_0 - \frac{RT}{(1-\alpha)F} \ln i_{red} \quad (30)$$



**Scheme 12**

Tafel plots for the anodic and cathodic directions of the reaction  $O + e^- \rightleftharpoons R$ .

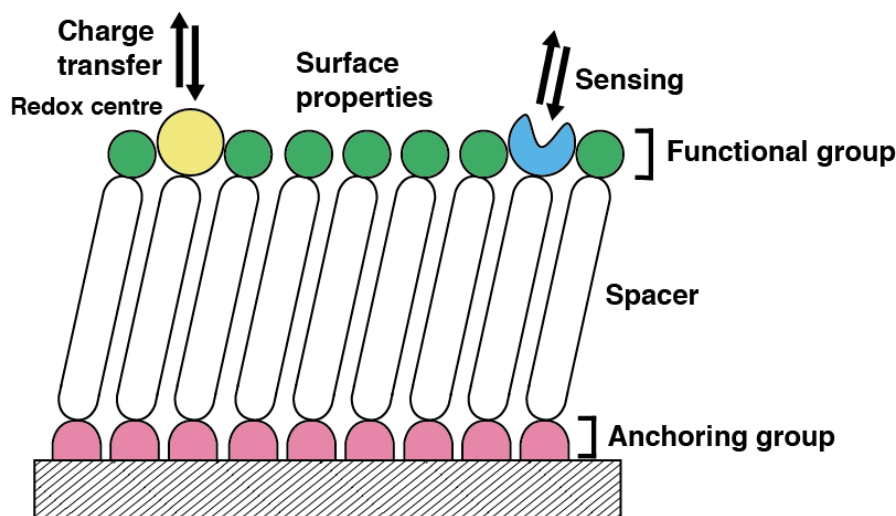
A plot of  $\log(i)$  against  $\eta$ , also known as a *Tafel plot*, will thus allow the exchange current  $i_0$  to be determined from the y-intercept, as shown in Scheme 12. At low overpotentials ( $< 50$  mV), the plots deviate from a linear behaviour as the back reaction ceases to be negligible. At large overpotentials the slope can also deviate due to mass-transfer limitations. The Tafel slope provides information on the response of the system to the applied potential and is highly dependent on the mechanism of the electrochemical process taking place. For multistep electrochemical processes that involve the transfer of several electrons or protons, the Tafel slope can provide an insight into the rate determining step and the mechanistic aspects of an electrochemical process.<sup>20</sup>

## 2.3 Surface modification of electrode materials

### 2.3.1 Chemically modified electrodes

A chemically modified electrode (CME) is a conducting or semiconducting material that has been modified with an adlayer of a monomolecular, multi-molecular, ionic or polymeric film that alters the electrochemical, optical or other properties of the electrode interface.<sup>21</sup> The substrates are derived from conventional electrode materials, while the adlayers may be very diverse in their nature and their properties. Modification may impart a number of improvements or properties on the electrode, such as increased sensitivity or selectivity, chemical and electrochemical stability, broadened useable potential windows and antifouling properties. Surface characterisation techniques, including electrochemical, spectroscopic or spectroelectrochemical techniques, have become essential tools not only to verify the function of CME's but also provide a basis upon which improvements or refinements of the modification approach can be made in order to enhance performance. A schematic representation of a CME is shown in Scheme 13, with an

anchoring group that binds the adlayer to the electrode surface, functional groups that impart particular properties or functions to the CME, and a spacer (such as an alkyl chain) that typically exists between the anchoring group and the functional groups.



**Scheme 13**  
Schematic representation of a chemically modified electrode.

The surface of electrodes can be modified in different ways, such as through:

- 1) Physisorption – long range or weak van der Waals attraction between the adsorbate and the substrate.
- 2) Chemisorption – the strong adsorption of molecules on the surface through the spontaneous formation of a chemical bond.
- 3) Covalent attachment – functional groups on the surface may be modified through the formation of a new, covalent chemical bond.
- 4) Polymer layers – attachment *via* physisorption, chemisorption or physical anchoring e.g. inside pores at the surface of the electrode, or due to the low solubility of the polymer in the contact/electrolyte solution.

Modification of oxides can be done using a number of chemistries including silanes, phosphonates, carboxylates, catechols, acetylacetonates, hydroxamates, alkenes, alkynes, amines, thiols, Grignard agents and more.<sup>22–28</sup> The following sections will focus on the most well-established methods for modifying electrode materials.

### 2.3.2 Langmuir-Blodgett assembly

The Langmuir-Blodgett (L-B) assembly technique was originally developed using amphiphilic molecules containing a hydrophobic tail and a hydrophilic head, such as surfactants and fatty acids; however, other systems such as nanoparticles or biological species may also be used. These species become spontaneously orientated at a liquid/gas interface e.g. when the

hydrophilic head group of a sparingly water-soluble species becomes partially solubilised and the hydrophobic tail extends into the gaseous phase in order to reduce the free energy of the system. Intermolecular interactions may exist between the orientated molecules. Homogenous films or films of mixed composition can be prepared. Amphiphiles commonly used to form L-B films include acids ( $C_nH_{2n+1}COOH$ ), alcohols ( $C_nH_{2n+1}OH$ ), esters ( $C_nH_{2n+1}COOR$ ), amides ( $C_nH_{2n+1}CONH_2$ ), amines ( $C_nH_{2n+1}NH_2$ ) and nitriles ( $C_nH_{2n+1}CN$ ).<sup>21</sup>

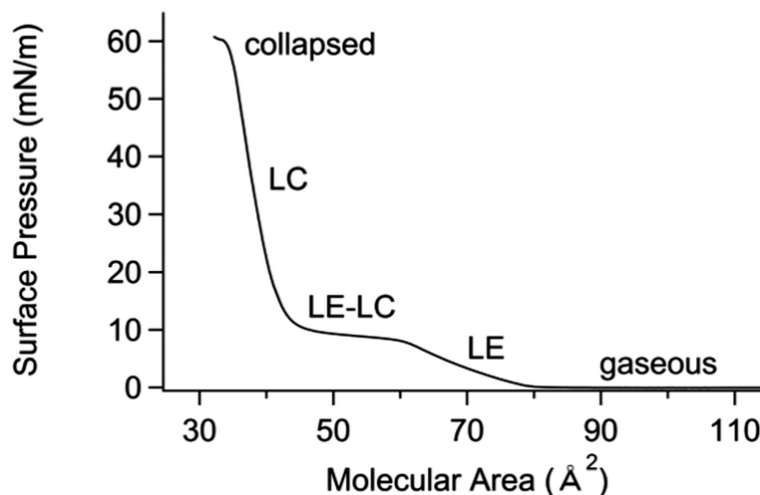


**Figure 1**

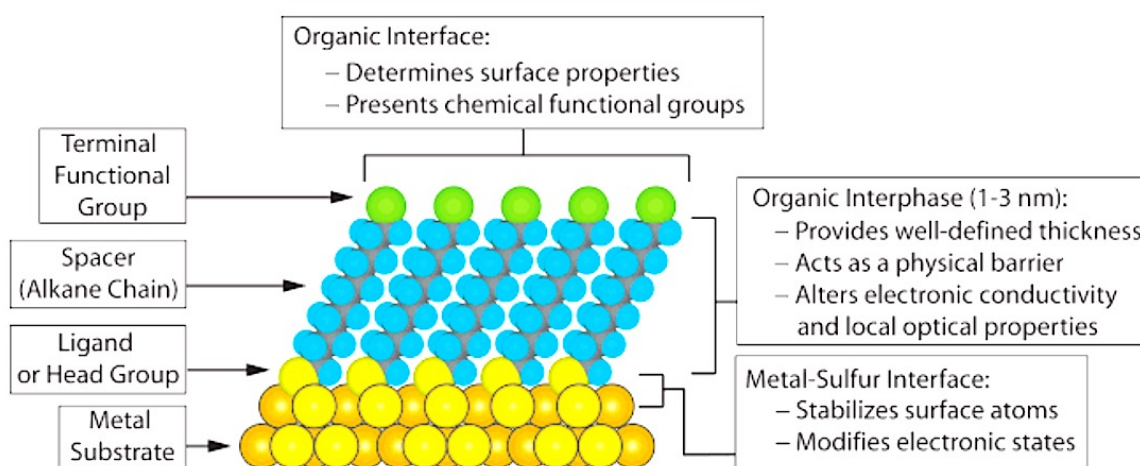
An example of a pressure-area isotherm for a monolayer of 1,2-dipalmitoyl-*sn*-glycero-3-phosphocholine on water at 25 °C, with the different phases assigned as gaseous, liquid-expanded (LE), the co-existence of LE and liquid-condensed (LC), LC, and collapsed phases.<sup>29</sup> Reproduced from <sup>29</sup> with permission from the PCCP Owner Societies.

A solution containing the molecules of interest is added to a solvent, such as water, and the lateral pressure at the gas/liquid interface is increased by using a moveable barrier in a Langmuir trough. As the molecular film is compressed, it goes through a series of phase transitions, as exemplified in Figure 1. Once a highly ordered, compressed film is formed, it can be transferred to the surface of an electrode by withdrawing the electrode substrate transversely out of (receding deposition) or advancing the substrate into (extending deposition) the liquid layer, while maintaining a constant pressure by moving the barrier. Receding deposition results in the hydrophobic tail depositing on the substrate surface, while extending deposition results in the hydrophilic head groups depositing on the substrate surface. In addition to simple monolayers, multi-layers and complex architectures can also be achieved using L-B assembly.<sup>21</sup> Given that the film is held in place through van der Waals forces, they suffer from poor thermal and mechanical resistance and may easily be removed from the surface using certain solvents.

### 2.3.3 Self-assembly

Modification of a substrate *via* the spontaneous adsorption of molecules is termed as self-assembly. The assembly mechanism may take place from the liquid phase or from the vapour phase. These molecules are typically bound to the surface of the substrate *via* chemisorption. In addition to chemisorption, intermolecular interactions within the film also provide a driving force

for the film formation and play an important role in the interface structure. When monolayers are formed as the result of self-assembly, they are known as self-assembled monolayers (SAMs). The molecules chemisorb onto the substrate surface *via* a head group and are separated from a tail group by a spacer, as illustrated in Scheme 14. The spacer is typically an alkyl chain; however, it can also be a different kind of molecular skeleton. Lateral interactions between the spacer chain and between tail groups orientate the molecules perpendicular (usually with a certain tilt angle) to the surface and can potentially facilitate an increase in coverage and thickness up to packing density limits. Functional groups on the tail end of the SAM may impart certain functionalities or properties to the electrode.<sup>30</sup>



**Scheme 14**

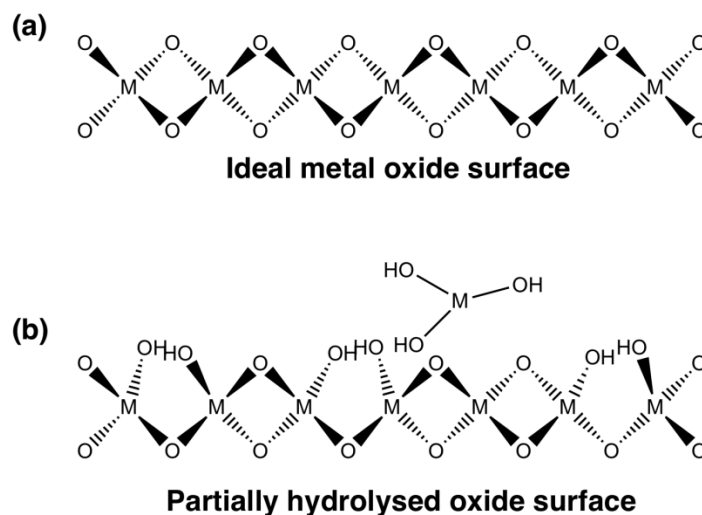
Schematic diagram of a single-crystalline SAM of an alkanethiol adsorbed on a (111) Au surface. Reprinted with permission from <sup>30</sup>, copyright 2005 American Chemical Society.

Commonly used adsorbates in SAMs are thiolates on metals, such as Au or Ag<sup>30</sup>; however, a number of different species are used on different substrates, including silane SAMs on oxides<sup>31</sup>, carboxylic acid SAMs on oxides or metals such as Ti or Ni<sup>30,31</sup>, or terminal-alkynes on Si<sup>22</sup> or Au.<sup>32</sup>

#### 2.3.4 Modification of TCO's

Chemical modification of oxides have been widely used to control their surface and interface properties and has found use in applications ranging from organic electronic devices, photovoltaic cells and biosensors, to devices with supported catalysts.<sup>33</sup> In particular, TCO electrodes such as ITO, TiO<sub>2</sub>, SnO<sub>2</sub>, ZnO etc. have been modified in order to enhance heterogeneous electron transfer processes with solution species that are thermodynamically favoured but inhibited due to kinetics e.g. hydrophobic solution species.<sup>34</sup> Confinement of redox species at the surface of these materials is meant to allow fast and reversible redox processes and mediation of charge transfer with solution species. Satisfactory electron transfer rates can be achieved by virtue of the redox species being in close proximity to electronically active sites on the metal oxide. Different oxides may differ significantly in terms of their properties, such as their conductivity, chemical or

mechanical stability etc.; however, most oxides have a similar propensity for surface modification as a result of surface hydroxyl groups (-OH), which can act as anchoring points for densely packed monolayers. A broad range of different chemistries may be used to modify oxides. Covalent modification can be carried out using silanes or alkenes/alkynes, or alternatively the surface can be modified through chemisorption of species such as carboxylic acids, phosphonic acids, thiols or amines.<sup>31,34</sup>



#### Scheme 15

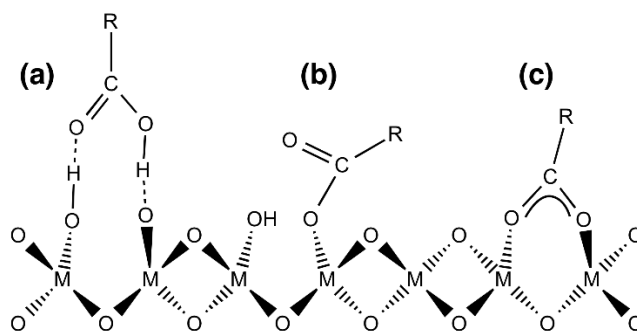
Schematic representation of (a) an ideal metal oxide surface and (b) an oxide surface that has been partially hydrolysed resulting in hydroxyl groups, in addition to possible physisorbed metal hydroxide species.

Scheme 15a is a representation of an ideal oxide surface. Hydrolysis of bridging oxygen species at the surface can result in the formation of hydroxyl species, while extensive hydrolysis can lead to the formation of fully hydrolysed, metal hydroxide species that may in turn physisorb on the surface, as shown in Scheme 15b. These hydroxide species, as well as variations in electron-rich defect or dopant sites, lead to heterogeneity in the electron transfer rates or chemical compatibility of oxide surfaces.<sup>34</sup> As such, electrical ‘hot spots’ and ‘dead spots’ may exist in varying degrees on oxide surfaces, such as on ITO.<sup>35</sup> Indium oxide has a favourable equilibrium constant for hydrolysis ( $K = 4.3 \times 10^1$ ), while the fully hydrolysed indium hydroxide species  $\text{In}(\text{OH})_3$  has a very low solubility product ( $K_{\text{sp}} = 1.3 \times 10^{-37}$ ). On the other hand, the hydrolysis of tin oxide is significantly less favourable ( $K = 4.3 \times 10^{-10}$ ), while the fully hydrolysed  $\text{Sn}(\text{OH})_2$  or  $\text{Sn}(\text{OH})_4$  species have a higher solubility than  $\text{In}(\text{OH})_3$ .<sup>34</sup> Such variations in the surface state of different oxides that have been synthesised or pre-treated using different methods should be taken into consideration when using chemical modification methods.

#### 2.3.4.1 Silanes

Silanes attach to oxide surfaces through metal-oxygen-silicon bonds that form on reaction with surface hydroxyl groups, with the removal of one or more leaving group. Suitable leaving groups on the silane include chloro or alkoxy groups (e.g. methoxy or ethoxy groups), and each silane modifier can form multiple bonds with the surface, as shown in Scheme 16. The functional group

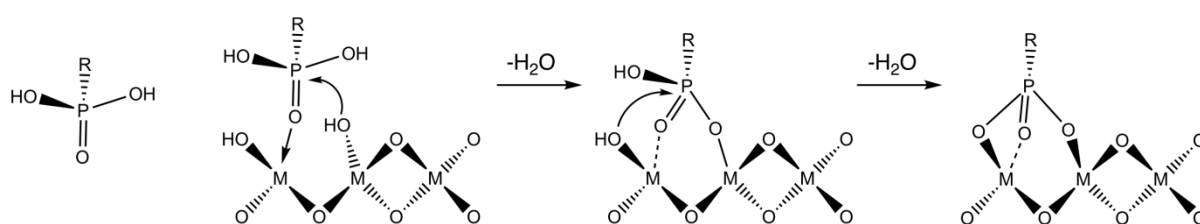




**Scheme 17**

Schematic representation of different possible binding motifs of carboxylic acids on an oxide surface, including (a) hydrogen bonding, (b) ester bonds to a metal centre, and (c) bridging chelation of two metal centres by the carboxylate ion.

### 2.3.4.3 Phosphonic acids/phosphonates



**Mono- to multidentate binding**

**Scheme 18**

Schematic representation of the binding mechanism of phosphonic acids to a Lewis acidic metal oxide, with mono-, bi- and tri-dentate binding modes due to differing degrees of heterocondensation with neighbouring hydroxyl groups.

Phosphonic acids and their ester derivatives are known to chemisorb strongly onto oxide surfaces. Both dissolved phosphonic acids and phosphonate esters can self-assemble on oxide surfaces and the outcome can be highly dependent on the type of solvent used, as well as its dielectric constant, the pH, and temperature. Weak van der Waals or hydrogen bonding interactions can often be superseded by inducing the formation of stronger covalent bonds through annealing. On Lewis acidic oxides, the phosphoryl oxygen (P=O) coordinates to a Lewis acidic site on the surface, which leads to the P atom becoming more electrophilic and inducing heterocondensation with neighbouring hydroxyl groups, as illustrated in Scheme 18. On oxides lacking Lewis acidity, initial hydrogen bonding interactions with the surface induce heterocondensation reactions, and this can also be enhanced by annealing. The P-O-M bonds formed are strong and a large number of different binding motifs are possible. Phosphonic acids and esters tend to form monolayers and, due to the stability of the P-O-M bond, are more resistant to hydrolysis than silane-derived interfaces; however, this only applies in pH's below around 5 to 6, thus limiting their use at basic pH's.<sup>25,38,39</sup>

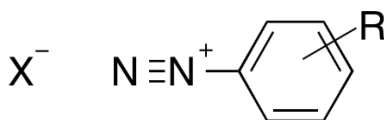
### 2.3.5 Electrochemical modification

Electrochemical modification (or electrografting) allows the surfaces of conductive materials to be modified with organic layers by transferring electrons between the electrode and the modifying reagent, or by using a reducing or oxidising agent. A large number of chemistries can be used on

a broad number of materials, ranging from carbon to metals, silicon and oxides.<sup>40</sup> Examples of oxidative electrochemical modifications include the use of amines on glassy carbon (GC), Au or Pt,<sup>41</sup> or carboxylates and alcohols on carbon materials.<sup>40</sup> Reductive electrochemical modifications include the use of vinylic species, which has been carried out on a number of metal, carbon, silicon and semiconductor substrates.<sup>42</sup> However, the most well-known and studied reductive electrochemical reduction chemistry is that of diazonium salts.

### 2.3.6 Modification using diazonium salts

Aryl diazonium salts are a group of compounds  $\text{Ar-N}_2^+\text{X}^-$  sharing a diazonium  $\text{N}_2^+$  functional group, where  $\text{X}^-$  is an organic or inorganic counter anion, as shown in Scheme 19. Their existence has been known since their first use in the synthesis of organic dyes in 1858. Diazonium salts react with activated aromatic molecules *via* an electrophilic aromatic substitution reaction to form azo compounds, a reaction known as azo coupling, which is still hugely important in the synthesis of dyes. The diazonium group also activates the aryl ring to nucleophilic aromatic substitution and can be displaced by a broad number of species, including halogens,  $\text{CN}$ ,  $\text{NO}_2$ ,  $\text{OH}$ ,  $\text{SH}$  etc.



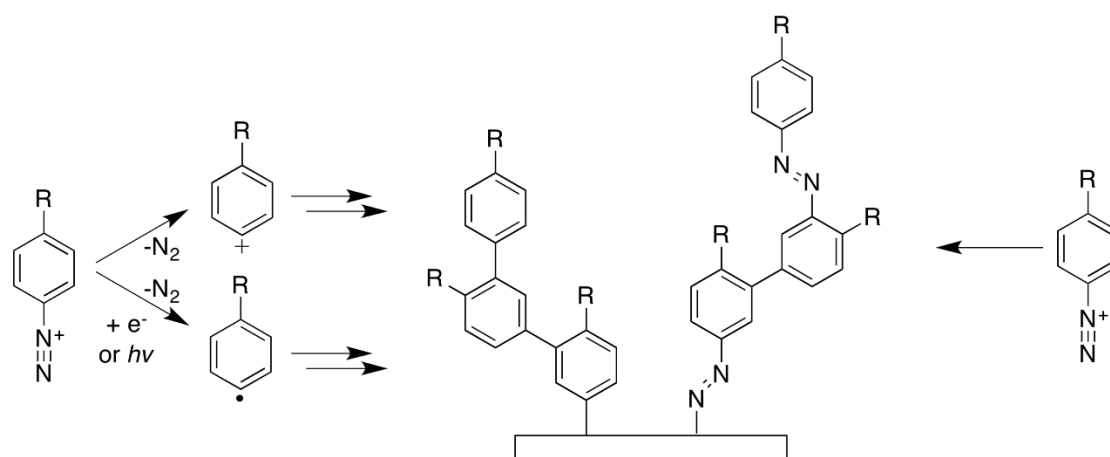
#### Scheme 19

The structure of a diazonium salt.

In 1992 Pinson and co-workers described the reaction mechanism of the modification of carbon electrodes by diazonium salts,<sup>43</sup> which led to a number of publications being published on the modification of surfaces with diazonium salts in the proceeding decades. They have found use in a wide variety of applications, including chemo- and biosensors, anti-corrosion coatings, and molecular electronics, to name but a few, and their use has been widely reviewed.<sup>40,44,45</sup> Their synthesis from the corresponding aromatic amines (anilines) is straightforward and can be carried out *via* diazotisation in acidic aqueous media in the presence of sodium nitrite ( $\text{NaNO}_2$ ), or in aprotic media in the presence of *tert*-butyl nitrite ( $(\text{CH}_3)_3\text{CONO}$ ) or nitrosonium tetrafluoroborate  $\text{NOBF}_4$ . Aqueous solutions of diazonium salts are generally unstable above  $5^\circ\text{C}$  and thus must be used *in situ* in the solution it was prepared in. The use of a stabilising anion, such as the tetrafluoroborate anion ( $\text{BF}_4^-$ ), can lead to enhanced thermal stability and allows the salts to be isolated and used at room temperatures. The functional group (R) does not necessarily have to be in the para-position of the aryl ring, and the ring itself may have more than one substituent.

A broad number of materials have been modified using diazonium salts, including electrodes such as carbon (including GC, highly oriented pyrolytic graphite<sup>46</sup>, pyrolysed photoresist films<sup>47</sup>,

mesoporous carbon<sup>48</sup>), metals (including noble metals, such as Au<sup>49</sup>, Pt<sup>50</sup> and Ag<sup>51</sup>, as well as base metals, such as Cu<sup>52</sup>, Fe<sup>41</sup>, Ni<sup>41</sup>, and Zn<sup>41</sup>), semiconductors (such as Si, gallium/indium arsenide<sup>53</sup>, or boron-doped diamond<sup>54</sup>) and oxides (including ITO<sup>55</sup>, tin oxide<sup>56</sup>, fluorine-doped tin oxide<sup>57</sup> and TiO<sub>2</sub><sup>58</sup>), as well as other substrates such as organic materials (including polyethylene<sup>59</sup>, polypropylene<sup>59</sup>, Teflon<sup>60</sup>), nitrides<sup>59</sup> and carbides<sup>59</sup>. Diazonium salts have also been used to modify particles in solution, including metallic or oxide nanoparticles, carbon nanotubes (CNTs) and nanodiamonds.<sup>61</sup> The reaction of the diazonium salt with a substrate or particle can be a spontaneous chemical or electrochemical (i.e. at open circuit potentials) reaction, or induced e.g. by external application of electrochemical potential, UV light, microwaves, ultrasound or mechanical grafting. Most studies and applications are carried out using carbon or metallic materials, and these are mainly modified by applying an electrochemical potential or by spontaneous processes.



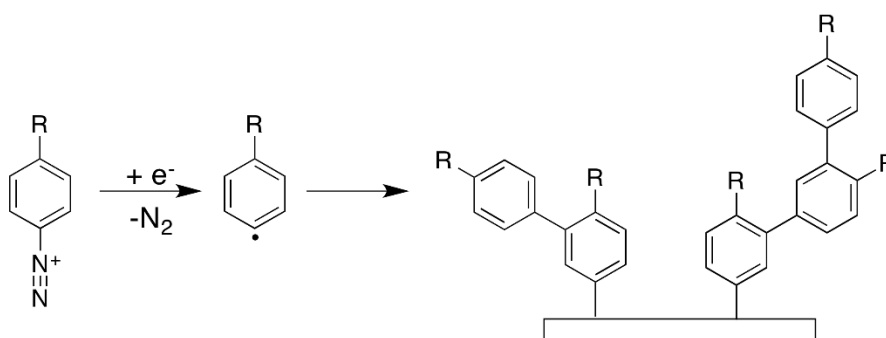
**Scheme 20**

An overview of the different mechanisms by which surfaces can be modified by diazonium salts.

An overview of the different mechanism by which a surface can be modified by diazonium salts is shown in Scheme 20. The surface can either be modified by the adsorption of the diazonium cation, or by the adsorption of a diazonium decomposition (dediazonation) product. Dediazonation can be heterolytic, whereby an aryl cation is formed, or homolytic, whereby an aryl radical is formed. Heterolytic decomposition can be thermally induced, while homolytic decomposition can be induced by electrochemical reduction at an electrode or by a reducing agent, or alternatively by photolysis. The dediazonation products can be highly reactive and form polymeric, branched structures as a result of addition at the meta-position of the aryl ring of already-grafted species. Furthermore, the diazonium cation can also add at the meta-position resulting in azo-linkages within the layer. The nature of the resulting film is highly dependent on the conditions used, as well as the diazonium salt itself and the nature of the substrate. Films can range from a monolayer thickness up to thicknesses of 100's of nm's.

### 2.3.7 Electrochemical grafting using diazonium salts

Electrochemical modification using diazonium salts is usually carried out in acetonitrile; however, it can also be carried out in other aprotic solvents, aqueous acidic solutions or ionic liquids. As previously mentioned, the diazonium salt undergoes homolytic decomposition upon reduction and an aryl radical is formed (illustrated again in Scheme 21 for clarity). When a potential is applied at an electrode, the reaction becomes self-limiting as the surface of the electrode is passivated and the charge transfer resistance of the interface inhibits the reduction of further diazonium species. This can be seen in cyclic voltammograms or chronoamperometry as a rapid decrease in cathodic current density, as demonstrated in Figure 2.



**Scheme 21**  
The electrochemical reduction of a diazonium salt at an electrode.

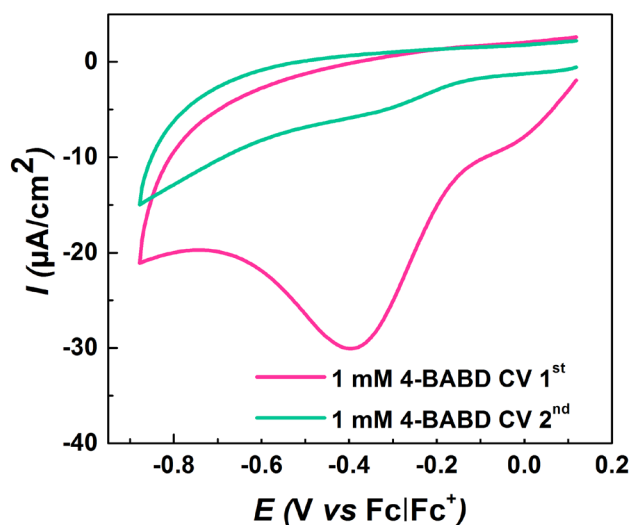
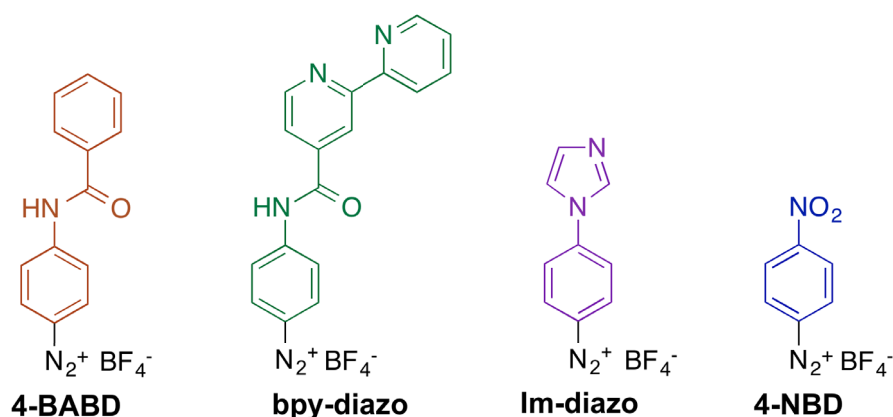


**Figure 2**  
The first and second cyclic voltammograms of 1 mM 4-benzamidobenzenediazonium tetrafluoroborate in acetonitrile (0.1 M TBAF) using a gold working electrode. Scan rate = 50 mV/s.

The reduction potential of a diazonium salt can be correlated to the Hammett constant of its substituent.<sup>62</sup> Comparing the reduction potentials (Table 1) of the diazonium salts used in this study (Scheme 22) using the same planar ITO working electrode, it is possible to see that the reduction potentials span a wide potential range from -0.92 to -0.25 V (vs  $\text{Fc}/\text{Fc}^+$ ), and that the order the potentials do indeed correlate to the expected electronic inductive effects of each respective diazonium salt.



**Scheme 22**

The diazonium salts used in this study in order of increasing reduction potential, with the most electron withdrawing substituents on the right.

**Table 1**

The electrochemical reduction potentials of the diazonium salts used in this study in acetonitrile, determined using cyclic voltammetry with a planar ITO working electrode.

<i>Diazonium salt</i>	<i>Reduction potential (V vs Fc/Fc<sup>+</sup>)</i>
4-nitrobenzenediazonium tetrafluoroborate ( <b>4-NBD</b> )	-0.25
4-(1H-imidazol-1-yl)benzenediazonium tetrafluoroborate ( <b>Im-diazo</b> )	-0.56
4-([2,2'-Bipyridine]-4-carboxamido)benzenediazonium tetrafluoroborate ( <b>bpy-diazo</b> )	-0.64
4-benzamidobenzenediazonium tetrafluoroborate ( <b>4-BABD</b> )	-0.92

### 2.3.8 Electrochemical response of adsorbed monolayers

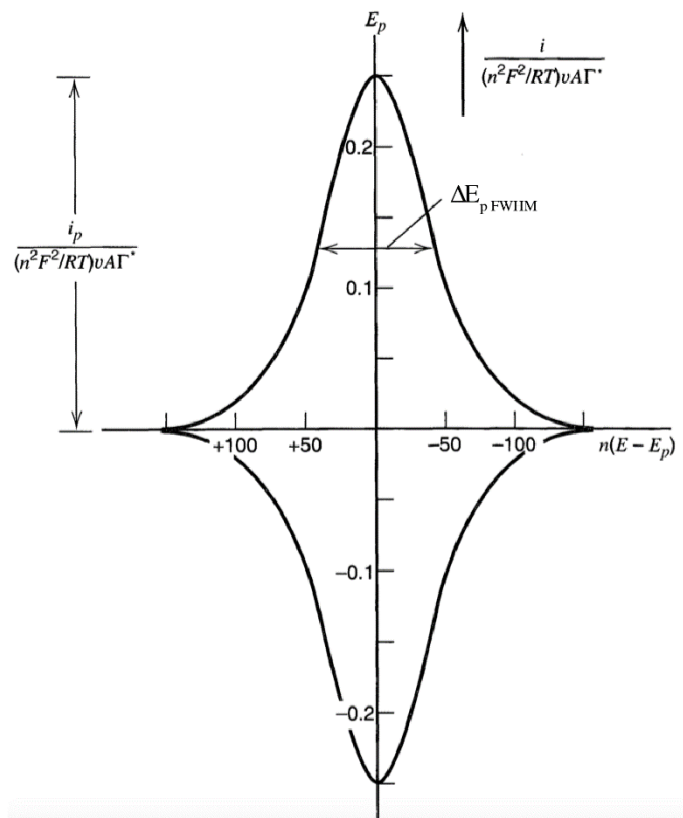
The electrochemical response of redox species for the reaction  $O + ne^- \rightleftharpoons R$  can be heavily influenced by the adsorption of O or R on the surface of the electrode. Assuming negligible current from dissolved O or R species, and that the coverages of the redox species  $\Gamma_O$  and  $\Gamma_R$  are independent of potential, i.e. there is no electrochemically-induced desorption/deactivation or adsorption/activation, and that all of the reduced adsorbed-O become adsorbed-R, i.e.

$$-\frac{\partial \Gamma_O(t)}{\partial t} = \frac{\partial \Gamma_R(t)}{\partial t} = \frac{i}{nFA} \quad (31)$$

then the current-potential equation can be given by:

$$i = \frac{n^2 F^2 v A \Gamma^* \left( \frac{b_O}{b_R} \right) \exp \left[ \left( \frac{nF}{RT} \right) (E - E^0) \right]}{RT \left\{ 1 + \left( \frac{b_O}{b_R} \right) \exp \left[ \left( \frac{nF}{RT} \right) (E - E^0) \right] \right\}^2} \quad (32)$$

where  $v$  is the scan rate,  $b_O$  and  $b_R$  are parameters related to the Gibbs free energies of adsorption of O and R, and  $\Gamma^*$  is the total coverage of species (i.e.  $\Gamma_O + \Gamma_R$  at a given time  $t$ ). A current-potential curve for such a system is shown in Scheme 23.



**Scheme 23**

A cyclic voltammogram curve for reduction and oxidation of the adsorbed species O showing the peak current and full width at half maximum (FWHM). Reproduced with permission from <sup>17</sup>, copyright John Wiley and Sons 2001.

The peak current  $i_p$  is given by:

$$i = \frac{n^2 F^2}{4RT} v A \Gamma^* \quad (32)$$

and the peak potential  $E_p$  is given by:

$$E_p = E^o - \left( \frac{RT}{nF} \right) \ln \left( \frac{b_O}{b_R} \right) \quad (33)$$

The peak current is proportional to the scan rate  $v$ , whereas for diffusing species it is proportional to the square root of the scan rate  $v^{1/2}$ . Once corrected for any residual current, such as charging current, the area beneath the reduction wave represents the total charge  $Q$  required to fully reduce the adsorbed layer and can thus be used to calculate the total coverage:

$$\Gamma^* = \frac{Q}{nFA} \quad (34)$$

For species whose adsorption is described by the Langmuir isotherm and follows ideal Nernstian behaviour, the cathodic peak is equal to the anodic peak ( $E_{p,c} = E_{p,a}$ ) and the full width at half maximum (FWHM) for a cathodic or anodic wave of is given by:

$$\Delta E_{p,FWHM} = 3.53 \frac{RT}{nF} = \frac{90.6}{n} \text{ mV} \quad (\text{at } 25 \text{ }^\circ\text{C}) \quad (35)$$

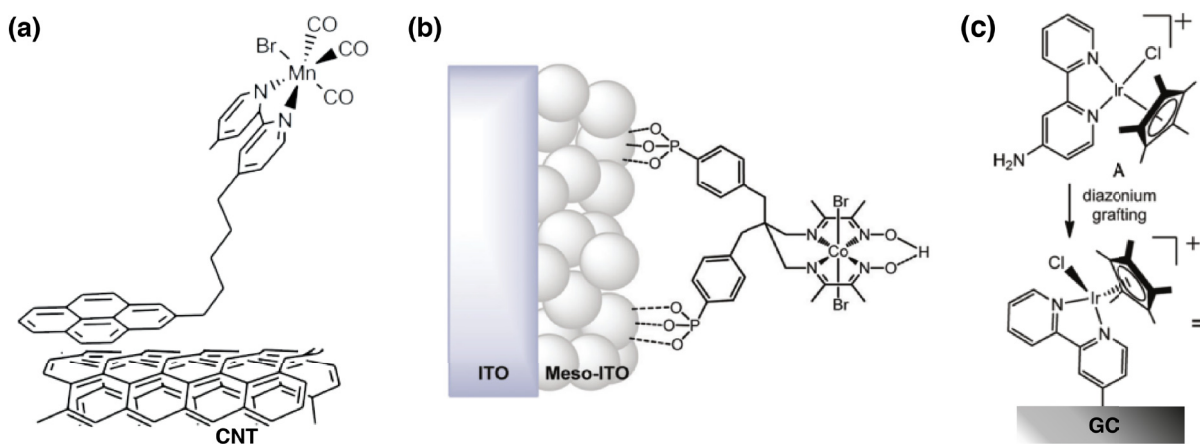
The degree to which the peak position  $E_p$  will deviate from  $E^\circ$  will depend on the relative adsorption strength of O and R. If  $b_O = b_R$  then  $E_p = E^\circ$ . If  $b_O > b_R$  then  $E_p$  will shift to more negative potentials, while if  $b_R > b_O$  then  $E_p$  will shift to more positive potentials. Lateral interactions between the redox species in the layer can also have an effect on the curve shape. Attractive interactions will lead to a reduction in  $\Delta E_{p,FWHM}$ , while repulsive interactions will lead to an increase in  $\Delta E_{p,FWHM}$ . Experimentally, modified electrodes deviate from such ideal behaviour due to a number of complex factors, such as limited mass and charge transport, structural changes upon reduction or oxidation, and inhomogeneity of the electrode and the adsorbed species.<sup>17</sup>

### 2.3.9 Immobilisation of electrocatalysts on electrode surfaces

The immobilisation, or heterogenisation, of enzymatic and molecular catalysts on electrode surfaces is imperative, thereby increasing the number of addressable active sites, separating half-reactions and facilitating electronic contact, especially when using hydrophobic catalysts in aqueous conditions. A number of different approaches can be used to immobilise electrocatalysts on electrode surfaces taking advantage of many of the aforementioned chemistries. For the most part, molecular (homogenous) electrocatalysts used in energy conversion and storage reactions contain one or more metal centres coordinated by organic ligands<sup>5,63-66</sup> (although some examples of metal-free molecular systems do exist<sup>67,68</sup>).

The immobilisation of electrocatalysts on surfaces can be broadly arranged into three categories:

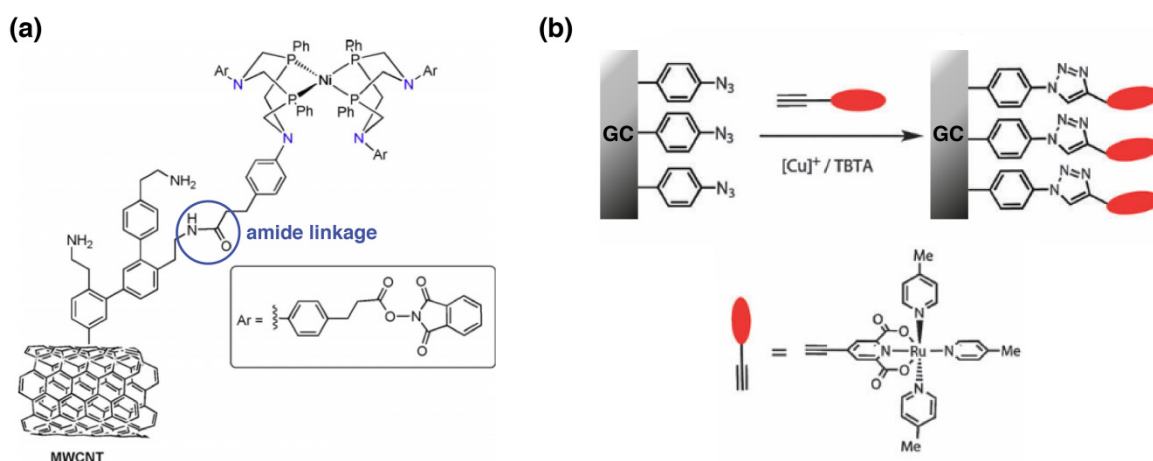
- i) the adsorption or covalent attachment of an electrocatalyst on to a surface *via* an anchoring group or reactive group on one or more of its ligands,
- ii) the formation of covalent bonds between the electrocatalyst and reactive groups on the surface, or
- iii) the *in situ* assembly of an electrocatalyst using ligands adsorbed or covalently attached to the surface.



**Scheme 24**

Schematic representation of three different examples where electrocatalysts have been immobilised on different electrode surfaces *via* an anchoring group or a reactive group on one or more of their ligands: (a) a manganese carbonyl bipyridyl  $\text{CO}_2$  reduction catalyst immobilised on a carbon nanotube (CNT) electrode *via* a pyrene anchoring group<sup>69</sup>, (b) a cobalt cobaloxime catalyst hydrogen evolution reaction (HER) catalyst immobilised on a mesoporous ITO electrode *via* phosphonic acid anchoring groups<sup>70</sup>, and (c) an iridium bipyridyl oxygen evolution reaction (OER) catalyst immobilised on a glassy carbon (GC) electrode *via* the electrochemical grating of a diazonium salt<sup>71</sup>.

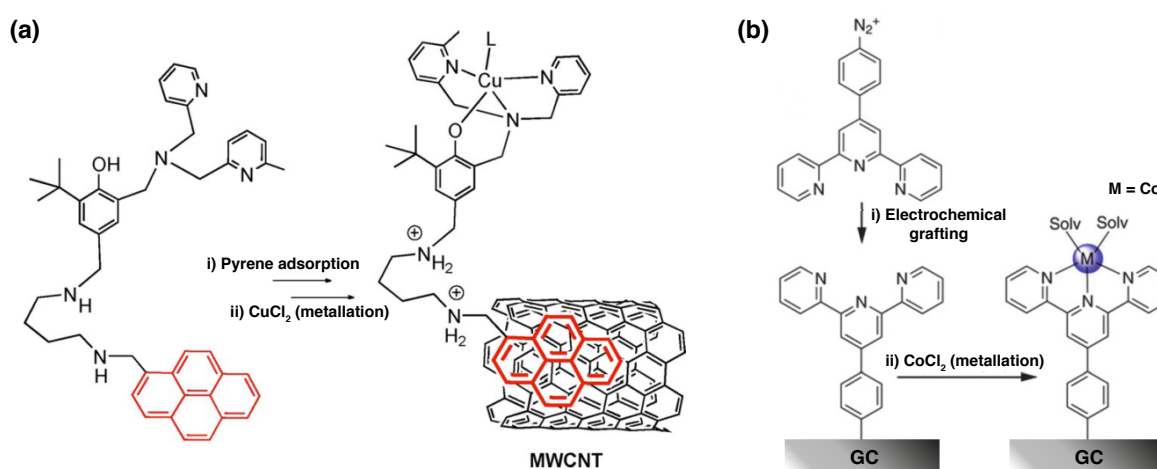
Several examples of electrocatalysts immobilised on different electrode surfaces *via* an anchoring group or reactive group on one or more of their ligands are displayed in Scheme 24. Scheme 24a shows an example by Reisner and co-workers of a manganese carbonyl bipyridyl  $\text{CO}_2$  reduction catalyst immobilised on a carbon nanotube (CNT) electrode using (non-covalent)  $\pi$ - $\pi$  interactions *via* a pyrene anchoring group attached to the bipyridine ligand.<sup>69</sup> Meanwhile, Scheme 24b shows another example by Reisner and co-workers of a cobalt cobaloxime hydrogen evolution reaction (HER) catalyst immobilised on a mesoporous ITO electrode *via* chemisorption of phosphonic acid anchoring groups<sup>70</sup>. Finally, Scheme 24c shows an example by Hinds, Lin and co-workers of an iridium bipyridyl oxygen evolution reaction (OER) catalyst immobilised on a glassy carbon (GC) electrode *via* the electrochemical grating of a diazonium group located on the bipyridine ligand.<sup>71</sup>



**Scheme 25**

Schematic representation of two different examples, where electrocatalysts have been immobilised *via* the formation of covalent bonds between the electrocatalysts and reactive groups on the electrode surfaces: (a) a nickel bisdiphosphine-based mimic of the active site of hydrogenase that catalyses the hydrogen oxidation reaction (HOR) and hydrogen evolution reaction (HER) immobilised on a multi-walled carbon nanotube (MWCNT) electrode *via* amide coupling to surface amino-groups<sup>72</sup>, and (b) a ruthenium oxygen evolution reaction (OER) catalyst immobilised on a glassy carbon (GC) electrode *via* azide-alkyne cycloaddition (or click reaction).<sup>73</sup>

Scheme 25 displays examples of electrocatalysts immobilised on different electrode surfaces *via* the formation of covalent bonds between the electrocatalysts and reactive groups on the electrode surfaces. Scheme 25a shows an example by Fontecave and co-workers of a nickel bisdiphosphine–based mimic of the active site of hydrogenase that catalyses the hydrogen oxidation reaction (HOR) and hydrogen evolution reaction (HER) immobilised on a multi-walled carbon nanotube (MWCNT) electrode *via* amide coupling between a carboxylic acid group on one of the catalysts ligands and amino groups grafted to the surface of the MWCNT.<sup>72</sup> Meanwhile, Scheme 25b shows an example by Sun and co-workers of a  $[\text{Ru}^{\text{II}}(\text{pdc})(\text{pic})_3]$  (pdc = 2,6-pyridine-dicarboxylate, pic = 4-picoline) OER catalyst immobilised on a glassy carbon (GC) electrode *via* copper-catalysed azide-alkyne cycloaddition (also known as a ‘click’ reaction) between an alkyne group located on a ligand of the catalyst and surface grafted azide groups.<sup>73</sup>



#### Scheme 26

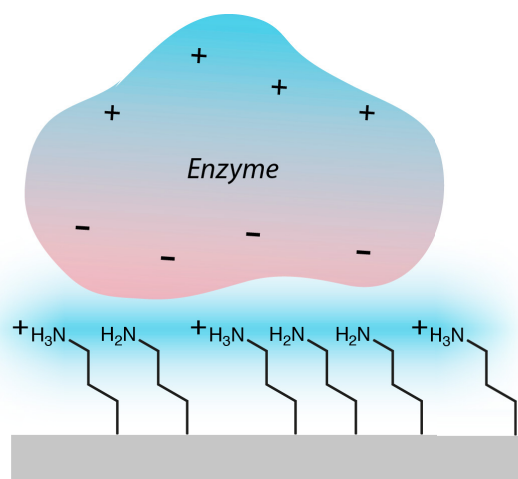
Schematic representation of two different examples of the *in situ* assembly of electrocatalysts on electrode surfaces using ligands adsorbed or covalently attached to the surface: (a) a copper phenolato oxygen reduction reaction (ORR) catalyst formed by incubating ligands that were immobilised on a multi-walled carbon nanotube (MWCNT) electrode *via* a pyrene anchoring group with  $\text{CuCl}_2$ ,<sup>74</sup> and (b) a bifunctional cobalt terpyridyl hydrogen evolution reaction (HER) and  $\text{CO}_2$  reduction catalyst formed by incubating terpyridine ligands that were immobilised on a glassy carbon (GC) electrode *via* the electrochemical grafting of a diazonium salt with  $\text{CoCl}_2$ .<sup>75</sup>

Finally, Scheme 26 displays examples of electrocatalysts immobilised on electrode surfaces *via in situ* assembly using ligands adsorbed or covalently attached to the surface. Scheme 26a shows an example by Thomas, Le Goff and co-workers of a copper phenolato oxygen reduction reaction (ORR) catalyst formed by incubating ligands that were immobilised on a MWCNT electrode *via* a pyrene anchoring group with  $\text{CuCl}_2$ .<sup>74</sup> In a similar manner, Scheme 26b shows an example by Fontecave and co-workers of a cobalt terpyridyl HER and  $\text{CO}_2$  reduction catalyst formed by incubating terpyridine ligands that were immobilised on a GC electrode *via* the electrochemical grafting of a diazonium salt with  $\text{CoCl}_2$ .<sup>75</sup>

Some of these aforementioned approaches can also be used to immobilise macromolecular catalysts, such as enzymes, onto electrode surfaces, e.g. the grafting of diazonium-modified horseradish peroxidase onto gold *via* electrochemical grafting<sup>76</sup>, or the commonly used approach

of forming of covalent bonds between amino-acids on the surface of proteins and reactive groups on the electrode surface. A number of coupling agents may be used for the latter approach, including glutaraldehyde<sup>77</sup>, N-Hydroxy-succinimide (NHS)<sup>78</sup> and N-ethyl-N'-(3-dimethylaminopropyl) carbodiimide (EDC) hydrochloride<sup>79</sup> agents. Otherwise, immobilisation also can be achieved using non-covalent adsorption driven by hydrophobic forces, electrostatic interactions, hydrogen bonding, van der Waals forces or affinity binding. Physical entrapment or encapsulation may be used as well. In depth descriptions of all of these approaches can be found elsewhere.<sup>3,80,81</sup> Enzyme immobilisation using electrostatic binding interactions will briefly be discussed further as this approach is applied in this work.

Ionisable functional groups on amino acids on the surface of proteins may be charged under certain pH's, depending on their pK values.<sup>82</sup> The coincident presence of electrostatic groups on the surface of an electrode can lead to electrostatic interactions between the electrode and individual amino acids on the enzymes' surface, or the enzyme as whole (i.e. if there is an overall polar charge distribution). This attraction and subsequent contact between the enzyme and the surface can lower the free energy of the system, and, in the case of an overall polar charge distribution across the enzyme, it can lead to an immobilisation of the enzyme with a preferential orientation, as illustrated in Scheme 27.<sup>81,83</sup> Interactions may be controlled by changing the pH or ionic strength of the solution, or the surface of the electrode. Certain functional groups may be introduced on the surface of the electrode to induce preferential orientation of enzymes, as demonstrated for a hydrogenase immobilised on SAM-modified gold electrodes by Heidary et al.<sup>84,85</sup>



#### **Scheme 27**

A schematic representation of an enzyme immobilised on an amino-functionalised electrode surface with a preferential orientation due to the electrostatic interaction between the overall positively charged surface (due to partial protonation of the amino functional groups) and the enzyme (which exhibits an overall polar charge distribution).

## 2.4 Spectroscopic methods

### 2.4.1 Spectroelectrochemistry

Spectroelectrochemistry (SEC) encompasses a whole range of different spectroscopic techniques that can be used to simultaneously obtain spectroscopic as well as electrochemical data for an electrochemical reaction inside an adequate cell. *In situ* techniques involve the study of a system while the electrode is immersed in the electrolyte of an electrochemical cell, and allows systems to thus be spectroscopically studied under potential control. This includes: UV-vis spectroscopy, infrared (IR) spectroscopy, Raman spectroscopy, X-ray adsorption spectroscopy (XAS), electron paramagnetic spectroscopy (EPR), luminescence spectroscopy and ellipsometry. *Ex situ* techniques involve the removal of the electrode from the electrolyte and allow spectroscopic studies to be carried out in air or under vacuum. This includes: X-ray photoelectron spectroscopy (XPS), low energy electron diffraction (LEED) and others. Removal of the electrode from the electrolyte or exposure to vacuum may change the nature of the electrode surface significantly.

The electrochemical cell setup is most often specific to each technique, and as such there is no standard setup. For example, *in situ* UV-Vis SEC requires the use of an optically transparent electrode (OTE). Light is transmitted through the electrode surface and the electrolyte, and the absorbance changes are measured using the detector of the spectrometer. In addition to transmission, measurements can also be done using (internal) reflection spectroscopy. The OTE in such systems may be a TCO, such as ITO or TiO<sub>2</sub>, or indeed any other conductor, provided it is sufficiently thin. Metal thin films such as Au or Pt are used, as well as fine wire meshes or minigrids that contain regions of alternating transparency in the cross-section of the light beam.<sup>86,87</sup> The diffusion layer for redox species in such systems can become larger than the openings in the minigrids. In general, species being probed by *in situ* SEC methods may be dissolved in the bulk of the solution or the diffusion layer, or they may be specifically adsorbed at the surface of an electrode. Certain techniques may be more sensitive to one of these, such as the use of UV-Vis or IR reflection SEC, which can be more sensitive to species closer to the surface of the working electrode. A number of different electrochemical techniques can in principle be employed in parallel, including voltammetry (cyclic voltammetry (CV), linear sweep voltammetry (LSV), chronoamperometry etc.), chronocoulometry, chronopotentiometry and step techniques.

### 2.4.2 UV-Vis spectroscopy

Absorption of UV and visible light involves the excitation of electrons in atoms and molecules from ground states to excited states. In chromophores, incident radiation can excite electrons from bonding ( $\sigma$  or  $\pi$ ) orbitals or non-bonding orbitals, to anti-bonding ( $\sigma^*$  or  $\pi^*$ ) orbitals. In the

case of transition metal complexes, incident light can excite electrons from the ligand molecular orbitals to the metal d-orbitals, if the ligand orbitals are all occupied. Likewise, incident light can excite an electron from metal d-orbital to a low-lying empty ligand molecular orbital. Such ligand-to-metal or metal-to-ligand charge-transfer electronic transitions result in intense adsorption bands. Adsorption may also take place due to excitation of electrons from metal d-orbitals to d-orbitals of higher energy.

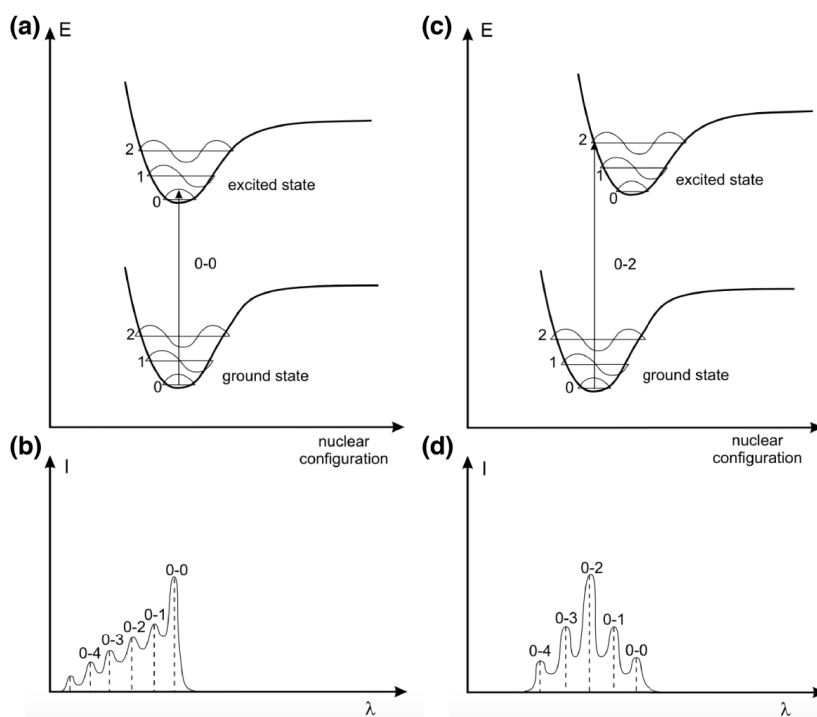
In UV-Vis spectroscopy, a sample is irradiated with light of continuously varying wavelengths and the adsorption of light at a given wavelength  $\lambda$  is given by the absorbance  $A(\lambda)$ :

$$A(\lambda) = \log \frac{I_0}{I} \quad (36)$$

where  $I_0$  is the intensity of the UV-Vis light source and  $I$  is the intensity of the detected light after passing through the sample. For dilute solutions, the adsorption follows the *Beer-Lambert Law*:

$$A(\lambda) = \log \frac{I_0}{I} = \varepsilon(\lambda)lc \quad (37)$$

where  $\varepsilon$  is the molar absorption coefficient,  $c$  is the concentration of the absorbing species and  $l$  is the (optical) path length of the absorbing solution.



**Scheme 28**

Potential energy diagrams showing vertical transitions between electronic states for a (a) 0-0 transition and a (c) 0-2 transition to a vibrationally excited state. The corresponding absorption spectra for the (b) 0-0 transition and (d) 0-2 transition with the dotted lines representing the absorption lines observed for a vapour, and the broadened solid spectra representing absorption spectra for a species in solution. Adapted with permission<sup>88</sup>, copyright Wiley 2001.

The motion of electrons is much more rapid than those of nuclei. The excitation of an electron to an empty orbital takes about  $10^{-15}$  s, whereas the characteristic time for a molecular vibration is around  $10^{-10} - 10^{-12}$  s. Therefore, the Franck-Condon principle states that electronic transitions are most likely to occur with no change in the position of the nuclei of the molecule and its environment. The resulting state is called a *Franck-Condon state* and the transition involved is called a *vertical transition*, as illustrated in Scheme 28. At room temperature, most of the molecules are in the vibrational ground state and so in addition to the purely electronic 0-0 transition shown, other vibrational transitions can take place whose intensities depend on the relative position and shape of the potential energy curves.<sup>88</sup>

Usually, broad absorption bands are observed in UV-Vis spectroscopy and this can be attributed to homogenous and inhomogeneous broadening. Homogenous broadening results from the existence of a continuous set of vibrational sublevels in each electronic state, whereas inhomogeneous broadening results from interactions between molecules in solution and the change in the solvation shell of a chromophore.

### 2.4.3 Vibrational spectroscopy

Vibrational spectroscopy is an invaluable, energy sensitive probe of molecular structures. It depends on periodic changes in the dipole moments (in infrared (IR) spectroscopy) or polarisabilities (in Raman spectroscopy) caused by molecular vibrations, and changes in frequencies during adsorption (in IR spectroscopy) or scattering (in Raman spectroscopy) of electromagnetic radiation. Each atom in a molecule has 3 degrees of freedom, resulting in  $3N$  degrees of freedom for  $N$  atoms. Since 3 degrees of freedom are translational and 3 are rotational,  $3N-6$  are fundamental vibrations for non-linear molecules (linear molecules have  $3N-5$  vibrations since rotation about the bond axis is not possible). These vibrations are normal modes, meaning all atoms vibrate with the same frequency and different amplitudes, while the centre of mass does not change. An expression can be derived from Hooke's law that gives the wavenumber of a vibration:

$$\tilde{\nu} = \frac{1}{2\pi} \sqrt{\frac{k}{\mu}} \quad (38)$$

where  $k$  is the force constant of the spring and  $\mu$  is the reduced mass  $\left(\frac{m_1 m_2}{m_1 + m_2}\right)$  of the diatomic molecules. Higher frequency vibrations are indicative of a stronger bond or a lower mass of the molecule. The potential energy of a vibration can be determined using the harmonic oscillator approximation. Solving the Schrödinger equation for the harmonic oscillator results in:

$$E_{\text{vib}} = \left( n + \frac{1}{2} \right) h\nu \quad (39)$$

where  $h$  is Planck's constant and  $n$  is the vibrational quantum number ( $n = 0, 1, 2 \dots$ ). Molecular vibrations are therefore quantised with equal distances between each energy level. Although the harmonic oscillator is a good approximation to describe molecular vibrations, they are essentially anharmonic.

#### 2.4.4 Infrared spectroscopy

IR spectroscopy is widely used to characterise organic, inorganic and biological species, for which the mid-IR is useful (wavelengths from 2.5 to 25  $\mu\text{m}$ , which correspond to wavenumbers of 4000 to 400  $\text{cm}^{-1}$ ). For a molecule to absorb IR radiation and undergo a transition to a vibrational excited state, the electric field of the incident radiation must be oscillating at the same frequency as a vibration in the molecule (i.e. resonant absorption). Another condition is that the molecular dipole moment must change during the vibrational oscillation. The transition dipole moment couples the total molecular wave function of the initial and final vibrational states of the molecule,  $\Psi_f$  and  $\Psi_i$ , via the molecular dipole moment operator,  $\mu$ :

$$\mu_{fi} = \langle \Psi_f | \mu | \Psi_i \rangle \quad (40)$$

The transition dipole moment must therefore be non-zero ( $\mu_{fi} \neq 0$ ) in order for a transition to occur. For a polyatomic molecule, the dipole moment is a vector quantity with three Cartesian components, and is the sum of the charges on each  $\alpha$ th atom  $e_\alpha$  and its distance from the centre of mass of the molecule  $q_\alpha$ :

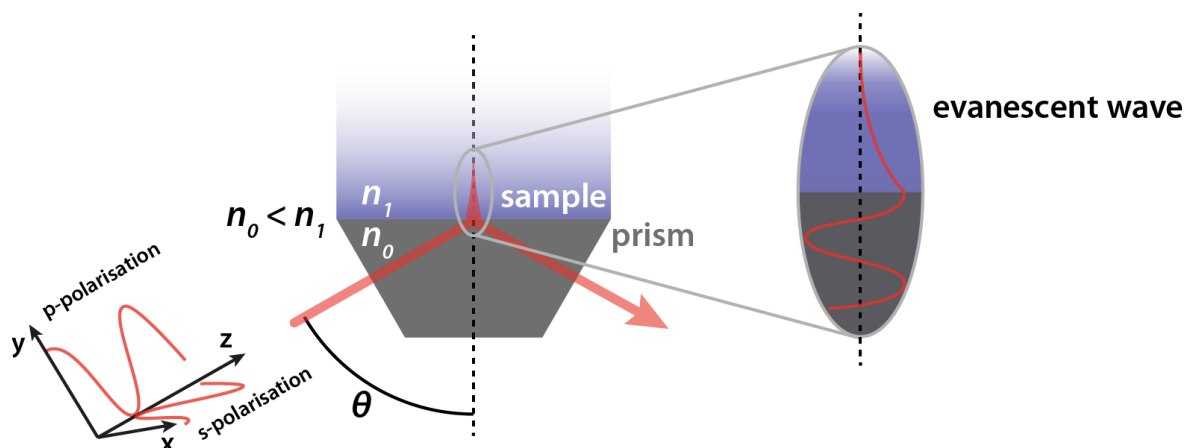
$$\mu = \sum_{\alpha} e_{\alpha} q_{\alpha} \quad (41)$$

For a transition to occur, the change in the dipole moment for a vibration must have a component in the same direction as the oscillation of the incident electric field. The probability  $A$  of a transition occurring is proportional to the square of  $\mu_{fi}$ , and for randomly orientated molecules to absorb unpolarised light, the probability is thus proportional to the sum of the transition probabilities along the three components:

$$A \propto \left( [\mu_x]_{if}^2 + [\mu_y]_{if}^2 + [\mu_z]_{if}^2 \right) \quad (42)$$

Molecular vibrations of polar molecules generally correspond to the strongest infrared absorption bands. Molecular vibrations that don't alter the dipole moment, and which are thus IR silent,

include homonuclear diatomic molecules, or the symmetric O=C=O stretch of CO<sub>2</sub>. As can be inferred from equation 38, the position of a vibration is related to the mass of the atoms involved, with lighter atoms vibrating at higher frequencies, as well as the strength of the bond (e.g. an sp, sp<sup>2</sup> or sp<sup>3</sup> bond). So-called 'group frequencies', which are characteristic of certain functional groups (e.g. C=O, -CH<sub>3</sub> etc.), may be used to assist in the interpretation of IR spectra.



**Scheme 29**

Schematic representation of attenuated total reflection (ATR) of incident IR radiation in an optical prism at an interface to an optically less dense medium. The incoming, unpolarised IR beam is defined by both perpendicular (s) and parallel (p) components relative to the plane of incidence.

Studying electrode-electrolyte interfaces using IR SEC can be complicated by the absorption of IR radiation by the bulk solution (especially when water is used, which adsorbs strongly throughout most of the mid-IR region). This can be overcome by using an attenuated total reflection (ATR) setup for IR studies. Total internal reflection of radiation takes place at an interface to an optically less dense medium when the angle of incidence is higher than a critical angle  $\theta_c$ , as illustrated in Scheme 29. The electric field of the reflected radiation penetrates the less dense medium without carrying any energy, and thus its intensity decays exponentially in the direction normal to the plane of incidence:

$$E = E_0 \exp\left(-\frac{z}{d_p}\right) \quad (38)$$

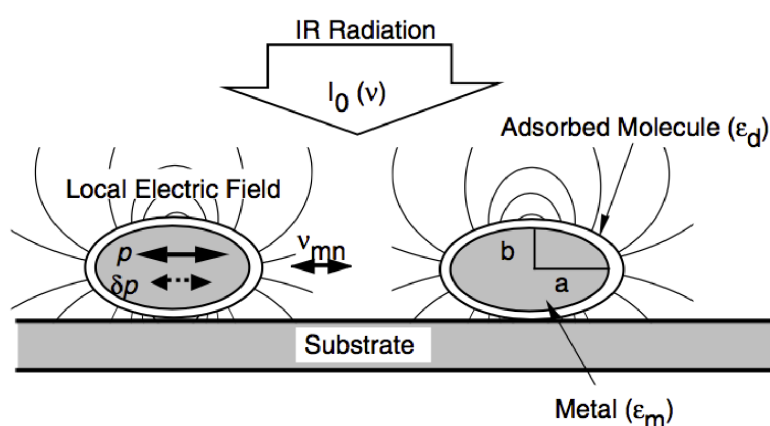
where  $d_p$  is the penetration depth at which the amplitude of the field has decayed to ca. 37% ( $\sim \exp^{-1}$ ) of its initial value. The penetration depth of this *evanescent wave* is a function of the angle of incidence  $\theta$ , the wavelength of the radiation  $\lambda$  and the ratio of the refractive indices of the optically more dense and less dense media,  $n_1$  and  $n_2$ , respectively:

$$d_p = \frac{\lambda}{2\pi \sqrt{\sin^2 \theta - \left(\frac{n_1}{n_0}\right)^2}} \quad (39)$$

An internal reflection element (IRE) or an ATR prism is coated with an electrode layer that is in contact with the electrolyte in a spectroelectrochemical cell. Typical materials used as IREs include silicon ( $n_{\text{Si}} = 3.42$ )<sup>89</sup>, germanium ( $n_{\text{Ge}} = 4.0$ )<sup>89</sup> or zinc selenide ( $n_{\text{ZnSe}} = 2.43$ )<sup>90</sup>. For a Si prism, an angle of incidence of  $60^\circ$  (as used in this work) results in a penetration depth of between 2.6 and  $0.7 \mu\text{m}$  for the spectral region of  $1000$  to  $4000 \text{ cm}^{-1}$ . To carry out SEC, the electrode material must be conductive and transparent for the IR beam. These conditions were fulfilled in this study either by using a very thin film (see below) of Au, or films of the transparent conductive oxides ITO ( $n_{\text{ITO}} \sim 1.5$  in near-IR)<sup>91</sup> or ATO ( $n_{\text{ATO}} \sim 2 - 4.5$  in mid-IR)<sup>92</sup>. The ATO used in this study is highly porous, meaning that the refractive index will be reduced by the presence of solvent within the pores.

#### 2.4.5 Surface Enhanced Infrared Absorption (SEIRA) spectroscopy

The optical properties of molecules can be dramatically altered when adsorbed on rough metal surfaces, islands or particles. This occurs in surface enhanced Raman scattering (SERS), which was first observed in 1973<sup>93</sup>, where enhancement in the Raman scattering of molecules of a million can be achieved compared to the free molecules. In 1980, it was discovered that a similar effect happens in the mid-IR spectral region, with an enhancement in IR adsorption of around 10-1000 times.<sup>94</sup> It was shown in studies correlating metal thickness and surface structure to the enhancement that this effect exists over a short-range which is within ca. 8 nm of the metal surface.<sup>95</sup>



#### Scheme 30

Schematic representation of the electromagnetic mechanisms of SEIRA on metal particles or islands. Incident IR radiation induces a dipole  $p$  in the particle, which in turn generates a local electric field around the particle that leads to enhanced adsorption in adsorbed molecules. Molecular vibrations can furthermore induce additional dipoles  $\delta p$  that perturb the optical properties of the metal. Adapted with permission from<sup>94</sup>.

The observed surface enhancement is presumably provided by a sum of individual effects<sup>94</sup>:

**1) Plasmon resonance (electromagnetic effect)** – the metal particles are polarised by the electric field of incident IR radiation due to the excitation of collective electron resonances (or localised plasmon modes). This induces a dipole in the metal, which in turn generates a local electromagnetic field around the particle that is stronger than that of the incident radiation. The induced electromagnetic field  $E_{\text{local}}$  is polarised along the surface normal to it at every point on the particle surface. The magnitude of the field depends on the induced dipole  $p$  and decays sharply with the distance  $d$  from the surface<sup>94</sup>:

$$|E_{\text{local}}|^2 = \frac{4p^2}{d^6} \quad (40)$$

The enhancement factor  $F$  at a distance  $d$  from the surface for a particle with a radius  $a_0$  can be estimated by<sup>94</sup>:

$$F_{\text{SEIRA}}(d) = F_{\text{SEIRA}}(0) \left( \frac{a_0}{a_0 + d} \right) \quad (41)$$

The enhanced electromagnetic field leads to an enhanced absorption by the molecules. The polarisation of the field along the surface normal means that only absorption due to vibrational modes perpendicular to the surface are enhanced, rather than modes parallel to the surface. This is known as the *surface selection rule*, which can be used to gain insight into the orientation of molecules at the surface of plasmonic structures.

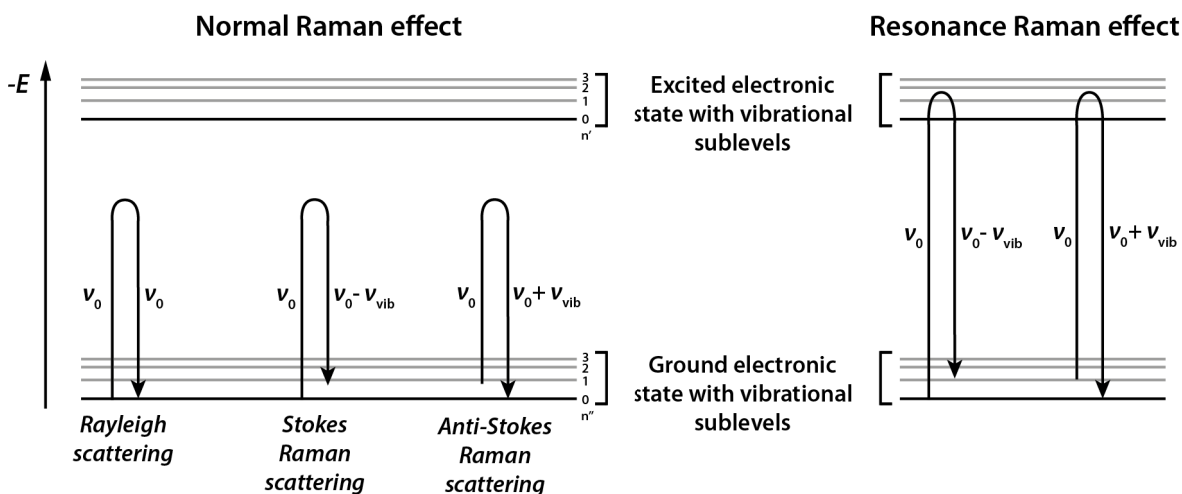
**2) Perturbation of the optical properties of the metal (electromagnetic effect)** – the dipoles of adsorbed molecules on the surface of a metal can induce dipoles that perturb the optical properties of the metal itself. This perturbation is enhanced around the vibrational frequencies of the molecule and in effect amplifies the corresponding absorption due to molecular vibrations.

**3) Chemical mechanism** – Chemisorption of molecules on the surface of the metal can lead to interactions that change the polarisability of the molecules due to donor-acceptor interactions, leading to an increase in the absorption coefficient.

#### 2.4.6 Raman spectroscopy

Raman spectroscopy is another, complementary form of vibrational spectroscopy that provides chemical and structural information like IR spectroscopy; however, rather than arising from a change in the dipole moment of a molecule, Raman spectroscopy arises from the change in polarisability of a molecule. A sample is irradiated with monochromatic (laser) light and most of this light passes through the system or is *elastically scattered* due to Rayleigh scattering with no

change in energy; however, a small amount of light is *inelastically* scattered due to the Raman effect.



### Scheme 31

Schematic representation of the Raman scattering effect and resonance Raman scattering effect.

The Raman effect is illustrated in Scheme 31. The incident photons of light excite electrons in the molecule, which is followed by the immediate re-emission of the photons as scattered light. Rayleigh scattering results in electrons in the ground state becoming excited and returning to the original ground state with no loss of energy ( $\nu_0 = \nu_0$ ). Raman scattering results in the excited electrons falling to a final energy state *other* than that original state. *Stokes* Raman scattering involves electrons excited from the ground state falling to a vibrational level with emission of a photon with *less* energy ( $\nu_0 = \nu_0 - \nu_{\text{vib}}$ ), whereas *anti-Stokes* Raman scattering involves electrons excited from a vibrational level falling to the ground state with emission of a photon with *greater* energy ( $\nu_0 = \nu_0 + \nu_{\text{vib}}$ ). In general, the intensity of scattering due to Stokes Raman scattering is greater than that due to anti-Stokes scattering; however, the ratio changes as the temperature of the sample rises and molecules become more vibrationally excited.

As only a very small proportion of photons undergo Raman scattering, techniques are employed to enhance scattering, including *surface enhanced Raman spectroscopy* (SERS) and *resonance Raman* (RR) spectroscopy. SERS functions in a similar way to SEIRA(S), with surface plasmon resonance at the surface of nanostructured metals inducing large electromagnetic fields that enhance scattering, or due to donor-acceptor interactions with adsorbed molecules. Resonance Raman scattering occurs when the wavelength of the incident light is similar to that of an electronic transition of the molecule, as illustrated in Scheme 31. Vibrational modes associated with excited electronic states are greatly enhanced, such as in chromophores like porphyrins where charge-transfer electronic transitions enhance metal-ligand stretching modes, in addition to vibrational modes associated with the ligand. The probability of Raman scattering can be enhanced by a factor up to  $10^6$  using RR.

#### 2.4.7 X-ray photoelectron spectroscopy

In X-ray photoelectron spectroscopy (XPS), a sample is irradiated with a high energy monochromatic X-ray source of a known wavelength (usually Al  $K_{\alpha}$  rays of 1486.7eV) in vacuum, which results in the ejection of electrons from core levels of atoms in the sample into the vacuum. The probability of these photoelectrons escaping without being inelastically scattered and losing energy decays exponentially with depth, meaning that XPS is a surface sensitive technique (< 10 nm). Because the energy of the incident irradiation is known ( $h\nu$ ), the kinetic energy of the emitted photoelectron  $E_k$  can be measured and the binding energy (BE) of the electron  $E_B$  can be determined according to:

$$E_B = h\nu - (E_k + \phi) \quad (42)$$

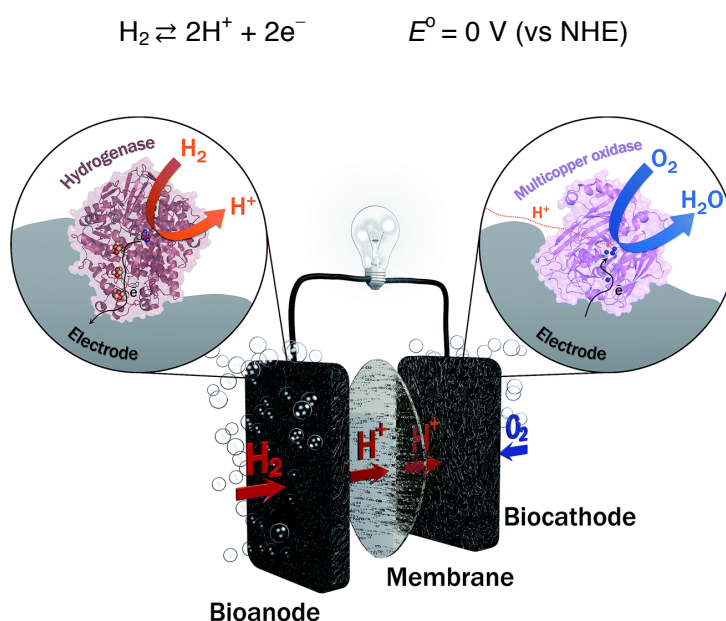
where  $\phi$  is the work function of the spectrometer and sample.

An XPS spectrum plots the number of ejected photoelectrons against their binding energy. Each element produces a set of well-defined peaks with characteristic binding energies corresponding to different atomic orbital levels e.g. 1s, 2s, 2p, 3s etc. The number of ejected photoelectrons corresponds directly to the amount of element in the sample and, therefore, atomic percentage value can be determined. The binding energies of electrons can provide information on the chemical state of elements in a sample. Changes in the oxidation state or chemical environment of an atom can lead to characteristic *chemical shifts* that can be compared to known materials. For example, it is possible to spectroscopically distinguish the different chemical environments of nitrogen in an amine, an imine or a protonated amine. In general, higher oxidation states lead to a greater coulombic interaction between the emitted electron and the ion core and, therefore, leads to higher binding energies.

The ejection of electrons from  $p$ ,  $d$  and  $f$  subshells leads to spectral peaks that are split into two components. The unpaired spin of an electron in a final state can be up or down, and when it occupies an orbital with non-zero orbital angular momentum there will be coupling between the unpaired spin and the orbital angular momentum, or *spin-orbit coupling*. The generated states  $j_+ = l + \frac{1}{2}$  and  $j_- = l - \frac{1}{2}$  are not degenerate and will therefore be observed in the spectrum. The lowest energy component is the one with the maximum  $j$  and the intensity ratio between the two components is given by the ratio of the multiplicities  $\frac{2j_++1}{2j_-+1} = \frac{2l+2}{2l}$ , which in turn determines the relative probability of transition to these states upon photoionisation.

## 2.5 Hydrogenases

The interconversion of chemical and electrical energy in fuel cells is seen as an alternative method of deriving power over the conventional combustion of fossil fuels. Use of hydrogen as an energy carrier results in relatively high efficiencies and the emission of water rather than CO<sub>2</sub>. Conventional fuel cells use Pt to catalyse the hydrogen oxidation reaction (HOR) at the cathode and the oxygen reduction reaction (ORR) at the anode. Hydrogenases are enzymes that can catalyse the interconversion of molecular hydrogen into protons and electrons with similar activities per active site to those of Pt catalysts<sup>96</sup>:

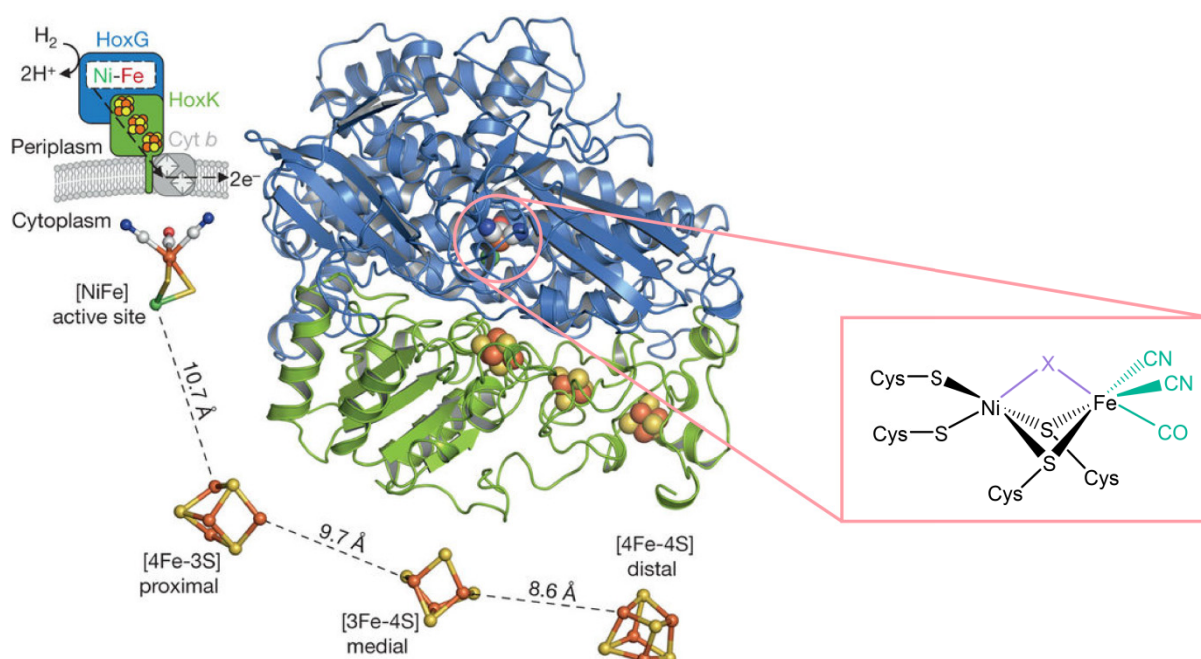


### Scheme 32

A schematic representation of a hydrogen-powered enzymatic cell with a hydrogenase to catalyse the hydrogen oxidation reaction (HOR) at the anode, and a bilirubin oxidase to catalyse the oxygen reduction reaction (ORR) at the cathode. In this case, an (optional) polymer electrolyte membrane (PEM) separates the two compartments. Reproduced with permission from <sup>97</sup>, copyright Royal Society of Chemistry 2017.

As such, hydrogenases have been proposed as alternative catalysts for the HOR. Because Pt catalyses both HOR and ORR at the cathode and anode, a proton exchange membrane (PEM) is required to separate both compartments in order to avoid the formation of mixed potentials due to cross-over, and to allow the selective transport of protons to the cathode. Due to the high specificity/selectivity of enzymes for a given substrate, an enzyme-based fuel cell (e.g. with bilirubin oxidase at the cathode) can use mixed fuel-oxidant feeds (in contrast to e.g. platinum). In addition, the absence of a PEM can save costs and offers potential for miniturisation.<sup>98</sup> A schematic representation of such an enzymatic fuel cell (in this case with a PEM) is shown in Scheme 32. In addition to being used in fuel-cells, hydrogenases can also be used to generate hydrogen (hydrogen evolution reaction – HER) either through fermentation using organic substrates<sup>99</sup>, or using solar energy or electricity.<sup>100–102</sup>

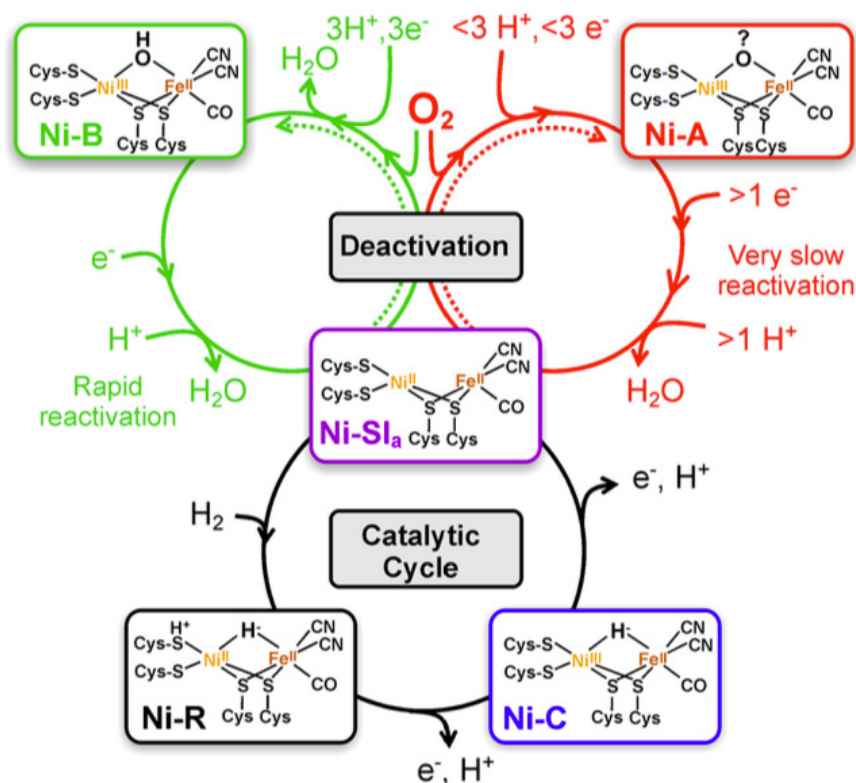
There are three major types of hydrogenases: [Fe]-, [FeFe]- and [NiFe]-hydrogenases. Due to the different binding of hydride at the active site, different catalytic activities for the HOR and HER are observed for different hydrogenases.<sup>103</sup> The [FeFe]-hydrogenase from *Desulfovibrio desulfuricans* is active for the HOR and HER under 1 bar of H<sub>2</sub>, whereas [NiFe]-hydrogenases show little or zero activity for the HER under the same conditions due to inhibition by H<sub>2</sub>. Currents for the HER can be observed for [NiFe]-hydrogenases under inert atmospheres, e.g. a small current can be observed for the [NiFe]-hydrogenase from *Ralstonia eutropha*. This preference for catalysis in one direction is known as the catalytic *bias* of the enzyme.<sup>96</sup> It was shown for the O<sub>2</sub>-tolerant [NiFe] hydrogenase from *Escherichia Coli* that the catalytic bias of [NiFe]-hydrogenases is pH sensitive, with the bias towards the HER maximised at low pH's.<sup>104</sup>



### Scheme 33

The overall structure of the heterodimeric membrane-bound hydrogenase (MBH) from *Ralstonia eutropha* with the cellular localisation of the enzyme shown in the upper left corner. The large subunit harbouring the [NiFe] catalytic active site (the molecular structure of which is drawn on the right) is coloured in blue, while the smaller subunit harbouring the three Fe-S cluster electron relay chain is coloured in green. The active site, enlarged for better visibility on the right, is connected through the electron relay to the respiratory chain *via* a *b*-type cytochrome. Adapted with permission from <sup>105</sup>, copyright Springer Nature 2011.

The focus in this thesis will be on [NiFe]-hydrogenase. [NiFe]-hydrogenases contain an active site with an Fe atom with one CO and two CN<sup>-</sup> ligands, and a Ni atom that is bridged to the Fe atom *via* two cysteine thiolate donors, as shown for the membrane-bound hydrogenase (MBH) from *Ralstonia eutropha* in Scheme 33. The Ni is further ligated by two more cysteine ligands that attach the entire active site to the protein backbone of the enzyme. The active site is electronically wired *via* an electron transfer relay chain of Fe-S clusters to a redox pool. In a bacterial membrane, this would be a cytochrome that is linked to the respiratory chain *via* electron-shuttling quinones inside the membrane.<sup>106</sup> In an enzymatic fuel cell or other electronic device, this would ideally be an electrode, as illustrated later in Scheme 35.



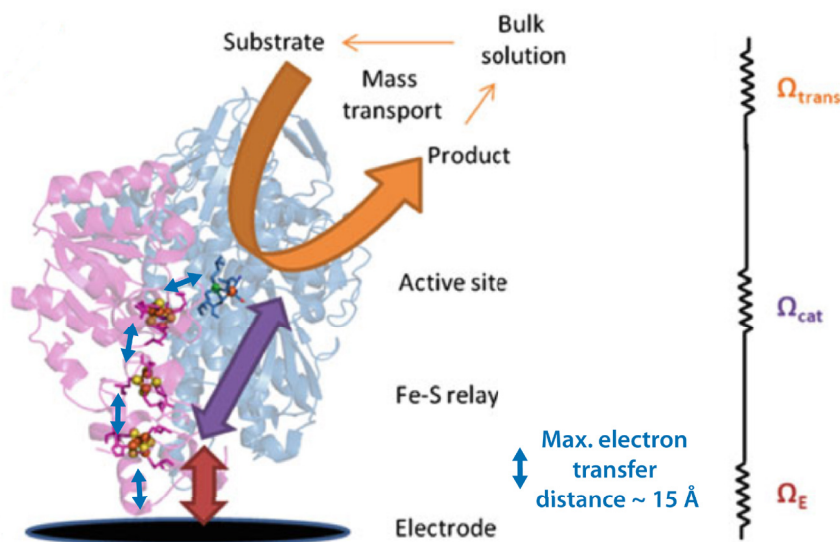
**Scheme 34**

The catalytic states for a [NiFe]-hydrogenases showing the deactivation and subsequent reactivation mechanism of the oxidised states. The catalytic cycle is indicated by the black arrows in the hydrogen oxidation reaction (HOR) direction. Deactivation is indicated by either the red or green arrows. In the case that electrons are readily available at the active site, the Ni-B state is formed with a hydroxide ligand, which can rapidly be reactivated upon a one electron, one proton reduction back to the Ni-SI<sub>a</sub> state. In the case that not enough electrons are available (i.e. in O<sub>2</sub> sensitive hydrogenases), the Ni-A state is formed, which requires low potentials and extended reactivation times to form the Ni-SI<sub>a</sub> state. Anaerobic inactivation (e.g. potential-induced) is indicated by the dotted lines. Reproduced with permission from <sup>103</sup>, copyright American Chemical Society 2014.

In [NiFe]-hydrogenases, O<sub>2</sub> reacts with the active site giving a mixture of inactive states, the so-called Ni-A or Ni-B states, depending on the nature of the oxygen ligand that bridges the Ni and Fe atoms (for the proposed key states existing in the catalytic cycle of [NiFe]-hydrogenases see Scheme 33). Certain [NiFe]-hydrogenases exhibit O<sub>2</sub> tolerance, which means that they form the Ni-B state (with a hydroxide ligand), which can be rapidly reactivated back to the Ni-SI<sub>a</sub> state upon a one electron, one proton reduction, removing the O<sub>2</sub> as water and giving rise to the O<sub>2</sub> tolerance. O<sub>2</sub> sensitive hydrogenases form the Ni-A state (which is believed to contain a peroxo ligand) in a poorly reversible process that requires low potentials and extended reactivation times to form the Ni-SI<sub>a</sub> state.<sup>107</sup> The Ni-B state only forms upon the availability and immediate delivery of electrons and protons at the active site. In the case that not enough electrons are available (i.e. in O<sub>2</sub> sensitive hydrogenases), the Ni-A state is formed.<sup>108,109</sup> This ‘fast’ delivery of electrons in the case of the O<sub>2</sub> tolerant hydrogenases is the result of the unique [4Fe-3S] proximal cluster (shown in Scheme 33), which differs significantly in its electronic structure from the [4Fe-4S] cubane proximal clusters found in O<sub>2</sub> sensitive hydrogenases function. This cluster can undergo two one-electron redox transitions, instead of a single one-electron redox transition, and

is thus capable of providing two electrons for complete oxygen reduction, with the other two electrons coming from the active site and the medial [3Fe4S]-cluster).<sup>105,109,110</sup>

The Knallgas bacterium *Ralstonia eutropha* (*Re*) H16 contains at least three such O<sub>2</sub> tolerant [NiFe]-hydrogenases<sup>105</sup>, with the MBH specifically being used in this study.



#### Scheme 35

Schematic representation of an enzyme with an Fe-S electron relay chain immobilised on an electrode in a direct electron configuration. Possible limitations are illustrated by a series of resistors, where  $\Omega_E$  represents interfacial electron transport,  $\Omega_{cat}$  the intramolecular electron transport, and  $\Omega_{trans}$  the mass transfer of substrates and products. Adapted with permission from<sup>107</sup>, copyright Springer 2014.

Enzymatic electrode devices (e.g. enzymatic fuel-cells, sensors) usually employ an electrode that is coated with a layer of enzymes. The enzymes may be orientated on the electrode in a direct electron transfer configuration or in an indirect configuration (see Scheme 36). A direct configuration means that there is a direct exchange of electrons between the electrode and the enzyme without the need of any additional electroactive mediators to ‘shuttle’ the electrons between the electrode and the enzymes’ active site, which is the case for an indirect configuration. Direct electron transfer *via* electron tunnelling is only possible if either the active site of the enzyme or the electron transfer relay chain (if there is one) is positioned close enough to the electrode surface. The interfacial electron transfer  $k_{ET}$  rate decreases exponentially with distance  $d$  from the electrode surface as follows:

$$k_{ET}(d) = k_0 \exp(-\beta d) \quad (43)$$

where  $k_0$  is the maximum value at closest contact, and  $\beta$  is a factor that depends on the height of the energy barrier and the nature of the medium between the redox site and the electrode.<sup>96,111</sup>

Enzymes are immobilised on different types of electrode materials using different approaches. They can adsorb onto metal oxide and carbon materials often without any prior modification of the surface, whereas metal electrodes like gold or silver often require a SAM to render the surface biocompatible and prevent the unfolding of the protein backbone, in particular during the application of electric fields. Enzymes can also be immobilised on an electrode in a bio-membrane like structure, such as a surfactant film or a lipid bilayer.<sup>112</sup> The binding interaction between the enzyme and the electrode may be covalent or non-covalent (for more details see section 5.3.9). For example, at moderate pH's, an amino-functionalised surface will have a positive charge and will therefore interact with negatively charged patches on the surface of a protein e.g. the negatively charged area around the distal Fe-S cluster of the *Desulfofiovibrio gigas* [NiFe]-hydrogenase.<sup>96</sup> The *Re* MBH lacks such a distinctive negatively charged surface patch.<sup>85</sup> The type of linker molecules or interface used to modify the electrode will have an effect on  $k_{ET}$ , with conjugated molecules having lower values of  $\beta$  than non-conjugated molecules, and, in general, larger values of  $k_{ET}$ .

Protein film voltammetry (PFV) is often used to study the electrochemical and catalytic behaviour of enzymes on electrodes. The maximum electrical current (when mass transport is not limiting, e.g. when using a rotating disc electrode) corresponds to the catalytic activity of the enzyme, and, if the coverage of enzyme  $\Gamma$  is known, then the catalytic current  $i_{cat}$  can be used to determine the turnover frequency  $k_{cat}$ :

$$k_{cat} = \frac{i_{cat}}{nFA\Gamma} \quad (44)$$

where  $A$  is the electrode surface area and  $n$  is the number of electrons transferred during the reaction.<sup>96</sup>

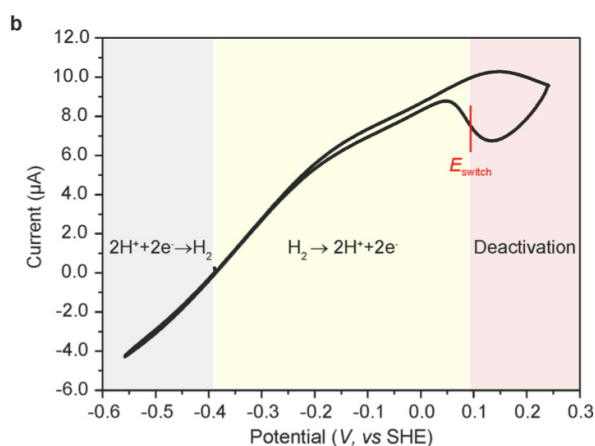
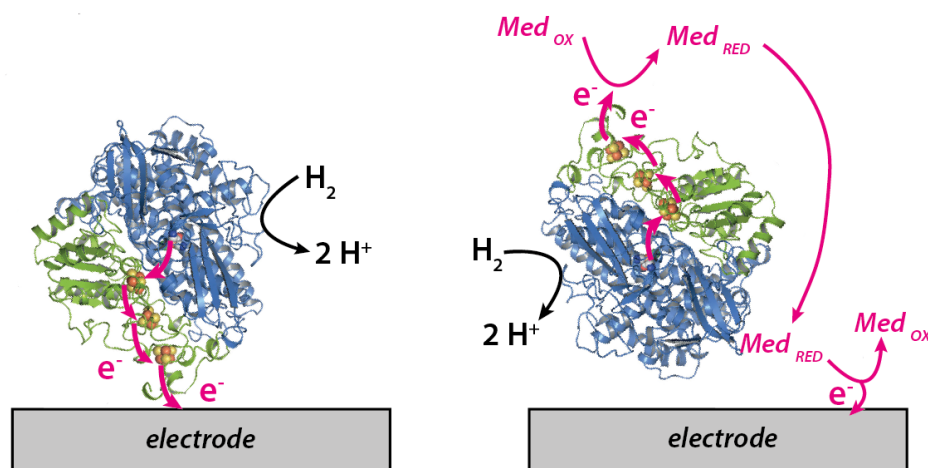


**Figure 3**

Protein film voltammogram of a [FeFe]-hydrogenase from the *Desulfovibrio desulfuricans* covalently attached to a pyrolytic graphite edge (PGE) electrode at 10 °C under 1 bar H<sub>2</sub> in pH 7.0 with a 2500 rpm electrode rotation rate. The reversible cleavage of H<sub>2</sub> via the hydrogen oxidation reaction (HOR) and hydrogen evolution reaction (HER) is indicated by positive and negative currents, respectively. The switch potential for reductive reactivation of the hydrogenase is indicated by  $E_{switch}$ . Reproduced with permission from <sup>103</sup>, copyright American Chemical Society 2014.

Figure 3 shows a protein film voltammogram of a hydrogenase displaying characteristic reversible cleavage of  $H_2$  via the HOR and the HER. Hydrogenases typically operate at the thermodynamic potential for both of these reactions, as indicated by the straight trace through the zero-current line. At high anodic overpotentials, the hydrogenase undergoes anaerobic oxidative inactivation via the reversible formation of the Ni-B state, and thus the current drops accordingly. On the reverse sweep, the hydrogenase is reductively reactivated close to the switch potential,  $E_{switch}$ , with the removal of the bridging hydroxide ligand.<sup>96</sup>



#### Scheme 36

Schematic representation of electrocatalysis proceeding through direct electron transfer between an electrode and an immobilised MBH from *Ralstonia eutropha* (left) or through mediated electron transfer via a mediator (in its oxidised  $Med_{OX}$  or reduced  $Med_{RED}$  state) in solution.

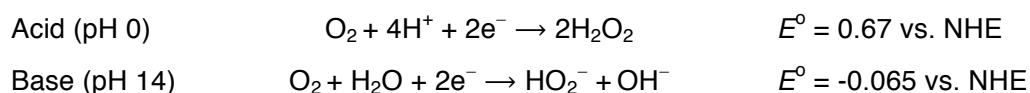
As previously mentioned, enzymes that are immobilised on an electrode in an indirect electron transfer configuration may require the use of electroactive mediators, such as methylene blue or methyl viologen, to 'shuttle' electrons between the active site and the electrode. When there is a potential difference between the electrode and the enzyme, the mediator is cycled between its oxidised and reduce state, as illustrated in Scheme 36. The mediator must be capable of fast and reversible electron transfer with little overpotential, meaning the choice of mediator and its redox potential is critical.<sup>113</sup> These mediators may be present in solution, attached to the protein, or present in a polymeric matrix such as a hydrogel that also contains the enzyme.<sup>114</sup> Such matrices can also afford additional stability against inactivation or damage to enzymes, such as oxygen protection for an  $O_2$  sensitive hydrogenase.<sup>115</sup> For diffusion-controlled mediators, interfacial electron transfer rates of the mediator at the electrode-electrolyte interface, as well as electron at the enzyme, will be determined by factors such as hydrophobic or electrostatic interaction, or the nature of an interface (e.g. the charge transfer resistance experienced by the mediator). Methylene blue is used as a mediator with the MBH from the *Ralstonia eutropha* hydrogenase because it overlays with the potential range in which the HOR efficiency is at its greatest. The electrocatalytic currents due to direct electron transfer (DET) can be compared to the currents due to mediated electron transfer (MET) in the presence of a mediator to get an idea about whether the enzymes in a system are in a direct or indirect electron transfer configuration.

## 2.6 Molecular catalysts

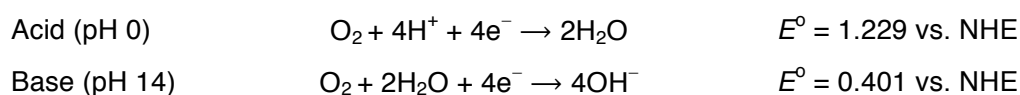
### 2.6.1 Oxygen reduction reaction at metal macrocycles

Catalysts are used on the cathode of a fuel cell to catalyse the reduction of oxygen *via* the ORR. The electrochemical reduction of oxygen is a multi-electron reaction that can proceed *via* two pathways: a two-electron reduction to give peroxide, or a four-electron reduction to give water.

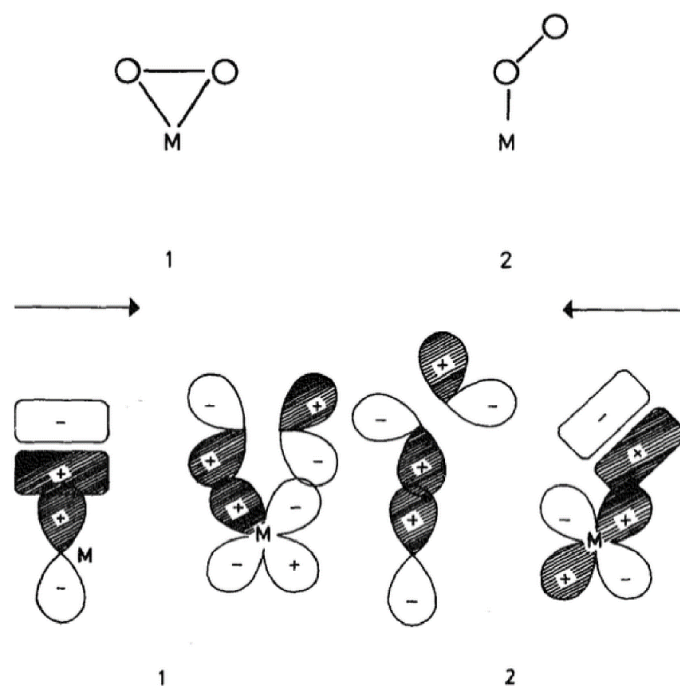
Two-electron pathway:



Four-electron pathway:



In order to provide the maximum free energy in a fuel cell, it is necessary to reduce  $O_2$  *via* the four-electron pathway. This requires the O–O bond to be broken and the nature of the catalyst being used will have a strong influence on the pathway followed. Most electrode materials catalyse the two-electron pathway. The  $O_2$  molecule has a bond order of two, with two unpaired electrons in a doubly degenerate antibonding  $\pi^*$  orbital and four bonding electrons, which explains its high stability (118 kcal/mol). When  $O_2$  is reduced on a catalyst surface such as Pt, electrons are added to the antibonding  $\pi^*$  orbitals e.g. through the back bonding of transition metal d-orbitals, weakening and lengthening the O–O bond and increasing the likelihood of oxygen reduction taking place. A number of possible interactions between  $O_2$  and the surface of a transition metal are possible, including end-on or side-on interaction with a single metal atom, or a bridging interaction between two metal atoms (see Scheme 37). It has been proposed that oxygen adsorbs on Pt *via* a bridging interaction, which favours oxygen reduction *via* a four-electron pathway.<sup>116</sup>

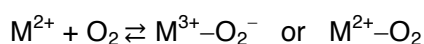


**Scheme 37**

Possible side-on and head-on modes of interaction of O<sub>2</sub> with a transition metal centre, indicating the respective molecular orbitals involved. Adapted with permission from <sup>117</sup>, copyright Elsevier 1992.

The high cost of Pt and other noble metals used for ORR has led to efforts to develop non-noble metal catalysts based on N<sub>4</sub> metal macrocycles, inspired by biological catalyst like cytochrome c and haemoglobin. Furthermore, N<sub>4</sub> metal macrocyclic complexes exhibit a high tolerance to methanol compared to platinum catalysts, making them interesting for methanol fuel-cell applications. A number of N<sub>4</sub> metal macrocyclic complexes have been shown to be active for ORR. Fe and Co porphyrins and phthalocyanines catalyse the reduction of oxygen either *via* two- or four-electron pathways, depending on the pH of the electrolyte. Certain complexes only catalyse the reaction *via* a two-electron pathway, as is the case for Co, Ni and Cu phthalocyanines.<sup>118</sup>

A one-electron reduction pathway of O<sub>2</sub> to give a superoxide occurs through an outer-sphere process, whereas a two- or four-electron pathway takes place through an inner-sphere process. Similar to Pt, O<sub>2</sub> interacts with an N<sub>4</sub> metal macrocycle by binding to the central metal d-orbitals either *via* an end-on or side-on interaction, weakening and lengthening the O–O bond. The strength of the interaction will depend on the electronic density of the d-orbitals. The metal should be in a M<sup>2+</sup> oxidation state, and an adduct is formed as follows<sup>116</sup>:



This adduct should be short-lived so that the interaction does not block the active site and is reduced as follows:



The final step is for the ORR in alkaline conditions and could also involve  $M^{2+}-O_2$ , while in acidic conditions protons are involved in the process.<sup>118</sup>

For Co complexes, oxygen reduction occurs at potentials more negative than the  $Co^{2+}/Co^{3+}$  couple, whereas for Fe complexes, reduction usually takes place close to the  $Fe^{2+}/Fe^{3+}$  couple. At very negative overpotentials,  $H_2O_2$  becomes the main product of the reaction.<sup>116</sup>

### 5.6.2 Water oxidation molecular catalysts

Water oxidation is the first step in photosynthesis, where water is used as a source of electrons and protons:



The reaction is thermodynamically and kinetically very demanding with many intermediate steps resulting in slow kinetics. Use of a catalyst that stabilises these intermediates can lower the kinetic barrier and lead to reduced overpotentials. Technologies based on the production of sustainable fuels from renewable energy or sunlight rely on having an abundant source of protons and electrons. Heterogeneous catalysts that catalyse the water oxidation reaction include transition metal oxides such as iridium, ruthenium, nickel or cobalt oxides.<sup>119</sup> Ir and Ru catalysts tend to operate in acidic conditions, while Ni and Co catalysts tend to operate in basic conditions (but not always). The first homogenous water oxidation catalyst developed was Meyer's "Blue Dimer" in 1982, which is based on Ru.<sup>120</sup> Many other catalysts have been developed since then that are highly active for water oxidation, in particular many Ir-based catalysts.<sup>121</sup> Given the scarcity and high cost of Ru and Ir, efforts have been made to develop non-noble metal catalysts based on Fe, Mn (like nature's oxygen-evolving photosystem II complex), Co and Cu. These efforts have recently been reviewed by Crabtree, Brudvig and co-workers.<sup>119</sup>

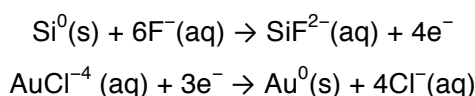
# Chapter 3

## Materials, instruments and methods

### 3.1 Electrode synthesis

#### 3.1.1 Gold SEIRA film preparation

An ATR Si prism coated was coated with a nanostructured gold film *via* electroless deposition.<sup>122</sup> The surface of the Si prism was first polished with alumina powder (Microgrit WCA-9, grain size: ca. 6  $\mu\text{m}$ ) and then thoroughly rinsed with water. The polished surface was then etched with a 400 g/L  $\text{NH}_4\text{F}$  solution for 2 min to remove the silicon oxides on the surface to leave a bare silicon surface. The gold film was deposited by heating the prism up to 65  $^\circ\text{C}$  in a water bath and dropping a gold plating solution (aqueous 1:1:1 volume ratio of 2% (w/w) HF, 0.03 M  $\text{NaAuCl}_4\cdot\text{H}_2\text{O}$  and a reduction solution comprised of 0.3 M  $\text{Na}_2\text{SO}_3$ , 0.1 M  $\text{Na}_2\text{S}_2\text{O}_3\cdot 5\text{H}_2\text{O}$ , and 0.1 M  $\text{NH}_4\text{Cl}$ ) on the surface for 1 min. The film is formed as a result of the reduction of  $\text{Au}^{\text{III}}$  species in the plating solution results and the concomitant oxidation of the Si surface<sup>122</sup>:



The gold films were cleaned electrochemically by repeated cycling between 0 and 1.4 V (vs  $\text{Ag}/\text{AgCl}$  3M KCl) at 100 mV/s in 0.1 M  $\text{HClO}_4$  under Ar bubbling until reproducible CV traces were obtained. The gold surface area was calculated using the Au(III) oxide reduction peak by using the following formula  $A = Q_1/Q_0$ , where  $Q_1$  is the measured charge and  $Q_0$  is the charge required to reduce 1  $\text{cm}^2$  of Au(III) oxide ( $Q_0 = 400 \mu\text{Ccm}^{-2}$ ).<sup>123</sup>

#### 3.1.2 Indium tin oxide electrode preparation

The ITO electrodes used in this work are ITO-coated glass electrodes (8-12  $\Omega/\text{sq}$ ) purchased from Sigma Aldrich (hereby denoted pl-ITO). ITO films are generally deposited on substrates using sputtering, whereby particles are ejected from a solid target material in a vacuum chamber as a result of bombardment using energetic particles, such as gas ions, and deposited on all surfaces in the chamber, including any substrate present. As sputtering thus requires specialised equipment, planar ITO films were deposited on a Si prism for ATR-IR measurements using a sol-gel method from the literature.<sup>124</sup> A 10% Sn-doped  $\text{In}_2\text{O}_3$  (ITO) indium-tin-acetylacetonate solution, where  $\text{Sn}\% = \text{Sn}/(\text{Sn}+\text{In})$ , was prepared by dissolving 20 mmol indium (III) nitrate hydrate ( $\text{In}(\text{NO}_3)_3\cdot x\text{H}_2\text{O}$ , 99.99%, Sigma Aldrich) and 2.2 mmol tin (IV) chloride hydrate

( $\text{SnCl}_4 \cdot x\text{H}_2\text{O}$ , Sigma Aldrich) in acetylacetone (Sigma Aldrich) and stirring overnight at 60 °C, resulting in a transparent brown solution. In a modification to the original literature method, and to improve the adhesion of this solution to the Si surface, an aliquot of warm indium-tin-acetylacetonate was diluted with an aliquot of toluene, before spin-coating on a freshly-polished Si-prism. The coated prism was then immediately placed on a hotplate set at 300 °C for 5 minutes and then calcined in air at 400 °C for 10 minutes, resulting in a blue-tinted film. A second calcination was carried out under a reducing atmosphere (10%  $\text{H}_2$ , 90%  $\text{N}_2$ ) at 300 °C for 90 min with a ramp-rate of 20 °C/min. The resulting films (hereby denoted sc-ITO) were characterised using scanning electron microscopy (SEM).

### 3.1.3 Antimony-doped tin oxide electrode preparation

Crystalline 8% Sb-doped  $\text{SnO}_2$  (ATO) nanoparticles, where  $\text{Sb}\% = \text{Sb}/(\text{Sb}+\text{Sn})$ , were synthesised *via* a non-hydrothermal synthesis route by dissolving 6.25 mmol of tin tetrachloride ( $\text{SnCl}_4$  Sigma Aldrich) and 0.55 mmol of antimony acetate (Sigma Aldrich) in 5 mL toluene in a glovebox and adding this solution dropwise into 15 mL benzyl alcohol under continuous stirring. The glass container with the resulting clear solution was removed from the glovebox and transferred into a Teflon-lined autoclave, sealed and heated at 150 °C for 3 hrs. The resulting brown particles were removed and sequentially cleaned using 15 min of ultrasonication twice in toluene and three times in acetone. Centrifugation was used for 20 min at 5,000 rpm to separate the supernatant from the particles.

Colloidally stable solutions of ATO nanoparticles were formed by sonicating and stirring 160 mg ATO nanoparticles and 80 mg Pluronic F127 (Sigma Aldrich) in 1 mL THF with a few microliters of conc. HCl added to aid the dispersion. Mesoporous ATO (me-ATO) films were electrogred on planar ITO-coated glass substrates (pl-ITO, 8-12  $\Omega/\text{sq}$ , Sigma-Aldrich) by evaporation induced self-assembly (EISA) whereby the substrates were immersed into the solutions using a dip-coater with a 200 mm/min withdrawal rate in a 50% relative humidity at 20 °C. The resulting films were aged for 12 hrs in air at 100 °C and calcined at 450 °C for 30 min with a temperature ramp rate of 0.6 °C/min. The resulting transparent films were characterised using scanning electron microscopy (SEM). pl-ITO were cleaned sequentially by sonication for 5 min in water, ethanol and acetone before coating with me-ATO or uncoated before electrochemical measurements.

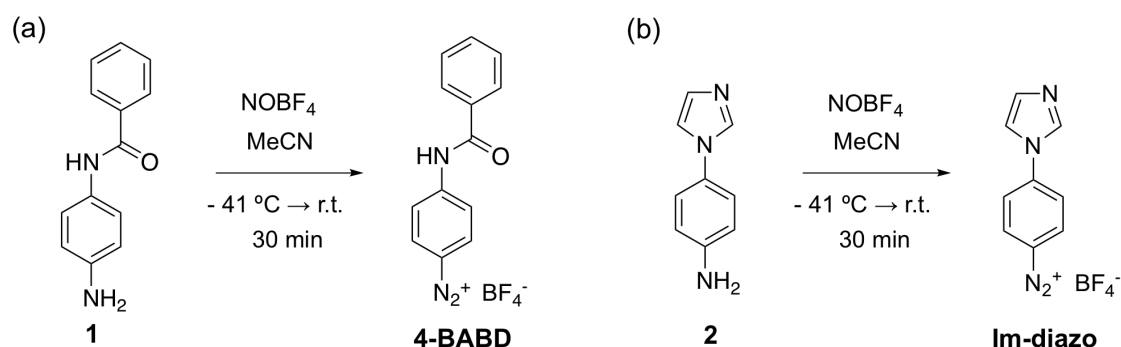
me-ATO films for attenuated total reflectance Infrared spectroscopy (ATR-IR) and rotating disk electrode (RDE) experiments were electrogred on an un-doped Si prism and glassy carbon tips (5 mm diameter, Pine Research) by spin coating the same colloidal solution of ATO nanoparticles as that used on pl-ITO, followed by the same ageing and calcination steps.

The me-ATO films on ITO used in section 9 were synthesised by Victoria Davis (from the group of Prof. Dr. Anna Fischer, Albert-Ludwigs-Universität Freiburg).

## 3.2 Precursor synthesis

### 3.2.1 Diazonium salts

4-benzamidobenzenediazonium tetrafluoroborate (**4-BABD**) and 4-(1H-imidazol-1-yl)benzenediazonium tetrafluoroborate salt (**Im-diazo**) were synthesised by diazotising the corresponding amines **1** 4'-aminobenzanilide (Sigma-Aldrich) and **2** 4-(1H-Imidazol-1-yl)aniline (Sigma-Aldrich) using nitrosonium tetrafluoroborate (NOBF<sub>4</sub>). The method used was adapted from literature methods for the synthesis of other diazonium salts.<sup>52,125</sup> Briefly, the amine was dissolved in a minimum amount of acetonitrile (MeCN) in a round-bottomed flask at -41 °C and kept under an inert Ar atmosphere on a Schlenk line. 1.1 equivalents of NOBF<sub>4</sub> dissolved in acetonitrile were added under stirring, and the mixture stirred for 30 min at -41 °C. After warming to room temperature, diethyl ether was added to precipitate the diazonium salt. The filtrate was filtered using a Büchner funnel, washed with diethyl ether and allowed to dry overnight under vacuum. The brightly coloured products (pink and orange-brown for 4-BABD and Im-diazo, respectively) were stored at 4 °C in the dark.



**Scheme 38**

The synthesis of (a) 4-benzamidobenzenediazonium tetrafluoroborate (**4-BABD**) and (b) 4-(1H-imidazol-1-yl)benzenediazonium tetrafluoroborate (**Im-diazo**) from the corresponding amines 4'-aminobenzanilide (**1**) and 4-(1H-Imidazol-1-yl)aniline (**2**).

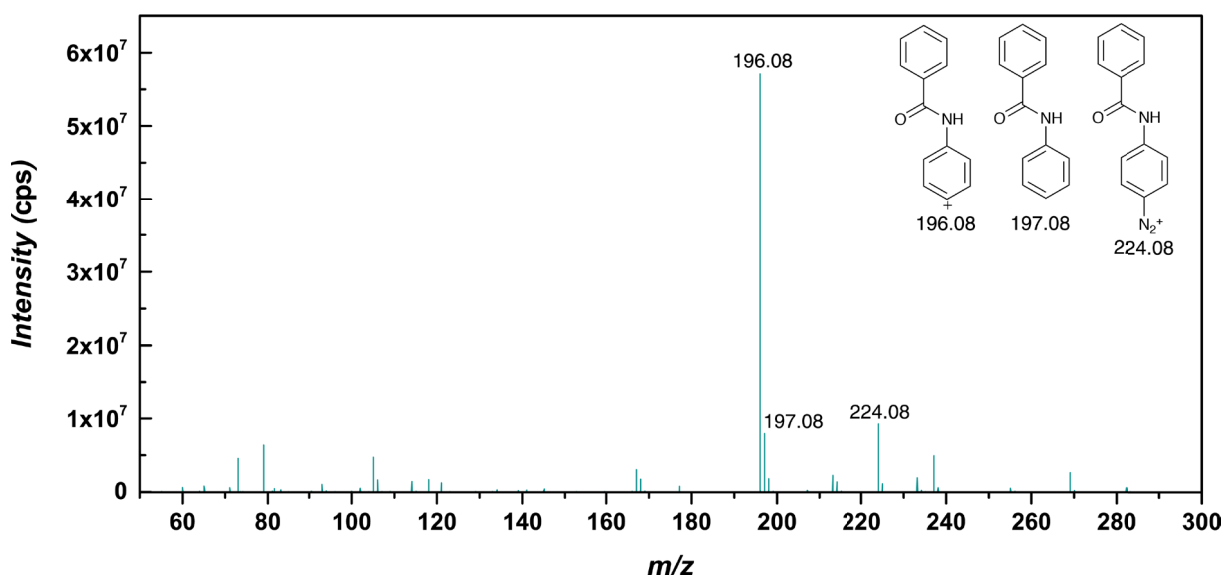


**Figure 4**  
Electrospray mass spectrum of 4-BABD.

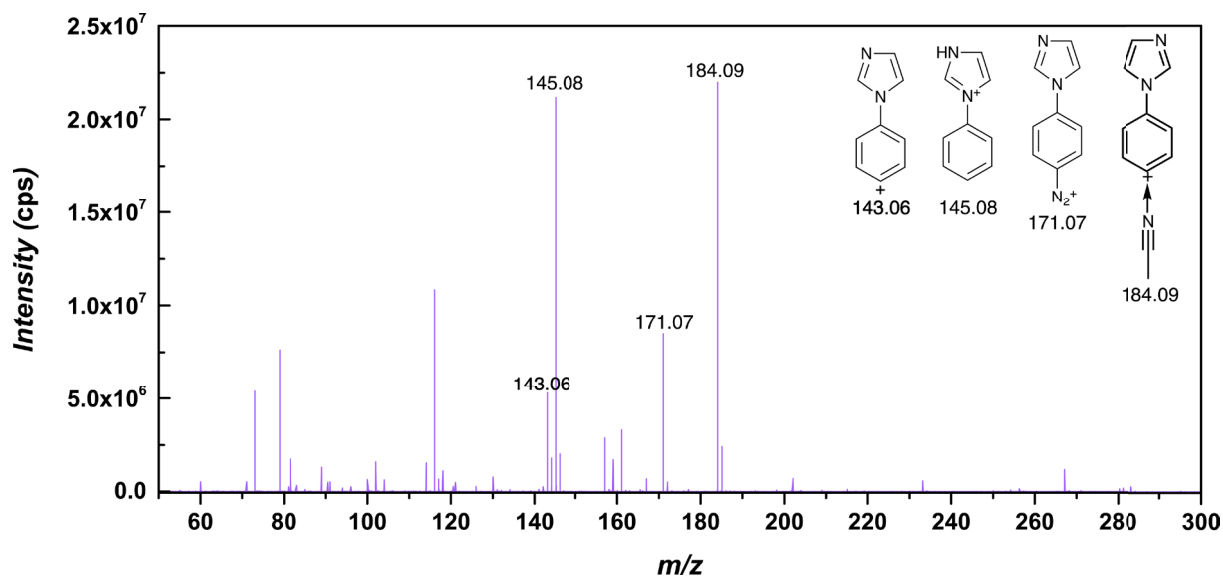


**Figure 5**  
Electrospray mass spectrum of Im-diazo.

Solutions of 4-BABD and Im-diazo were prepared in acetonitrile and characterised using electrospray ionisation mass spectroscopy (ESI-MS) (see Figure 4 and Figure 5). Peaks due to the intact diazonium cations are present in both spectra at  $m/z$  224.08 and 171.07, respectively. Peaks for the aryl cations that form as the result of dediazonation taking place during the ionisation process are also visible for 4-BABD and Im-diazo at  $m/z$  196.08 and 143.06, respectively, and such cationic species have previously been observed in the literature.<sup>126</sup> In the case of Im-diazo, there is a greater contribution from product fragments that form due to the reaction between the aryl cation and solvent molecules. This reflects the higher reactivity of the aryl cation due to less stabilisation *via* inductive effects from the para-substituent compared to 4-BABD. The difference in the inductive effect of each substituent can clearly be seen in the electrochemical reduction potentials measured for each salt in Table 1 (page 27).

4-([2,2'-Bipyridine]-4-carboxamido)benzenediazonium tetrafluoroborate (**bpy-diazo**) was synthesised by Dr. Anja Sokolowski (formerly from the group of J.Prof. Dr. Carl Christoph Tzschucke, Freie Universität Berlin) from N-(4-Aminophenyl)-[2,2'-bipyridine]-4-carboxamide.

### 3.3 Protein purification and catalyst preparation

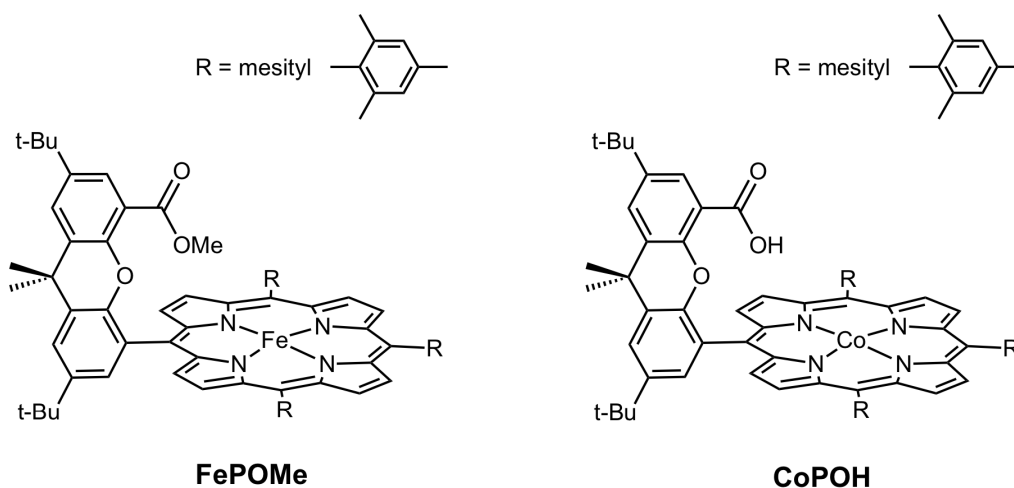
#### 3.3.1 Membrane-Bound Hydrogenase (MBH) from *Ralstonia eutropha*

The heterodimeric MBH was purified using a *Strep*-tag II peptide as an affinity tag, which was attached to the protein by genetically engineering the small subunit of the MBH (HoxK). The growth conditions and purification are described in detail by Goris et al.<sup>109</sup> The samples were purified by Dr. Stefan Frielingsdorf (from the group of Dr. Oliver Lenz, Technische Universität

Berlin). The purified MBH heterodimer samples were buffered in 50 mM  $\text{KPO}_4$  buffer at pH 5.5 with 150 mM NaCl and subsequently stored in liquid  $\text{N}_2$ .

### 3.3.2 Hangman complexes

The different Hangman porphyrin complexes used in this work (**FePOMe** and **CoPOH**) were synthesised by Dr. Pierre Wrozek (from the group of Dr. Matthias Schwalbe, Humboldt - Universität zu Berlin) using methods published in the literature.<sup>127–129</sup>



**Scheme 39**

The molecular structures of the Hangman porphyrin complexes used this work.

### 3.4 Electrochemistry

Electrochemical measurements were performed using a three-electrode set-up that employed a working electrode (a gold SEIRA film, me-ATO film, pl-ITO film or sc-ITO film), a Pt wire as counter electrode and an adequate reference electrode. Control of the working electrode was achieved using either a Metrohm  $\mu$ AutolabIII potentiostat, or a CHI potentiostat. For measurements in aqueous solvents an Ag/AgCl 3M KCl (Dri-Ref, WPI) reference electrode was used, while for measurements in acetonitrile, either an Ag/AgNO<sub>3</sub> 0.1 M AgNO<sub>3</sub> (homemade) reference electrode or a Ag/AgCl 3M KCl (Leak-Free, Warner Instruments) reference electrode was used. Potentials in acetonitrile were measured relative to the Fc/Fc<sup>+</sup> couple of a 0.1 or 1 mM ferrocene solution in acetonitrile (0.1 M TBAF or TBAP). For electrochemical impedance spectra using a 1 mM Fc, a  $\mu$ AutolabIII (Metrohm) was used and controlled with FRA2 software and spectra were recorded in a frequency range of 0.00001 to 1000 kHz with an amplitude of 25 mV (rms).

For ATR-IR and SEIRA spectroelectrochemical measurements, a home-made electrochemical cell was used. For more details, see 6.6.1

Electrochemical measurements using pl-ITO (i.e. on a glass substrate) or me-ATO films on pl-ITO as a working electrode were performed in a home-made PTFE cell. A Viton® O-ring was

used to seal the spectroelectrochemical cell on top of the electrodes, forming a working electrode with a geometric area of ca.  $0.4 \text{ cm}^2$ . The geometric surface area was used to calculate current densities. For UV-Vis spectroelectrochemical measurements, a home-made electrochemical cell was used. For more details see 6.6.5.

For rotating disk electrode (RDE) measurements (using me-ATO films coated on a glassy carbon RDE tips), an RDE setup from PINE Research Instrumentation was used. The geometric surface area was used to calculate current densities.

### 3.5 Electrode modification

The electrochemical reduction potentials of all the diazonium salts used in this study in acetonitrile, determined using cyclic voltammetry with a pl-ITO working electrode, were shown previously in in Table 1 (page 27).

#### 3.5.1 Functionalisation of gold

4-NTP and 4-ATP SAMs were deposited overnight on gold from 1mM ethanolic (HPLC grade) solutions and thoroughly rinsed with copious amounts of ethanol.

Electrochemical grafting and desorption measurements were performed in acetonitrile with 0.1 M tert-butylammonium hexafluorophosphate (TBAF) electrolyte. All electrochemical measurements, unless stated otherwise, were performed under inert argon atmosphere.

Benzanilide interfaces were electrochemically grafted on gold from 1 mM 4-BABD solutions in acetonitrile by cycling two-times between +0.12 and -0.88 V (vs vs  $\text{Fc}/\text{Fc}^+$ ) at a scan rate of 50 mV/s.

Nitrophenyl interfaces were electrochemically grafted from 1 mM 4-NBD solutions in acetonitrile with and without the addition of different molar equivalents of the radical scavenger 2,2-diphenyl-1-picrylhydrazyl (DPPH) using chronoamperometry by applying a potential of -0.445 V (vs  $\text{Fc}/\text{Fc}^+$ ) for 60 s, followed by rinsing the electrode in copious amounts of acetonitrile, followed by ethanol. The nitrophenyl interface was spontaneously deposited from a 20 mM 4-NBD solution in acetonitrile without any application of potential for 60 min, followed by copious rinsing in acetonitrile and ethanol. Nitrophenyl interfaces were electrochemically reduced to aminophenyl interfaces by cycling the electrode between 0 and -1.2 V (vs  $\text{Ag}/\text{AgCl}$  3M KCl) at a scan rate of 50 mV/s in a 0.1 M  $\text{NaClO}_4$  1:9 ethanol:water solution. Final SEIRA spectra of the reduced interfaces were recorded in dry acetonitrile. Details regarding the MBH immobilisation and bioelectrocatalysis are given in 6.5.4.

Bipyridine interfaces were electrochemically grafted from 1 mM bpy-diazo solutions in 0.1 M TBAF by cycling five times between 0.351 and -0.948 (vs Fc/Fc<sup>+</sup>) at a scan rate of 50 mV/s. Manganese carbonyl bipyridyl interfaces were formed by incubating the electrografted bipyridine interface with a 1 mM Mn(CO)<sub>5</sub>Br solution in acetonitrile for 60 min, followed by copious rinsing in acetonitrile. Manganese carbonyl bipyridyl interfaces were also electrochemically grafted from mixed 1 mM bpy-diazo and 1 mM Mn(CO)<sub>5</sub>Br solutions, which were allowed to react for 60 min prior to electrochemical grafting. Electrocatalysis was carried out in acetonitrile (0.1 M TBAP) after bubbling the solution with CO<sub>2</sub>.

### 3.5.2 Functionalisation of ITO

Electrochemical grafting and desorption measurements were performed in acetonitrile with 0.1 M tert-butylammonium perchlorate (TBAP) electrolyte. All electrochemical measurements, unless stated otherwise, were performed under inert argon atmosphere. Prior to modification, the pl-ITO electrodes were sonicated for 5 min sequentially in water, ethanol and acetone, before drying under a stream of nitrogen. Nitrophenyl interfaces were electrochemically grafted from 1 mM 4-NBD solutions in acetonitrile (0.1 M TBAP) with and without the addition of different molar equivalents of DPPH using chronoamperometry by cycling between 0.14 and -0.76 V (vs Fc/Fc<sup>+</sup>) at a scan rate of 50 mVs<sup>-1</sup>, followed by rinsing the electrode in copious amounts of acetonitrile, followed by ethanol. In the same way as was carried out on gold, the nitrophenyl interfaces were electrochemically reduced to aminophenyl interfaces by cycling the electrode between 0 and -1.2 V (vs Ag/AgCl 3M KCl) at a scan rate of 50 mV/s in a 0.1 M NaClO<sub>4</sub> 1:9 ethanol:water solution. Details regarding the enzyme immobilisation and bioelectrocatalysis are given in 6.5.4.

Bipyridine-functionalised interfaces were electrochemically grafted from 1 mM bpy-diazo solutions in acetonitrile (0.1 M TBAP) by cycling between -0.16 and -1.06 V (vs Fc/Fc<sup>+</sup>) at a scan rate of 50 mVs<sup>-1</sup>, followed by rinsing the electrode in copious amounts of acetonitrile, followed by ethanol. After modification, the bipyridine-functionalised interface was incubated with 2 mM CuSO<sub>4</sub> (in DI water) for 10 min followed by copious rinsing with water. Electrocatalysis was performed in 0.1 M NaOH in air.

Imidazole-functionalised interfaces were electrochemically grafted from 1 mM Im-diazo solutions in acetonitrile (0.1 M TBAP) by using chronoamperometry and applying a potential of -0.56 V (vs Fc/Fc<sup>+</sup>) for 120 s, followed by rinsing the electrode in copious amounts of acetonitrile and dichloromethane. Alternatively, interfaces were also electrografted from 1 mM Im-diazo solutions in acetonitrile (0.1 M TBAP) by applying a linear sweep voltammogram between 0.04 V and -0.86 V (vs Fc/Fc<sup>+</sup>) at a scan rate of 50 mV/s. FePOMe was immobilised on pl-ITO using two different strategies: (a) a two-step 'post-coordination' process whereby imidazole-functionalised interfaces were first electrografted from 1 mM Im-diazo using the aforementioned methods, followed by incubation with 1.2 mM FePOMe; and (b) a one-step process whereby an interface is

electrochemically grafted on pl-ITO directly from 1 mM Im-diazo and 1.2 mM FePOMe (after mixing them for 5 min i.e. pre-coordinating the iron centre to the axial ligand). In each case a potential of -0.56 V (vs Fc/Fc<sup>+</sup>) is applied for 120 s, followed by copious rinsing with acetonitrile and dichloromethane. Electrocatalysis was carried out in a pH 7 0.1 M phosphate buffer (PB).

### 3.5.3 *Functionalisation of ATO*

Electrochemical grafting and desorption measurements were performed in acetonitrile with 0.1 M TBAP electrolyte. All electrochemical measurements, unless stated otherwise, were performed under an inert argon atmosphere.

Imidazole-functionalised interfaces were electrochemically grafted from 1 mM Im-diazo solutions in acetonitrile (0.1 M TBAP) by using chronoamperometry and applying a potential of -0.42 V (vs Fc/Fc<sup>+</sup>) for 120 s, followed by rinsing the electrode in copious amounts of acetonitrile and dichloromethane. FePOMe was immobilised on me-ATO using two different strategies: (a) a two-step 'post-coordination' process whereby imidazole-functionalised interfaces were first electrografted from 1 mM Im-diazo using the aforementioned method, followed by incubation with 1.2 mM FePOMe; and (b) a one-step process whereby an interface is electrochemically grafted on me-ATO directly from 1 mM Im-diazo and 1.2 mM FePOMe (after mixing them for 5 min i.e. pre-coordinating the iron centre to the axial ligand). In each case a potential of -0.42 V (vs Fc/Fc<sup>+</sup>) is applied for 120 s, followed by copious rinsing with acetonitrile and dichloromethane. Electrocatalysis was carried out either in pH 7 0.1 M PB, or in 0.1 M KOH under O<sub>2</sub> bubbling.

CoPOH was immobilised on me-ATO using the two-step 'post-coordination' process whereby imidazole-functionalised interfaces were first electrografted from a 1 mM Im-diazo solution, followed by incubation with 1.2 mM CoPOH. Electrocatalysis was carried out in 0.1 M NaOH in air.

### 3.5.4 *Enzyme immobilisation*

MBH was immobilised by adsorption onto the electrode surfaces for protein film voltammetry (PFV) and spectroelectrochemical studies.

MBH was immobilised on aminophenyl-functionalised SEIRA gold electrodes (functionalised using the method introduced in 6.1.1) by incubating the electrodes in a 1 μM solution of MBH in 10 mM phosphate buffer (PB) pH 7 at 5 °C for 15 min. Electrodes were rinsed with 10 mM PB pH 7 and bio-electrocatalysis was performed at 5 mV/s in 10 mM PB pH 5.5 at 25 °C, after saturation of the buffer with O<sub>2</sub>-free Ar or O<sub>2</sub>-free H<sub>2</sub> gas.

MBH was immobilised on bare pl-ITO and sc-ITO, as well as aminophenyl-functionalised pl-ITO and sc-ITO electrodes (functionalised using the method introduced in 6.1.1) by incubating the

electrodes in a 1  $\mu\text{M}$  solution of MBH in 10 mM phosphate buffer (PB) pH 7 at 5  $^{\circ}\text{C}$  for 15 min. Electrodes were rinsed with 10 mM PB pH 7 and bio-electrocatalysis was performed at 10 mV/s in 10 mM PB pH 5.5 at 25  $^{\circ}\text{C}$ , after saturation of the buffer with  $\text{O}_2$ -free Ar or  $\text{O}_2$ -free  $\text{H}_2$  gas. Blank measurements of the modified electrodes without MBH were recorded in the same conditions.

### 3.6 Spectroscopic characterisation

#### 3.6.1 ATR-IR and SEIRA

All ATR-IR and SEIRA measurements were performed with a Kretschmann ATR-type configuration implementing a Si prism, as described elsewhere.<sup>130</sup> The Si ATR prism is a trapezoidal Si crystal ( $L \times W \times H = 25 \text{ mm} \times 20 \text{ mm} \times 10 \text{ mm}$ ) and was coated with either a SEIRA gold, sc-ITO or me-ATO film using the methods outlined in 6.1. Either a Bruker IFS66v/s or a Tensor 27 spectrometer equipped with a liquid  $\text{N}_2$  cooled photoconductive Mercury Cadmium Telluride (MCT) detector was used. A globar was used as an IR radiation source in both spectrometers and the prism was irradiated at an angle of incidence of  $60^{\circ}$ , with a resulting cross-sectional measuring area of  $7 \times 3 \text{ mm}$ . A temperature-controlled electrochemical cell was used, maintaining a temperature of 25  $^{\circ}\text{C}$ , unless stated otherwise. Spectra were collected between 4000 and 1000  $\text{cm}^{-1}$  with a spectral resolution of 4  $\text{cm}^{-1}$  and each spectrum made up of 400 scans, which takes 3 min to accumulate, were averaged per IR spectrum with spectra allowed to stabilise before a final spectrum was recorded. For spectroelectrochemical measurements, a home-made spectroelectrochemical cell was used with a three-electrode configuration. Control of the working electrode was achieved using a Metrohm  $\mu\text{AutolabIII}$  potentiostat. A PTFE-coated O-ring was used to seal the spectroelectrochemical cell on top of the coated prism, forming a working electrode with a geometric area of ca.  $0.79 \text{ cm}^2$ . The surface area of the SEIRA gold films were determined electrochemically (*vide infra*). Spectra were evaluated using OPUS 7.0 software (Bruker).

The electrochemical stability window of the electrografted interfaces on gold and me-ATO were determined by applying increasingly anodic or cathodic potential steps for a set amount of time and then recording IR adsorption/SEIRA spectra after each application. These spectra were recorded under a constant potential to avoid charge-induced differences in the orientation of the organic molecules at the interface due to fluctuating open circuit potentials, or, in the case of me-ATO, changes in the transparency of the film under different potentials. Desorption measurements on modified gold SEIRA electrodes were carried out in acetonitrile (0.1 M TBAF) using potential application steps of 15 s. Desorption measurements on me-ATO were carried out in both pH 7 PB buffer (0.1 M) and acetonitrile (0.1 M TBAP) using potential application steps of 120 s. In all cases, separate samples were prepared and measured for desorption measurements in each cathodic and anodic direction and in different media.

### 3.6.2 Density functional theory

To ease the assignment of the measured SEIRA spectra, theoretical IR spectra of benzanilide-Au, nitrobenzene-Au, nitrothiophenol-Au, aminobenzene-Au, aminothiophenol-Au, 4-mercapto-N-phenylquinone-Au and nitrosobenzene-Au were calculated using density functional theory (DFT) in vacuum. These DFT calculations were performed by Dr. Jacek Kozuch (formerly from the group of Prof. Peter Hildebrandt). The thiol or benzene hydrogen was substituted by an Au atom to account for structural changes upon binding to the Au surface. Geometry optimisation and vibrational analysis were performed on the BP86 level of theory using Gaussian 09.<sup>{FormattingCitation}</sup> For C, H, N, and O atoms the 6-31g\* basis set was chosen. For the heavier S the TZVP basis set, and for Au LanL2DZ (using a pseudo core potential) were employed.<sup>{FormattingCitation}</sup> Geometry optimisations were performed using the keywords “opt=tight” and “int=ultrafine” before calculating the vibrational frequencies. Experimental vibrational frequencies were assigned by analyzing the potential energy distribution of the normal modes obtained from the DFT calculations.

To assign the measured ATR-IR spectra on Im-interfaces on me-ATO, DFT calculations were performed in vacuum. These DFT calculations were performed by Robert Götz (from the group of Prof. Dr. Inez Weidinger, Technische Universität Dresden/Technische Universität Berlin). A phenyl-imidazole species bound to an Sn(OH)<sub>3</sub> cluster *via* a Sn-O-C bond was used to account for structural changes upon binding to the ATO surface. Geometry optimisation and vibrational analysis were performed using the BP86 level of theory through Gaussian 09.<sup>131–133</sup> For C, H, N, and O atoms the 6-31g\* basis set was employed, while for Sn the LanL2DZ (using a pseudo core potential) was employed.<sup>134–136</sup> Geometry optimisations were performed using the keywords “opt=tight” and “int=ultrafine” before calculating the vibrational frequencies.

### 3.6.3 X-ray photoelectron spectroscopy

X-ray photoelectron spectroscopy (XPS) was carried out using a Thermo Scientific K-Alpha instrument with monochromatic Al-K $\alpha$  radiation at 1486.6 eV on an area of 400  $\mu\text{m}^2$ . All spectra were charge corrected relative to the C-C component of the C 1s fitted spectra (285 eV). Survey scans were recorded with a resolution of 3 eV, while high resolution scans of the individual elements were recorded with a resolution of 5 eV. All spectra were charge corrected relative to the C-C component of the C 1s fitted spectra (285 eV). Spectra were fitted using the CasaXPS software (2.3.16) with mixed 30%/70% Gaussian/Lorentzian profiles and a Shirley background. N 1s spectra were fitted without any constraints. O 1s spectrum of the unmodified me-ATO were fitted using a Sb 3d<sub>5/2</sub> spin-orbit component with a constrained area and peak position (9.39 eV separation from the Sb 3d<sub>3/2</sub> component). The modified me-ATO O 1s spectrum was fitted using the same Sb 3d<sub>3/2/5/2</sub> spin-orbit separation and the ratio between the bulk lattice oxygen

component and the Sb 3d<sub>5/2</sub> was constrained to the same ratio determined for the unmodified me-ATO.

#### **3.6.4 Resonance Raman**

Resonance Raman measurements of the FePOMe species were performed by Robert Götz, while measurements of the CoPOH species were performed by Dr. Patrycja Kielb (formerly from the group of Prof. Dr. Inez Weidinger). Measurements were carried out using a confocal Raman spectrometer (LabRam HR-800, Jobin Yvon) equipped with a liquid N<sub>2</sub> cooled CCD Symphony detector. The samples were excited using the 413 nm line of the Kr ion continuous wave laser and the laser beam was focussed on the sample using a 20× Olympus objective. The scattered light was collected in a 180° back-scattering geometry. The laser power was adjusted for each experiment, with a final laser power of between 1-2 MW. Spectra were calibrated against the Raman shift of Hg, which is positioned at 435.834 nm. Spectra were collected with a spectral resolution of 1-2 cm<sup>-1</sup>. Spectroelectrochemical measurements were performed using the home-made PTFE cell mentioned previously with a three-electrode configuration. The cell consisted of a Ag/AgCl 3M KCl (Leak-Free, Warner Instruments) reference electrode, a platinum wire counter electrode a me-ATO film on ITO-coated glass as a working electrode. Control of the working electrode was achieved using a Metrohm potentiostat. The cell was rotated by means of a rotating table to avoid photoinduced processes, such as photodegradation or photoreduction. Measurements were performed at room temperature. Spectra were evaluated using the home-made qippsi software, with component fit analysis used to assign porphyrin vibrational modes. Peaks were fitted with Lorentzian curves.

#### **3.6.5 UV-Vis**

UV-vis spectroelectrochemical measurements were performed in a UV-Vis spectrometer (Agilent) using a home-made spectroelectrochemical cell with a three-electrode configuration. The cell consisted of a 3,500 uL optical glass cuvette, a Ag/AgCl 3M KCl (Leak-Free, Warner Instruments) reference electrode, a platinum wire counter electrode and a me-ATO film on ITO-coated glass as a working electrode. PTFE film was used to obtain a measureable surface area. Control of the working electrode was achieved using a Metrohm  $\mu$ AutolabIII potentiostat.

# Chapter 4

## Spectroelectrochemical investigation into the electrochemical grafting of diazonium salts on electrodes for the immobilisation of biological and molecular catalysts

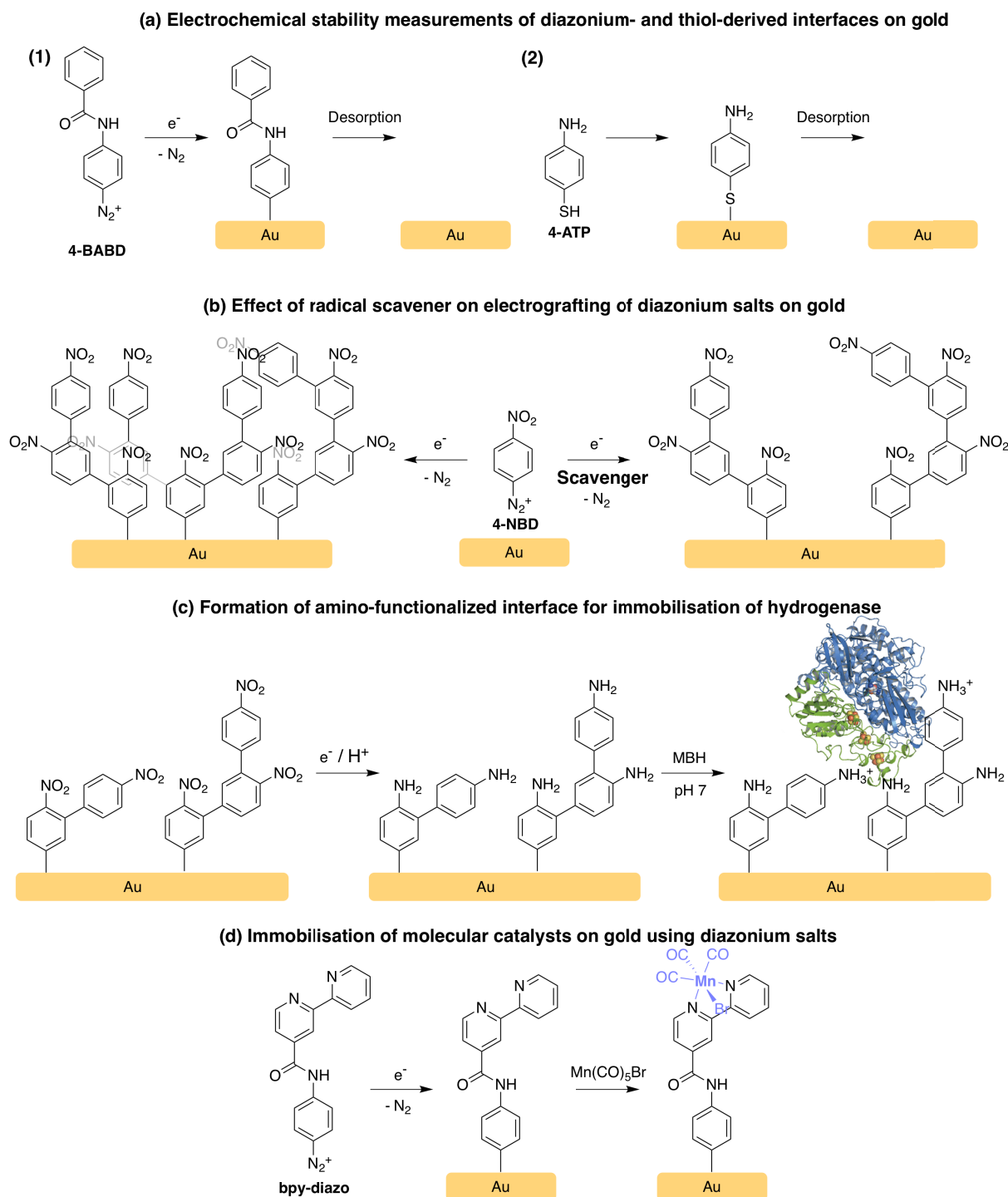
### 4.1 Introduction

In electrocatalysis, the interface between redox catalyst and electrode surface plays a critical role in terms of catalytic activity, stability and hence applicability in (bio-) technological applications. Despite its higher cost, gold still finds many applications as an electrode material due to its inherent inertness, low toxicity and applicability in a large number of spectroscopic and analytical techniques, including surface plasmon resonance spectroscopy, surface enhanced infrared and (resonance) Raman spectroscopies.<sup>30</sup> In order to produce functional electrocatalytic devices based on molecular or enzymatic catalysts and take advantage of their particular activities or study the structure or the mechanism by which these species function (e.g. by using spectroscopic techniques) it is necessary to attach them in a stable and direct electron transfer (DET) favourable configuration onto an electrode surface. In this context, thiols and other organosulfur compound self-assembled monolayers (SAMs) and are widely utilised in order to functionalise gold surfaces. However, SAMs suffer from poor chemical and electrochemical stabilities and, therefore, have limited application in electrochemical devices.<sup>137</sup> To overcome this limitation, much effort has been invested into finding alternative methods for modifying gold electrode materials. One very promising method is based on diazonium chemistry, which is applicable not only on gold but also on a broad range of other materials, as mentioned previously in (5.3.7, page 26).<sup>45</sup>

Electrografted diazonium interfaces take advantage of a strong covalent carbon-electrode bond formed between the diazonium bearing organic molecule and the substrate interface; a bond that has been shown to be very resistant to oxidation. Consequently, such interfaces were shown to exhibit excellent chemical, electrochemical and physical stabilities on a wide range of materials, including gold and carbon. However, a direct proof by any spectroscopic technique was not provided so far and the true electrochemical stability window of such diazonium-derived interfaces on gold remains unknown.<sup>62,138–140</sup>

The potential to immobilise enzymes on electrografted diazonium interfaces *via* electrostatic adsorption or covalent coupling has been demonstrated on carbon materials as well as on

gold,<sup>141–147</sup> and many examples exist where diazonium chemistry has been used to attach molecular complexes and catalysts to carbon materials.<sup>71,75,148–152</sup> One main disadvantage of diazonium chemistry is, however, the tendency to form thick multilayers due to branching polymerisation reactions, especially on gold. This often results in interfaces with insufficient conductivity and, hence, slow or suppressed heterogeneous electron transfer kinetics between the immobilised redox species and the electrode. Small changes in the deposition method or conditions can lead to significantly different outcomes in terms of interface structure, electron transfer properties and hence applicability, as was demonstrated by Brozik and co-workers for pyrroloquinoline quinone immobilised on gold.<sup>153</sup> De Lacey and co-workers obtained catalytic current for a laccase immobilised on gold by electrochemically depositing sub-monolayers using diazonium salts and filling in the areas in-between with thiol SAMs. Such mixed interfaces will, however, only be as stable as the thiol component. Alternatively, enzymes or molecules may themselves be functionalised with diazonium groups and directly electrografted onto an electrode surface, as demonstrated for diazonium-modified horseradish peroxidase grafted onto gold.<sup>76</sup> For large molecules like enzymes, this approach leads to a distribution of orientations on the electrode surface due to the lack of site-specific modification, and furthermore, the harsh modification conditions may not be suitable for many enzymes.<sup>76</sup> Correct orientation of the redox active enzyme at the electrode surface is crucial for ensuring high direct electron transfer rates between the electrode and the redox centre of the protein, thus eliminating the need for redox mediators. Orientation control can in general be achieved through the correct selection of surface functionality and adsorption conditions (such as pH etc.), as shown for the electrostatically adsorbed bilirubin oxidase on SAM-coated gold electrodes.<sup>154</sup>



#### Scheme 40

Overview of the different reactions and modification approaches used in this chapter: (a) shows the formation of diazonium- and thiol-derived interfaces on gold and their subsequent electrochemically-induced desorption, (b) shows the formation nitro-functionalised electrografted diazonium interfaces on gold with or without the addition of a radical scavenger to moderate interface growth, (c) shows the formation of amino-functionalised interfaces from the nitro-functionalised electrografted diazonium interfaces *via* electrochemical reduction for the immobilisation of membrane-bound hydrogenase (MBH), and (d) shows the immobilisation of a molecular catalyst on gold using similar diazonium chemistry.

The first part of this chapter will focus on the electrochemical stability of electrografted diazonium interfaces on gold electrodes and will compare them to thiol SAMs (Scheme 40a). To do so, a spectroelectrochemical method using a combination of electrochemical polarisation and *in situ* SEIRA spectroscopy was used. This technique is featured throughout this chapter and allows one

to follow the formation of interfaces and observe structural changes, e.g. under different chemical or electrochemical conditions, and is ideally suited to determine the electrochemical stability of the electrografted interfaces. Amine-terminated interfaces were used in this chapter as it has been shown that amine-terminated aliphatic SAMs facilitate the immobilisation of the oxygen-tolerant [NiFe] membrane bound hydrogenase (MBH), suitable for biotechnological fuel cell applications, in a direct-electron transfer configuration (Scheme 1c).<sup>85,155,156</sup> 4-aminothiophenol (**4-ATP**) is structurally more similar to diazonium salts than aliphatic amine thiols due to the presence of the phenyl ring and is therefore used for better comparison. Amino-terminated diazonium-derived interfaces are usually deposited by first functionalising the surface with a 4-nitrobenzene diazonium salt, such as 4-nitrobenzene tetrafluoroborate (**4-NBD**), and then electrochemically reducing the deposited nitro-groups to amino-groups (Scheme 1c). Isolating or synthesising diazonium salts from p-phenylenediamine is difficult due to the presence of two phenyl-amine groups, both of which may be diazotised. As such, a benzamide diazonium salt 4-benzamidobenzenediazonium tetrafluoroborate (**4-BABD**) was synthesised and used instead for the corresponding electrochemical stability study (Schemes 1a, 2a).

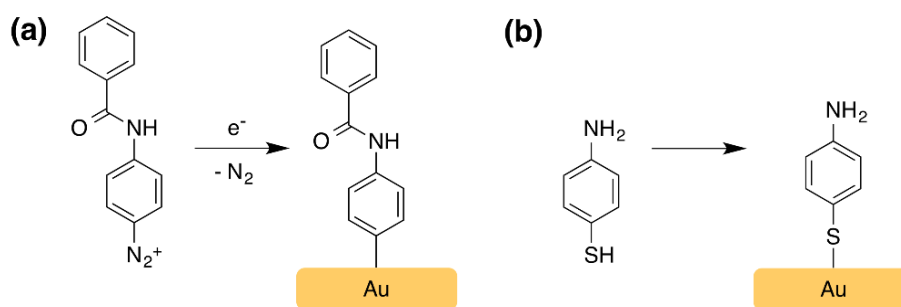
In the second part of this chapter, the effect of adding a radical scavenger during electrochemical grafting of gold with 4-NBD is studied (Scheme 40b). It was shown by Breton and co-workers that the addition of a radical scavenger such as 2,2-diphenyl-1-picrylhydrazyl (DPPH) during the reduction of 4-NBD on glassy carbon (GC) inhibits the polymerisation mechanism by which multilayers are formed, and thereby promotes monolayer formation.<sup>157</sup> This method was deployed on gold in this thesis in an attempt to obtain thinner interfaces that facilitate the direct electron transfer between an immobilised MBH enzyme and the electrode surface (Scheme 1c). As previously mentioned, this enzyme can be used in the reversible cleavage of dihydrogen with nearly no overpotential, i.e. close to thermodynamic potential, and is, therefore, of interest in applications involving the hydrogen oxidation reaction (HOR) as well as the hydrogen evolution reaction (HER). *In situ* SEIRA measurements were carried out in combination with protein film voltammetry (PFV), allowing structure-function studies to be carried out in order to determine the best modification conditions for achieving the highest catalytic currents from the immobilised enzyme.

In the last part of this chapter, diazonium salts are assessed for their suitability for immobilising molecular complexes and catalysts on gold electrodes (Scheme 40d). *In situ* SEIRA spectroelectrochemistry can be used to yield important structural insights into the mechanisms by which surface immobilised molecular and bio-catalysts function. A number of electrode materials used in the field of electrocatalysis are not IR transparent, such as carbonaceous materials (although studies have been carried out on carbon black and carbon nanotubes in ATR mode<sup>158,159</sup>), or lack the surface enhancement properties of nanostructured gold. Thiol-based

SAMs are not suitable for immobilising catalysts used in a number of important reactions, such as the CO<sub>2</sub> reduction reaction (COR), the HER and the oxygen evolution reaction (OER), due to their electrochemical instability in the potential ranges that these reactions take place in. Cathodic electrochemical desorption typically takes place at  $0 \pm 0.25$  V (vs RHE) in 0.1 M KOH.<sup>160–162</sup> A bipyridine-containing ligand **bpy-diazo** was synthesised for this purpose as bipyridine ligands are found in many molecular complexes that are relevant for electrocatalysis. In particular, carbonyl bipyridyl complexes of metals such as Re<sup>163</sup> and Ru<sup>164</sup> have been shown to be excellent molecular catalysts for the reduction of CO<sub>2</sub>. Recently, it was shown that manganese carbonyl bipyridyl complexes are also excellent catalysts for the selective electrochemical reduction of CO<sub>2</sub> to CO under mild conditions,<sup>165</sup> which generated significant interest given that Mn is an earth-abundant element, with numerous new derivatives and mechanistic studies being published.<sup>166–171</sup> Infrared spectroelectrochemical methods are particularly useful in this regard given the IR-activity of the carbonyl vibrational modes and those of intermediate species formed during the catalytic cycle. Kubiak and co-workers have carried out a number of studies using IR spectroelectrochemical methods to study such homogenous catalytic species in solution.<sup>166,169,171</sup> More recently, manganese carbonyl bipyridyl complexes were immobilised in Nafion/multi-walled carbon nanotube (MWCNT) membranes by Cowan and co-workers<sup>167,172</sup>, as well as on mesoporous TiO<sub>2</sub><sup>173</sup> and carbon nanotubes (CNTs)<sup>159</sup> electrodes by Reisner and co-workers. In the latter two examples, the bipyridine ligands were modified with phosphonic acid or pyrene moieties, respectively, to allow immobilisation *via* chemisorption or  $\pi$ - $\pi$  stacking. In this thesis, using the previously mentioned bpy-diazo linker, Mn(bpy)(CO)<sub>3</sub>Br was immobilised on gold starting from Mn(CO)<sub>5</sub>Br *via* different methods, studied using SEIRA spectroscopy and assessed for catalytic activity.

#### 4.2 Electrochemical reduction of diazonium salts on gold

A freshly prepared, bare gold SEIRA electrode coated on a Si-prism was incubated with 4-BABD within the spectroelectrochemical cell in acetonitrile (0.1 M TBAF), and, upon incubation, SEIRA spectroscopy showed that 4-BABD species are adsorbed onto the electrode surface from solution (Figure 6). This is indicated by the appearance of the corresponding  $\nu(\text{N}\equiv\text{N})$  stretching vibration band at 2262 cm<sup>-1</sup> and bands corresponding to the benzanilide moiety, as summarised in Table 1. Band assignments were made with the assistance of DFT calculations (see Appendix 1a) and refer in the allocation given here to the dominant vibrational modes.



**Scheme 41**

Formation of diazonium and SAM-derived interfaces on gold. These are formed by (a) electrochemical reduction of **4-BABD** and (b) spontaneous adsorption of **4-ATP**.

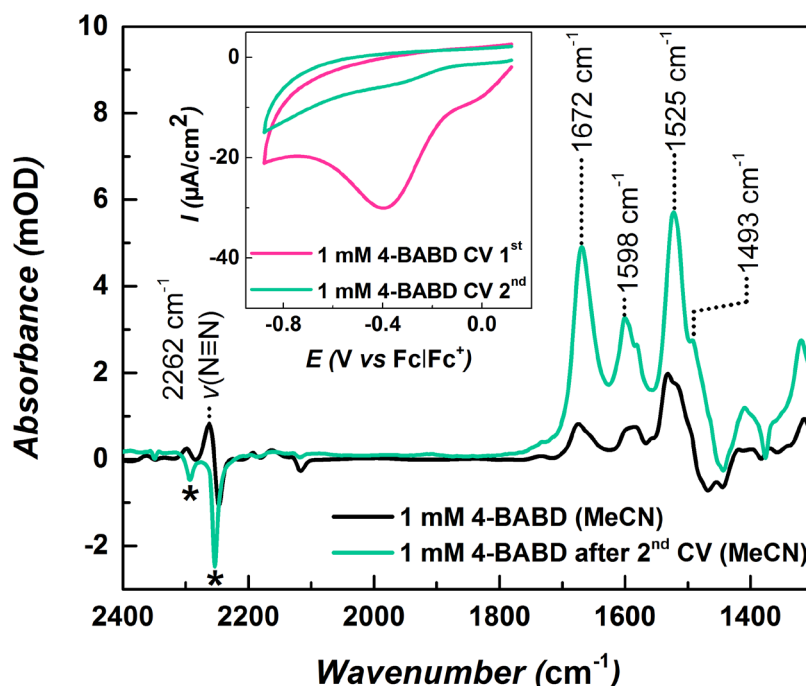


**Figure 6**

*In situ* SEIRA spectra of a gold thin film electrode incubated with 1 mM 4-BABD in acetonitrile (0.1 M TBAF) before (black trace) and after application (green trace) of two CVs at a scan rate of 50 mV/s between +0.12 and -0.88 V (vs Fc/Fc<sup>+</sup>), starting in the cathodic direction (see inset for CVs). The reference spectrum was recorded for unmodified gold in acetonitrile (0.1 M TBAF). The negative bands corresponding to the displaced acetonitrile solvent molecules at the interface are asterisked.

As seen in Figure 6 (inset), electrochemical reduction resulted in the passivation of the electrode. This is indicated by a sharp decrease in reductive current upon subsequent cycling and by the growth of the benzanilide band intensities, along with the simultaneous disappearance of the  $\nu(\text{N}\equiv\text{N})$  band and two negative bands (asterisked) that surround it, corresponding to acetonitrile solvent displaced from the interface. After electrochemical reduction, non-covalently bound species were removed by cycling the gold electrode several times to mild anodic potentials in fresh acetonitrile (0.1 M TBAF). For comparison, thiol-derived SAMs were deposited *via* the spontaneous adsorption of 4-ATP. The successful formation of these interfaces is seen in the SEIRA spectra (Figure 7c and d) and is indicated by the appearance of characteristic absorption bands corresponding to the aminothiophenol moiety, as summarised in Table 2.

**Table 2**

Assignment of the major absorption bands to the characteristic dominating vibrational modes made with the assistance of DFT calculations for Au covering interfaces deposited by electrochemical reduction of 1 mM 4-BABD or by spontaneous adsorption of 1 mM 4-ATP on gold electrodes.

<b>Sample</b>	<b>Band position (cm<sup>-1</sup>)</b>	<b>Band assignment</b>	<b>Dominant vibration</b>
<b>4-BABD</b>	1493	$\delta(\text{C-H}) + \nu(\text{C=C})_{\text{ar}}$	C-H bending coupled with a C=C aromatic stretching
	1525	$\delta(\text{N-H})$	N-H bending vibration
	1598	$\nu(\text{C=C})_{\text{ar}} + \delta(\text{N-H})$	C=C aromatic stretching coupled with a N-H bending
	1672	$\nu(\text{C=O})$	C=O stretching
	2262	$\nu(\text{N}\equiv\text{N})$	N≡N stretching
<b>4-ATP</b>	1488	$\delta(\text{C-H}) + \nu(\text{C=C})_{\text{ar}}$	C-H bending coupled with a C=C aromatic stretching
	1593	$\nu(\text{C=C})_{\text{ar}}$	C=C aromatic stretching
	1627	$\delta(\text{NH}_2)$	NH <sub>2</sub> bending
	3370	$\nu_{\text{s}}(\text{NH}_2)$	NH <sub>2</sub> symmetric stretching

### 4.3 Electrochemical stability of electrografted diazonium interfaces on gold

In order to assess the anodic and cathodic stability of the electrografted diazonium interfaces and the SAMs, SEIRA spectra were recorded under a constant potential of -0.58 V (vs Fc/Fc<sup>+</sup>) after polarising the respective modified electrodes at different cathodic and anodic potentials (in 100 mV steps) for 15 s (Figure 7a – d) to avoid charge-induced differences in the orientation of the organic molecules at the interface due to fluctuating open circuit potentials. Plots of the SEIRA band intensities against the applied potentials allow one to follow potential-induced changes in the interface structure and composition and thereby assess their electrochemical stability range (see Appendix 2a - d).

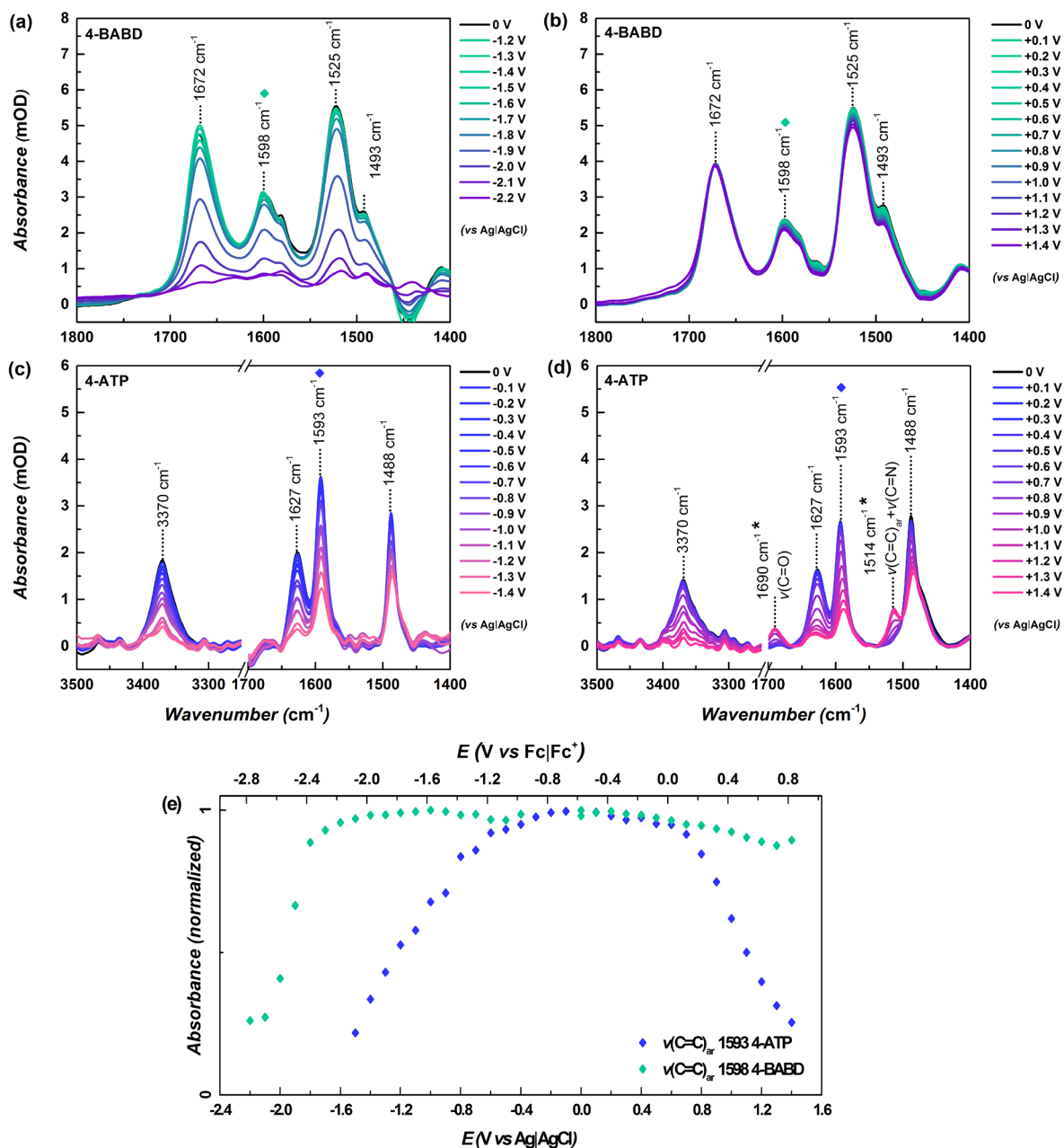


**Figure 7**

*In situ* SEIRA spectra recorded at -0.58 V (vs Fc/Fc<sup>+</sup>) (0 V (vs Ag/AgCl 3M KCl)) in acetonitrile (0.1 M TBAF) following the interfacial desorption induced by electrode polarisation at different potentials: behaviour of an electrografted 4-BABD diazonium interface under (a) cathodic and (b) anodic polarisation and behaviour of a 4-ATP SAM-based interface under (c) cathodic and (d) anodic polarisation (asterisked bands assigned to the dimerised 4-mercapto-N-phenylquinone monoimine (NPQM) species). (e) Normalised ν(C=C)<sub>ar</sub> absorption band intensities at 1598 and 1593 cm<sup>-1</sup> plotted against polarisation potential for spectra (a) (b), and (c) (d), respectively.

In order to better compare the difference in the electrochemical stabilities of the Au—C and Au—S bound interfaces, the normalised SEIRA intensities of an aromatic C=C stretching vibration, common to both molecular systems, are plotted against the applied potential (Figure 7e). As one can see, the electrografted diazonium interface is stable over a much broader potential window in acetonitrile than the SAM-derived interface. The electrografted diazonium interface is stable up to +0.8 V (vs Fc/Fc<sup>+</sup>), above which gold oxidation occurs, and down to -2.2 V (vs Fc/Fc<sup>+</sup>), after which a sharp decrease in band intensity is observed due to reductive

desorption. The small decrease in band intensity observed between -0.6 and 0.8 V (vs Fc/Fc<sup>+</sup>) in Figure 3 may be due to potential-induced desorption of remaining physisorbed species that resist post-modification rinsing and electrochemical treatments; such species could arise from homogeneous coupling between reactive species in solution. It has been suggested by others that this accounts for such a loss of material observed during sonication or refluxing.<sup>139</sup> In contrast, the SAM is only stable up to around 0 V (vs Fc/Fc<sup>+</sup>), at which point oxidative desorption begins to occur. In acetonitrile, there is no spectroscopic evidence of oxidised species such as sulfonites (S=O vibration), as is the case for oxidative desorption in aqueous solvents.<sup>162</sup> Two new absorption bands (asterisked) at 1690 cm<sup>-1</sup> and 1514 cm<sup>-1</sup> begin to appear at around 0.4 V (vs Fc/Fc<sup>+</sup>) and may be attributed to a dimerised species, 4'-mercapto-N-phenylquinone monoimine (NPQM), that is known to be formed as a result of head-to-tail coupling between adjacent oxidised aminothiophenol species.<sup>174–176</sup>

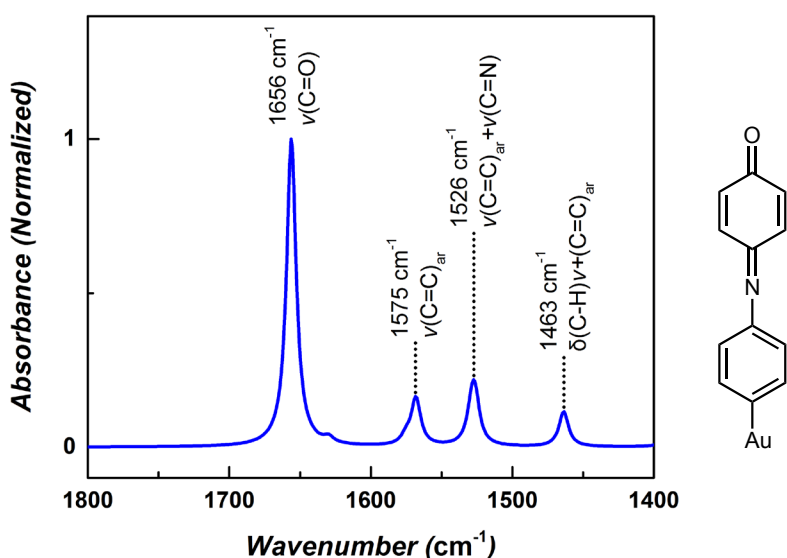


**Figure 8**

Calculated spectrum of 4-mercapto-N-phenylquinone (NPQM) monoamine bound to a gold atom using DFT and assignment of the main absorptions to the dominating, characteristic vibrational modes.

The corresponding calculated spectrum of this species bound to gold (Appendix 3) supports the hypothesis that a dimerised species NPQM is formed, with an absorption band at 1656 cm<sup>-1</sup> characteristic for the  $\nu(\text{C}=\text{O})$  stretching vibration of the quinone, and another band at 1526 cm<sup>-1</sup> related preferentially to a  $\nu(\text{C}=\text{C})$  aromatic stretching vibration coupled with a C=N stretching vibration of the imine bond. In the cathodic range, significant desorption of the thiolate begins to occur at around -1.2 V (vs Fc/Fc<sup>+</sup>) and the entire desorption process takes place over a wider potential window than that observed for the reductive desorption of the electrografted diazonium interface. This can be explained by the reversible nature of the one-electron thiolate desorption/re-adsorption process. The exact potential at which thiolate species are reduced depends not only on the substrate-adsorbate interaction but also on the adsorbate-adsorbate intermolecular interactions.<sup>161</sup>

#### 4.4 Effect of radical scavenger on interface formation

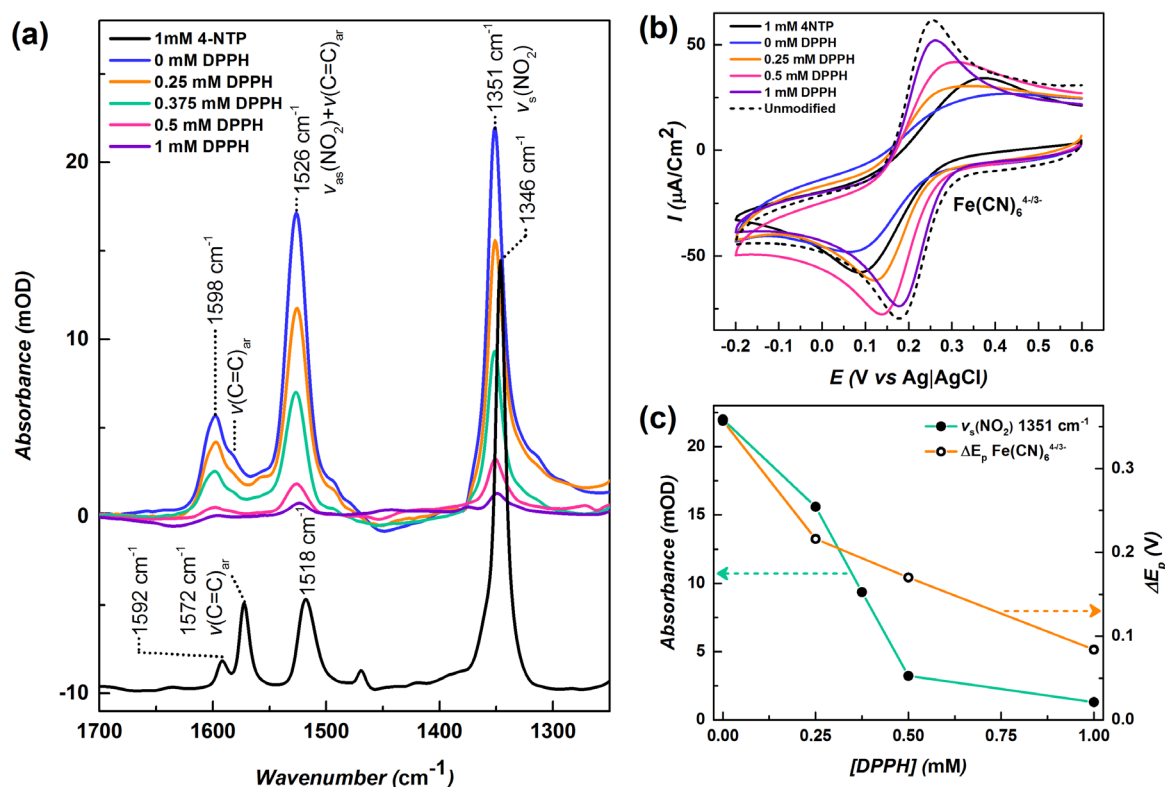


**Figure 9**

(a) SEIRA spectra recorded in acetonitrile of interfaces that were deposited on gold electrodes by electrochemical reduction of 1 mM 4-NBD with increasing molar equivalents of added DPPH (coloured traces), as well as a SAM deposited by spontaneous adsorption of 1 mM 4-NTP (black trace), (b) cyclic voltammograms of 1 mM  $\text{K}_3[\text{Fe}(\text{CN})_6]$  recorded at 50 mV/s in 0.1 M PB (pH 7) of the same interfaces and (c) plots showing the change in the  $\nu_s(\text{NO}_2)$  band intensity, as well as the change in the peak separation  $\Delta E_p$  for the  $[\text{Fe}(\text{CN})_6]^{4-/3-}$  couple with increasing concentration of DPPH.

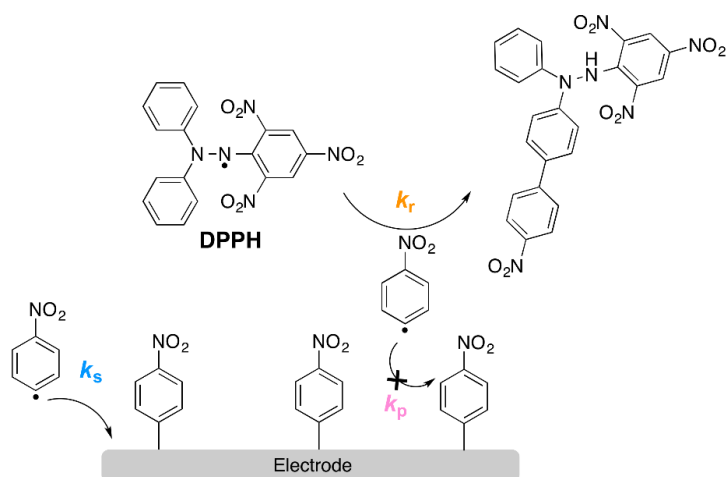
Electrochemical reduction of 1 mM 4-NBD results in the passivation of the gold surface with a dense polymeric interface, as has previously been reported.<sup>139</sup> SEIRA spectra were recorded after the reduction with and without the addition of different molar equivalents of the radical scavenger DPPH (see Figure 3(a)). The spectrum of gold modified with 4-NTP is included for comparison. Band assignments were made with the assistance of DFT calculations (see Appendix 1b and c) and are in line with previous literature reports.<sup>139</sup>

**Table 3**

Assignments of the most prominent absorption bands to the dominant characteristic vibrational modes were made with the assistance of DFT calculations for interfaces deposited on gold by electrochemical reduction of 1 mM 4-NBD or spontaneous adsorption of 1 mM 4-NTP.

<b>Sample</b>	<b>Band position (cm<sup>-1</sup>)</b>	<b>Band assignment</b>	<b>Dominant vibration</b>	
<b>4-NBD</b>	1351	$\nu_s(\text{NO}_2)$	Symmetric stretching	$\text{NO}_2$
	1526	$\nu_{as}(\text{NO}_2)+\nu(\text{C}=\text{C})_{ar}$	Antisymmetric stretching coupled with a C=C aromatic stretching	$\text{NO}_2$
	1598	$\nu(\text{C}=\text{C})_{ar}+\nu_{as}(\text{NO}_2)$	C=C aromatic stretching coupled with an antisymmetric $\text{NO}_2$ stretching	$\text{NO}_2$
<b>4-NTP</b>	1346	$\nu_s(\text{NO}_2)$	Symmetric stretching	$\text{NO}_2$
	1518	$\nu_{as}(\text{NO}_2)+\nu(\text{C}=\text{C})_{ar}$	Antisymmetric stretching coupled with a C=C aromatic stretching	$\text{NO}_2$
	1572	$\nu(\text{C}=\text{C})_{ar}$	C=C aromatic stretching	$\text{NO}_2$
	1592	$\nu(\text{C}=\text{C})_{ar}+\nu_{as}(\text{NO}_2)$	C=C aromatic stretching coupled with an antisymmetric $\text{NO}_2$ stretching	$\text{NO}_2$

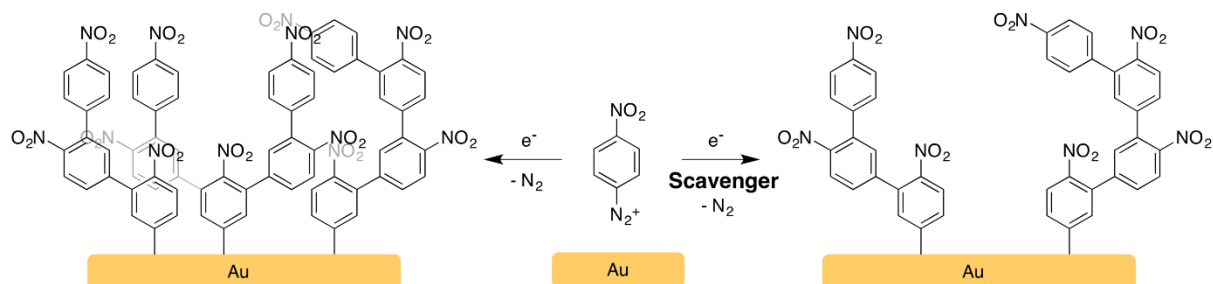
Having a closer look, one can see a difference in the ratio between the  $\nu_s(\text{NO}_2)$  and the  $\nu_{as}(\text{NO}_2)+\nu(\text{C}=\text{C})_{ar}$  adsorption band intensities –  $I[\nu_s(\text{NO}_2)]/I[\nu_{as}(\text{NO}_2)+\nu(\text{C}=\text{C})_{ar}]$  – for each interface. This ratio is related to the way molecules arrange at the corresponding interface. Indeed, due to the SEIRA surface selection rules, only modes which preferentially exhibit dipole moment changes perpendicular to the surface are enhanced, indicating that, with a large value of  $I[\nu_s(\text{NO}_2)]/I[\nu_{as}(\text{NO}_2)+\nu(\text{C}=\text{C})_{ar}]$ , 4-NTP forms a monolayer where the molecules are arranged uniformly. Conversely, with a value of  $I[\nu_s(\text{NO}_2)]/I[\nu_{as}(\text{NO}_2)+\nu(\text{C}=\text{C})_{ar}]$  of almost 1, diazonium salts form disordered, polymeric interfaces, where the formation of a preferential orientation is not possible.<sup>139</sup>



#### Scheme 42

Proposed mechanism by which radical scavengers inhibit polymerisation during the electrochemical grafting of diazonium salts on electrode surfaces. For monolayer coverage, the rate of phenyl radical adsorption on the electrode surface ( $k_s$ ) must be greater than the rate of radical coupling to the radical scavenger ( $k_r$ ), which in turn must be greater than the rate of radical coupling to already grafted phenyl moieties ( $k_p$ ). The coupling product of DPPH and the nitrophenyl radical, 2-[4-(4-nitro)phenyl]-2-phenyl-1-picrylhydrazine, was detected by Breton and co-workers in experiments carried out using GC electrodes.<sup>157</sup>

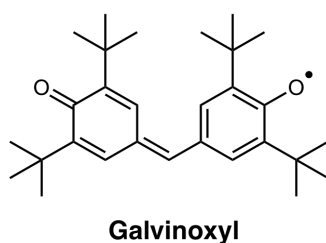
It was shown by Breton and co-workers that the addition of a radical scavenger such as DPPH during the reduction of 4-NBD on GC inhibits the polymerisation mechanism by which multilayers are formed, and thereby promotes monolayer formation.<sup>157</sup> This effect would, if occurring in the case of the gold electrodes presented here, result in an increase in  $I[v_s(\text{NO}_2)]/I[v_{as}(\text{NO}_2)+v(\text{C}=\text{C})_{ar}]$ . However, as seen in Figure 9a, when gold is used as substrate,  $I[v_s(\text{NO}_2)]/I[v_a(\text{NO}_2)+v(\text{C}=\text{C})_{ar}]$  remains roughly the same at all concentrations of DPPH, while the band intensities decrease proportionally until at 1 equivalent of DPPH almost no material is electrografted on the gold surface anymore. CVs of a ferricyanide electrochemical probe (see Figure 9b) measured for the electrografted diazonium interfaces deposited in the presence of various DPPH concentrations confirm this finding: the peak-to-peak separation ( $\Delta E_p$ ) of the oxidation/reduction features of the  $[\text{Fe}(\text{CN})_6]^{4-/3-}$  ( $\text{Fe}^{2+/3+}$ ) couple decreases with increasing DPPH concentration, indicating a substantial decrease in the charge transfer resistance  $R_{CT}$  of the interface, until at 1 equivalent DPPH the electrochemical response is almost the same as for an unmodified electrode. A CV of a gold electrode modified with a 4-NTP SAM is included for comparison.



#### Scheme 43

The proposed structures for interfaces electrochemically grafted from 4-NBD, with and with the addition of a radical scavenger.

The behaviour observed for gold is in sharp contrast to the one observed for GC where surface coverage and  $R_{CT}$  reach a steady-state minimum corresponding to approximate monolayer coverage. For such a monolayer coverage, the rate of phenyl radical adsorption on the electrode surface ( $k_s$ ) must be greater than the rate of radical coupling to the radical scavenger ( $k_r$ ), which in turn must be greater than the rate of radical coupling to already grafted phenyl moieties ( $k_p$ ),<sup>157</sup> as illustrated in Scheme 42. In the case of gold, the obtained results indicate that the rate of coupling with the radical scavenger is greater than with the gold surface, so that both surface adsorption of radicals and polymerisation is suppressed, leading to less material being deposited in a less dense, albeit still polymeric, interface, as illustrated in Scheme 43. This difference in behaviour can be related to the lower adsorption energy of the phenyl moiety on gold (predicted to be 24 kcal/mol) compared to greater adsorption energies on carbon materials (predicted to be as great as 63 kcal/mol for graphene), meaning that radical adsorption is energetically favoured on GC.<sup>177,178</sup>



**Scheme 44**  
Chemical structure of the radical scavenger galvinoxyl.

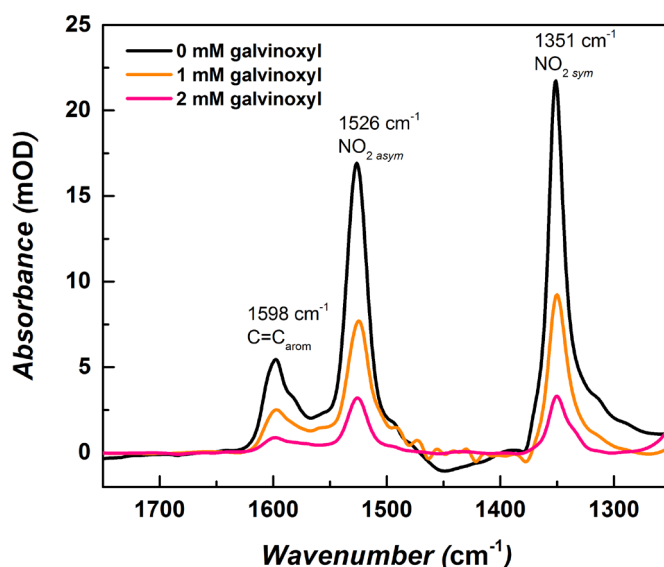


**Figure 10**  
SEIRA spectra recorded in acetonitrile of interfaces deposited by electrochemical reduction of 1 mM 4-NBD under the same conditions with increasing molar equivalents of the radical scavenger galvinoxyl added.

Even though a monolayer coverage could not be achieved on gold, this method of using radical scavenger leads to reproducible, less dense interfaces with decreased interfacial charge transfer resistance. Trials using the less reactive radical scavenger galvinoxyl (for structure see Scheme 44) showed a similar behaviour, and comparable results as with DPPH could be achieved using

higher radical scavenger concentrations, as shown in Figure 10. Thus, the addition of radical scavenger can reduce the  $R_{CT}$  of the deposited interfaces sufficiently to allow the use of the functionalised interfaces for the immobilisation and utilisation of electroactive species, while still taking advantage of the interfaces superior stability.

#### 4.5 Spontaneous adsorption of diazonium salts on gold

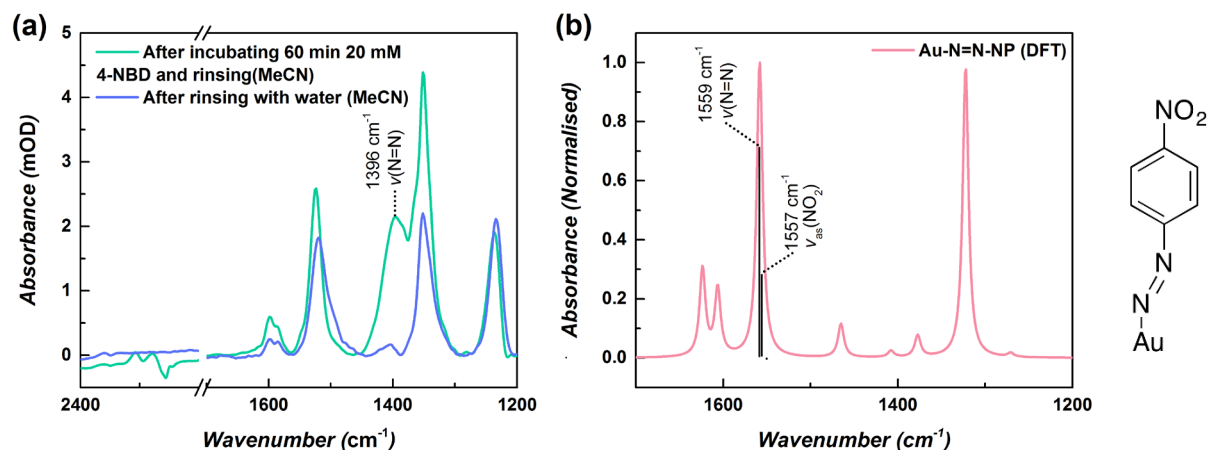
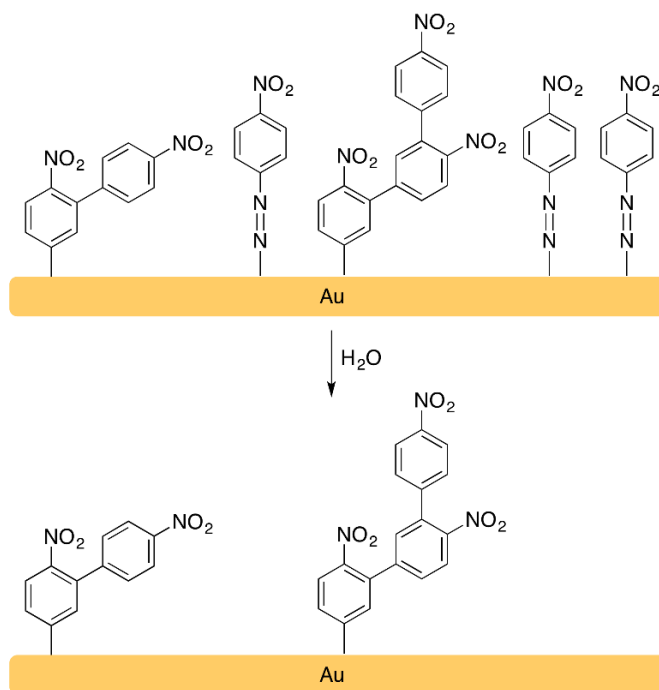


**Figure 11**

(a) SEIRA spectra recorded in acetonitrile of interfaces deposited by the spontaneous adsorption of 4-NBD from a 20 mM solution in acetonitrile, before (green trace) and after (blue trace) rinsing in water. (b) Spectrum calculated using DFT of a nitrophenyl moiety bound to a gold atom *via* a terminal azo N=N bond.

It has been widely reported that diazonium salts adsorb spontaneously onto a range of materials including GC,<sup>56,179–181</sup> various metals<sup>52,56</sup> and gold.<sup>52,182,183</sup> The exact mechanism by which these interfaces are formed on gold has not been fully elucidated yet, but is known to occur *via* different routes in various media and conditions, with possible routes involving the adsorption of cationic, radical or diazonium species at the surface of the gold, or at already grafted/adsorbed moieties. Figure 11a displays the SEIRA spectrum of gold after incubation with a 20 mM 4-NBD solution in acetonitrile for 60 min (at this point no further increase in adsorption intensity can be observed) and thorough rinsing with fresh acetonitrile. Overall band intensities are low compared to the electrochemically grafted interfaces (<5 mOD), while the  $\nu(\text{C}=\text{C})_{\text{arom}}$ ,  $\nu(\text{NO}_2)_a$  and  $\nu(\text{NO}_2)_s$  bands appear at or near the same wavenumbers. An increase in the value of  $|\nu_s(\text{NO}_2)|/|\nu_{as}(\text{NO}_2)+\nu(\text{C}=\text{C})_{ar}|$  to 1.7 is observed, suggesting an increased ratio of monomeric surface-bound species compared to the electrochemically grafted interfaces. A broad band of medium intensity appears at  $1396\text{ cm}^{-1}$ , which is absent from the electrochemically grafted interfaces. This value is similar to bands observed at  $1377$  and  $1392\text{ cm}^{-1}$  by Calvo and co-workers in IR absorption spectra of 4-carboxybenzene diazonium and 4-carboxy-2,3,5,6-tetrafluorobenzene diazonium tetrafluoroborate salts on gold, which are claimed to be due to the  $\nu(\text{N}=\text{N})$  stretching vibration of azo-linkages, with indications given to the existence of branched azo-bonds (i.e. to already-grafted moieties) and terminal Au-N=N- azo-bonds.<sup>184</sup> The bands observed here and by Calvo and co-workers appear at much lower wavenumbers than one would

normally expect for azo-bonds, and indeed, a calculated spectrum for Au-N=N-PhNO<sub>2</sub> (Figure 11b) shows a band for the  $\nu(\text{N}=\text{N})$  stretching vibration at 1559 cm<sup>-1</sup> (which overlaps with the  $\nu_{\text{as}}(\text{NO}_2)$  vibration at 1557 cm<sup>-1</sup>). This phenomena was explained by Calvo and co-workers as resulting from conjugation through the azo bond.<sup>184</sup>



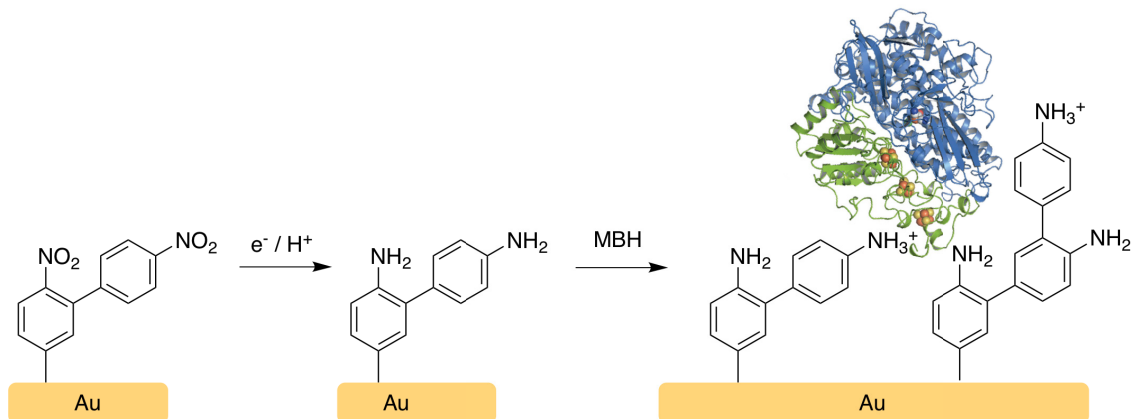
#### Scheme 45

Proposed structure of interface deposited from the spontaneous adsorption of 4-NBD on gold from an acetonitrile solution, before and after rinsing with water.

The binding of the nitrophenyl moieties to the gold *via* terminal Au-N=N- azo-bonds would explain the increase in  $I[\nu_{\text{s}}(\text{NO}_2)]/I[\nu_{\text{as}}(\text{NO}_2)+\nu(\text{C}=\text{C})_{\text{ar}}]$  compared to the electrochemically grafted interfaces. Upon rinsing the electrode with water there was a marked decrease in intensity for all bands and a decrease in  $I[\nu_{\text{s}}(\text{NO}_2)]/I[\nu_{\text{as}}(\text{NO}_2)+\nu(\text{C}=\text{C})_{\text{ar}}]$  from 1.7 to 1.2, which was also accompanied by the almost-complete disappearance of the  $\nu(\text{N}=\text{N})$  band at 1396 cm<sup>-1</sup> (Figure 11a), suggesting the removal or hydrolysis of monomeric, terminal bound azo-bound species from the gold (as illustrated in Scheme 45). Any remaining species must be bound to the surface *via* Au-C bonds and, therefore, be deposited from cationic- or radical-phenyl species, which can form as a result of the spontaneous homo- or heterolytic decomposition of diazonium species. Palacin and co-workers show evidence from XPS of some species bound to gold *via* an azo-bond deposited from solutions of diazonium salts in both water and acetonitrile.<sup>52</sup> They propose an interaction between a vacant 2p orbital on the terminal nitrogen of the diazonium species and the full 5d orbitals of gold. Such a binding motif would correspond well with the observation of a band at 1396 cm<sup>-1</sup>, with the release of electrons from the gold 5d orbitals into the vacant nitrogen 2p orbital weakening the N=N bond and leading to a decrease in the wavenumber of the  $\nu(\text{N}=\text{N})$  band. Due to the instability of these interfaces in aqueous environments, they were deemed unsuitable for further utilisation for the immobilisation on MBH.

#### 4.6 Immobilisation of hydrogenase on electrografted diazonium interfaces

As previously mentioned, electrografted diazonium interfaces have been used to immobilise enzymes on a range of electrode materials.<sup>141–146</sup> It was previously shown by Heidary et al. that it is possible to immobilise the strep-tag MBH onto amino-terminated SAMs on gold, resulting in a compact enzyme monolayer. The enzyme does not denature upon immobilisation and allows interfacial, preferentially direct electron transfer processes, and it keeps its catalytic functionality. Hence, second, ternary and quaternary structures are preserved.<sup>84,85</sup>



**Scheme 46**

Electrochemical reduction of a nitrophenyl interface electrografted on gold and the subsequent immobilisation of MBH under orientation control.

Nitrophenyl moieties can be reduced chemically or electrochemically in protic conditions to aminophenyl moieties (see Scheme 46), as has been widely reported.<sup>185,186,147</sup> Reduction of the nitrophenyl moieties is necessary to allow the adsorption and immobilisation of the MBH onto the surface *via* electrostatic and hydrogen bonding interactions between the surface of the enzyme and the amino-terminated surface. The electrodes that were electrografted with 4-NBD and DPPH were subsequently electrochemically reduced by cycling the electrode between 0 and -1.2 V (vs Ag/AgCl 3M) in a 0.1 M NaClO<sub>4</sub> 1:9 ethanol:water solution. SEIRA spectra were recorded after reduction and are shown in Figure 12a. As for the previous spectra, band assignments were made with the assistance of DFT calculations (see Appendix 1d). A pronounced decrease in the band intensity of the  $\nu_s(\text{NO}_2)$  and  $\nu_{as}(\text{NO}_2)$  absorption bands is observed upon electrochemical reduction, as previously reported by Vaz-Domínguez et al.<sup>147</sup> The  $\nu(\text{C}=\text{C})_{ar}$  band at 1600 cm<sup>-1</sup> remains with similar intensity, while a broad shoulder appears around 1626 cm<sup>-1</sup> corresponding to the  $\delta(\text{NH}_2)$  band. It must be noted that the  $\nu_s(\text{NO}_2)$  adsorption at 1350 cm<sup>-1</sup> does not vanish completely after reduction, indicating the presence of residual NO<sub>2</sub> within the interfaces, in line with previous studies. Nevertheless, the contribution is negligible. In line with this conclusion, it is also possible to see a shoulder close to the  $\delta(\text{C}-\text{H})+\nu(\text{C}=\text{C})_{ar}$  band at 1520 cm<sup>-1</sup>, which may correspond to the  $\nu(\text{N}=\text{O})$  stretching vibration of incompletely reduced nitrosophenyl species (a spectrum for this species was calculated and is shown in Appendix 3). The SEIRA spectra of the electrochemically reduced interface is similar to that of a SAM deposited from the

spontaneous adsorption of 4-ATP (Appendix 1e). All band intensities decrease proportionally with the amount of DPPH added during the nitrophenyl interface formation.

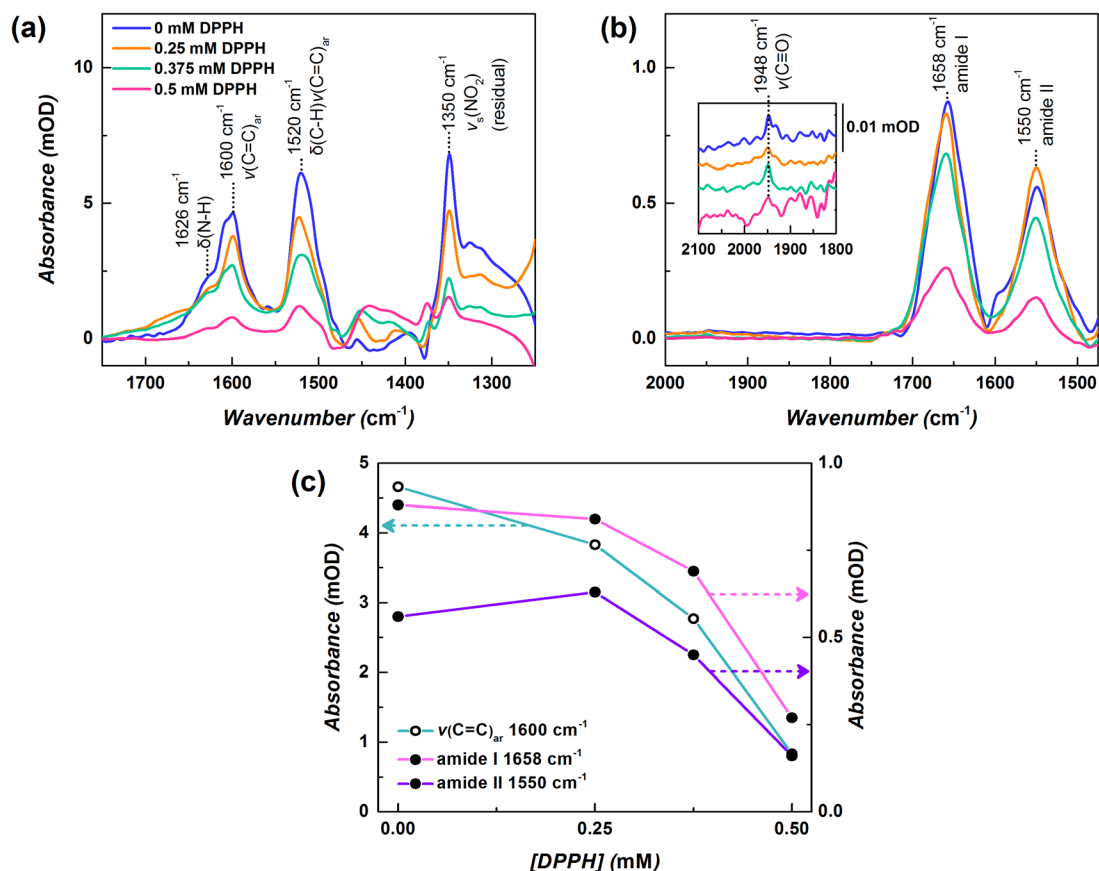


**Figure 12**

(a) SEIRA spectra in acetonitrile of the amino functionalised interfaces deposited by the electrochemical grafting of 1 mM 4-NBD with increasing molar equivalents of DPPH added that were subsequently electrochemically reduced in 0.1 M NaClO<sub>4</sub>, 1:9 ethanol:water solution, (b) SEIRA spectra in buffer (pH 7, 10 mM phosphate buffer (PB)) of MBH adsorbed onto the same amino functionalised interfaces after rinsing with buffer (inset: shows a characteristic active site band of the enzyme, namely the  $\nu(\text{C}=\text{O})$  stretching vibration of the Fe-coordinated carbon monoxide ligand, which can be detected at 1948  $\text{cm}^{-1}$  for the so called “Ni<sub>r</sub>-B” state of the oxidised enzyme) and (c) plots showing the change in the  $\nu(\text{C}=\text{C})_{\text{ar}}$  band intensities, as well as the amide I and II band intensities, for all spectra with increasing concentration of DPPH.<sup>85</sup>

In order to evaluate the suitability of the electrografted interfaces for enzyme immobilisation and bio-electrocatalysis, we studied the electrostatically-controlled adsorption of the MBH onto the amino functionalised surfaces from a bulk solution at pH 7. Previous studies demonstrated that SEIRA spectroelectrochemistry is a powerful tool for the investigation and knowledge-based optimisation of protein immobilisation on electrode surfaces for optimally exploiting enzymatic processes in bioelectronic devices.<sup>84,85</sup> Additionally, it is an invaluable tool for elucidating underlying molecular catalytic mechanisms by directly probing active site states. In case of hydrogenases this is possible due to the absorption properties of Fe-bound CN<sup>-</sup> and CO ligands.<sup>187</sup> The appearance of two broad absorption bands at 1658 and 1550  $\text{cm}^{-1}$  in the SEIRA spectra (see Figure 12b) corresponding to the amide I and amide II bands of the protein backbone proves the successful binding of the MBH to the electrografted diazonium interface. The appearance of the band at 1948  $\text{cm}^{-1}$ , related to the  $\nu(\text{C}=\text{O})$  stretching vibration of the CO ligand coordinated to the [Ni-Fe] active site and characteristic for the highest oxidised ‘Ni<sub>r</sub>-B’

state,<sup>188</sup> indicates that also the enzyme's active integrity is preserved upon surface immobilisation.<sup>130,189</sup> These results are in good agreement with the previous SEIRA study by Heidary et al. reporting the electrostatic immobilisation of MBH onto amino-1-hexanethiol gold modified electrodes under the same conditions. These results clearly underline the “binding” similarity between diazonium-derived and thiol-derived amino-terminated interfaces.<sup>85</sup> The  $pK_a$  of an amino-1-hexanethiol SAM was determined at close to 6 and is assumed to be 8% protonated at pH 7.<sup>190</sup>  $pK_a$  values for amino functionalised surfaces derived from the aliphatic-amine containing 4-aminobenzylidiazonium and 4-(2-aminoethyl)benzenediazonium have been previously reported to be around 10.0 and 10.5 respectively<sup>191</sup>, while a  $pK_a$  of 6.9 was determined for 4-ATP SAMs on gold.<sup>192</sup> We assume that the  $pK_a$  values of our aminophenyl surfaces are at least greater than 6 and therefore a significant proportion of the surface will be protonated leading to an electrostatic binding. A decrease in MBH adsorption is observed with decreasing aminophenyl density (i.e. when increasing amounts of scavenger are added), as indicated by a decrease in amide band intensity (plotted in Figure 12c). It is tentatively proposed that this is a result of decreasing electrostatic attraction, due to a decrease in protonated aminophenyl moieties at the interface.

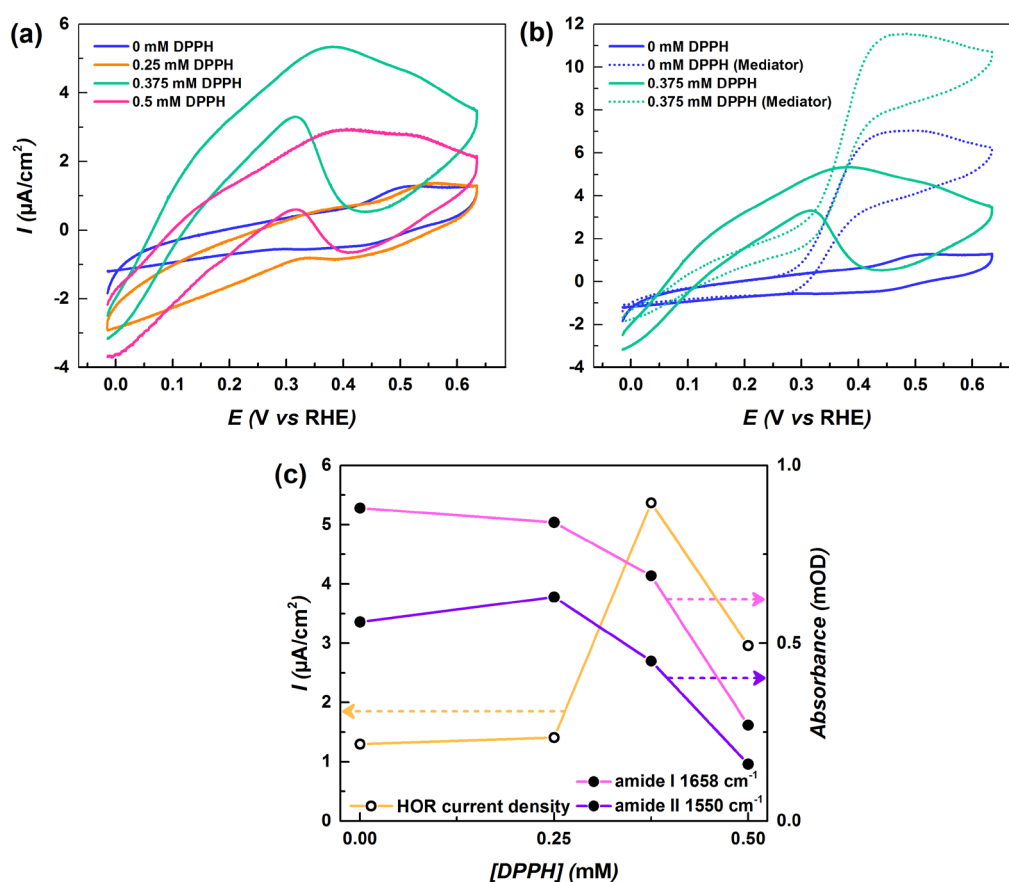


**Figure 13**

Protein film voltammograms recorded in 10 mM PB buffer at pH 5.5 saturated with  $\text{H}_2$  with a scan rate of 5 mV/s on MBH adsorbed onto amino-functionalised interfaces (a) after and (b) before addition of the redox mediator methylene blue. (c) Plots showing the change in the maximum electrocatalytic current for  $\text{H}_2$  oxidation reaction (HOR) due to direct electron transfer and the corresponding MBH amide I and II band intensities with increasing concentration of DPPH added during interface formation.

Cyclic voltammograms of the samples incubated with MBH were conducted in a H<sub>2</sub> saturated, aqueous PB buffer at pH 5.5 and are shown in Figure 13a. Activity has previously been shown to be highest at pH 5.5.<sup>193</sup> The sigmoidal shape of the CV traces indicates the electrocatalytic oxidation of H<sub>2</sub> into protons (H<sup>+</sup>) and electrons as a result of direct electron transfer (DET) between the catalytic redox centre of the MBH and the electrode. The interface remains stable in the potential range probed. Similar overpotentials to those reported by Heidary et al. for amino-terminated SAM derived surfaces are observed.<sup>85</sup> In Heidary's study, a peak current of 1.8  $\mu\text{A}/\text{cm}^2$  was obtained,<sup>85</sup> whereas in the present study, peak currents between 1.3 and 5.4  $\mu\text{A}/\text{cm}^2$  were obtained. These differences must result from the difference in surface protonation (e.g. resulting from different  $\text{p}K_{\text{a}}$  values), interface thickness (around 1 nm for a SAM, whereas up to 2.5 nm can be obtained for the polymeric interface<sup>139</sup>), and lastly differences in charge transfer resistance. The lower currents of around 1.3/1.4  $\mu\text{A}/\text{cm}^2$  observed for the thick interfaces obtained with 0 mM or 0.25 molar equivalent of DPPH reflect the higher charge-transfer resistance of these interfaces, despite them having relatively more adsorbed MBH catalyst (as revealed by SEIRA). Typically tunnelling can take place across distances of 2-3 nm.<sup>194,195</sup> An increase in current to 5.6  $\mu\text{A}/\text{cm}^2$  with 0.375 equivalent DPPH is observed, despite a decrease in adsorbed MBH (again, as revealed by SEIRA). This either indicates a decrease in the charge transfer resistance of the interface, or a decrease in the distance between the distal cluster of the electron transfer conduit of the adsorbed MBH and the electrode surface, or a combination of both. The current then decreases to 3  $\mu\text{A}/\text{cm}^2$  with 0.5 equivalent DPPH, despite the fall in the charge transfer resistance of the interface, which corresponds to a decrease in MBH adsorption (again, as revealed by SEIRA). The change in current and MBH adsorption with DPPH concentration is plotted in Figure 13c. The results shown here suggest that there is a trade-off between coverage of the electrode surface (and thus the adsorption of MBH) and the charge-transfer resistance off the interface (and thus the electrochemical accessibility of the adsorbed species).

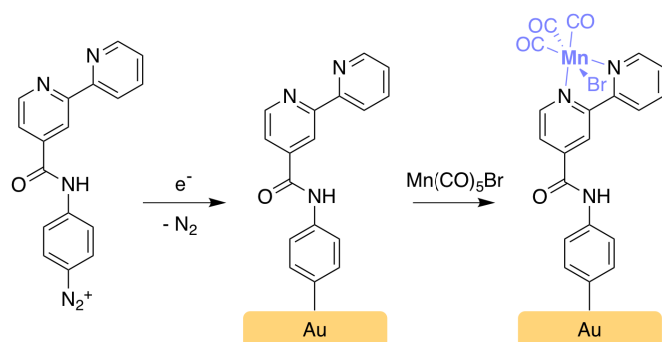
Addition of the redox mediator methylene blue results in an increase in current as a result of mediated electron transfer (MET), as shown for the interfaces deposited with 0 and 0.375 equivalents of DPPH in Figure 13b. The proportional increase observed is much greater than that observed on by Heidary on the amino-terminated SAM-on gold, and might be attributed to the polymeric nature of the interface, which results in a substantial number of enzyme molecules immobilised in greater distance from the electrode surface.<sup>85</sup>

#### 4.7 Immobilisation of molecular catalysts on gold using electrografting of diazonium salts

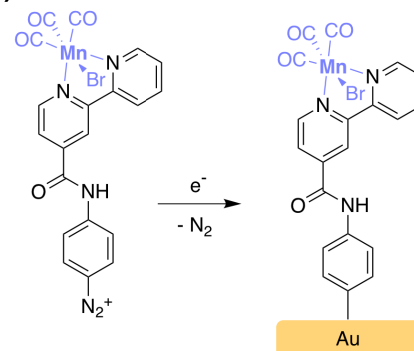
A freshly prepared, bare nanostructured gold SEIRA electrode coated on a Si-prism was incubated with bpy-diazo in acetonitrile within the spectroelectrochemical cell, and, upon incubation, SEIRA spectroscopy was used to observe the adsorption of the 4-bpy species onto

the electrodes surface (Figure 14b, pink trace). This is indicated by the appearance of characteristic absorption bands corresponding to the 4-([2,2'-Bipyridine]-4-carboxamido)benzene moiety, as summarised in Table 1. The band assignment was made with aid of DFT calculations (for more details, see Appendix 4). As can be seen in Figure 14a, electrochemical reduction resulted in the passivation of the electrode. This is indicated by a sharp decrease in reductive current upon subsequent cycling and by the growth of the related 4-([2,2'-Bipyridine]-4-carboxamido)benzene band intensities displayed in Figure 14b. The growth in SEIRA spectroscopic band intensities decreases with each consecutive CV due to passivation of the electrode. The electrode was subsequently rinsed in acetonitrile and non-covalently bound species were removed by cycling the gold electrode several times to mild anodic potentials in fresh TBAF, resulting in the spectrum shown in Figure 14c.

**(a) 'Post-coordination'**



**(b) 'Pre-coordination'**



**Scheme 47**

The formation of manganese carbonyl bipyridyl interfaces *via* the electrochemical grafting of bpy-diazo *via* a 'pre-coordination' or 'post-coordination' method.

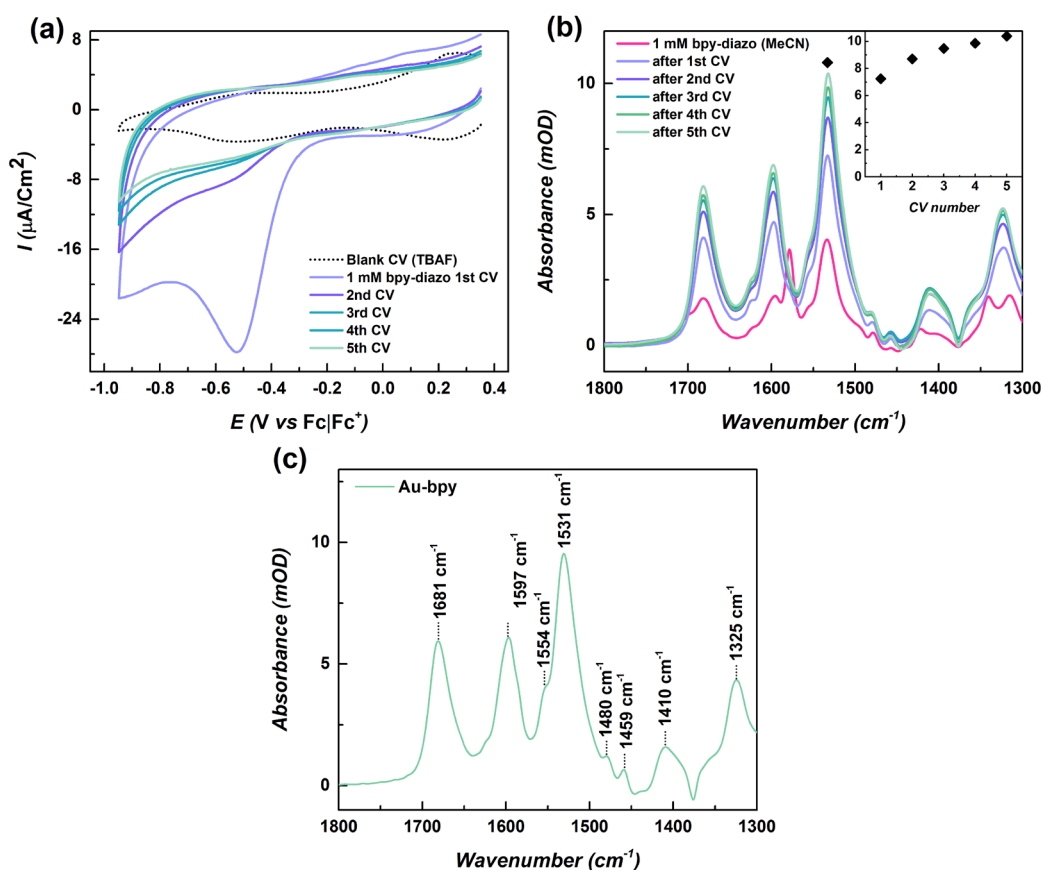


**Figure 14**

(a) CVs showing the electrochemical reduction of a 1 mM solution of bpy-diazo in acetonitrile (0.1 M TBAF) using the gold SEIRA electrode as a working electrode. Scan rate = 50 mV/s. (b) The corresponding SEIRA spectra of the surface species on gold in a 1mM bpy-diazo solution in acetonitrile before electrochemical grafting (pink trace), and after each consecutive CV/reduction (lilac to teal traces). The inset plots the absorbance of the  $\delta(\text{N-H})+\nu(\text{C=C})_{\text{ar}}$  band at  $1531\text{ cm}^{-1}$  after each CV. (c) SEIRA spectrum of the electrode after modification and rinsing in acetonitrile.

**Table 4**

Major band assignments made with the assistance of DFT calculations for interfaces deposited by electrochemical grafting of 1 mM bpy-diazo on gold electrodes.

<b>Sample</b>	<b>Band position (<math>\text{cm}^{-1}</math>)</b>	<b>Band assignment</b>	<b>Dominant vibrational modes</b>
<b>bpy-diazo</b>	1325	$\nu(\text{C=C})_{\text{ar}}$	C-H bending coupled with a C=C aromatic stretching
	1410	$\delta(\text{C-H})$	C-H bending vibration of the amide
	1459	$\delta(\text{C-H})_{\text{bpy}}$	C-H bending vibration of the first bipyridine ring
	1480	$\delta(\text{C-H})_{\text{bpy}}$	C-H bending vibration of the second bipyridine ring
	1531	$\delta(\text{N-H})+\nu(\text{C=C})_{\text{ar}}$	N-H bending vibration of the amide coupled with the C=C aromatic stretching of the phenyl ring
	1554	$\nu(\text{C=C})_{\text{bpy}}+\nu(\text{C=N})_{\text{bpy}}$	C=C and C=N stretching of the first bipyridine ring
	1597	$\nu(\text{C=C})_{\text{ar}}+\delta(\text{N-H})$	C=C aromatic stretching of the phenyl ring coupled with the N-H bending vibration of the amide
	1681	$\nu(\text{C=O})_{\text{bpy}}+\delta(\text{N-H})$	C=O stretching of the carbonyl coupled with the N-H bending vibration of the amide

To determine the electrochemical window in which the electrografted bpy-interfaces on gold is stable, modified electrodes were cycled to cathodic and anodic potentials, as shown in Figure 15a, and SEIRA spectra were recorded after each cycle. Difference spectra were calculated (with respect to the initially deposited interface, Figure 15b) and exhibited little change for electrodes cycled to 0.76 V (vs  $\text{Fc}/\text{Fc}^+$ ), above which gold oxidation occurs, while band intensities for the 4-([2,2'-Bipyridine]-4-carboxamido)benzene moiety begin to decrease (as indicated by the negative bands in the difference spectra) when the electrode was cycled to potentials of -2.14 V (vs  $\text{Fc}/\text{Fc}^+$ ) and lower. The thereby determined electrochemical stability potential window corresponds well to the potential window of -2.2 to +0.8 V (vs  $\text{Fc}/\text{Fc}^+$ ) as determined for interfaces electrografted on gold from 4-BABD in section 7.2.

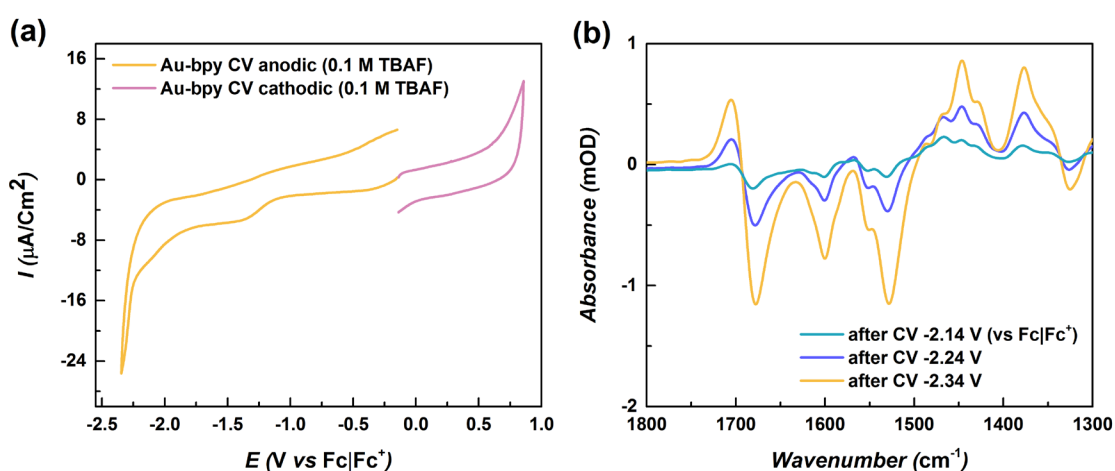


**Figure 15**

(a) CVs acetonitrile (0.1 M TBAF) under Ar bubbling showing the electrochemical stability window of interfaces electrografted from bpy-diazo on gold. Scan rate = 50 mV/s. (b) SEIRA difference spectra of the interfaces on gold calculated (with respect to the initially deposited interface) after consecutive CVs to increasingly cathodic potentials showing the removal of bpy species from the surface of the electrode.

As previously mentioned, manganese carbonyl bipyridyl complexes are excellent catalysts for the selective electrochemical reduction of  $\text{CO}_2$  to CO under mild conditions.<sup>165–171</sup> A gold SEIRA electrode was electrochemically grafted with bpy-diazo by applying 2 CVs and then incubated with a 1 mM  $\text{Mn}(\text{CO})_5\text{Br}$  solution in acetonitrile for 2 hours inside the spectroelectrochemical cell and subsequently rinsed repeatedly with further acetonitrile (hereby named the ‘post-coordination’ method, Scheme 47a). Two prominent bands appear at 2043 and 1953  $\text{cm}^{-1}$ , with a shoulder band at around 1927  $\text{cm}^{-1}$ , in the SEIRA spectrum of the electrode after incubation, which are in the spectral region expected for carbonyl  $\nu(\text{C}\equiv\text{O})$  stretching vibrations. Furthermore, changes are visible in the lower wavenumber region containing bands belonging to vibrational modes of the 4-([2,2'-Bipyridine]-4-carboxamido)benzene moiety, thereby suggesting that a coordination of Mn species to bipyridine groups on the surface of the electrode has occurred. Literature values for the  $\nu(\text{C}\equiv\text{O})$  bands in  $\text{Mn}(\text{CO})_5\text{Br}$  are given at 2138, 2052 and 2007  $\text{cm}^{-1}$ <sup>196</sup> and are not observed here. Literature values for the  $\nu(\text{C}\equiv\text{O})$  bands of *fac*-[ $\text{MnBr}(\text{2,2}'\text{-bipyridine})(\text{CO})_3$ ] in acetonitrile with 0.1 M TBAF are at 2028, 1933 and 1923  $\text{cm}^{-1}$ ,<sup>165</sup> while values of 2030, 1946 and 1930  $\text{cm}^{-1}$  were obtained for *fac*-[ $\text{MnBr}(4,4'\text{-bis}(\text{phosphonic acid})\text{-2,2}'\text{-$

bipyridine)(CO)<sub>3</sub> immobilised on mesoporous TiO<sub>2</sub>.<sup>173</sup> The higher wavenumbers reported here may be explained by the electron-withdrawing nature of the bipyridine amide-substituent, which reduces the electron density at the Mn metal centre and thus reduces backbonding of Mn d-orbital electrons into the antibonding  $\pi^*$  orbitals of the CO ligands, leading to stronger C≡O bond and higher energy stretching bands. This would also explain the higher wavenumbers compared to *fac*-[MnBr(2,2'-bipyridine)(CO)<sub>3</sub>] for *fac*-[MnBr(4,4'-bis(phosphonic acid)-2,2'-bipyridine)(CO)<sub>3</sub>], which also contains electron-withdrawing phosphonic acid substituents.

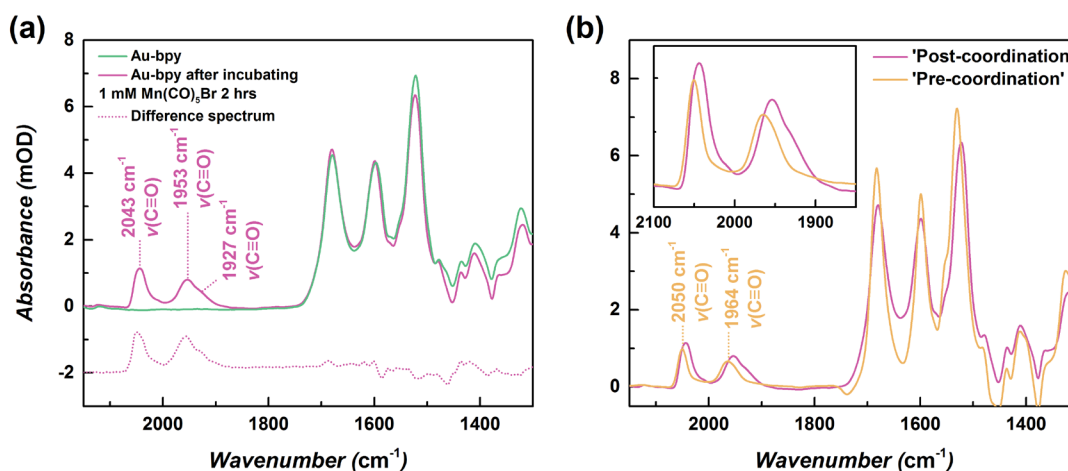


**Figure 16**

SEIRA spectra (a) of the electrografted bipyridine interface on gold in acetonitrile (0.1 M TBAF) before (teal trace) and after incubation (pink tail) with a 1 mM solution of Mn(CO)<sub>5</sub>Br in acetonitrile for 2 hrs ('post-coordination' method), including a difference spectrum (dotted pink trace), and (c) of the Mn-bipyridine interfaces electrografted on gold *via* both the 'post-coordination' and 'pre-coordination' methods.

Mn-bpy interfaces were also electrografted on gold SEIRA electrodes directly from pre-mixed 1 mM bpy-diazo and 1 mM Mn(CO)<sub>5</sub>Br solutions (hereby named the 'pre-coordination' method, Scheme 47b). A gold electrode was electrochemically grafted with the Mn(CO)<sub>5</sub>Br bpy-diazo solution by applying 2 CVs and rinsed repeatedly in acetonitrile. Carbonyl  $\nu(\text{C}\equiv\text{O})$  bands appear in the SEIRA spectrum of the electrode after surface modification, albeit at slightly shifted wavenumbers to those obtained using the 'post-coordination' method, in addition to bands corresponding to the 4-([2,2'-Bipyridine]-4-carboxamido)benzene moiety, indicating that the 'pre-coordination' was successful.  $\nu(\text{C}\equiv\text{O})$  bands appear at 2050 and 1964 cm<sup>-1</sup>, with a less prominent shoulder band compared to that observed for the 'post-coordination' method. Overall the intensity ratio between the bands corresponding to the 4-([2,2'-Bipyridine]-4-carboxamido)benzene moiety and the  $\nu(\text{C}\equiv\text{O})$  bands is less, which suggests that 'pre-coordination results in less coordinated Mn species.

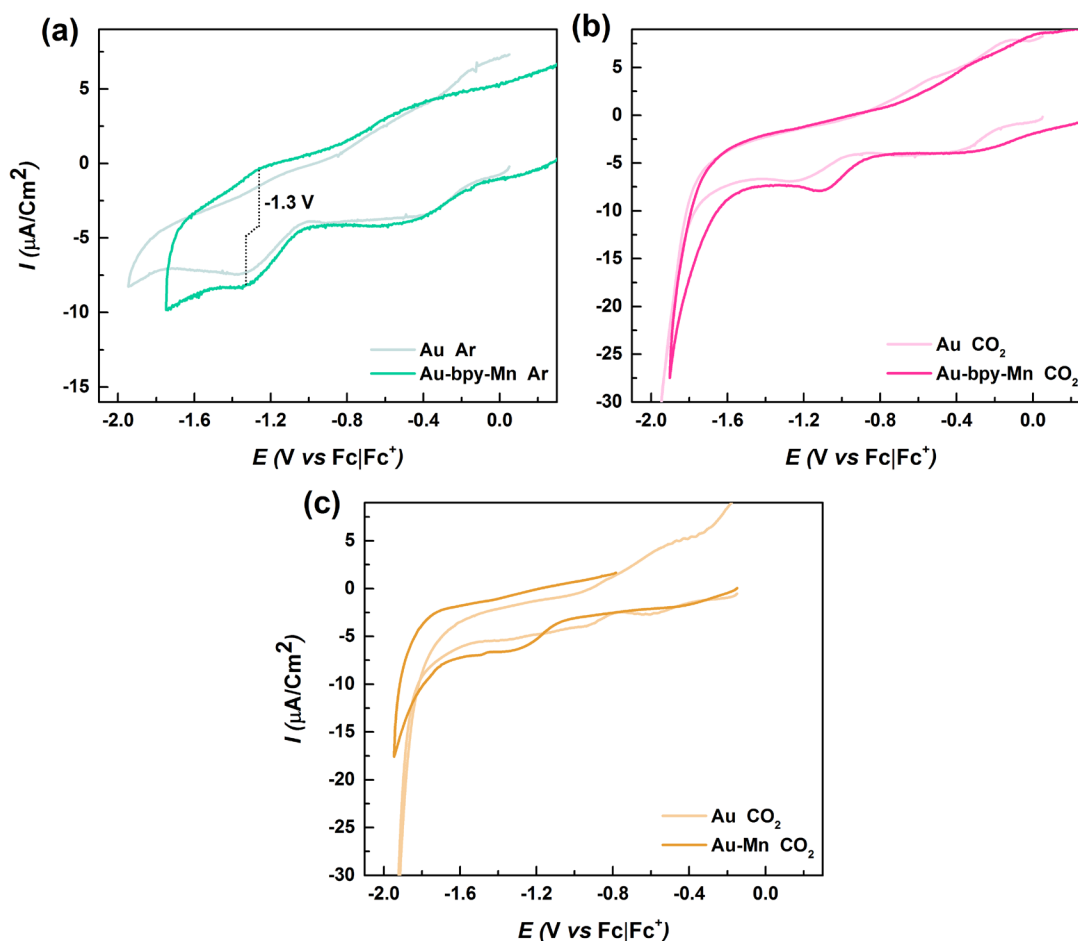
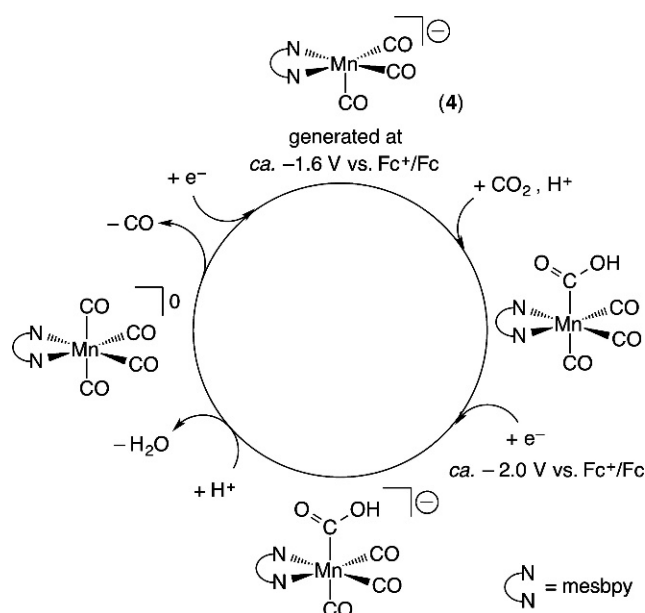


**Figure 17**

CVs in acetonitrile (0.1 M TBAF) of (a) unmodified gold, and gold electrografted with a Mn-bipyridine interface using the ‘pre-coordination’ method, under Ar bubbling, (b) unmodified gold, and gold electrografted with a Mn-bipyridine interface using the ‘pre-coordination’ method, under CO<sub>2</sub> bubbling, and CVs of (c) unmodified gold and gold electrografted with only a bipyridine interface, under CO<sub>2</sub> bubbling. Scan rate = 50 mV/s.

CVs in acetonitrile (0.1 M TBAF) under Ar bubbling of a Mn-bipyridine interface electrografted on gold *via* the ‘pre-coordination’ method (Figure 17a, teal trace) show a reversible peak at around -1.3 V (vs Fc/Fc<sup>+</sup>). It is difficult to determine if this peak is related to the reduction of Mn<sup>I</sup> to Mn<sup>0</sup> species, as a CV of the electrode before electrografting also reveals an irreversible feature around the same potential (Figure 17a, light teal trace). However, the reversible peak does become irreversible in CO<sub>2</sub>, as reported for Mn carbonyl bipyridyl species (Figure 17b), and is absent in CVs of a gold electrode electrografted with only a bipyridine interface (Figure 17c). It should be noted that it was not possible to obtain gold SEIRA electrodes that are completely featureless in CVs in acetonitrile, regardless of how many cleaning cycles were applied after electroless deposition on the gold. In either case, there was a small shift in onset potential under CO<sub>2</sub> bubbling for the Mn-bipyridine species, compared to the unmodified gold, which becomes active for CO<sub>2</sub> reduction around -1.8 V (vs Fc/Fc<sup>+</sup>). This shift may also be a result of the solvent adsorbing water from the atmosphere during the course of the experiment. Passivation of the gold surface does suppress reduction of CO<sub>2</sub> at the gold surface to a large extent, as can be

seen in the CVs of gold under CO<sub>2</sub> bubbling before and after electrografting with a bipyridine interface i.e. without Mn (Figure 17c).



#### Scheme 48

Proposed catalytic mechanism for the reduction for CO<sub>2</sub> using a Mn carbonyl bipyridyl catalyst with a bulky bipyridyl ligand (in this case mesbpy (6,6'-dimesityl-2,2'-bipyridine)), which eliminates dimerisation at the Mn centre. Reprinted with permission from <sup>169</sup>, copyright 2014 American Chemical Society.

It has been shown that upon initial one-electron reduction at around -1.6 V (vs Fc/Fc<sup>+</sup>), manganese carbonyl bipyridyl species form dimeric species, which can be further reduced to form doubly-reduced monomeric species.<sup>165</sup> Reisner and co-workers suggest that the low overpotential obtained for electrocatalytic CO<sub>2</sub> reduction using *fac*-[MnBr(4,4'-bis(phosphonic acid)-2,2'-bipyridine)(CO)<sub>3</sub>] immobilised on TiO<sub>2</sub> is due to the temporary desorption of the phosphonic-acid bound species from the surface, which allows the formation of dimeric species that, in the presence of water, react directly with CO<sub>2</sub> to form CO.<sup>173</sup> In the case presented here, it is not expected that the Mn-bpy bound to the gold will show any lability due to the strength of the rigid Au-C bond at the interface (the electrografted diazonium interfaces on gold do not show the same flexibility as, say, thiol SAMs do). As such, further reduction of the monomeric manganese carbonyl bipyridyl species to the catalytically active, doubly-reduced monomeric species would need to take place at lower potentials, which would in turn result in a larger overpotential. A study by Kubiak and co-workers for a manganese carbonyl bipyridyl species in solution with bulky substituents on the bipyridine that eliminate dimerisation at the Mn centre shows that the doubly-reduced Mn species forms at around -2 V (vs Fc/Fc<sup>+</sup>)<sup>169</sup>, which is close to the stability limit of the interface. Furthermore, the formation of thick, branched, polymeric interfaces may have resulted in most of the Mn centres being redox inactive, which would explain the absence of defined redox peaks for the Mn<sup>0/+1</sup> transition. For these reasons, further spectroelectrochemical measurements were not carried out.

## 4.8 Conclusions

*In situ* SEIRA spectroscopy was used to provide an insight into the formation and structure of interfaces electrografted on gold electrodes *via* electrochemical reduction of diazonium salts, while *in situ* spectroelectrochemical investigations allowed the determination of the electrochemical stability window of such interfaces, which was determined to be 3.0 V wide in acetonitrile. This is the first time that spectroscopic methods have been used in this way to determine the electrochemical stability window of electrografted diazonium interfaces and this results in larger sets of information than can be obtained using conventional electrochemical methods (e.g. regarding structure). The superior stability of the electrografted diazonium interfaces over thiol-derived SAMs demonstrated herein emphasises their potential for use in electrochemical devices.

A radical scavenger was deployed during electrochemical grafting of the 4-nitrobenzene diazonium salt, resulting in the moderation of interfacial growth and a concomitant decrease in the charge transfer resistance of the interface. After subsequent conversion into biocompatible amino-functionalised interfaces, this led to an increase in the direct electron transfer between the electrode and an immobilised oxygen-tolerant hydrogenase that could be correlated to the concentration of scavenger added during interface deposition and the structural/functional properties of the interface, highlighting the potential for *in situ* spectroelectrochemical methods to be used in the design and optimisation of interfaces for electrochemical devices.

In addition to using electrografted diazonium interfaces for immobilising enzymes on the surface of gold electrodes, a manganese carbonyl bipyridyl was also immobilised as a model molecular catalyst for the electrochemical CO<sub>2</sub> reduction reaction. Here it could be demonstrated, using *in situ* SEIRA spectroelectrochemical methods, that it is possible to use a bipyridine-containing diazonium salt to immobilise and subsequently characterise a manganese carbonyl bipyridyl interface on the surface of gold, either *via* a one-step 'pre-coordination' method, or a two-step 'post-coordination' method. However, due to the limited electrochemical stability window in the region of interest for the catalytic reduction of CO<sub>2</sub> it was not possible to study this system further under turnover conditions.

Despite not being able to use the electrografted diazonium interfaces to study the manganese carbonyl bipyridine system under turnover conditions, the broad potential stability window of these interfaces permits many other catalytic systems or reactions to be studied using electrochemical or spectroelectrochemical methods under highly anodic and cathodic potentials that are not possible using thiol SAMs. This includes the study of enzymes, such as the study of hydrogenases under hydrogen evolution conditions.

# Chapter 5

## Electrochemical grafting of diazonium salts on transparent conductive oxide (TCO) electrodes for the immobilisation of enzymes

### 5.1 Introduction

Electrocatalytic devices based on enzymes, such as enzymatic fuel cells (EFCs) or biosensors, use enzymes to catalyse the oxidation or reduction reactions taking place and do this without noble metals that are otherwise often used as catalysts e.g. in proton exchange membrane fuel cells (PEMFCs). The concept of a hydrogenase-based EFC was already introduced in section 1.5 (page 42). Such devices are attractive not only due to potential cost savings that can be achieved e.g. through avoiding the use of noble metals, but also because they can be used in implantable or portable electronic devices (i.e. in physiological conditions), and, in the case of biosensors, they may show particularly high selectivity towards specific analytes due to specific binding affinities of enzymes to specific substrates.<sup>197,198</sup> Glucose-powered EFCs that run off glucose and oxygen in the extra-cellular body fluid have been proposed as alternative power sources to batteries for medical implants. A prominent example is that of a glucose-oxidase/laccase-based EFC that successfully operated implanted in a rat with a power output of 38.7  $\mu\text{W}$ .<sup>199</sup> In order to make such devices scalable and cost-efficient to produce, low cost electrode materials must be used. A number of high surface area nanomaterials (HSMs), such as carbon materials like carbon nanotubes (CNTs), have been used and developed as bioelectrodes in recent years, in particular due to the numerous advantages that they offer in terms of protection against enzyme denaturation, enhanced loadings and increased current outputs due to enhanced surface areas, as well as improved electrical contact between the enzymes and the electrode material.<sup>200</sup> In this context, TCO materials, such as ITO or ATO, are highly suited for use as bioelectrode materials due to the ease with which nanostructured TCOs can be fabricated, their broad potential range (especially under highly anodic potentials), and their biocompatibility and ease with which enzymes adsorb on native oxide surfaces. The inherent transparency of these materials also allows their use in photoelectrochemical devices and in spectroelectrochemical investigations e.g. of enzyme behaviour.<sup>201–209</sup> The use of low cost TCOs, such as ATO or FTO, offer potentially large cost-savings compared to conventional electrode materials like Au, and could be used in low-cost, disposable devices.

While certain enzymes may adsorb on native oxide surfaces, the lack of control over the orientation of the enzyme can lead to poor electronic coupling between the enzyme and the electrode, as recently demonstrated for certain heme proteins on mesoporous ITO by Reisner and co-workers.<sup>208</sup> Orientation control for enzymes immobilised on mesoporous ITO electrodes was demonstrated by Schuhmann, Shleev and co-workers by using silanes to functionalise the ITO surface with amine or epoxide functional groups prior to immobilisation of a cellobiose dehydrogenase and a bilirubin oxidase.<sup>209</sup> These functionalities further allowed the covalent attachment of the enzymes to the electrode. Fattakhova-Rohlfing and co-workers also covalently attached cytochrome c to mesoporous ATO, which had been functionalised with amine functional groups using a silanisation procedure, and demonstrated greater stability to leaching compared to cytochrome c immobilised on the native, bare ATO surface.<sup>206</sup>

Despite the widespread use of diazonium salts to modify carbon materials, only few examples exist where metal oxide materials have been modified, including titanium dioxide, ITO and fluorine-doped tin oxide (FTO).<sup>55,57,210–214</sup> Conventional approaches to functionalising oxides, such as using phosphonate, carboxylates and silanes, have their drawbacks, including varying stabilities as mentioned in section 5.3.4 (page 20), or poor electronic coupling, as will be discussed further in section 9.6 (page 161). Using the specific example of the silanes used to functionalise the ITO and ATO in the work of Schuhmann, Shleev and co-workers, as well as Fattakhova-Rohlfing and co-workers, drawbacks include a propensity to polymerise, as well as a weak electronic coupling between the conductive oxide and the immobilised redox species.

In an attempt to develop a new approach to immobilising enzymes on TCOs electrodes, planar ITO electrodes were electrochemically modified using a similar approach to that previously developed for gold electrodes (section 7.4, page 71). In that work, a radical scavenger was added in an attempt to inhibit the polymerisation mechanism whereby multilayers are formed, and thereby promote monolayer formation. The ITO electrodes are similarly electrochemically grafted with 4-NBD to introduce nitrophenyl moieties that are electrochemically reduced to aminophenyl moieties in order to allow the immobilisation of the MBH enzyme under orientation control and to allow protein film voltammetry (PFV) to be carried out. A greater understanding of how such electrografted diazonium interfaces function on simple, planar surfaces will allow their eventual use on more complex TCO HSMs for use in functional devices.

## **5.2 Effect of radical scavenger on interface formation and immobilisation of hydrogenase**

pl-ITO electrodes were electrochemically grafted with 1mM 4-NBD using cyclic voltammetry with the addition of 0, 1 or 2 molar equivalents of the radical scavenger DPPH. As can be seen in Figure 18, addition of DPPH changes the reduction peak shape and position compared to the trace obtained with only 4-NBD. With 2 molar equivalents of DPPH added (lilac trace), the reversible 1 electron reduction and re-oxidation of the DPPH itself can be observed overlapping

with the irreversible reduction wave of the 4-NBD. As a reference, a CV showing the redox behaviour of 1 mM DPPH with no 4-NBD is also shown in Figure 18 (black trace, short dots). Passivation of the pl-ITO electrodes upon repeated cycling can be seen Figure 19.

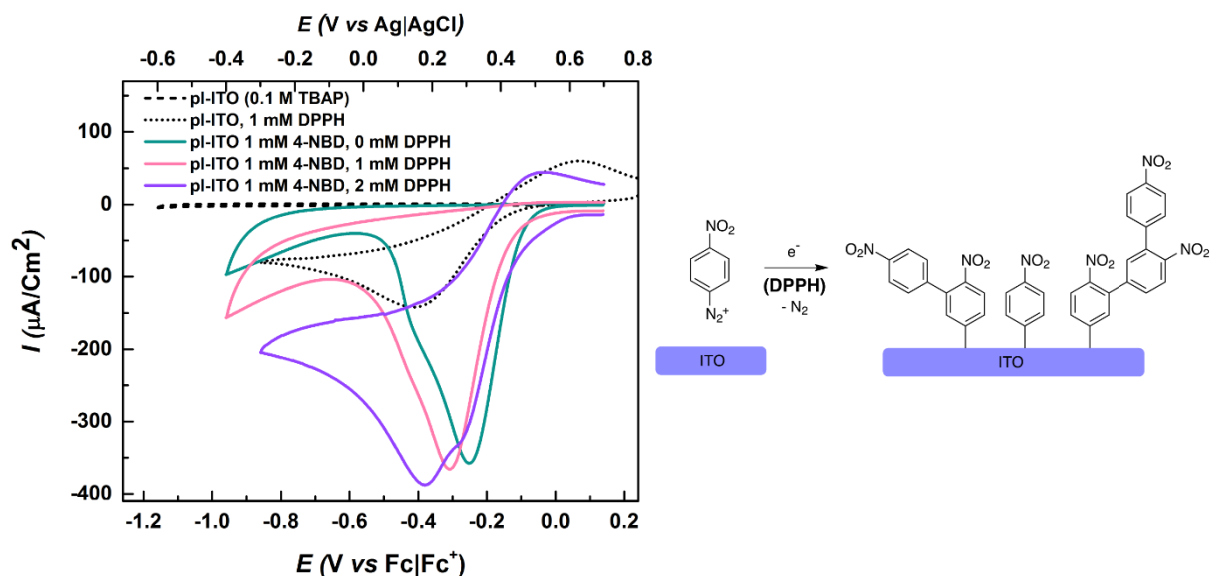


**Figure 18**

CVs of a 1 mM solution of 4-NBD in acetonitrile (0.1 M TBAP) with increasing molar equivalents of DPPH added (coloured traces), and a CV of only 1 mM DPPH (black trace, short dots) using pl-ITO as a working electrode. Scan rate = 50 mV/s.

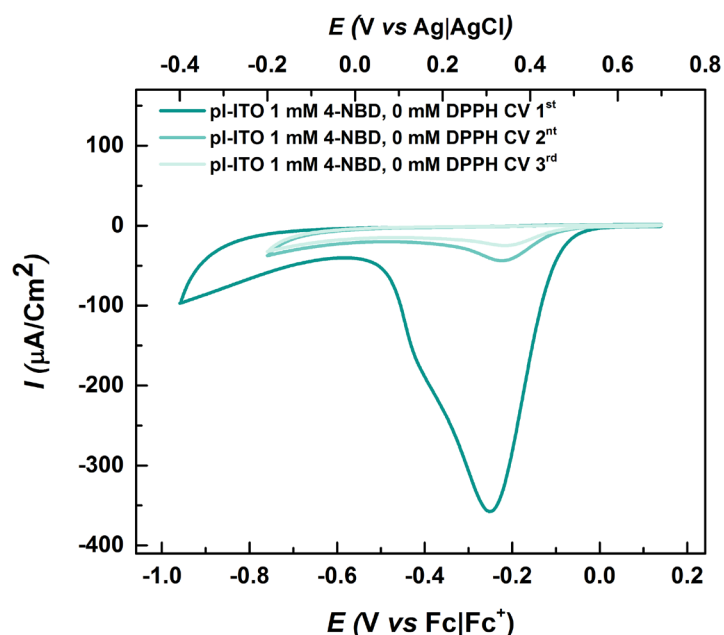


**Figure 19**

CVs of 1 mM solutions of 4-NBD in acetonitrile (0.1 M TBAP) using pl-ITO as a working electrode. Scan rate = 50 mV/s.

Passivation of the electrodes grafted with 4-NBD (and DPPH) is further confirmed by comparative CV measurements of the unmodified and modified pl-ITO electrodes (modified with 0 or 1 molar equivalent DPPH) in the presence of the ferrocene/ferrocenium ( $\text{Fe}/\text{Fc}^+$ ) redox probe (Figure 20a). In addition to an increase in peak separation  $\Delta E_p$ , a significant decrease of 59% in the ferrocene oxidation current is observed for pl-ITO electrografted with no added DPPH, while a

smaller decrease of 35% is observed for pl-ITO modified with 1 molar equivalent of DPPH added. First of all, this result confirms that electrochemical grafting of 4-NBD results in the passivation of the ITO surface, and second of all it indicates that the addition of the radical scavenger DPPH leads to the deposition of a thinner or less dense interface.

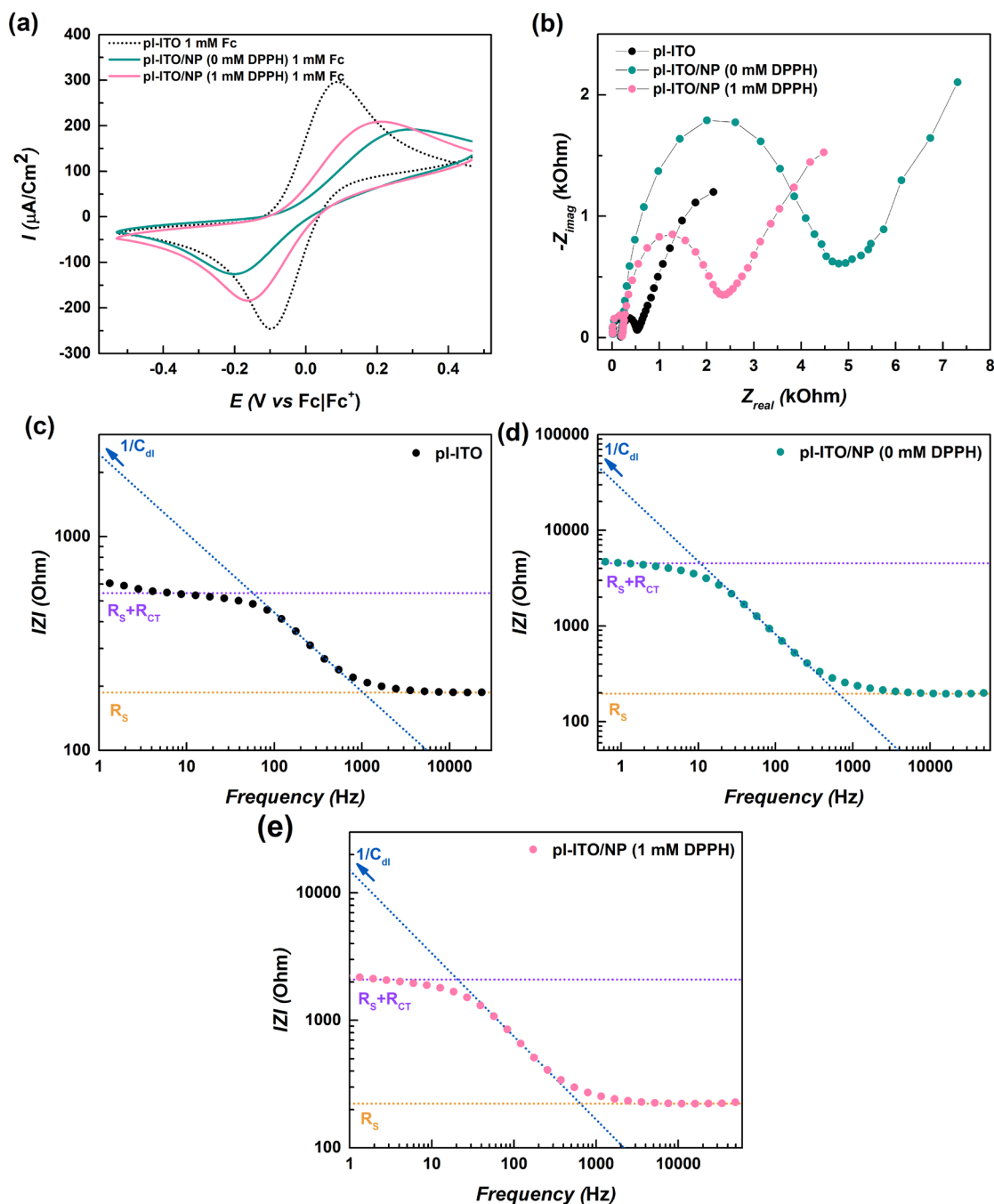
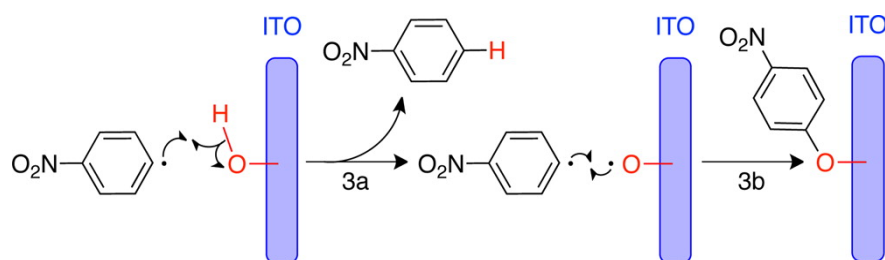


**Figure 20**

CVs of 1 mM ferrocene in acetonitrile (0.1 M TBAP) using unmodified pl-ITO (black dotted trace), or pl-ITO electrografted with (pink trace) or without (dark green trace) the addition of 1 molar equivalent DPPH, as a working electrode (pl-ITO/NP = nitrophenyl). Scan rate = 50 mV/s. (b) Nyquist plots comparing the electrochemical impedance of the unmodified and modified electrodes in 1 mM ferrocene and the corresponding Bode plots (c-e) used to calculate the solution resistance  $R_s$ , the charge transfer resistance  $R_{CT}$  as well as the double layer capacitance  $C_{dl}$ .

Stevenson and co-workers demonstrated that planar ITO electrodes could be modified *via* the electrochemical grafting of the 4-NBD aryl diazonium salt in acetonitrile, with films of thicknesses in the order of 1-6 nm deposited on the surface. It was suggested that these films were strongly physisorbed to the ITO surface, since X-ray photoelectron spectroscopy (XPS) did not reveal any significant changes in the In 3d or Sn 3d spectra, or any apparent evidence of In-O-C or Sn-O-C bonds in the O 1s spectra. More recently, Stevenson and co-workers used iodonium tetrafluoroborate salts to electrochemically modify ITO.<sup>215</sup> Iodonium salts form aryl radical species upon electrochemical reduction that are analogous to those formed by the electrochemical reduction of diazonium salts and, once formed, the adsorption or interaction of these radical species with surfaces or other species in solution or at the interface can be considered the same. XPS indicate that Sn-C or In-C bonds are not formed, while there are suggestions that In-O-C or Sn-O-C species may form. The differentiation of these latter species is hindered due to strong overlapping contributions from the nitro groups in the O 1s spectra.<sup>215</sup> Notwithstanding, a mechanism was proposed by Stevenson and co-workers for the abstraction of hydrogen from the ITO surface and the subsequent formation of covalent bonds between the ITO and the aryl species, as shown in Scheme 49.



**Scheme 49**

Proposed hydrogen abstraction mechanism proposed by Stevenson and co-workers showing how aryl radicals abstract hydrogen from surface hydroxyl groups, leaving radical oxygen species, which may couple with further aryl radicals to form covalent M-O-C bonds. Reprinted with permission from <sup>215</sup>, copyright 2015 American Chemical Society.

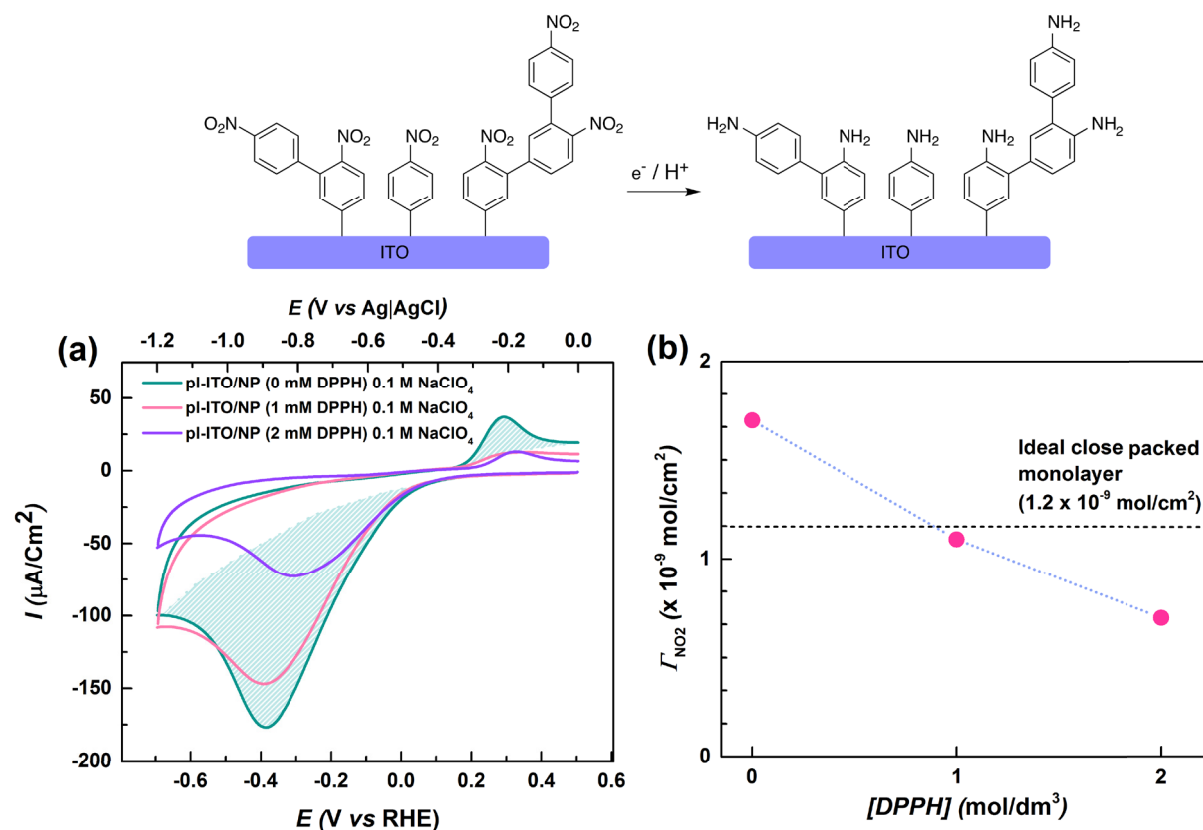
Electrochemical impedance spectroscopy (EIS) was used to measure the electron transfer properties of the electrografted interfaces using a similar approach to that used by Stevenson and co-workers for ITO modified with an iodonium salt.<sup>215</sup> The impedance response of the unmodified and modified pi-ITO electrodes (modified with 0 or 1 molar equivalent DPPH) is shown in the Nyquist plot in Figure 20b. The plots are characterised by a semi-circular trace in the complex impedance plane at high frequencies, corresponding to the sum of the double layer capacitance  $C_{dl}$  and the charge transfer resistance of the electrode  $R_{CT}$ , and a Warburg line at low frequencies due to impedance caused by diffusion of ions. These features indicate that a Randle equivalent circuit may be used to model the properties of these systems.<sup>216</sup> The impedance data are represented in Bode plots in Figure 20c – d, showing how  $C_{dl}$ ,  $R_{CT}$  and the solution resistance  $R_S$  for each electrode was calculated. These values are summarised in Table 5.

**Table 5**

The values of  $R_S$ ,  $R_{CT}$  and  $C_{dl}$  calculated from the impedance data for unmodified and modified pI-ITO electrodes.

Sample	$R_S$ ( $\Omega$ )	$R_{CT}$ ( $\Omega$ )	$C_{dl}$ ( $\mu F/cm^2$ )
pI-ITO/NP (0 mM DPPH)	196	4337	2.69
pI-ITO/NP (1 mM DPPH)	229	1871	8.20
pI-ITO	186	359	185.00

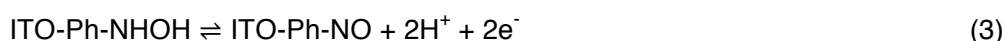
Electrochemical grafting of ITO with 4-NBD without any addition of DPPH results in an order-of-magnitude increase in  $R_{CT}$ , as well as a very large decrease in  $C_{dl}$ , which suggests the deposited interface interrupts the adsorption of electrolyte ions onto the native oxide surface. Addition of 1 molar equivalent of DPPH during electrochemical grafting significantly reduces  $R_{CT}$  in agreement with the deposition of a thinner or less dense interface. Similar reductions in  $R_{CT}$  were observed by Breton and co-workers when electrochemically grafted GC electrodes with 4-NBD in the presence of molar equivalents of DPPH.<sup>157</sup>

**Figure 21**

Electrochemical reduction of the nitrophenyl (NP) moieties to aminophenyl moieties in a 0.1 M NaClO<sub>4</sub>, 1:9 ethanol:water solution, and (b) the corresponding surface coverage of electroresponsive nitrophenyl moieties  $\Gamma_{NO_2}$  derived using the integrated charge of the nitrophenyl reduction peaks (as shown for 0 mM DPPH in (a)). Scan rate = 50 mV/s.

As shown already for gold in section 7.6 (page number 77), the electrografted nitrophenyl moieties can be reduced chemically or electrochemically in protic conditions *via* an irreversible multi-electron reduction to aminophenyl (-NH<sub>2</sub>) and hydroxyaminophenyl (-NHOH) moieties, as has been widely reported<sup>147,185,186,217</sup>, and this results in amino functionalised interfaces that allow

the electrostatically-controlled adsorption of the MBH. Figure 21a shows the electrochemical reduction of these nitrophenyl moieties using cyclic voltammetry, where the first reduction wave corresponds to mixed four and six electron reductions of nitrophenyl moieties to hydroxyaminophenyl and aminophenyl moieties, respectively. Equations (1) and (2) show both reduction processes involved. Instead of undergoing further reduction to aminophenyl moieties, hydroxyaminophenyl moieties may undergo a two-electron oxidation to nitrosophenyl moieties with a certain reversibility, as shown in equation (3).



Integrating the charge of the first reduction wave and the subsequent smaller oxidation wave gives the charge for a total six-electron redox reaction, which may be used to calculate the surface coverage  $\Gamma_{\text{NO}_2}$  of electrochemically accessible nitrophenyl moieties.<sup>217,218</sup> The values of  $\Gamma_{\text{NO}_2}$  calculated using this method are plotted in Figure 21b as a function of molar equivalents of DPPH used during the electrochemical grafting. A significant reduction in coverage can be observed from around  $1.7 \times 10^{-9}$  mol/cm<sup>2</sup> for pi-ITO electrografted without DPPH to  $1.1 \times 10^{-9}$  mol/cm<sup>2</sup> for pi-ITO electrografted with one molar equivalent of DPPH added. For pi-ITO electrografted with two molar equivalents of DPPH added, a coverage of around  $0.7 \times 10^{-9}$  mol/cm<sup>2</sup> is obtained, which corresponds to a near monolayer coverage and is the same value ( $0.65 \times 10^{-9}$  mol/cm<sup>2</sup>) as that obtained by Breton and co-workers on GC with added DPPH. An ideal close packed monolayer of nitrophenyl moieties is expected to give a surface coverage of  $1.2 \times 10^{-9}$  mol/cm<sup>2</sup>; however, given the rapid nature of the adsorption of radical species on surfaces and the strong bonds that they form, an ordered self-assembly of molecules is not expected to take place and therefore a value of less than  $1.2 \times 10^{-9}$  mol/cm<sup>2</sup> will always be achieved for non-branched interfaces. The differences in the reduction peak potentials and shapes are further indications of differences in the interface structures.<sup>219</sup> Further measurements would need to be carried out with greater molar equivalents of DPPH added to observe if a plateau in coverage is reached at higher concentrations. This plateau occurs at around 1-2 molar equivalents of DPPH in the case of GC. It would seem as though the behaviour observed on ITO is similar to that observed on GC, where the rate of phenyl radical adsorption on the electrode surface ( $k_s$ ) is greater than the rate of radical coupling to the radical scavenger ( $k_r$ ), which in turn is greater than the rate of radical coupling to already grafted phenyl moieties ( $k_p$ ) (as illustrated previously in Scheme 42, page 73).

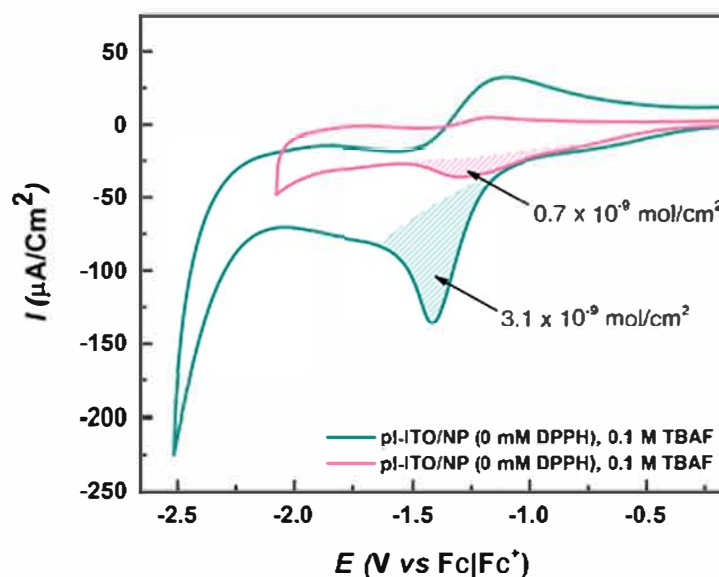
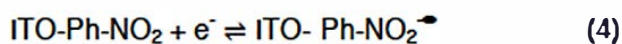


**Figure 22**

CVs in acetonitrile (0.1 M TBAF) under Ar of the nitrophenyl (NP) interfaces on pI-ITO electrodes electrochemically grafted with 1 mM 4-NBD with (pink trace) or without (dark green trace) the addition of DPPH. The surface coverages of electroresponsive nitrophenyl moieties  $\Gamma_{\text{NO}_2}$  indicated here were calculated using equation (4) and the integrated charge of the (semi)-reversible  $\text{NO}_2$  reduction peak. Scan rate = 50 mV/s.

In aprotic solvents, such as acetonitrile, nitrophenyl moieties on electrodes can be reversibly reduced by one electron to the radical anion:



which may also be used to calculate  $\Gamma_{\text{NO}_2}$ .<sup>217</sup> CVs of the unmodified and modified pI-ITO electrodes (electrografted with 0 or 1 molar equivalent DPPH) in acetonitrile are shown in Figure 22. The semi-reversibility observed here may be attributed to residual water in the acetonitrile, which may protonate  $\text{Ph-NO}_2^{\bullet-}$ .<sup>220</sup> The integrated cathodic peaks give coverages of  $3.1 \times 10^{-9}$  mol/cm<sup>2</sup> for pI-ITO electrografted without DPPH and  $0.7 \times 10^{-9}$  mol/cm<sup>2</sup> for pI-ITO modified with one molar equivalent of DPPH added, with peak separations  $\Delta E_p$  of 88 mV and 215 mV, respectively. While the coverage obtained using this method for pI-ITO electrografted with one molar equivalent of DPPH added is the same as that obtained from the reduction of the nitrophenyl moieties in water, the higher coverage of  $3.1 \times 10^{-9}$  mol/cm<sup>2</sup> for pI-ITO modified without DPPH is closer to the  $3.4 \times 10^{-9}$  mol/cm<sup>2</sup> originally reported by Stevenson and co-workers for pI-ITO electrodes electrochemically grafted with 4-NBD, and suggests that the measurements in water underestimate the coverage. Underestimated coverages determined using voltammetry in protic solvents have previously been reported for thick films on carbon electrodes and were attributed to the presence non-electroactive, or non-electrochemically accessible (electronically contacted) moieties.<sup>219,221</sup> Certain parts of the interface may be particularly hydrophobic in thick films and therefore more difficult to irreversibly reduce in protic media. Differences in coverages determined for thick films in protic and aprotic solvents are therefore highly likely, given the differences in the ion or solvent molecules that diffuse in the interface and the subsequent

changes in the intermolecular interactions between the redox species and the dielectric constant of the interface etc. In any case, these results indicate that addition of a radical scavenger during the electrochemical grafting of ITO with 4-NBD results in a decrease in coverage  $\Gamma_{\text{NO}_2}$ , with near monolayer values approached using a higher concentration of DPPH.

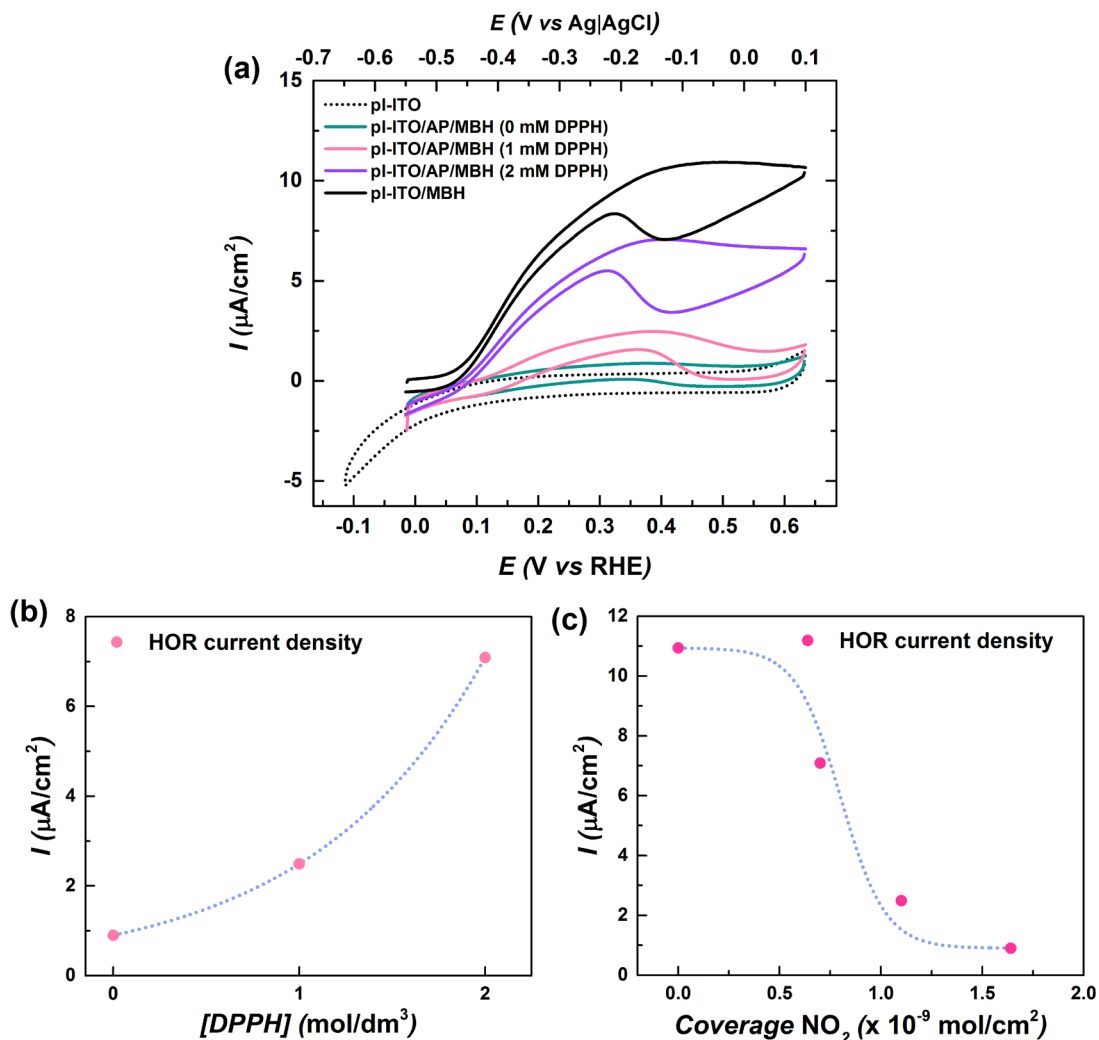


**Figure 23**

(a) Protein film voltammograms recorded in 10 mM PB buffer at pH 5.5 saturated with  $\text{H}_2$  with a scan rate of 10 mV/s of strep-MBH adsorbed onto aminophenyl (AP)-functionalised pi-ITO interfaces, and plots of electrocatalytic HOR current due to direct electron transfer as a function of (b) concentration of DPPH added during interface formation and (c) the coverage  $\Gamma_{\text{NO}_2}$  of the pi-ITO electrodes.

In order to evaluate the suitability of the electrografted interfaces for enzyme immobilisation and bio-electrocatalysis, strep-tagged MBH was electrostatically absorbed onto unmodified pi-ITO and amino functionalised pi-ITO electrodes from a bulk solution at pH 7 in a similar way to that used in section 7.6 on functionalised gold. PFVs of the electrodes incubated with MBH were recorded in a  $\text{H}_2$  saturated, aqueous PB buffer at pH 5.5 and are shown in Figure 23. The sigmoidal shapes of the CV traces indicate the electrocatalytic oxidation of  $\text{H}_2$  into protons ( $\text{H}^+$ ) and electrons as a result of direct electron transfer (DET) between the catalytic redox centre of the strep-MBH and the electrode in a similar way to that observed for strep-MBH on the modified gold electrodes in section 7.6, as well as by Heidary, Utesch et al on SAM-modified gold

electrodes.<sup>85</sup> The behaviour is also similar to that observed by Heidary for strep-MBH on planar tin-rich ITO.<sup>84</sup> There is a slight anodic shift in overpotential for HOR of around 50 mV compared to those obtained on gold. A plot of the peak current as a function of DPPH amount added during electrochemical grafting is shown in Figure 23b, and a plot of peak current as a function of the interface coverage (using the higher coverage calculated using CVs in acetonitrile for the thickest interface electrografted without the addition of DPPH) is shown in Figure 23c. The peak currents increase with increasing concentrations of DPPH added during electrografting, from 0.90  $\mu\text{A}/\text{cm}^2$  for 0 equivalents DPPH, to 2.49  $\mu\text{A}/\text{cm}^2$  for 1 equivalent and finally to 7.09  $\mu\text{A}/\text{cm}^2$  for 2 equivalents DPPH; the highest overall current recorded was 10.94  $\mu\text{A}/\text{cm}^2$  for the unmodified ITO. A peak current of around 2.3  $\mu\text{A}/\text{cm}^2$  was obtained by Heidary for strep-MBH on planar tin-rich ITO.<sup>84</sup>

On gold, the peak current was shown to increase as the interface density decreased, presumably due to the decrease in  $R_{\text{CT}}$ ; however, at the lowest density interface there was a subsequent drop in current due to a decrease in MBH adsorption. Proteins adsorb well onto native oxide surfaces, as has been widely reported<sup>201–209</sup>, therefore it is not surprising that the highest current density is observed on the unmodified ITO, as the MBH will also experience the lowest  $R_{\text{CT}}$  due to the absence of any grafted interface. While further data points should be collected to get a better fit of the data, there appears to be a sigmoidal shape to the plot of peak current as a function of interface coverage, which would be consistent with a simple model where the peak currents tend to zero as the coverage and thickness of the interface becomes high, and tend to a maximum as the coverage tends to zero. In reality, the interface itself will have an effect on the orientation of the MBH and, therefore, will affect the current density to a certain degree.

Addition of the redox mediator methylene blue (MB) results in an increase in current as a result of mediated electron transfer (MET) for all samples, as shown in Figure 24. The currents are compared to the DET currents in Table 6, and the enhancement in current as a result of adding the mediator is indicated for each electrode. The values obtained by Heidary for strep-MBH immobilised on tin-rich ITO and SAM-coated Au are also included for comparison.<sup>84</sup> For the results obtained in this work, there is an overall decrease in the current enhancement as the interface coverage decreases, as would be expected as  $R_{\text{CT}}$  experience by the MBH falls. For thicker interfaces, a large increase in current is anticipated as the mediator allows electrons to be shuttled to and from the non-electrically contacted MBH adsorbed on top of the interface.

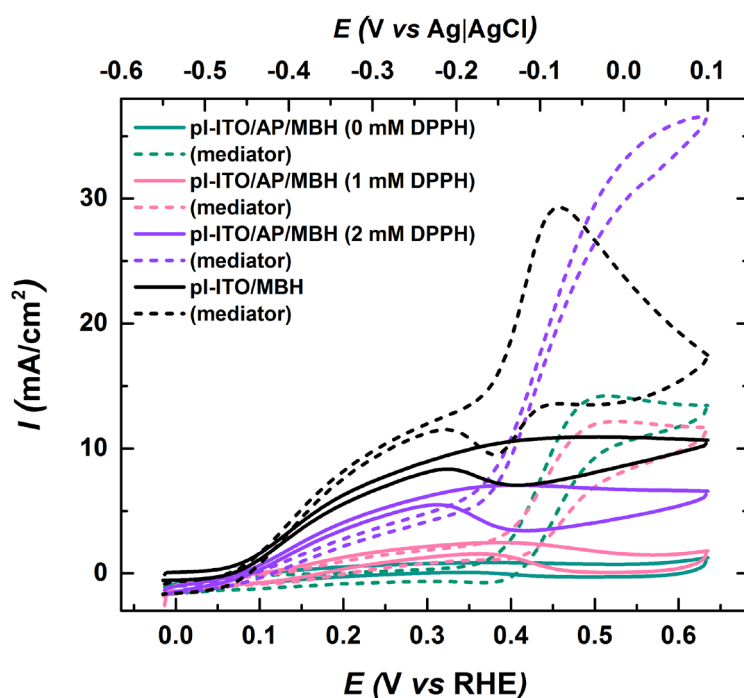


**Figure 24**

Protein film voltammograms recorded in 10 mM PB buffer at pH 5.5 saturated with H<sub>2</sub> with a scan rate of 10 mV/s on MBH adsorbed onto aminophenyl (AP)-functionalised interfaces, and unmodified ITO before (solid traces) and after (dashed traces) addition of the redox mediator methylene blue.

**Table 6**

Electrocatalytic HOR peak current due to direct electron transfer (DET) and mediated electron transfer (MET) and the resulting enhancement in current for strep-MBH immobilised on each sample. Values obtained for by Heidary for strep-MBH immobilised on tin-rich ITO and SAM-coated Au are also included for comparison.

<b>Sample</b>	<b>DET (<math>\mu\text{A}/\text{cm}^2</math>)</b>	<b>MET (<math>\mu\text{A}/\text{cm}^2</math>)</b>	<b>Enhancement</b>
<b>0 mM DPPH</b>	0.90	14.17	x 15.7
<b>1 mM DPPH</b>	2.49	12.28	x 4.9
<b>2 mM DPPH</b>	7.09	36.58	x 5.2
<b>Bare ITO</b>	10.94	29.31	x 2.7
<b>Bare tin-rich ITO</b> <sup>84</sup>	2.3	9.7	x 4.2
<b>NH<sub>2</sub>-SAM coated Au</b> <sup>84</sup>	2	4	x 2
<b>NH<sub>2</sub>/OH-SAM (1:9) coated Au</b> <sup>84</sup>	3.3	9.8	x 3

Care should be exercised when interpreting the enhancement in currents given the changing nature of the electrografted interface on the pi-I-TO and the corresponding change in  $R_{CT}$  experienced by the mediator. For the denser interfaces, electron transfer between the electrode and the mediator may be inhibited and this may in turn influence the kinetics of the HOR (see Figure 20 and Table 5 for the influence of the interface structure on the electron transfer with the Fc/Fc<sup>+</sup> redox couple). This can also be inferred from the appearance of a reversible redox peak for the methylene blue on the unmodified ITO that is absent for the modified electrodes.

The increase in catalytic current observed for the bare ITO suggests that either a significant amount of the MBH molecules are orientated in a non-direct electron transfer configuration i.e. with the distal cluster pointing away from the electrode surface, or that multi-layers of MBH adsorb onto the electrode surface, or a combination of both. The formation of multi-layers would explain why the currents observed for MET are substantially larger than those obtained by Heidary for monolayers (confirmed by atomic force microscopy) of strep-MBH immobilised on planar tin-rich ITO or NH<sub>2</sub>/OH-SAM (1:9 ratio) coated Au (29.3  $\mu\text{A}/\text{cm}^2$  vs 9.7  $\mu\text{A}/\text{cm}^2$  and 9.8  $\mu\text{A}/\text{cm}^2$ , respectively).<sup>84</sup>

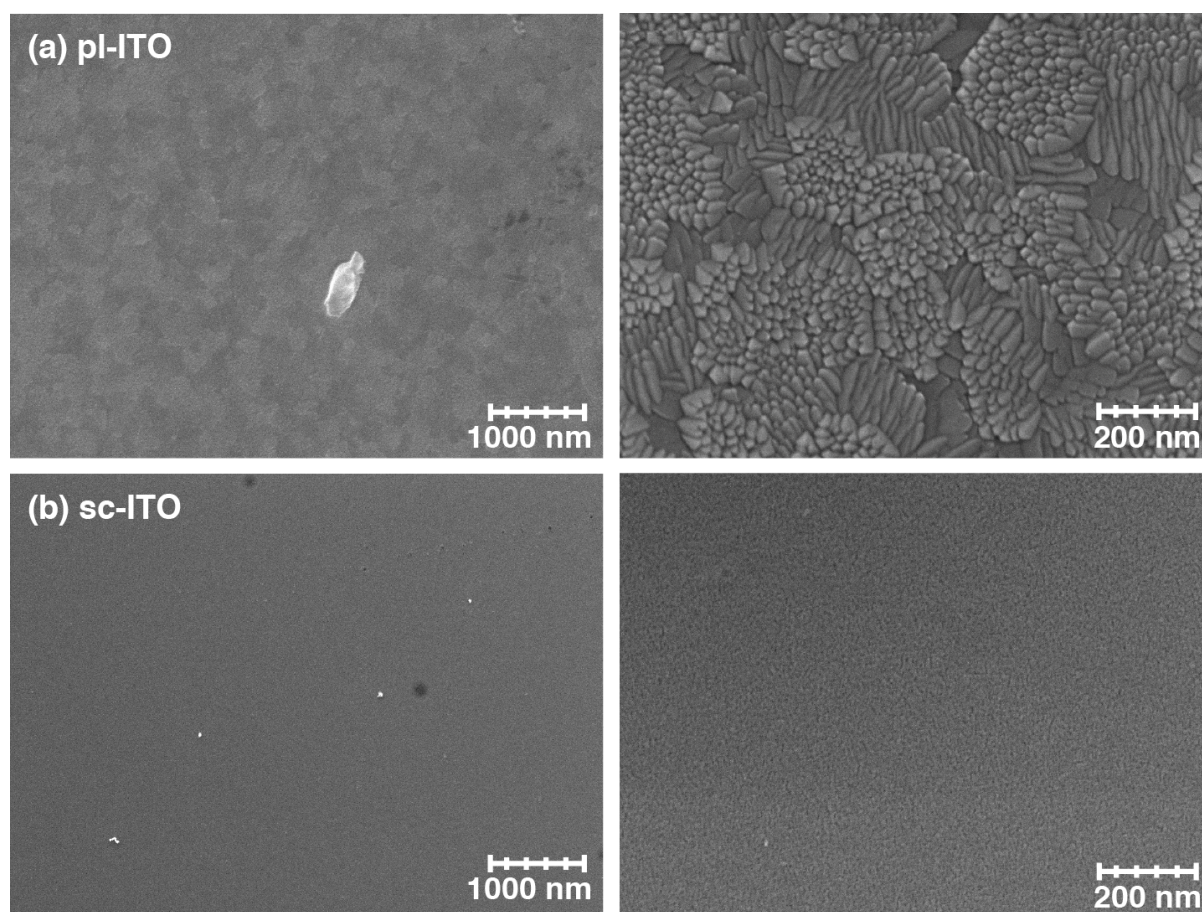


**Figure 25**

SEM images of the (a) commercial planar ITO-coated glass (pl-ITO), and (b) spin-coated ITO deposited on a Si prism.

To follow the adsorption of the MBH on modified and unmodified ITO using IR spectroscopy, ITO was spin coated onto a Si-prism (hereby denoted sc-ITO) following a modified literature method from Xu, Cheng and co-workers that produces ITO films with a low surface roughness, comparable to sputtered ITO.<sup>124</sup> SEM images of the pl-ITO electrodes used in this study compared to SEM images of the sc-ITO on a Si-prism are shown in Figure 25. The images of the sc-ITO resemble those reported in by Xu, Chening and co-workers, with an apparent lower-surface roughness than the pl-ITO. The sc-ITO electrodes were studied using *in situ* ATR IR in a Kretschmann-type configuration.

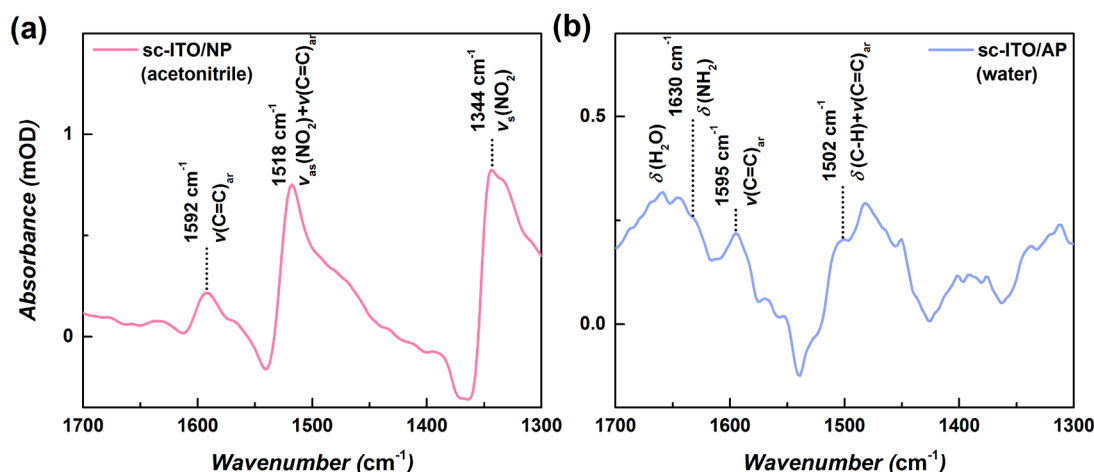


**Figure 26**

ATR IR absorption spectrum of spin-coated ITO (sc-ITO) (a) in acetonitrile after electrochemical grafting with 1 mM 4-NBD with 1 equivalent DPPH added to give nitrophenyl (NP)-functionalised ITO, and (b) in water after electrochemical reduction of the nitrophenyl (NP) moieties to aminophenyl (AP) moieties.

A sample was successfully electrochemically grafted with 1 mM 4-NBD in the presence of 1 mM DPPH, as can be seen by the appearance of absorption bands characteristic of a nitrophenyl interface in the IR adsorption spectrum in Figure 26. Due to the lack of enhancement like in SEIRA spectroscopy, the adsorption intensities obtained are very low, and no polarised light was used. Thus, no information can be obtained about any preferential orientation of the molecules on the ITO surface. Compared to the nitrophenyl interfaces measured on Au, there is a shift of 6-8  $\text{cm}^{-1}$  to lower wavenumbers for each of the bands marked in Figure 26. The band positions on Au and ITO are compared in Table 7.

**Table 7**

A comparison between the IR adsorption band positions of nitro-phenyl moieties electrografted on Au and ITO.

<b>Sample</b>	<b>Band position (<math>\text{cm}^{-1}</math>)</b>		<b>Band assignment</b>
	<b>Au</b>	<b>ITO</b>	
<b>4-NBD</b>	1351	1344	$\nu_s(\text{NO}_2)$
	1526	1518	$\nu_{as}(\text{NO}_2)+\nu(\text{C}=\text{C})_{ar}$
	1598	1592	$\nu(\text{C}=\text{C})_{ar}+\nu_s(\text{NO}_2)$

The nitrophenyl moieties were electrochemically reduced in 0.1 M  $\text{NaClO}_4$ , 1:9 ethanol:water and a new IR adsorption spectrum was recorded (Figure 26b). This spectrum was recorded in water, unlike the spectrum of the aminophenyl interface on gold in Figure 12a in section 7.6 (page 78), which was recorded in dry acetonitrile, resulting in a broad band around  $1640 \text{ cm}^{-1}$  due to water that obscures the broadened  $\delta(\text{NH}_2)$  band for the partially protonated aminophenyl moieties. While there are significant changes in the baseline after reduction of the interface, making the characterisation of the spectrum difficult, it is possible to identify bands characteristic of the aminophenyl interface, including the  $\nu(\text{C}=\text{C})_{ar}$  band at  $1594 \text{ cm}^{-1}$  and the  $\delta(\text{C}-\text{H})+\nu(\text{C}=\text{C})_{ar}$  band at  $1502 \text{ cm}^{-1}$ . The IR adsorption spectra of aminophenyl interfaces on gold and ITO recorded in

water are compared in Figure 27a, while the corresponding difference spectra calculated after reduction of the aminophenyl interface are compared in Figure 27b. The IR adsorption spectra appear similar, while the behaviour during reduction also appears similar, as confirmed by looking at the second derivatives in Figure 27b.

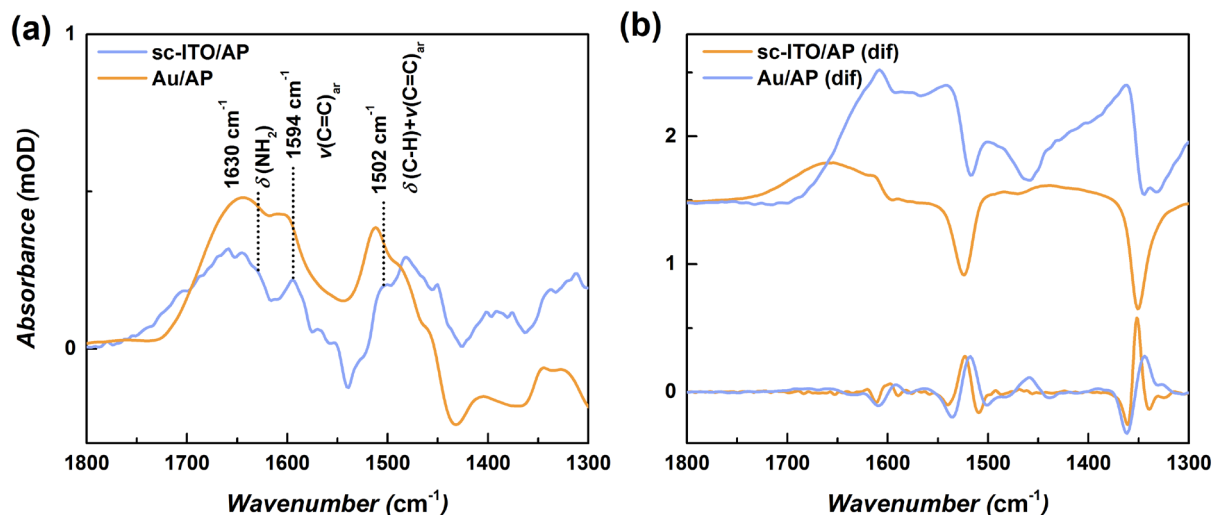


**Figure 27**

(a) ATR IR absorption spectra in water comparing the aminophenyl (AP) interface electrografted on spin-coated ITO (sc-ITO) and gold. (b) Difference spectra recorded in 0.1 M NaClO<sub>4</sub>, 1:9 ethanol:water after electrochemical reduction of the nitrophenyl (NP) moieties to the aminophenyl (AP) moieties. The second derivatives of the difference spectra are also shown.

Upon incubating the unmodified and amino-functionalised sc-ITO electrodes with strep-MBH at pH 7, two broad absorption bands appear at 1650 and 1544 cm<sup>-1</sup> (Figure 28) corresponding to the amide I and amide II bands of the protein backbone, indicating that the MBH binds to the unmodified and amino-functionalised surfaces. Compared to the spectra recorded on gold, these bands are shifted 4-8 cm<sup>-1</sup> to lower wavenumbers. Spectra were recorded at 3-minute time intervals over the course of the incubation process and the amide I and II band intensities were plotted as a function of time and fitted using a biexponential function:

$$A = A_0 + A_1 \exp(-t/\tau_1) + A_2 \exp(-t/\tau_2)$$

where  $A_0$ ,  $A_1$  and  $A_2$  are the final adsorption intensities for the individual adsorption processes, and  $\tau_1$  and  $\tau_2$  are the time constants for the respective adsorption processes. What is clear from the plots and the kinetic data analysis is that the first adsorption process occurs at a faster rate on both electrodes compared to the second, slower adsorption process.

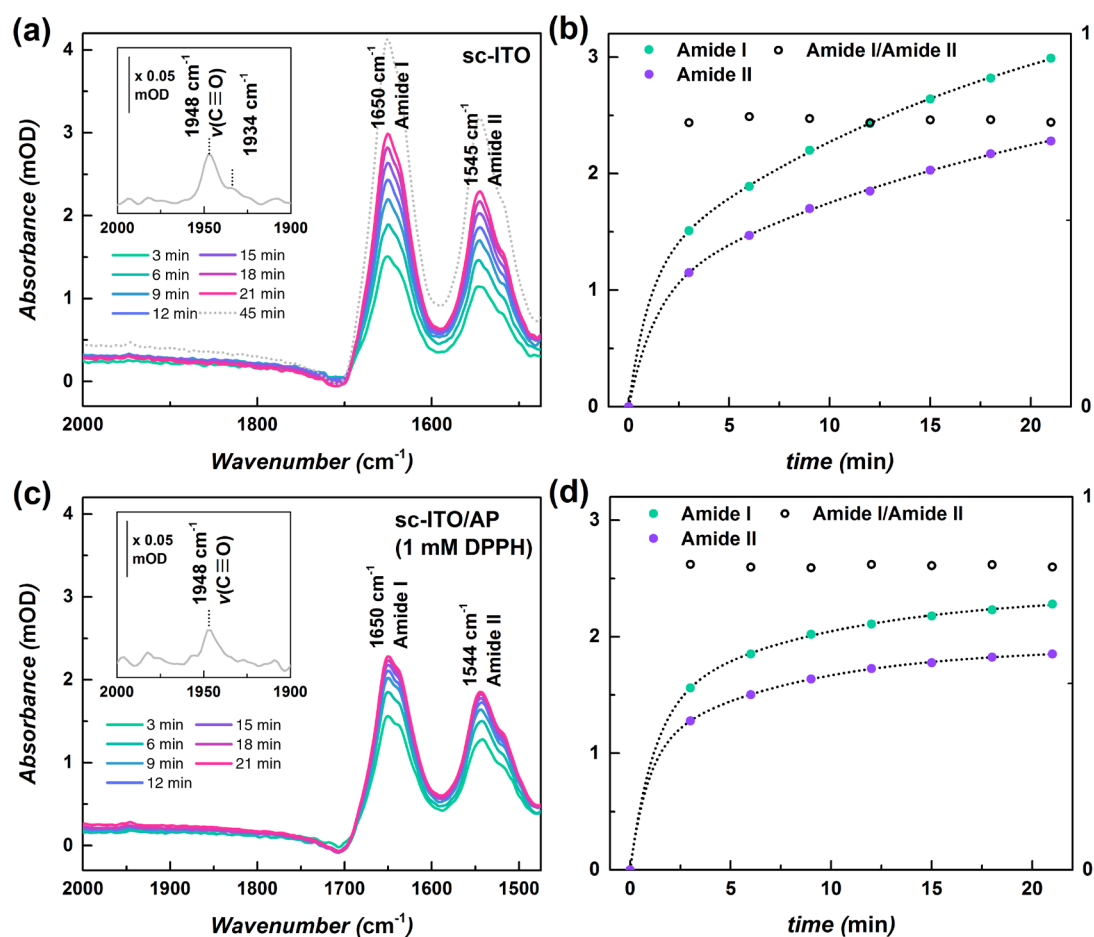


**Figure 28**

ATR IR absorption spectra in buffer (pH 7, 10 mM PB) of MBH being adsorbed (a) onto bare sc-ITO and (c) onto amino functionalised sc-ITO (modified with 1 molar equivalent DPPH) (inset: shows a characteristic active site band of the enzyme, namely the  $\nu(\text{C}\equiv\text{O})$  stretching vibration of the Fe-coordinated carbon monoxide ligand, which can be detected at  $1948\text{ cm}^{-1}$  with a shoulder at  $1934\text{ cm}^{-1}$  for the so called “Ni<sub>i</sub>-B” and the “Ni<sub>i</sub>-S” states of the oxidised enzyme). Kinetic analysis of the adsorption of the MBH onto the (b) bare sc-ITO and (d) the amino functionalised sc-ITO (using 1 mM DPPH).

**Table 8**

Kinetic analysis of the MBH amide I and II band intensities recorded during adsorption on the unmodified and amino functionalised sc-ITO electrodes. A biexponential fitting ( $A = A_0 + A_1 \exp(-t/\tau_1) + A_2 \exp(-t/\tau_2)$ ) was applied over the first 21 minutes of MBH adsorption in both cases.

Sample / band	$A_0$ (mOD)	$A_1$ (mOD)	$\tau_1$ (min)	$A_2$ (mOD)	$\tau_2$ (min)
<b>Bare ITO</b>					
$1650\text{ cm}^{-1}$	$3.97 \pm 0.18$	$1.19 \pm 0.06$	$0.70 \pm 0.11$	$2.78 \pm 0.13$	$13.98 \pm 1.75$
$1545\text{ cm}^{-1}$	$3.16 \pm 0.33$	$0.99 \pm 0.08$	$0.92 \pm 0.16$	$2.17 \pm 0.25$	$15.97 \pm 4.42$
<b>1 mM DPPH</b>					
$1650\text{ cm}^{-1}$	$2.37 \pm 0.04$	$1.39 \pm 0.10$	$0.82 \pm 0.12$	$0.98 \pm 0.07$	$6.21 \pm 1.07$
$1544\text{ cm}^{-1}$	$1.91 \pm 0.01$	$1.03 \pm 0.04$	$0.61 \pm 0.08$	$0.88 \pm 0.03$	$5.29 \pm 0.34$

$A_0$ ,  $A_1$  and  $A_2$  are the final adsorption intensities for the individual adsorption processes, and  $\tau_1$  and  $\tau_2$  are the time constants for the respective adsorption processes.

The first process occurs at a slightly faster rate on the amino-functionalised sc-ITO compared to the unmodified sc-ITO, while the second, slower adsorption process occurs at a substantially slower rate on the amino-functionalised sc-ITO. These results suggest that while strep-MBH monolayer formation is fast on both substrates, substantial multilayer formation is preferentially observed in the case of the unmodified sc-ITO, which would explain the substantial mediated currents obtained for unmodified pl-ITO in Figure 24. The reasons for the preferential multilayer growth of strep-MBH on unmodified ITO remains unclear; however, the difference in immobilisation observed for the unmodified and amino-functionalised ITO shows that surface modification clearly impacts on the immobilisation behaviour of the MBH. One possible explanation may be that the orientation at which the first monolayer of MBH adsorbs onto the unmodified ITO further facilitates adsorption of more MBH molecules on top of them. The surface charge of the unmodified ITO is likely different to the amino functionalised ITO, and thus likely to lead to a different distribution of orientations of MBH molecules. The unmodified ITO will mainly have hydroxyl groups present and exposed metal sites, which may interact with amino-acids on the protein back-bone. For strep-MBH adsorbed on tin-rich ITO by Heidary, a nearly mono-exponential increase in band intensity was observed, where a large proportion of the MBH molecules are adsorbed in an unfavourable orientation, given the 5-fold increase in HOR current upon addition of MB mediator.<sup>84</sup> A similar behaviour was observed for MBH adsorbed on a hydrophobic alkane-thiol SAM<sup>84</sup> and may point to the hydrophobic nature of the tin-rich ITO surface.

The appearance of a band at  $1948\text{ cm}^{-1}$ , related to the  $\nu(\text{C}=\text{O})$  stretching vibration of the CO ligand coordinated to the [Ni-Fe] active site and characteristic for the highest oxidised 'Ni<sub>r</sub>-B' state for both the unmodified sc-ITO and the amino functionalised sc-ITO indicates that the enzyme's integrity is preserved upon surface immobilisation in both cases.<sup>130,189</sup> A small shoulder band at  $1934\text{ cm}^{-1}$  in the case of the unmodified sc-ITO may be due to the ready silent 'Ni<sub>r</sub>-S' state.<sup>188,222</sup> No shoulder band was observed by Heidary for strep-MBH immobilised in tin-rich ITO.<sup>84</sup>

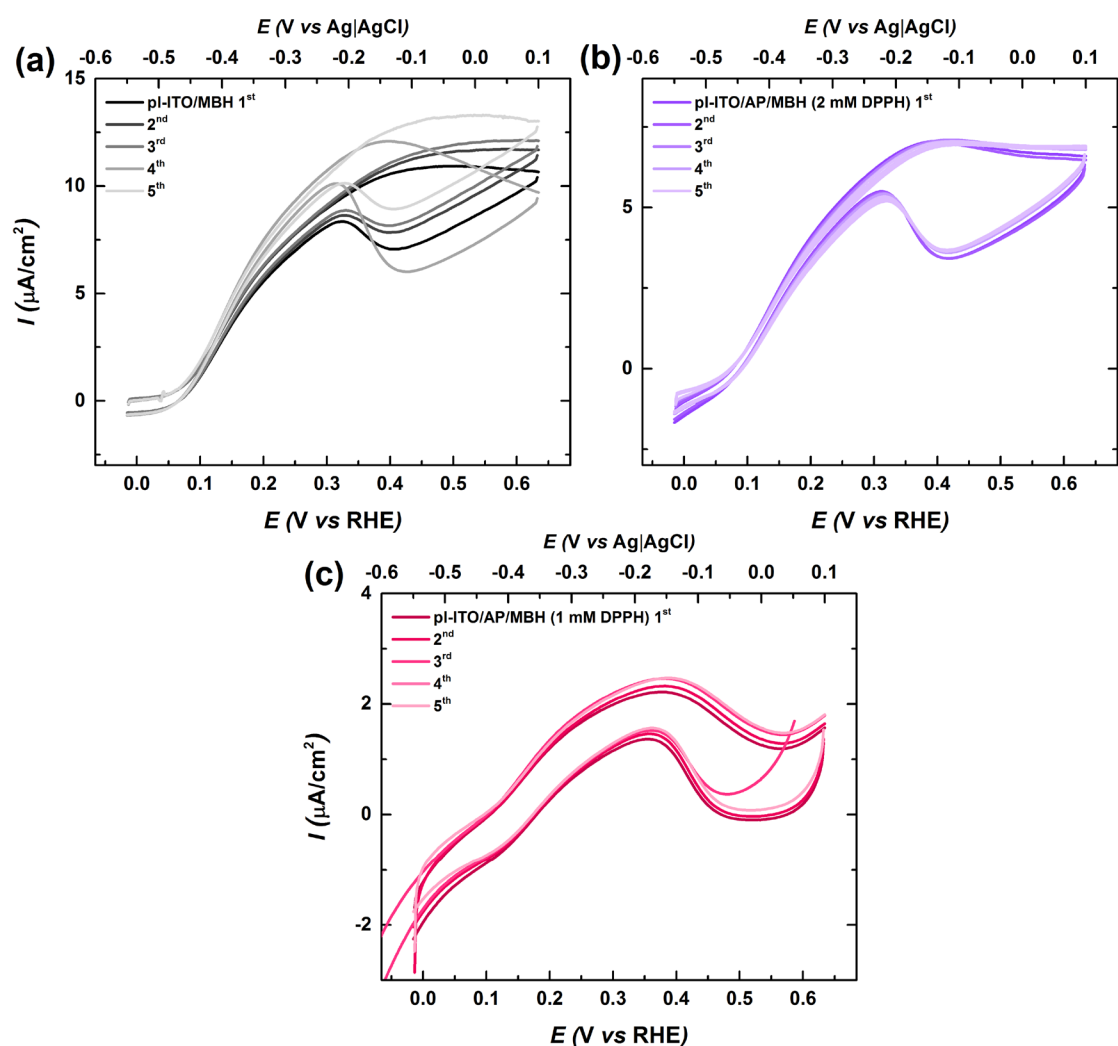


**Figure 29**

First 5 cycles of the protein film voltammetry recorded in 10 mM PB buffer at pH 5.5 saturated with  $\text{H}_2$  with a scan rate of 10 mV/s for strep-MBH adsorbed onto unmodified and amino-functionalised pI-ITO.

Further differences in the behaviour of the MBH on modified and unmodified ITO can be observed in repeated PFV cycles of MBH in  $\text{H}_2$  on the unmodified and amino functionalised pI-ITO electrodes. The shape of the traces on unmodified pI-ITO slowly change upon repeated cycling, with the electrocatalytic current increasing with each subsequent cycle. This behaviour points to a gradual change in the orientation of the MBH molecules in the first monolayer and is in stark contrast to that observed on the amino functionalised pI-ITO electrodes, where the trace shape and electrocatalytic currents remain relatively stable. The change in orientation on the unmodified ITO may be promoted by a change in the MBH-surface interaction energy landscape induced upon changing the pH of the buffer from pH 7, at which the MBH was adsorbed onto the surface, to pH 5.5, at which the electrochemistry is performed. The stabilities in current exhibited here upon repeated cycling are in contrast to the behaviour of strep-MBH on tin-rich ITO, which is reported to decrease by 50% after 5 minutes of potential application. A lower decrease of 12% was reported for the selectively bound his-tagged MBH on tin-rich ITO.<sup>84</sup>

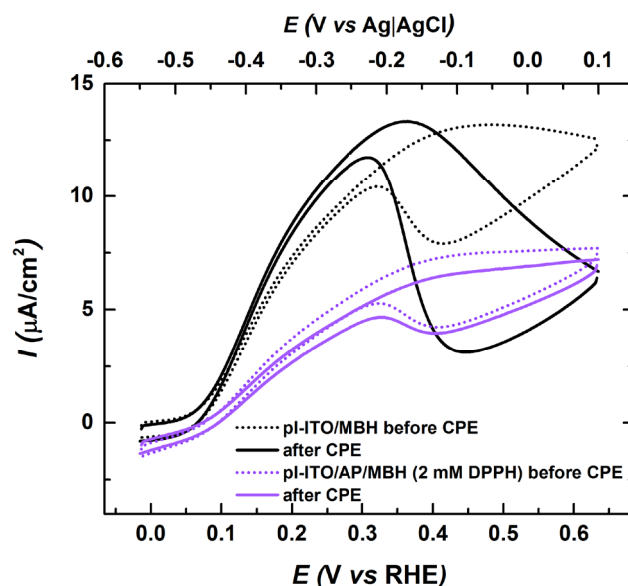
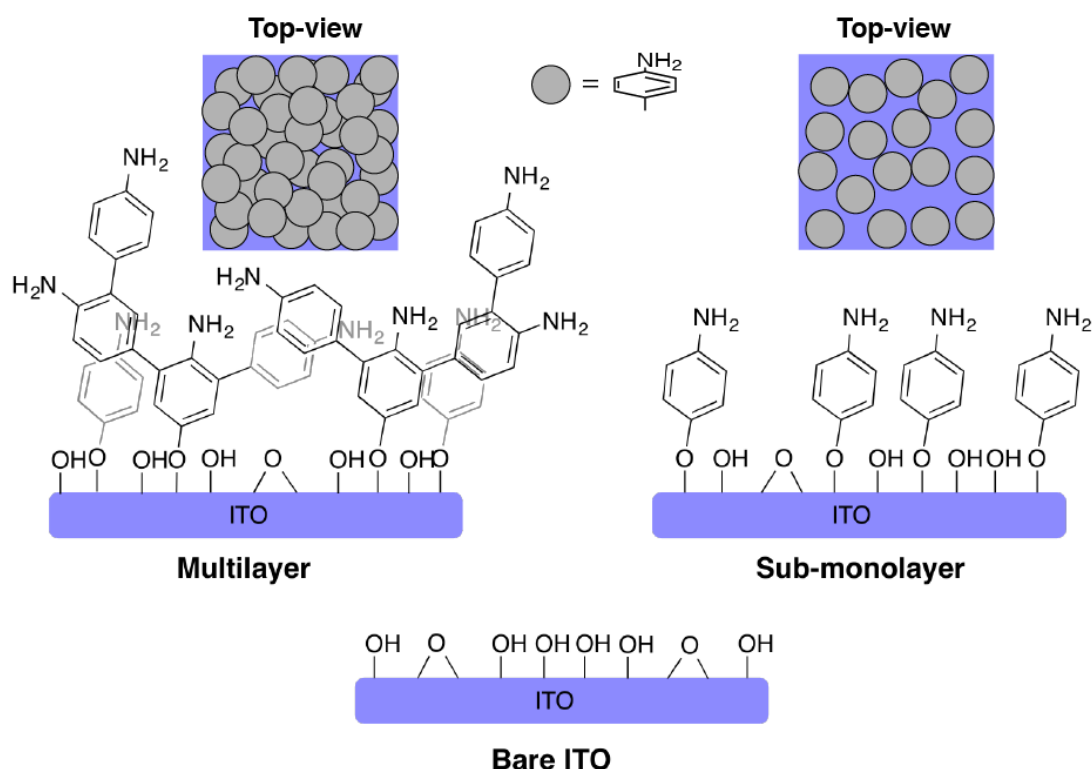


**Figure 30**

(a) Constant potential electrolysis (CPE) recorded at  $-0.15$  V (vs Ag/AgCl 3M) in 10 mM PB buffer at pH 5.5 saturated with  $H_2$  for MBH adsorbed on unmodified pl-ITO (black trace) and amino functionalised pl-ITO (using 1 molar equivalent DPPH, violet trace), and (b) protein film voltammetry recorded before (dotted traces) and after CPE, scan rate = 10 mV/s.

After repeated cycling, constant potential electrolysis (CPE) was performed for 1000 s at  $-0.15$  V (vs Ag/AgCl 3M) using the MBH immobilised on the unmodified pl-ITO electrode and the pl-ITO electrografted with the addition of 2 molar equivalents DPPH. A comparison of the PFV traces recorded before and after CPE (Figure 30) show that while the trace shape doesn't change in the case of the amino functionalised ITO (other than for an 8% decrease in maximum current that reflects the decrease in activity over the course of the CPE), the trace shape for the unmodified pl-ITO changes substantially with a slight increase in maximum current. Furthermore, above a potential of  $-0.15$  (vs Ag/AgCl 3M) there is a substantial decrease in current due to the reversible, electrochemically induced anaerobic inactivation of the hydrogenase to the Ni-B state. This suggests that the overpotential for deactivation decreases, which may result from a reorientation on of MBH on unmodified pl-ITO. This would indicate a different interaction between the MBH and the unmodified and amino-modified interfaced, i.e. a stronger interaction for the latter and higher energetic barriers for reorientation. In any case, these results indicate that diazonium salts with various functionalities may be used to immobilise enzymes *via* electrostatic interactions on TCO materials in an electrochemically accessible manner, and potentially allows for immobilisation *via* covalent bonds (e.g. through amide coupling).



#### Scheme 50

Proposed structures of interfaces electrochemically grafted onto ITO surfaces *via* the electrochemical reduction of diazonium salts.

As previously mentioned, close packing of the interface is not possible during the electrochemical grafting of the ITO, and, as more radical scavenger is added during modification, the coverage eventually plateaus at a sub-monolayer coverage. This will result in a 'mixed' interface, where a certain area of the ITO substrate is left exposed (e.g. with hydroxyl groups), which could, for example, affect the surface charge of the electrode. ITO has been reported to have a point of zero charge (PZC) of around 7<sup>223</sup>; while the PZC of the amino-functionalised surface still needs to be measured.

### 5.3 Conclusions

Interfaces were electrografted on ITO electrodes *via* the electrochemical reduction of diazonium salts, in this case 4-NBD. The radical scavenger DPPH was added during electrografting resulting in the moderation of the interface formation with near monolayer coverages achieved, and in so doing displayed similar behaviour to carbon electrode materials.<sup>157</sup> After subsequent conversion to amino-functionalised interfaces, an oxygen-tolerant hydrogenase was immobilised on the electrodes and the behaviour of the enzyme in electrocatalytic tests was related to the coverage and properties of the interfaces. Substantial differences were observed between the hydrogenase immobilised on unmodified ITO and amino functionalised ITO, with indications of stronger electrostatic interactions between the MBH and the amino functionalised ITO. Charge transfer resistance could be sufficiently lowered with the radical scavenger to allow high electrocatalytic currents to be obtained. Diazonium salts may therefore be used to immobilise

enzymes on TCO materials instead of other anchoring groups, such as silanes or phosphonates. Diazonium chemistry may offer potential advantages over these aforementioned anchoring groups in terms of electrochemical and hydrolytic stability, and charge transfer properties, and these aspects will be explored further in the next chapter.

# Chapter 6

## Electrochemical grafting of diazonium salts on transparent conductive oxide (TCO) electrodes for the immobilisation of molecular catalysts

### 6.1 Introduction

As mentioned in section 5.3.9 (page 29), the immobilisation, or heterogenisation, of enzymatic and molecular catalysts on electrode surfaces is imperative in functional devices. Immobilisation increases the number of addressable active sites, separates half-reactions and facilitates electronic contact, especially when using hydrophobic catalysts in aqueous conditions.<sup>224,225</sup> Conductive metal oxide supports offer many advantages over other electrode materials like gold (including significantly lower costs and broader possibilities for functionalisation<sup>31</sup>) or carbon-based materials (including improved corrosion resistance, particularly under oxidative conditions).<sup>226</sup> Semi-conducting oxides have several properties that make them highly suitable for energy storage and conversions devices, including transparency or band gaps that allow the adsorption of visible light for solar-driven reactions, as well as diverse possibilities for nanostructuration of the material e.g. using templating methods. Nanostructuration can induce desirable properties in the material, such as high surface areas (giving HSMs) in order to achieve a higher density of catalytic species (per cm<sup>2</sup> of electrode), and hence higher outputs from e.g. electrocatalytic devices like electrolyzers or fuel-cells.

In order to immobilise catalysts on oxides, a number of anchoring groups are typically used, including phosphonic acids, carboxylic acids, silanes and their derivatives, amongst others.<sup>5,6,25,28,36,70,227–235</sup> Each approach has its own merit, which may be related to stability or charge transfer properties; however, one property (stability or good charge transfer properties) often comes at the expense of another.<sup>27,231,236</sup> New approaches must be developed which, in no particular order, are: (1) sufficiently robust to withstand a range of chemical and electrochemical conditions, (2) synthetically straightforward to realise, and (3) facilitate fast and efficient charge transfer.

Aryl diazonium salts have been used to functionalise a broad range of electrode materials, including carbon materials, metals and silicon because of the strong covalent bond formed between the phenyl ring of the salt and the electrode surface.<sup>45,237,238</sup> However, the formation of thick, insulating interfaces often prevents their use in the field of electrocatalysis, where a fast heterogeneous charge transfer between the immobilised redox species and the electrode is

required e.g. in electrolyzers or sensor devices.<sup>237</sup> So far, diazonium salts have been widely used to modify carbon materials, such as glassy carbon (GC) or carbon nanotubes (CNTs), and they have recently been used to successfully immobilise molecular catalysts on such materials. This includes the immobilisation of an iridium-based oxygen evolution reaction (OER) catalyst on GC<sup>71</sup>, the immobilisation of a cobalt terpyridine-based catalyst on GC with activity towards proton and CO<sub>2</sub> reduction<sup>75</sup>, the immobilisation of an iron porphyrin on CNTs with activity for CO<sub>2</sub> reduction<sup>152</sup>, and the immobilisation of iron porphyrin<sup>151</sup> and iron phthalocyanine<sup>150</sup> species on CNTs with activity for the oxygen reduction reaction (ORR). Highlighting some of the potential drawbacks of using carbon materials, the GC electrodes used to immobilise the iridium-based catalyst and perform water oxidation were rapidly oxidised under the anodic potentials applied, leading to loss of the catalyst from the electrode surface.<sup>71</sup>

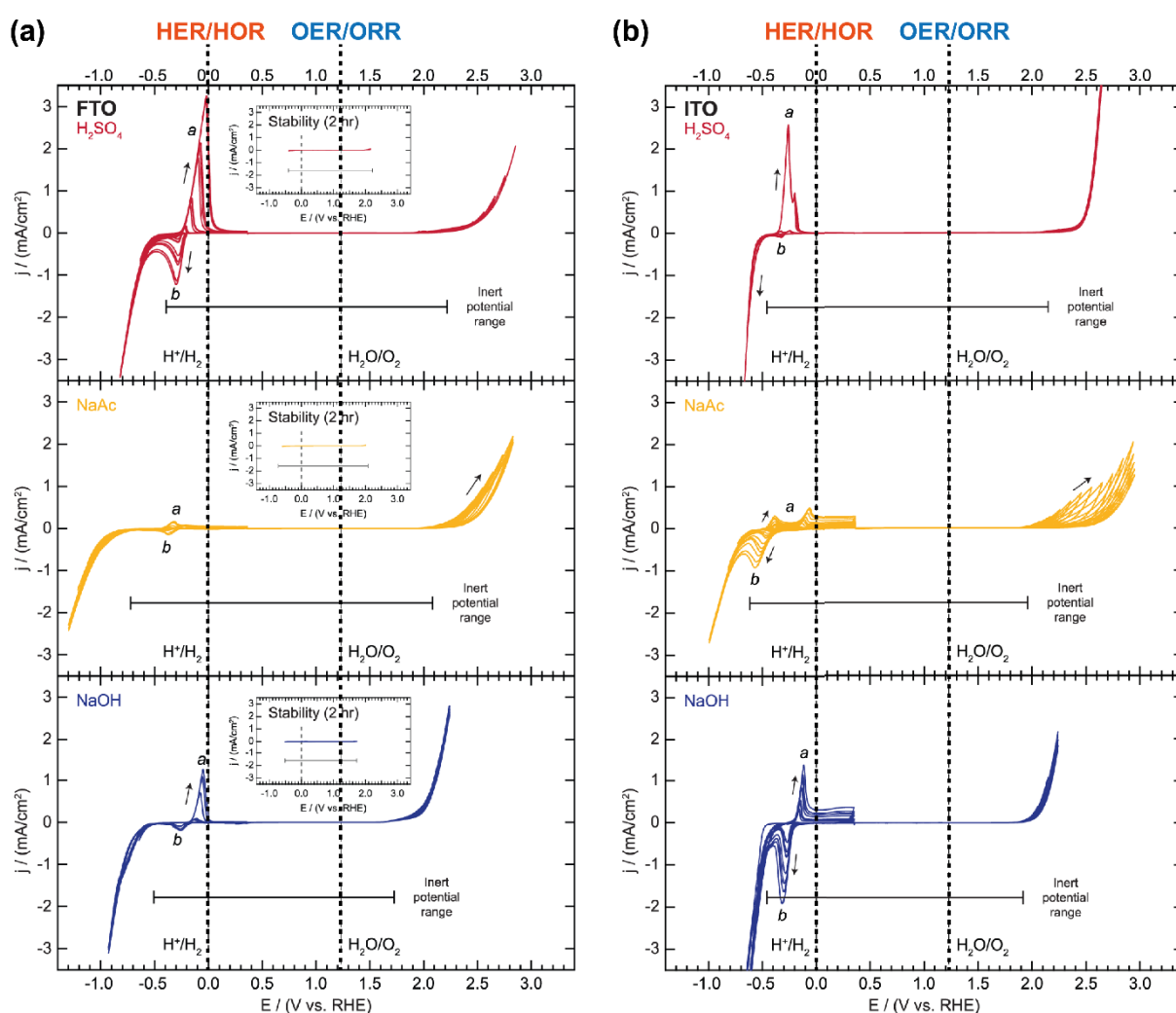


**Figure 31**

CVs of commercially available (a) FTO and (b) ITO substrates in pH 1 (0.1 M H<sub>2</sub>SO<sub>4</sub>), pH 7.2 - 7.8 (0.1 NaAc) and pH 13 (0.1 M NaOH) electrolytes indicating their electrochemical activity and electrochemically inert potential range (adapted from Figure 3 and 4, Benck et al. "Substrate Selection for fundamental studies of electrocatalysts and photoelectrodes: inert potential windows in acidic, neutral, and basic electrolyte." *PLoS One* **9**, e107942 (2014)). Scan rate = 25 mV/s. The theoretical potentials for the HER/HOR and OER/ORR reactions are highlighted, and lie within the inert potential range for FTO and ITO in all electrolytes/pH's tested.<sup>226</sup>

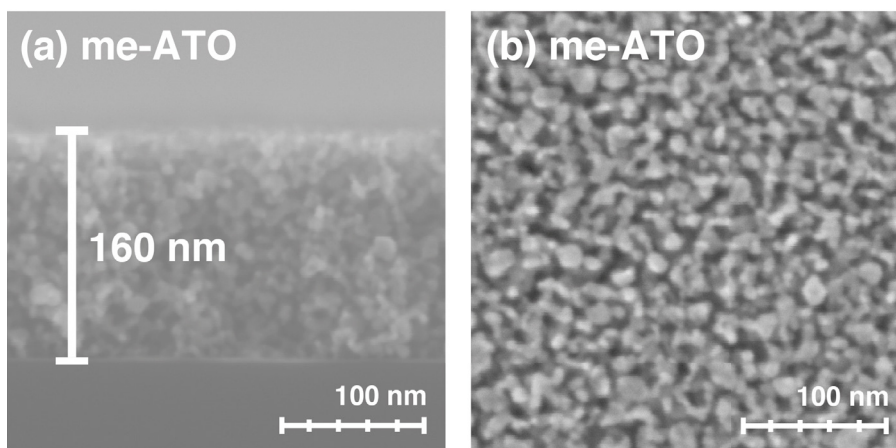
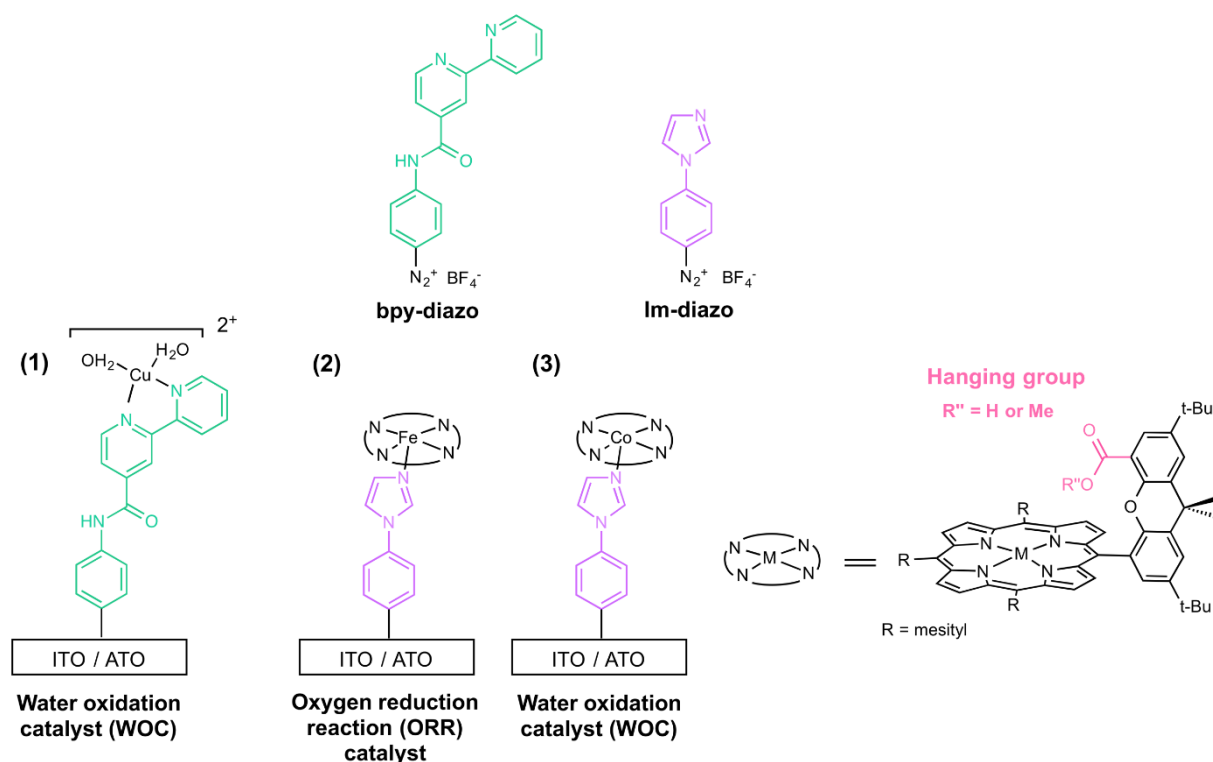


**Figure 32**

SEM images of the (a) cross-sectional view and (b) top view of the me-ATO films deposited on a Si wafer showing the nanostructuring and open, mesoporous structure of the me-ATO films, as well as the film thickness.

For the following work, mesoporous antimony-doped tin oxide (me-ATO) thin film electrodes were used as a model nanostructured TCO system due to their high surface areas, interconnected porosity and ease of synthesis.<sup>205,239–241</sup> ATO has gained attention as a catalyst support material due to its low cost compared to semi-precious indium-based ITO (indium tin oxide) and due to its high electrical conductivity and stability in the electrochemical range required for a diverse range of important energy conversion and storage reactions, including ORR and water oxidation.<sup>4,242</sup> The electrochemically inert potential window of ITO and fluorine-doped tin oxide (FTO) was determined by Jaramillo and co-workers and found to encompass the thermodynamic potentials for the HER/HOR and OER/ORR reactions, as shown in Figure 31.<sup>226</sup> The same electrochemical experiments carried out on me-ATO for this study show that it is stable in a similarly broad stability window (-0.77 to 1.83 V (vs RHE) in pH 7 0.1 M PB, see Appendix 8). As a result, ATO has found use as a corrosion-resistant electrode materials in dye sensitised solar cells<sup>243,244</sup>, optoelectronic devices<sup>241</sup> and for electrocatalysis.<sup>4,242</sup> The high transparency of me-ATO should also allow the use of *in-situ* UV-Vis, Raman and Infrared spectroelectrochemical techniques to characterise interfaces at the surface of the ATO during and after electrografting, as well as under catalytic conditions, and as such these techniques were used in this work.

In order to synthesise the me-ATO electrodes used in this work, ATO nanoparticles synthesised using a non-aqueous hydrothermal synthesis route were deposited on planar ITO coated glass slides from a colloidal solution containing the amphiphilic block co-polymer F127, as described in 6.1.3. After calcination, the resulting films were crack-free and had an open, mesoporous structure and a film thickness of around 160 nm, as shown in Figure 32. The small crystal size of the ATO (3-4 nm) reduces scattering and makes these films highly suitable for *in-situ* spectroscopic studies.



#### Scheme 51

Overview of the different catalytic systems synthesised in this chapter and the diazonium salts used to form them (bpy-diazo and Im-diazo). For more information see text.

In this chapter, the **bpy-diazo** ligand used to functionalise gold in section 7.7 is also used to functionalise ITO to determine if diazonium salts can be used to graft/immobilise molecular catalysts on these oxide surfaces in a series of electrochemical experiments. While the theoretical potentials for  $\text{CO}_2$  reduction lie within the stability window of ITO and FTO,  $\text{CO}_2$  reduction catalysts usually require very large overpotentials that push the real potential outside the stability window. As ATO (and ITO and FTO) is not stable in the electrochemical conditions required for the reduction of  $\text{CO}_2$ , i.e. with the manganese bipyridine catalyst, an attempt is made to assemble a copper-bipyridine complex for water oxidation purposes instead (as shown in Scheme 51).

In order to immobilise certain metalloporphyrins, which are a highly important class of molecules used in a broad range of applications (including DSSCs and catalytic devices<sup>116,245</sup>) on the TCO electrodes *via* axial coordination, an imidazole-containing diazonium salt **Im-diazo** (4-(1H-imidazol-1-yl)benzenediazonium tetrafluoroborate) was synthesised from 4-(1H-imidazol-1-yl)aniline. Axial metal-ligand coordination has been widely employed to immobilise a range of molecular catalysts or other molecular complexes<sup>70,233,246,247</sup>, such as photosensitisers<sup>231,236,248</sup>, on solid supports. The resulting reactivities of complexes immobilised in this way can further be tuned by modulating their electronic properties using ligands with different electron-donor abilities.<sup>249</sup> In fact, it has been shown that axial coordination of imidazole species to iron tetraphenylporphyrin can anodically shift the  $\text{Fe}^{2+/3+}$  redox couple potential, enhance its activity for ORR and improve its selectivity towards water (as opposed to  $\text{H}_2\text{O}_2$ ).<sup>250</sup> First, an iron

Hangman porphyrin is immobilised on ITO and ATO, as this species is known to be active for the ORR.<sup>251</sup> A number of electrochemical and spectroelectrochemical measurements (resonance Raman and UV-Vis) are carried out to obtain insights into the interface formation and its structure, thus facilitating rational interface design. Secondly, a cobalt Hangman porphyrin is immobilised on me-ATO, as this species is known to be active for the HER,<sup>252</sup> and similar cobalt tetrapyrrole species have also been shown to be active for the OER.<sup>253–259</sup> As the name suggests, hangman porphyrins (depicted in scheme 9) contain a 'hanging' group positioned at a fixed distance from the metal centre *via* a xanthene bridge (i.e. in the second coordination sphere of the complex), which may introduce certain non-covalent interactions that can influence electron transfer during reduction and alter the behaviour or catalytic activity of the complex.<sup>128,129</sup>

As well as using *ex situ* XPS measurements to characterise the interfaces electrografted on me-ATO from Im-diazo, *in situ* ATR-IR spectroelectrochemistry is used to determine their electrochemical and hydrolytic stabilities. This information is important for determining the types of catalysts and reactions that can be catalysed using electrografted diazonium interfaces on oxide materials.

## 6.2 Immobilisation of a molecular oxygen evolution reaction catalyst on indium tin oxide (ITO) using the electrografting of a diazonium salt

It was shown recently by Mayer and co-workers that copper–bipyridine–hydroxo complexes can be formed *in situ* from simple copper salts and bipyridine at high pH's, and that they can be used as homogenous catalysts in the OER with an overpotential of around 750 mV and a turnover frequency of around 100 s<sup>-1</sup>.<sup>260</sup> An improvement in reducing overpotential to 640 mV was demonstrated by Lin and co-workers using a 6,6'-dihydroxy-2,2'-bipyridine ligand.<sup>261</sup> While the overpotential for this catalyst is large compared to those typically obtained for ruthenium- or iridium-based molecular catalysts<sup>119</sup>, copper is several orders of magnitude lower in price. These results have spurred further work in the direction of copper-based OER catalysts<sup>262–265</sup>, with an overpotential as low as 520 mV being obtained by Crabtree, Brudvig and co-workers for a Cu(pyalk)<sub>2</sub> (pyalk = 2-pyridyl-2-propanoate) OER catalyst.<sup>266</sup> A number of publications have recently demonstrated the successful immobilisation of noble metal-based molecular OER catalysts on nanostructured TCO materials. Sheehan, Brudvig and co-workers recently demonstrated the use of iridium-based [Ir(pyalc)(H<sub>2</sub>O)<sub>2</sub>(μ-O)]<sub>2</sub><sup>2+</sup> (pylac = 2-(2'pyridyl)-2-propanolate) OER catalyst immobilised on mesoporous ITO *via* Ir-O-MO<sub>x</sub> bonds (where MO<sub>x</sub> = metal oxide).<sup>235</sup> Batista, Crabtree, Brudvig and co-workers immobilised a Ir-based pentamethylcyclopentadienyl OER pre-catalysts on mesoporous ITO using a silatrane anchoring group.<sup>232</sup> Meyer and co-workers immobilised a Ru-based [Ru<sup>II</sup>(Mebimpy)(4,4'-(PO<sub>3</sub>H<sub>2</sub>)<sub>2</sub>bpy)(OH<sub>2</sub>)]<sup>2+</sup> (mebimpy = 2,6-bis(1-methylbenzimidazol-2-yl)pyridine) OER catalyst on mesoporous ATO using a phosphonic-acid based anchoring group.<sup>267</sup> Llobet, Jooss, Meyer and

co-workers immobilised a Ru-based 3,5-bis(bipyridyl)pyrazolate (bbp)-based diruthenium OER precatalyst on mesoporous ITO using a carboxylate anchoring group.<sup>268</sup>

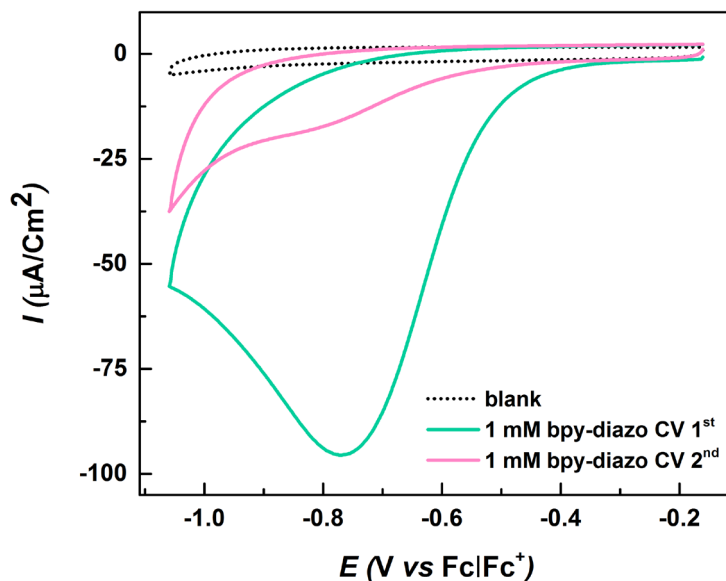


**Figure 33**

CVs of a 1 mM solution of bpy-diazo in acetonitrile (0.1 M TBAP) using pl-ITO as a working electrode. Scan rate = 50 mV/s.

Cyclic voltammetry was used to electrochemically graft bpy-diazo on the surface of the pl-ITO, as shown in Figure 33. The electrode was passivated after 2 CVs, showing similar behaviour to the gold electrodes in 7.7. The reduction potential of bpy-diazo on pl-ITO is -0.64 V (vs Fc/Fc<sup>+</sup>) compared to a potential of -0.53 V (vs Fc/Fc<sup>+</sup>) on Au. Small variations in diazonium salt reduction potentials on different substrates are commonly reported.<sup>186</sup> The bipyridine interfaces previously electrografted on gold were already characterised using SEIRA spectroscopy, and, as such, it can be assumed that similar bipyridine-functionalised interfaces are electrografted in this instance on pl-ITO. In order to assess the activity of pl-ITO towards the OER before and after electrochemical grafting, CVs were applied in 0.1 M NaOH, as shown in Figure 34. Bare, unmodified pl-ITO shows current for OER with an onset potential of around 1.9 V (vs RHE), which is the same as that reported by Jaramillo and co-workers for ITO.<sup>226</sup> After incubating the unmodified ITO electrode for 10 min in 2 mM CuSO<sub>4</sub> (in DI water) and rinsing, the same CV shows slightly increased current for the OER and a marginally lowered onset potential, as can be seen in Figure 34. Meyer and co-workers have previously shown CuSO<sub>4</sub> and other Cu<sup>2+</sup> salt solutions to be active for the OER at high overpotentials in basic solutions.<sup>269</sup> For bare pl-ITO that has been electrografted with bpy-diazo, the same CVs show decreased currents for the OER, which indicates that the surface of the ITO is passivated by a bipyridine-functionalised interface. CVs of the electrografted ITO electrode after incubation with 2 mM CuSO<sub>4</sub> (in DI water) for 10 min and rinsing result in greatly increased currents for OER (0.63 mA/cm<sup>2</sup> vs 0.05 mA/cm<sup>2</sup> at 2 V (vs RHE)) with the onset potential shifting to 1.73 V (vs RHE), suggesting that addition of Cu and complexation with the bipyridine-functionalised interface is necessary in order to form a species that is active for OER. The overpotential required to achieve OER is 0.5 V.

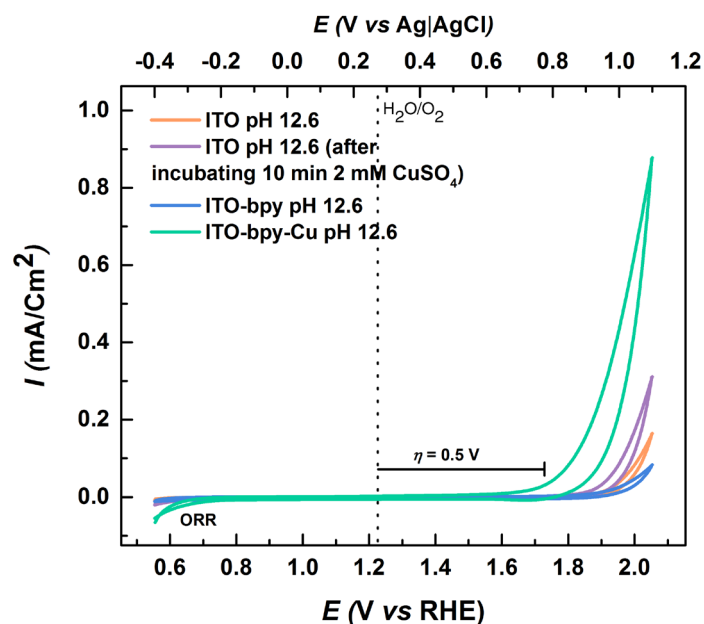
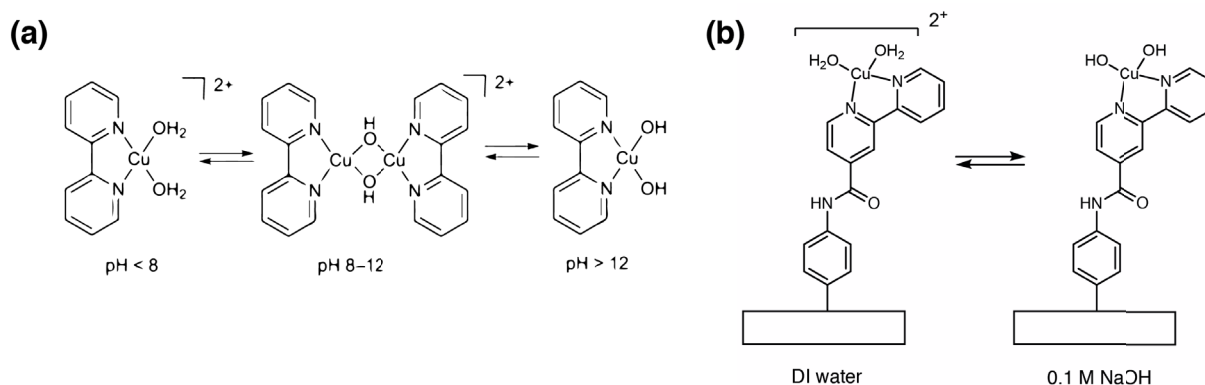


**Figure 34**

CVs of pl-ITO electrodes in 0.1 M KOH (in air): bare (orange trace), after incubating for 10 min in 2 mM CuSO<sub>4</sub> (purple trace), after electrografting with bpy-diazo (blue trace), and after electrografting and incubating for 10 min with 2 mM CuSO<sub>4</sub> (turquoise trace). Scan rate = 50 mV/s.



**Scheme 52**

(a) The copper-bipyridine species present at different pHs in the work of Mayer and co-workers (adapted with permission from <sup>260</sup>, copyright 2012 Macmillan Publishers Ltd). (b) The proposed structures of the immobilised copper-bipyridine species present in this work.

As previously mentioned, Mayer and co-workers achieved water oxidation using a homogenous copper–bipyridine–hydroxo catalyst. Salts of the dimeric bis- $\mu$ -hydroxide cation  $[(\text{bpy})\text{Cu}(\mu\text{-OH})]_2^{2+}$  are isolated from alkaline solutions of 1:1  $\text{Cu}^{2+}$ :bipyridine, where the anion is an acetate, triflate or sulphate anion, or alternatively generated *in situ* from the copper salt and bipyridine. It was shown using electron paramagnetic resonance (EPR) spectroscopy that below pH 8 the copper species exists as a monomeric aquo-complex  $[(\text{bpy})\text{Cu}(\text{H}_2\text{O})_2]^{2+}$ . As the pH increases, the dimeric species are formed  $[(\text{bpy})\text{Cu}(\mu\text{-OH})]_2^{2+}$ , while at highly alkaline pHs the dominant species is the monomeric  $(\text{bpy})\text{Cu}(\text{OH})_2$ , which is the catalytically active species.<sup>260</sup> The structures of these species are shown in Scheme 52a. It is proposed that during incubation with the 2 mM CuSO<sub>4</sub> solution (in DI water) the monomeric copper-bipyridine aquo-complexes form at the electrografted interface and in 0.1 M NaOH they form the monomeric bis-hydroxide structure (as

shown in Scheme 52b). The overpotential for OER calculated using the half-peak potential for the homogenous system by Mayer and co-workers at pH 12.5 is 0.75 V, while the overpotential calculated using the onset potential is around 0.64 V.<sup>260</sup> Comparing the overpotentials of this homogenous system to the heterogeneous system demonstrated in this work is complicated due to the absence of a well-defined redox peak in the latter system from which a half-peak potential can be calculated. These peaks are a result of diffusion limitations of the catalytically active species from the solution to the electrode surface in the homogenous system, which does not occur in heterogeneous systems (although mass transfer of reactants and products and lead to diffusion limitations, this tends not to be an issue in the case of the OER). Nevertheless, the difference in onset potential between the homogenous system of Mayer and co-workers and the immobilised system presented here is determined at around 0.14 V. This decrease in overpotential may partly be explained by the electron-withdrawing amide substituent on the bipyridine ligand used in this work, which may stabilise the electron-deficient Cu(III) or Cu(IV) centre required for catalysis. Mechanistic studies for the copper-6,6'-dihydroxy-2,2'-bipyridine hydroxide OER can be found in a work by Lin and co-workers.<sup>262</sup> The use of electron-donating or electron-withdrawing groups on a catalysts ligand can have a substantial effect on its activity, as has been demonstrated for a Re(bpy)(CO)<sub>3</sub>Cl CO<sub>2</sub> reduction reaction catalyst, where the use of either an electron withdrawing or donating amide substituent on the bipyridine ligand was used.<sup>270</sup>

Immobilisation of a catalyst on the ITO surface should not affect its catalytic activity per se. In work by Grätzel and co-workers it was shown for another Re(bpy)(CO)<sub>3</sub>Cl CO<sub>2</sub> reduction catalyst (with phosphonic acid anchoring groups on the bipyridyl ligand) that there was no shift in the onset potential for CO<sub>2</sub> reduction when immobilised on TiO<sub>2</sub> compared to the unbound species used in solution with a GC working electrode.<sup>271</sup> Intermolecular interactions between immobilised catalytic species may have an effect on their catalytic activity however, as will be demonstrated later for the Fe Hangman porphyrin ORR catalyst.

A semi-irreversible current at cathodic potentials for the Cu<sup>+</sup>/Cu<sup>2+</sup> couple was observed by Mayer and co-workers at ca. 0.65 V (vs RHE) in nitrogen. There is no current observable in Figure 34 for the Cu<sup>+</sup>/Cu<sup>2+</sup> couple, rather there is non-reversible current below 0.7 V vs RHE, which corresponds to electrocatalytic current for the ORR. Other examples exist in the literature where copper complexes have been used for the ORR.<sup>272–274</sup>

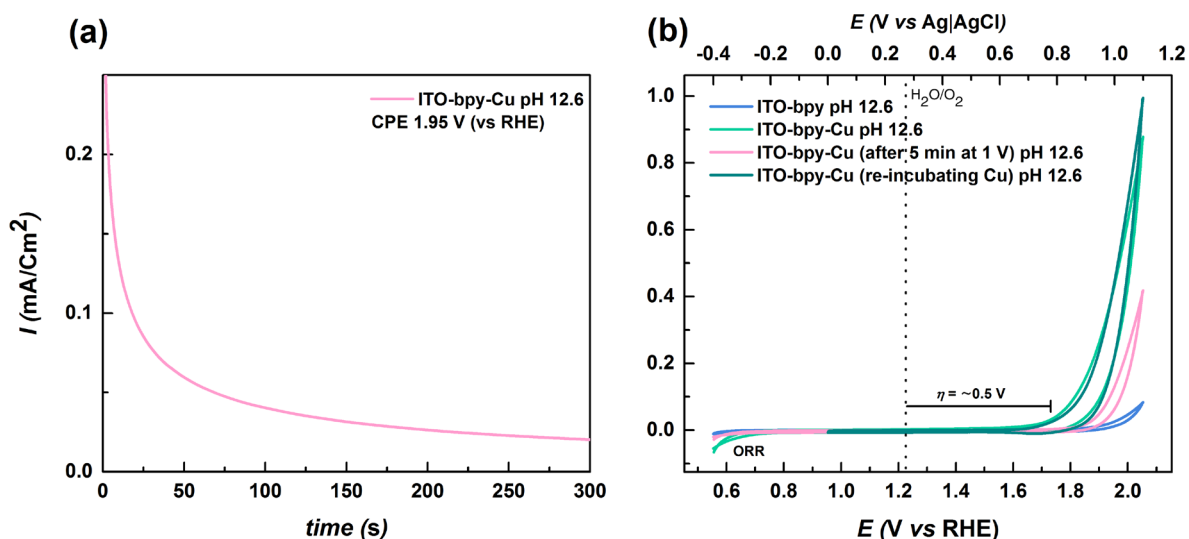


**Figure 35**

(a) Controlled potential electrolysis (CPE) at 1 V vs 3M Ag/AgCl (1.95 V vs RHE) of the Cu-bpy species immobilised on pl-ITO (ITO-bpy-Cu) in 0.1 M NaOH (in air), and (b) CVs of the electrode before CPE (turquoise trace), after CPE (pink trace) and after subsequent re-incubation for 10 min with 2 mM CuSO<sub>4</sub> (teal trace). Scan rate = 50 mV/s.

Controlled potential electrolysis (CPE) at 1.95 V (vs RHE) was performed in 0.1 M NaOH after the 2 CVs that were performed initially (Figure 35a). There is a rapid and almost total decrease in current over the 5 min, indicating that the catalytic species is not stable. Applying another CV after CPE shows a large decrease in current and a significant anodic shift in the onset potential (pink trace, Figure 35b). Re-incubating the electrode in 2 mM CuSO<sub>4</sub> solution (in DI water) and rinsing results in the restoration of the current for OER in 0.1 M NaOH (teal trace, Figure 35b), thereby indicating that the bipyridine ligand is stable on the ITO surface and that the loss of catalytic activity is presumably due to the loss of copper species e.g. by decomplexation from the bipyridine terminated interface.

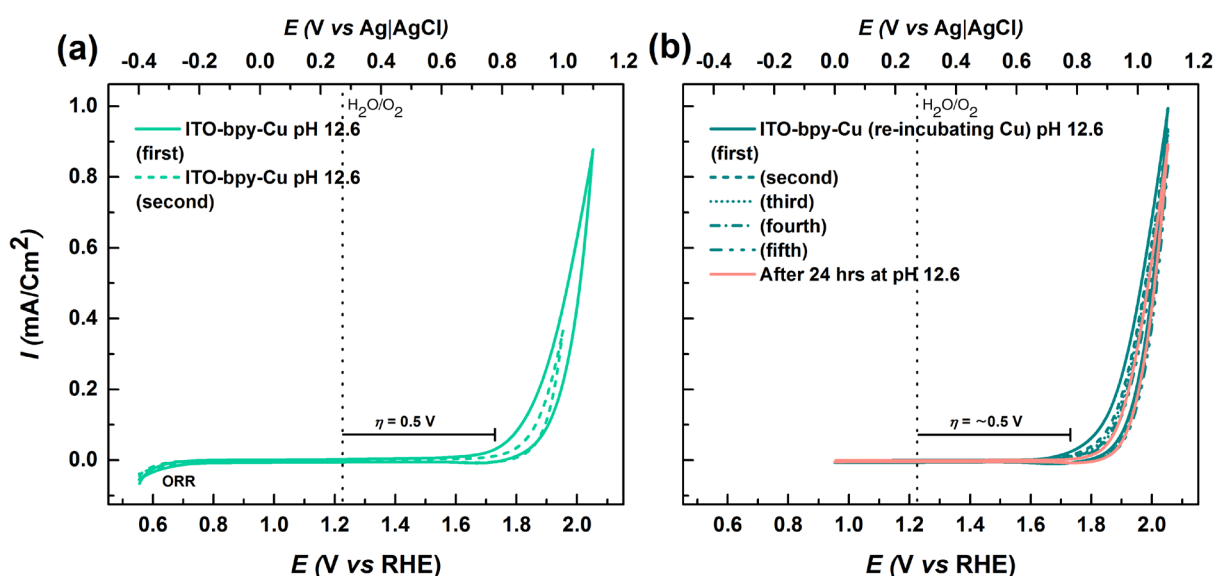


**Figure 36**

CVs of pl-ITO in 0.1 M NaOH (a) after initial electrografting and incubation for 10 min in 2 mM CuSO<sub>4</sub> (turquoise trace), and (b) after CPE and re-incubation with 2 mM CuSO<sub>4</sub> (dark green and pink trace). Scan rate = 50 mV/s.

As can be seen in Figure 36, the activities remain more stable after re-incubation with  $\text{CuSO}_4$ , which could also be an indication that some of the previous lost activity was due to the desorption of loosely bound or physisorbed bipyridine-ligands from the surface, as has been previously reported for other electrografted diazonium interfaces on electrodes.<sup>215,275</sup> A CV of the electrode after 24 hrs under non-turnover conditions in 0.1 M NaOH (pink trace, Figure 36b) indicates that there was no loss of activity during this time (i.e. no substantial hydrolysis of the interface). This is particularly significant, given that commonly used carboxylate and phosphonate anchoring groups show very poor stability in basic pH's.<sup>25,39</sup>

Both Mayer and co-workers, and Lin and co-workers reported good stabilities for their homogenous copper bipyridine catalysts, as well as high turnover numbers of 100 and  $400 \text{ s}^{-1}$ , respectively.<sup>260,262</sup> A 35% decomposition of the former catalyst was partly attributed to the deposition of copper metal on the Pt counter electrode (due to the absence of a membrane) and there was no indication of copper oxide deposits on the working electrode or any heterogeneous catalysis taking place. Given that the homogenous copper bipyridine hydroxide catalysts are readily formed *in situ* in solution at basic pH values, it is reasonable to expect that any catalytic species that decomposes as result of the decomplexation of copper from the bipyridine may regenerate, providing that the bipyridine ligand is not damaged and the copper remains in solution as an ion. Loss of copper from the surface of the modified electrodes in this work would result in a miniscule concentration of Cu in solution (compared to the mM equimolar concentrations of bipyridine and copper salts used in the homogenous systems), meaning that the equilibrium for the formation of copper bipyridine species will not be favourable. Another possibility for the loss of activity may be due to the absence of a supporting electrolyte (other than NaOH). Coordinating anions may play an important role in stabilising transition states or charged species, such as aquo complexes.

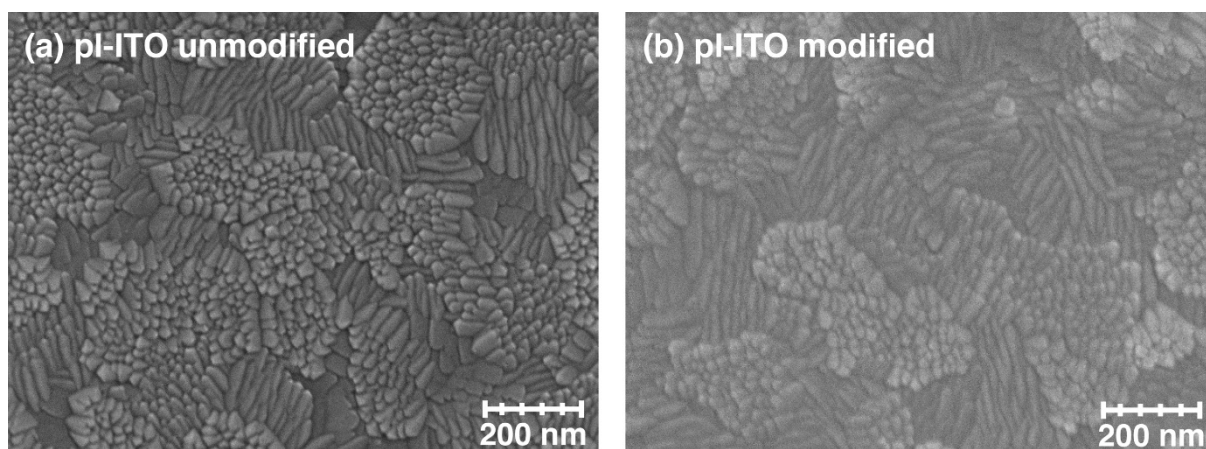


**Figure 37**

SEM images of a pi-ITO electrode (a) before and (b) after electrochemical grafting with bpy-diazo, incubation with  $\text{CuSO}_4$ , and electrolysis in 0.1 M NaOH.

Scanning electron microscopy (SEM) images were made of the bare, unmodified pI-ITO and of the modified pI-ITO electrode after the CPE and other electrochemical experiments. As can be seen in Figure 37, electrochemical grafting results in the formation of an insulating film on the ITO that is still present, even after 24 hrs in 0.1 M NaOH. There is no indication of the formation of oxides, as expected, although it is unlikely such trace amounts of oxide could be observed at such resolutions. Ideally, XPS would need to be conducted on the modified electrodes before and after electrolysis to determine the loss of Cu or detect the formation of non-catalytically active species. Given the apparent stability of the electrografted interface, the addition of copper salt (e.g. in the form of mM concentrations of  $\text{CuSO}_4$ ) to the NaOH electrolyte may result in stable currents for OER, as this would favour the regeneration of copper bipyridine hydroxide species at the interface (assuming that this is the reason for the loss of activity observed).

### 6.3 Chemical and electrochemical stability of electrografted diazonium interfaces on mesoporous antimony-doped tin oxide (me-ATO)

As mentioned previously in 9.1, the stability of a catalytic interface deposited on an electrode is of utmost importance when it comes to the fabrication of practical catalytic devices with long-term stabilities. In order to determine the stability of electrografted diazonium interfaces on TCOs using ATO as a model electrode material, me-ATO films were electrochemically grafted with Im-diazo and the electrochemical and chemical stability of the electrografted interface was investigated using *in situ* IR spectroscopy in ATR mode.

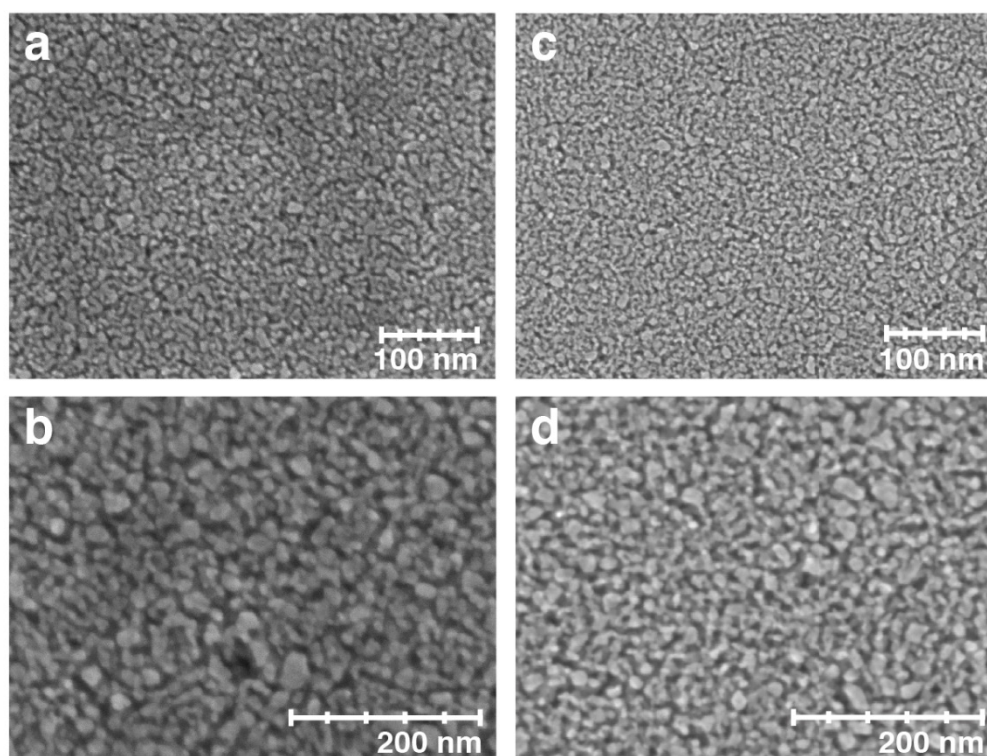


**Figure 38**  
SEM images of me-ATO films deposited on (a) (b) Si-prisms *via* spin-coating and (c) (d) ITO-coated glass slides *via* dip-coating.

The me-ATO films were deposited on a Si-prism *via* spin-coating, as outlined in 6.1.3. SEM images (Figure 38 a, b) show that the obtained films are crack-free and exhibit an open, porous structure similar to films deposited on ITO slides *via* dip-coating (Figure 38 c, d). The only difference is the somewhat greater extension of the ATO nanocrystals in the case of spin-coating. Given the similarity in structure between the films (and that the surfaces are essentially the same) it can be assumed that the corresponding desorption behaviour of the interfaces on the Si-prism will be representative of interfaces on samples used in electrochemical experiments.

IR spectra were recorded in ATR mode in acetonitrile (0.1 M TBAP or TBAF) before and after addition of 1 mM Im-diazo and subsequent electrochemical grafting, and the calculated difference spectra are shown in Figure 39. Adsorption of the Im-diazo on the ATO surface from solution can be deduced from the first spectrum, due to the appearance of a band at  $2253\text{ cm}^{-1}$  corresponding to the diazonium  $\text{N}\equiv\text{N}^+$  related stretching vibration  $\nu(\text{N}\equiv\text{N})$ , as well as bands at lower wavenumbers corresponding to modes of the respective phenyl and imidazole rings. The  $\nu(\text{N}\equiv\text{N})$  absorption band is partially obscured by two negative bands corresponding to the  $\delta(\text{CCN})$  and  $\nu(\text{C}\equiv\text{N})$  bands of acetonitrile molecules (asterisked) that are displaced from the surface of the ATO by the diazonium species. The adsorption of positively-charged species such as diazonium cations on ATO may be enhanced due to ATO's inherent negative charge, as previously observed in a range of pH's.<sup>276</sup> Relative to the rapid, initial adsorption observed, further growth in band intensity, e.g. due to the spontaneous heterolytic decomposition of Im-diazonium species, is negligible.

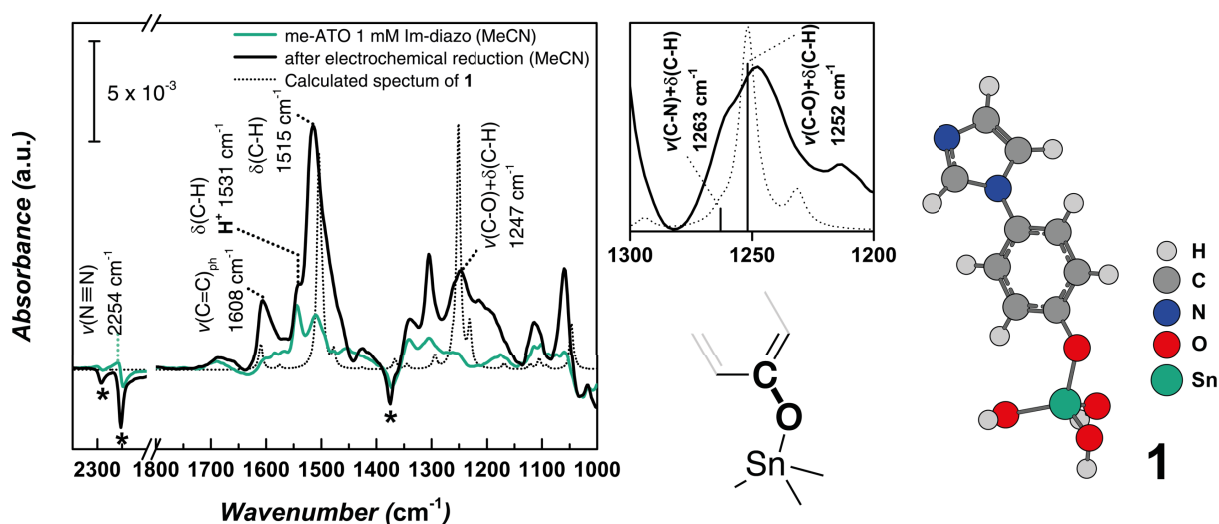


**Figure 39**

ATR-IR absorbance spectrum of me-ATO in a 1 mM solution of Im-diazo (0.1 M TBAF, Acetonitrile) before electrochemical grafting is shown in dark green. The corresponding spectrum in fresh 0.1 M TBAP (without Im-diazo) after electrochemical reduction is shown in black. On the right is the optimised structure of Im-Sn(OH)<sub>4</sub> (**1**), atom labels: carbon (dark grey), hydrogen (light grey), nitrogen (blue), oxygen (red), tin (green). The corresponding IR spectrum of **1** calculated using DFT (dotted line) is shown in black (dashed). The inset displays the overlapping bands at  $1247\text{ cm}^{-1}$  ( $\times 4$ ) overlaid with calculated contributions from  $\nu(\text{C-N})+\delta(\text{C-H})$  and  $\nu(\text{C-O})+\delta(\text{C-H})$  modes. Negative bands resulting from the displacement of acetonitrile molecules from the surface are asterisked.

Electrochemical reduction of Im-diazo was performed by cyclic voltammetry, resulting in a sharp increase in the intensity of the vibrational bands and a disappearance of the  $\nu(\text{N}=\text{N})$  absorption band at  $2254\text{ cm}^{-1}$ . DFT calculations were carried out to assign the experimentally observed vibrational modes. As previously mentioned, it is anticipated that phenyl radicals generated by the electrochemical reduction of diazonium salts will result in the formation of M-O-C bonds (in this case Sn-O-C) at the interface.<sup>215</sup> In order to model such surface-bound species, DFT calculations were run for the compound **1** (see Figure 39), a phenyl-imidazole species bound to an  $\text{Sn}(\text{OH})_3$  cluster *via* a Sn-O-C bond. As can be seen in the IR spectra, there is a reasonably good agreement between the experimental and calculated spectra despite using a small (less expensive) monoatomic Sn hydroxide model to simulate the ATO surface instead of a bigger cluster, such as the larger 9 Ti atom  $\text{TiO}_2$  cluster recently used by Brudvig and co-workers to model a molecular species bound to  $\text{TiO}_2$ .<sup>232</sup> Notable bands assigned here in the spectrum include those at  $1608\text{ cm}^{-1}$ , corresponding preferentially to the aromatic C=C stretching vibration  $\nu(\text{C}=\text{C})_{\text{ph}}$  of the phenyl ring, and those at  $1515\text{ cm}^{-1}$ , corresponding predominantly to the coupled  $\delta(\text{C}-\text{H})$ ,  $\nu(\text{C}=\text{C})_{\text{ph}}$  and  $\nu(\text{C}-\text{N})$  modes of the imidazole ring.

The absorption band intensities appear constant with respect to repeated rinsing in multiple solvents (acetonitrile, dichloromethane, ethanol), strongly indicating that the electrografted diazonium interface is covalently attached to the ATO surface. The inset in Figure 39 shows an absorption centred at  $1247\text{ cm}^{-1}$ , which is composed of two overlapping bands at  $1263\text{ cm}^{-1}$  and  $1252\text{ cm}^{-1}$  corresponding to the  $\nu(\text{C}-\text{N})+\delta(\text{C}-\text{H})$  and  $\nu(\text{C}-\text{O})+\delta(\text{C}-\text{H})$  modes calculated for **1**. This indicates the presence of Sn-O-C bonds at the interface, which supports the assumption that the phenyl radicals bind to surface hydroxyl groups.

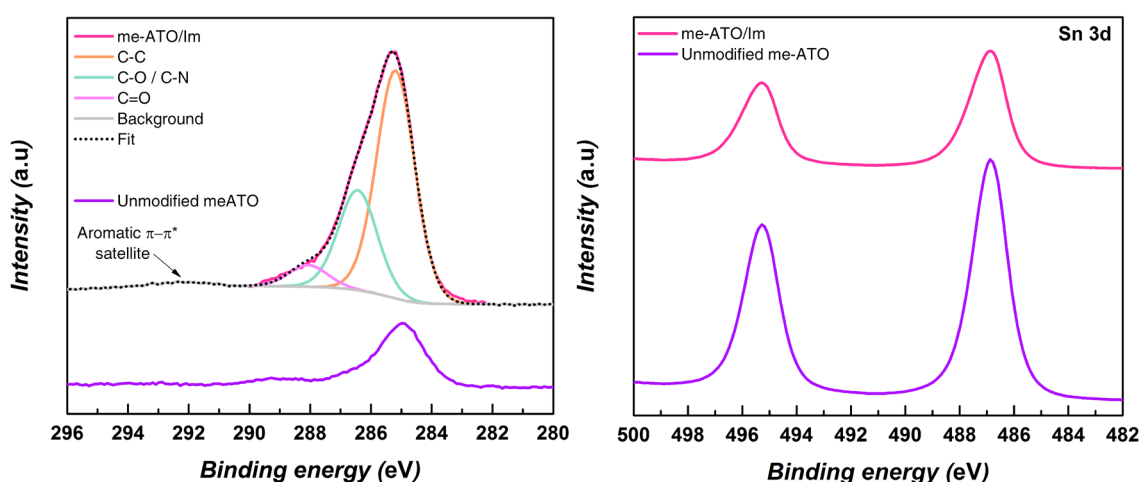


**Figure 40**

The deconvoluted C 1s and Sn 3d XP spectra of me-ATO before and after electrochemical grafting with Im-diazo.

In order to gain further information about the nature of the interface formed between the linker molecule and the ATO, X-ray photoelectron spectroscopy (XPS) measurements were conducted on me-ATO before and after electrochemical grafting with Im-diazo. The samples were freshly

prepared and calcined prior to electrografting and duly stored in flushed, sealed glass containers to reduce the adsorption of adventitious species from the atmosphere. For details on the fitting procedure used to de-convolute the components of the different spectra, see 6.6.3 (page 41). Figure 40 shows the C 1s and Sn 3d spectra of me-ATO before and after electrochemical modification with Im-diazo. XPS is a surface sensitive technique with a limited penetration depth of a few nm's and successful modification of the me-ATO can be inferred from the suppression of the Sn 3d<sub>5/2</sub> and Sn 3d<sub>3/2</sub> peak intensities after modification, and the increase in the C 1s peak intensity. Deconvolution of the C1s signal reveals the presence of peaks that correspond to aliphatic C-C, as well as C-O/C-N, and a  $\pi$ - $\pi^*$  satellite peak at with a binding energy (BE) of around 292 eV indicative of aromatic carbon species.

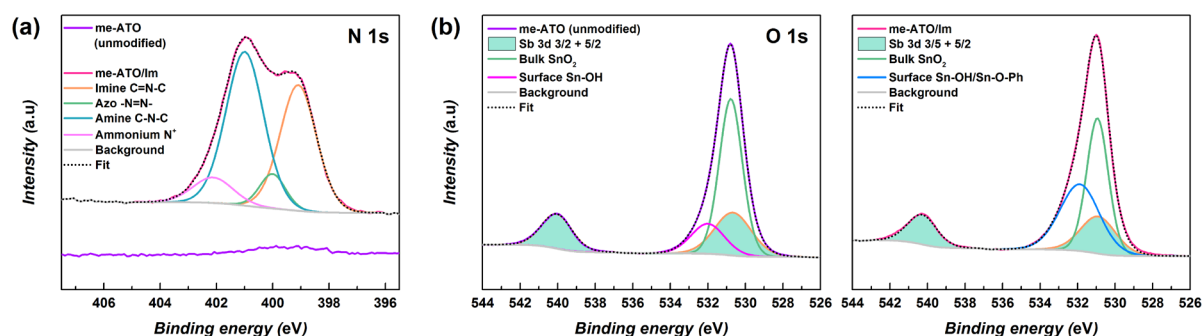
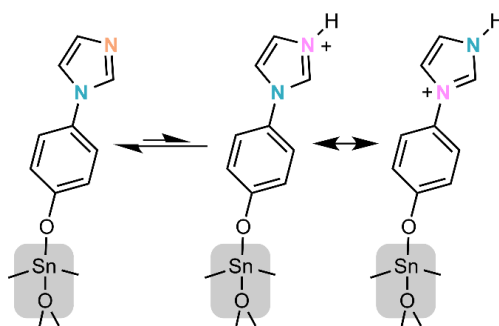


**Figure 41**

The deconvoluted N 1s and O 1s XPS spectra of (a-b) me-ATO before and after electrochemical grafting with Im-diazo.



**Scheme 53**

Scheme illustrating the different chemical environments for the nitrogen atoms present in the protonated and unprotonated linker molecule. The colours of the nitrogen atoms are colour co-ordinated with the corresponding environments in the fitted XP spectra.

**Table 9**

Binding energies (in eV) of the individual deconvoluted components of the N 1s and O 1s spectra recorded for modified and unmodified me-ATO.

	<b>Binding energy (eV)</b>	
	N 1s	O 1s
me-ATO		530.8
		532.0
me-ATO/Im	399.2	530.9
	400.1	531.9
	401.1	
	402.1	

The N 1s and O 1s spectra are shown in Figure 41. The N 1s spectra of me-ATO after electrochemical modification shows peaks at 399.2 and 401.1 eV that can be assigned to the amine and imine nitrogen environments, further indicating the successful grafting of Im-moieties onto the ATO surface (the different chemical environments are illustrated in Scheme 53). The peak with a BE of 402.1 eV is assigned to the iminium environment that results from protonation of imine nitrogen and represents a shift in BE of 2.8 eV. Summing together the atomic percentages imine and iminium nitrogen results in an almost 1:1 ratio with the amine nitrogen and suggests that 14% of the interface molecules are protonated. A peak with a BE of 400.1 eV is assigned to azo-bridges formed as a result of addition of non-reduced diazonium ions to already-grafted species.<sup>221</sup>

XPS studies on ITO modified iodonium salts rule out the formation of In-C or Sn-C bonds at the interface and suggest instead the formation of M-O-C bonds; however, the results are not conclusive due to overlapping signals from the nitro groups in the O 1s spectra.<sup>215</sup> Given the absence of oxygen in the Im-diazo used to modify me-ATO, the O 1s spectrum was fitted in an attempt to observe the Sn-O-C bond. The spectra were fitted taking into account the overlap with the Sb 3d<sub>5/2</sub> peak and the result was a peak at 530.8 eV attributed to the bulk lattice oxygen component and a peak at 532 eV for surface hydroxide oxygen. While the ratio between these peaks does decrease after modification of me-ATO, it was not possible to distinguish any Sn-O-C bonds. Sn-O-C bonds have been previously reported to have a binding energy of 532.2 eV, which is too close to that of oxygen in surface hydroxide species to allow for a clear differentiation.<sup>277</sup>

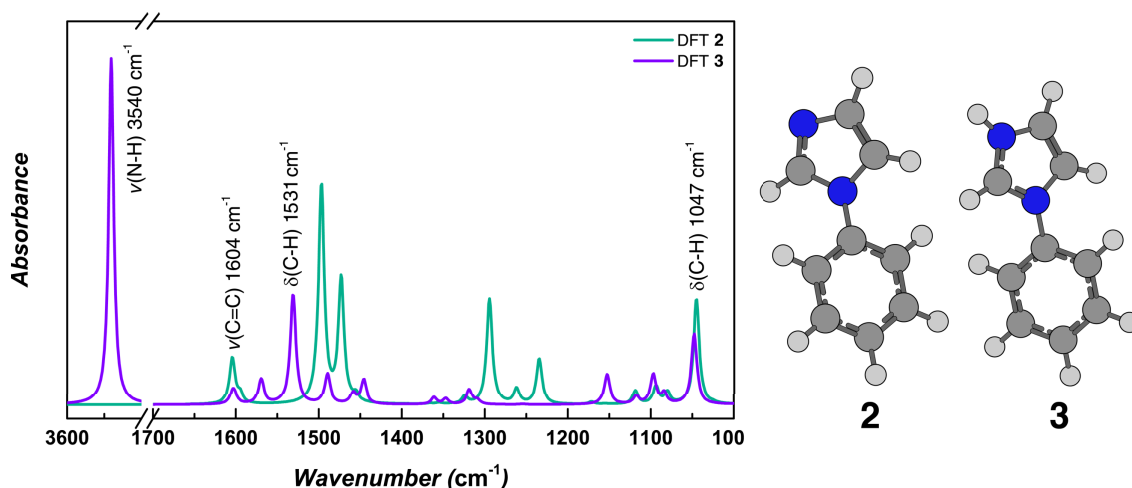


**Figure 42**

IR spectra calculated using DFT of 1-phenyl-1H-imidazole **2** and its protonated imidazolium analogue **3**. Right: optimised structures of **2** and **3**, atom labels: carbon (dark grey), hydrogen (light grey), nitrogen (blue).

IR spectra calculated using DFT of 1-phenyl-1H-imidazole **2** and its protonated imidazolium analogue **3** indicate that distinct bands exist for each species, as shown in Figure 42. The noticeable differences between the spectra of the protonated and unprotonated species are due to the strong coupling of the vibrational modes throughout the molecules. Vibrational modes that

are mostly confined to the phenyl ring, such as the  $\nu(\text{C}=\text{C})_{\text{ar}}$  band at  $1604\text{ cm}^{-1}$  and C-H bending mode  $\delta(\text{C}-\text{H})$  at  $1407\text{ cm}^{-1}$ , remain almost unchanged. New bands appear for the protonated species e.g. at  $3540\text{ cm}^{-1}$  for the N-H stretching mode  $\nu(\text{N}-\text{H})$ , or at  $1531\text{ cm}^{-1}$  for the imidazole-ring C-H bending mode  $\delta(\text{C}-\text{H})$ .

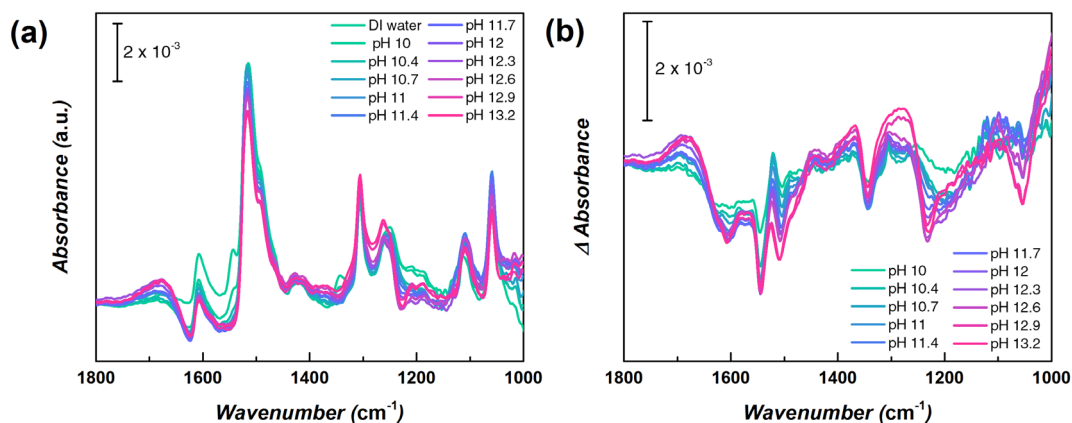


**Figure 43**

(a) ATR-IR absorbance spectra of an Im-interface electrografted on me-ATO in increasingly basic KOH solutions and (b) difference spectra showing the change in absorption  $\Delta A$  of the interfaces in the increasingly basic solutions calculated with respect to the initial spectrum of the interfaces in DI water. The broad negative band around  $1600\text{ cm}^{-1}$  is due to the desorption of water molecules from the surface. pH DI water  $\sim 6$ .

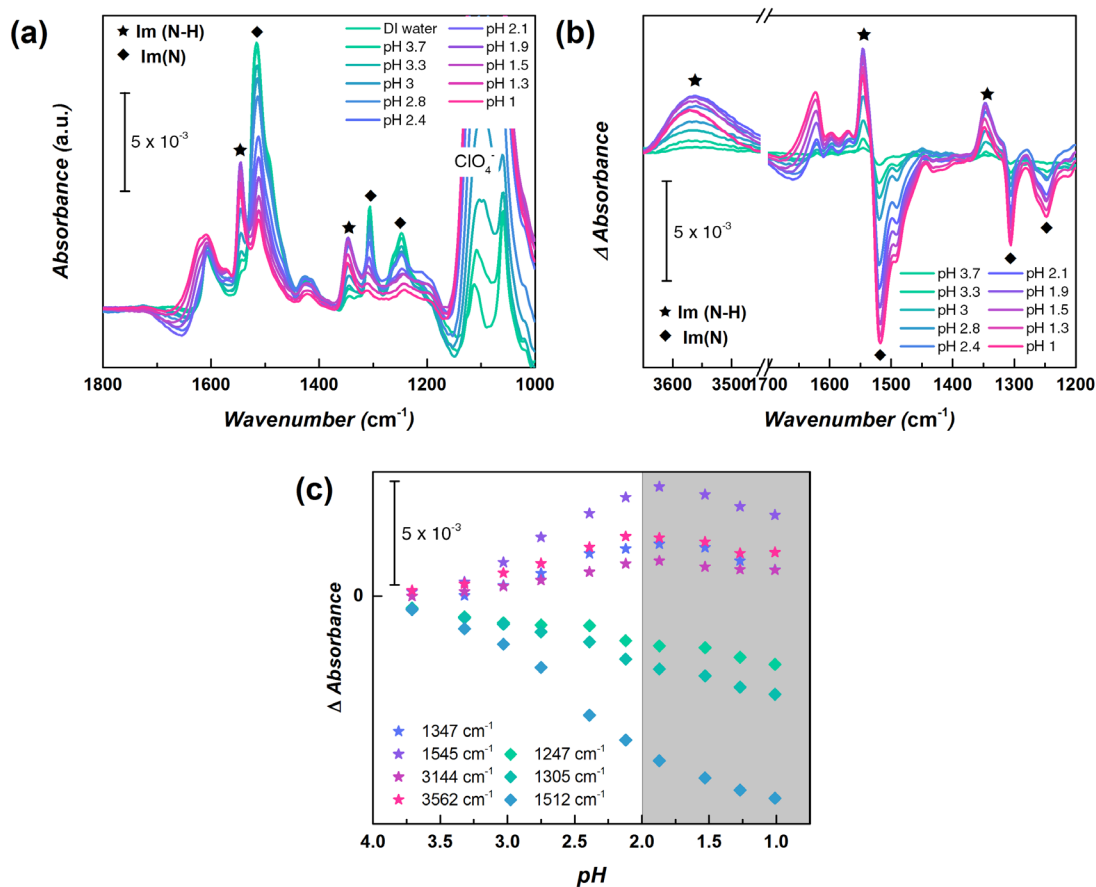


**Figure 44**

(a) ATR-IR absorbance spectra of an Im-interface electrografted on me-ATO in increasingly acidic  $\text{HClO}_4$  solutions and (b) difference spectra showing the change in absorbance  $\Delta A$  of the interfaces in the increasingly acidic solutions calculated with respect to the initial spectrum of the interface in DI water. (c) Plot of intensity  $\Delta A$  as a function of pH. Bands marked with a star or a diamond correspond to vibrational modes of the protonated Im species, **Im(N-H)**, or un-protonated species, **Im(N)**, respectively. pH DI water  $\sim 6$ .

pH dependent spectroscopic stability measurements were conducted in basic and acidic solutions of KOH and HClO<sub>4</sub> (Figure 43 and Figure 44, respectively) to determine the hydrolytic stability window of the electrografted interfaces, which is of paramount importance in catalytic applications. In both cases, difference spectra at each pH were calculated with respect to the initial spectrum recorded for the same interfaces in DI water (pH ~ 6) (Figure 43b and Figure 44b), therefore indicating the change in absorbance  $\Delta A$  at each pH. The differences in the spectra of **2** and **3** calculated by DFT due to protonation of the imidazole are also observed experimentally.

Upon increasing the pH of the solution, an overall decrease in the band intensities corresponding to both the protonated and deprotonated imidazole species can be observed (Figure 43b). The spectra stabilise before slow desorption takes place at very high pH's (>12). Plotting the changes in  $\Delta A$  over pH is somewhat complicated due to shifts in the baseline as the pH changes. Upon decreasing the pH of the solution, the protonation of the imidazole is clearly visible, in particular due to the appearance of the band at 3562 cm<sup>-1</sup>, corresponding to N-H stretching mode  $\nu(\text{N-H})$  of the protonated imidazole ring. Due to the dynamic changes taking place upon changes in pH,  $\Delta A$  was plotted versus pH (Figure 43 c) allowing any desorption of linker molecules or instability in the interface to be followed. There is an increase in  $\Delta A$  for the protonated Im-species (marked by a star) upon decreasing the pH. This decrease is accompanied by a concomitant decrease in  $\Delta A$  for the de-protonated species (marked by a diamond), until a point of inflection is reached around pH 2, beyond which there is an overall decrease in  $\Delta A$  for all species, indicating the removal of the grafted species from the ATO surface. On closer inspection of the plots of  $\Delta A$  as a function of pH, one can see they exhibit a sigmoidal shape (see Appendix 7), which is characteristic for a pH titration. At very low pH's this sigmoidal shape is disrupted due to desorption of the interface.

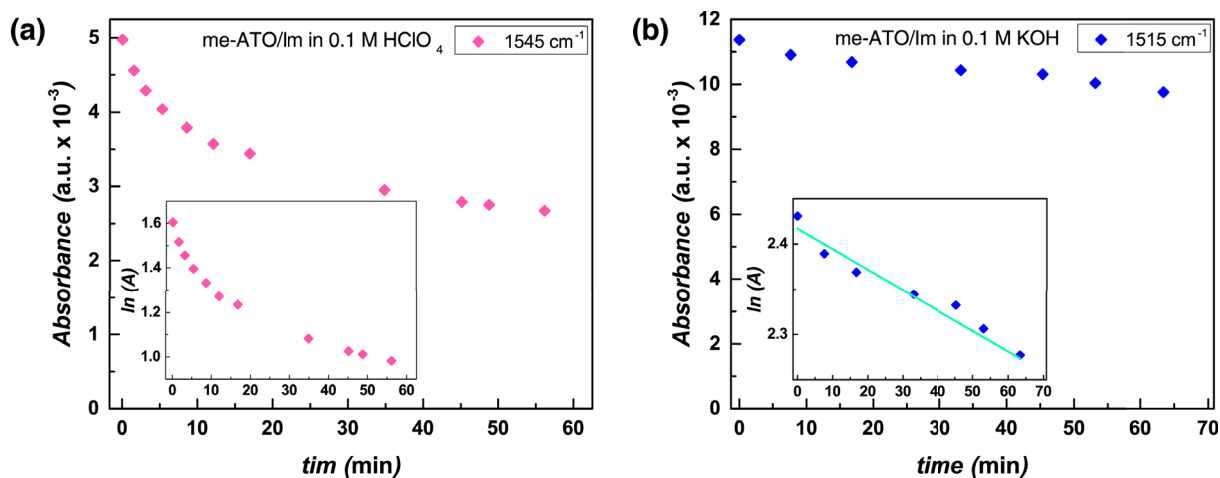


**Figure 45**  
Plots of  $\delta(\text{C-H})$  IR band intensities versus time for Im-interface electrografted on me-ATO in (a) 0.1 M HClO<sub>4</sub> and (b) 0.1 M KOH. The wavenumber of the bands used are indicated in the legend. Plots of the natural logarithm (ln) of the absorbance versus time are shown in the insets.

In order to gain an insight into the desorption of the electrografted interface under acidic and basic conditions and any underlying hydrolytic processes taking place, IR adsorption spectra of freshly prepared interfaces were measured between various time intervals in 0.1 M HClO<sub>4</sub> and in 0.1 M KOH, respectively. The absorbance is proportional to the concentration of molecules in the interface. The absorbance for particular bands were plotted as a function of time in Figure 45a and b, with the bands used to plot the change are indicated in the legend. Under basic conditions (0.1 M KOH) a plot of the natural logarithm (ln) of the absorbance as a function of time is linear (see inset Figure 45b), and therefore exhibits (pseudo-) first-order kinetics with an apparent hydrolysis rate of  $k = 3.77 \times 10^{-5} \pm 0.34 \text{ s}^{-1}$ , which corresponds to a half-life of 5.5. hours. Under acidic conditions (0.1 M HClO<sub>4</sub>) a higher-order reaction takes place (Figure 45a)

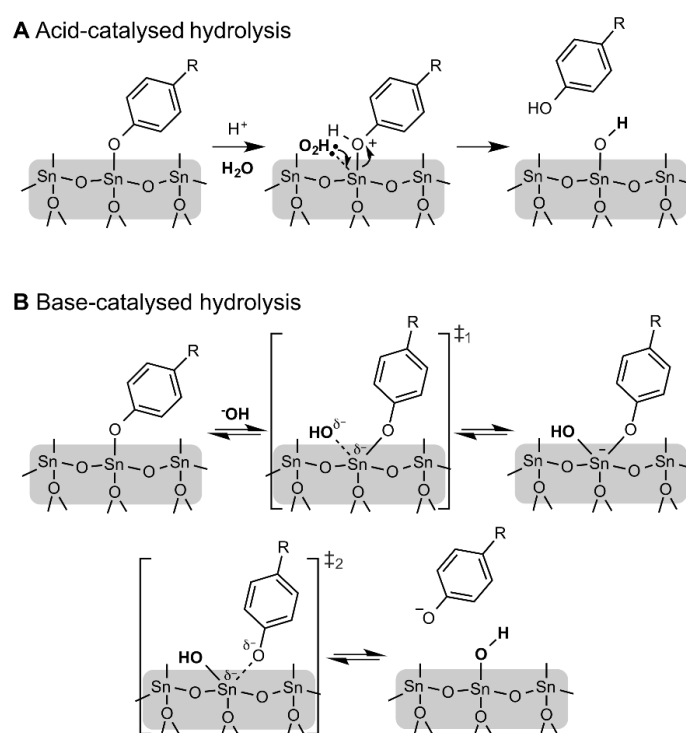


**Figure 46**  
Schematic representation of possible mechanisms for acid-catalysed (A) and base-catalysed (B) hydrolysis of electrografted diazonium interfaces on oxide materials, such as ATO.

Assuming hydrolysis of Sn-O-C bonds at the interface of the ATO, a classical S<sub>N</sub>2-type hydrolysis is not expected to take place, neither under acidic nor basic conditions, because of the impossibility of symmetry inversion at the interface of the bulk SnO<sub>2</sub> and the linker molecule. A more plausible mechanism for acid-catalysed hydrolysis involves flank-side attack of the Sn atom by a water molecule *without* inversion of symmetry, in which the oxygen atom is protonated in a first step, as illustrated by mechanism A in Figure 46 and similar to mechanisms proposed for the hydrolysis of silicates<sup>278</sup>, where Si has a similar Lewis acidity to Sn. A possible mechanism for base-catalysed hydrolysis may involve a similar attack of the Sn atom by a hydroxide anion, resulting in the formation of a 5-coordinate intermediate and a subsequent displacement and removal of the phenoxide anion, again, as also proposed for silicates.<sup>278</sup>

It is expected that hydrolysis rates will differ depending on the nature of the metal to which the molecule is grafted (e.g. Sn/Sb/In/Ti etc.), as well as the type of crystallographic facet to which the anchoring group is bound. In the case where other diazonium salts are used, inductive effects depending on the nature of the phenyl-substituents (in this case imidazole-1-yl) are also expected to affect the reactivity of the Sn-O-C bond towards hydrolysis. It is known that the reactivity of diazonium salts to certain reactions differ depending on the inductive effect of substituents.<sup>181</sup>

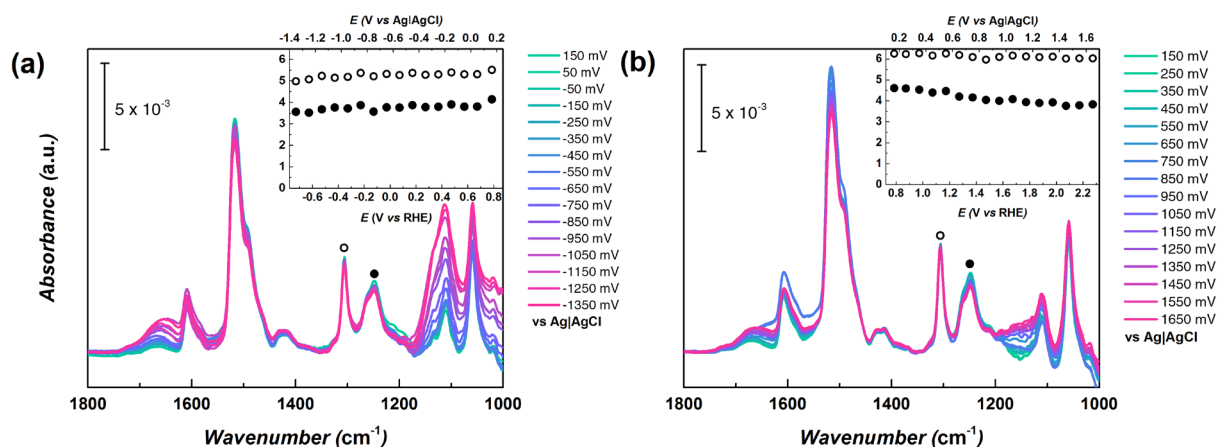


**Figure 47**

ATR-IR absorbance spectra recorded at 163 mV (vs Ag/AgCl 3M) of Im-interfaces electrografted on me-ATO in pH 7 (0.1 M PB) after 2-minute-long applications of increasingly (a) cathodic or (b) anodic potential steps. Inset: plots of band intensities at 1247 and 1306  $\text{cm}^{-1}$  versus applied potential.

Spectroelectrochemical titrations were also carried out in a similar fashion to measure and determine the electrochemical stability window of the electrografted interfaces on ATO at pH 7 (i.e. in 0.1 M PB electrolyte). Different samples were used for the investigation of the cathodic and anodic potential regions. Spectra were recorded at an applied potential of 163 mV (vs Ag/AgCl 3M), which is close to the initial OCP of the functionalised ATO electrode, after having applied an increasingly positive or negative potential step for 2 minutes each (Figure 47 a and b). The band intensities of two  $\delta(\text{C-H})$  modes at 1247 and 1306  $\text{cm}^{-1}$  are plotted versus the applied potential in the insets of Figure 47. These plots indicate only a small decrease in intensity over the measured potential ranges. This decrease may be attributed to the loss of physisorbed species, as has been previously reported for other electrografted diazonium interfaces<sup>215,275</sup>, or simply to small changes in the baseline. The electrochemical cleavage of the Au-C interfacial bond in electrografted diazonium interfaces on gold was observed as a rapid decrease in absorbance intensities in the IR spectra, as shown in Figure 7e in 7.3, and is not observed in this case. The electrografted diazonium interfaces on ATO studied here therefore exhibit high stabilities in a broad potential window (at least -0.73 to 2.23 V vs RHE) at pH 7 (0.1 M PB) that encompasses the intrinsic electrochemical stability window of ATO (-0.77 to 1.83 V vs RHE) measured at pH 7 (0.1 M PB) (see Appendix 8). This also encompasses the stability window of ITO and FTO electrode materials (-0.62 to 1.96 V vs RHE and -0.51 to 1.73 V vs RHE,

respectively, as determined by Jaramillo and co-workers) in neutral electrolyte (0.1 M sodium acetate).<sup>226</sup> The stability of these electrografted diazonium interfaces in such a wide potential window broadens the possibilities for conducting electrocatalysis using covalently immobilised species on TCO materials.

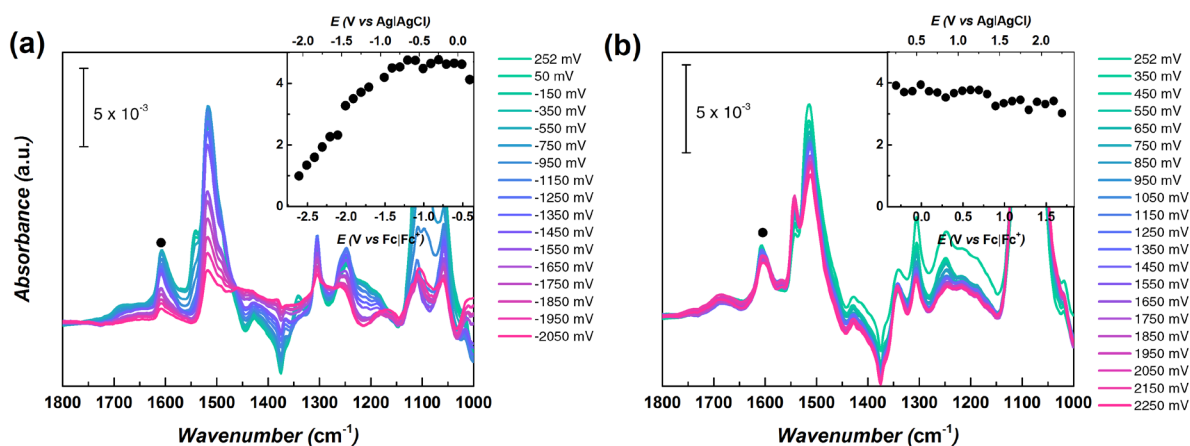


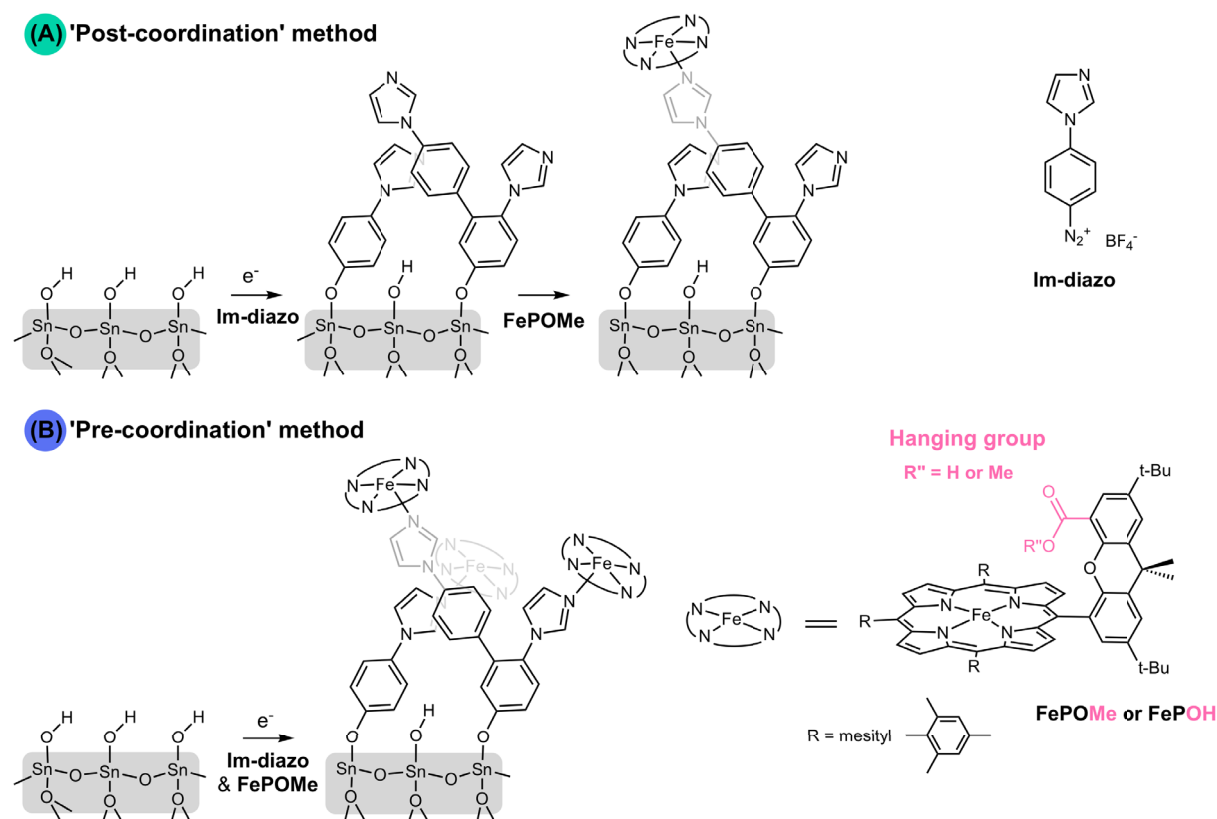
**Figure 48**

ATR-IR absorbance spectra of Im-interfaces electrografted on me-ATO in acetonitrile (0.1 M TBAP) after 2-minute-long applications of increasingly (a) cathodic or (b) anodic potential steps. Insets: plots of the corresponding band intensities at 1608 cm<sup>-1</sup> versus applied potential.

Further measurements were conducted in organic media (acetonitrile, 0.1 M TBAP), as shown in Figure 48 a and b. The interface is stable over the entire anodic potential range probed from at least 1.6 V until -1.3 V (vs Fc/Fc<sup>+</sup>), after which desorption is observed.

To summarise, *in situ* IR spectroscopic and spectroelectrochemical methods were used to determine the hydrolytic and electrochemical stability windows of electrografted diazonium interfaces on ATO. Previous attempts to probe the stability of interfaces on oxides applied mainly UV-Vis spectroscopy or electrochemical techniques.<sup>25,36,231,279,280</sup> Using instead *in situ* IR spectroscopy allows one to probe the hydrolytic and electrochemical stability of an anchoring group without having to rely on chromophoric or electroactive components (which may themselves be unstable for other reasons) and allows the intrinsic stability of specific linker/anchoring groups to be determined. The high surface area of the me-ATO films leads to very high IR absorption band intensities that usually can't be obtained without some surface/plasmonic enhancement, as is the case for the Au SEIRA electrodes. For comparison, the IR absorbance spectra obtained for planar ITO films in chapter 5 just about allow for characterisation of interfaces formed at their surface.

## 6.4 Fe-Hangman complexes immobilised on planar and porous TCOs using the electrografting of a diazonium salt for oxygen reduction reaction



**Scheme 54**

Scheme depicting the different immobilisation strategies employed for grafting/immobilising FePOME on an electrode: (A) a two-step 'post-coordination' process whereby the electrode is first electrochemically grafted with a linker molecule Im-diazo, followed by incubation with FePOME, and (B) a one-step 'pre-coordination' process where the electrode is electrochemically grafted with Im-diazo and FePOME together. The chemical structure of the iron Hangman porphyrins is depicted by 1.

As previously mentioned, hangman porphyrin complexes contain a heme-group with a rigid xanthene scaffold at one of the meso-positions that contains a "hanging" group, which may introduce certain non-covalent interactions in the second coordination sphere that can alter the behaviour or activity of the complex.<sup>129,251</sup> Iron hangman porphyrins containing a carboxylic acid or methyl ester group (hereby denoted FePOH and FePOME, respectively) were synthesised per published procedures in the group of Dr. M. Schwalbe.<sup>127,128</sup> The same complexes were previously immobilised on SAM-coated silver and gold electrodes by Ly et al<sup>251</sup>, whereby it was suggested that the acid group takes part in a proton coupled electron transfer reaction that may be beneficial in ORR. For these immobilisation studies on TCOs, the ester-containing FePOME was used in order to exclude the possibility of the porphyrin binding to oxide surfaces *via* the carboxylic acid hanging group.

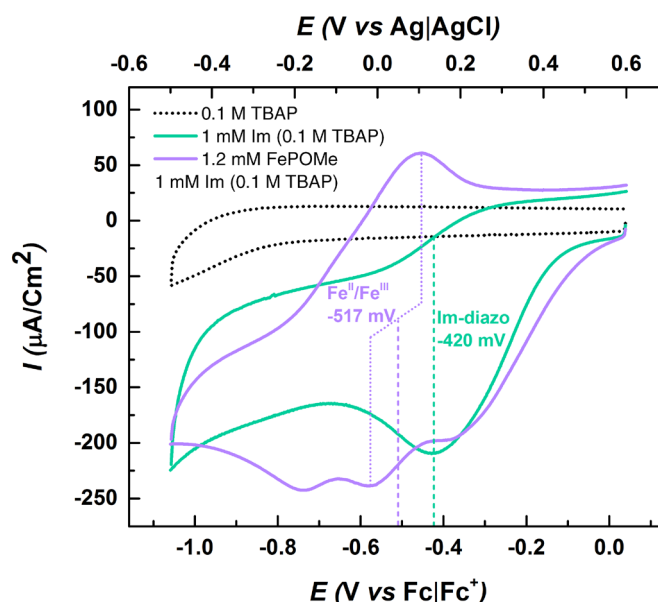


**Figure 49**

CVs of 1 mM solutions of Im-diazo in acetonitrile (0.1 M TBAP) using me-ATO as a working electrode, with (purple trace) and without (green trace) addition of 1.2 mM FePOMe. Scan rate = 50 mV/s.

Two distinct immobilisation strategies were developed and employed for immobilising FePOMe on me-ATO: (A) a two-step ‘post-coordination’ process whereby me-ATO is first electrochemically grafted with 1 mM Im-diazo in acetonitrile (in a fashion similar to that done in 9.3), thereby providing a ‘ligand’ terminated interface for axial coordination through the imidazole, followed by incubation with 1.2 mM FePOMe (Scheme 54A); and (B) a one-step ‘pre-coordination’ process whereby me-ATO is electrochemically grafted with 1 mM Im-diazo and 1.2 mM FePOMe together, after mixing them for 5 min i.e. pre-coordinating the iron centre to the axial ligand (Scheme 54B). In each case, a potential of -0.42 V (vs  $\text{Fc}/\text{Fc}^+$ ) is applied to the me-ATO working electrode for 120 s, corresponding to the reduction potential of Im-diazo. CVs of 1 mM Im-diazo in acetonitrile (0.1 M TBAP), as well as 1 mM Im-diazo and 1.2 mM FePOMe in acetonitrile (0.1 M TBAP), using me-ATO as a working electrode are shown in Figure 49. An irreversible Im-diazo reduction peak is clear in the trace for a 1 mM Im-diazo solution, while the trace for a 1 mM Im-diazo and 1.2 mM FePOMe solution shows the Im-diazo reduction peak overlapping with the reversible redox peak for the  $\text{Fe}^{2+}/3+$  couple of the FePOMe.

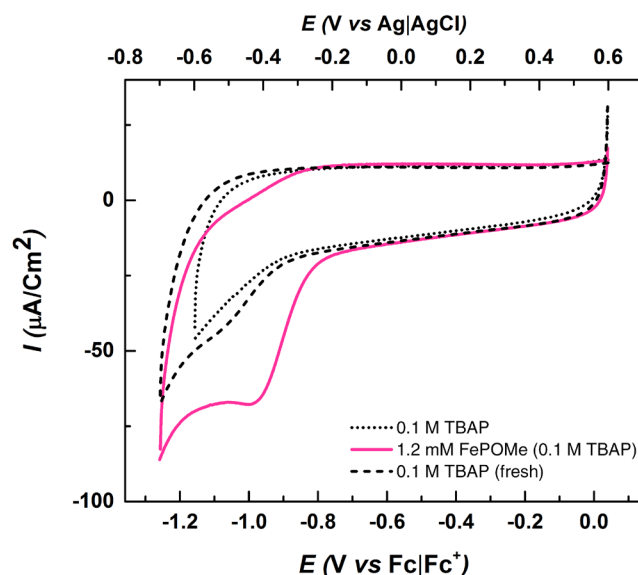


**Figure 50**

CVs of a 1.2 mM solution of 1.2 FePOMe in acetonitrile (0.1 M TBAP) using me-ATO as a working electrode (pink trace). The electrode was rinsed with acetonitrile and a second blank CV was recorded (dashed black trace). Scan rate = 50 mV/s.

A CV of 1 mM FePOMe without any Im-diazo is shown in Figure 50. A semi-reversible redox peak for the  $\text{Fe}^{2+/3+}$  couple that is around 0.3 V more negative than that measured in the presence of Im-diazo. It was shown for iron protoporphyrin IX immobilised on either pristine MWCNTs (*via* pi-stacking) or on imidazole-functionalised polypyrrole coated MWCNTs (*via* axial coordination to the pyrrole) that the  $\text{Fe}^{2+/3+}$  redox potential shifts by 0.1 V to more positive potentials upon coordination with the imidazole terminated surface.<sup>281</sup> The 0.3 V shift to more positive potentials for the FePOMe in the presence of Im-diazo can thus be attributed to the coordination and/or immobilisation of the FePOMe by Im-species, as well as the otherwise weak or repulsive interaction between the hydrophobic uncoordinated FePOMe and the hydrophilic oxide surface. After rinsing the electrode with acetonitrile and applying another CV, it is possible to see that no FePOMe adsorbed onto the surface of the unmodified ATO.

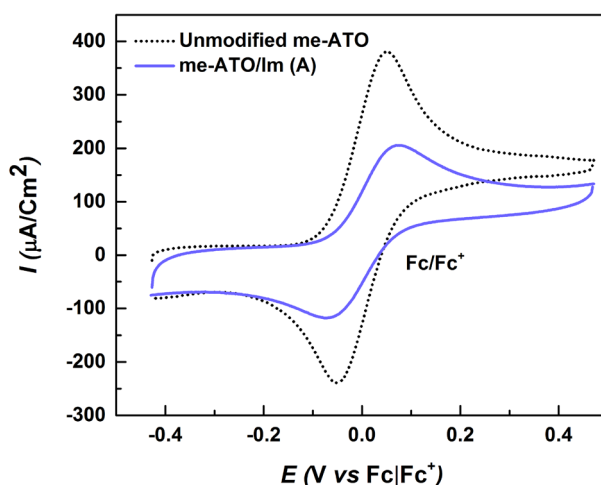


**Figure 51**

CVs of 1 mM ferrocene in acetonitrile (0.1 M TBAP) using unmodified me-ATO and me-ATO electrografted with Im-diazo using -0.42 V (vs  $\text{Fc}/\text{Fc}^+$ ) for 120 s. Scan rate = 50 mV/s.

Copious rinsing in acetonitrile and dichloromethane is used to remove non-covalently bound species. Passivation of a me-ATO electrode electrochemically grafted with Im-diazo (i.e. before incubating with FePOMe) is indicated by comparative CV measurements of an unmodified me-ATO electrode and an electrografted me-ATO electrode in the presence of the ferrocene/ferrocenium ( $\text{Fc}/\text{Fc}^+$ ) redox probe (Figure 51). In addition to an increase in peak separation  $\Delta E_p$ , a significant decrease of 52% in the ferrocene oxidation current is observed for the electrografted me-ATO electrode, confirming the passivation of the ATO surface.

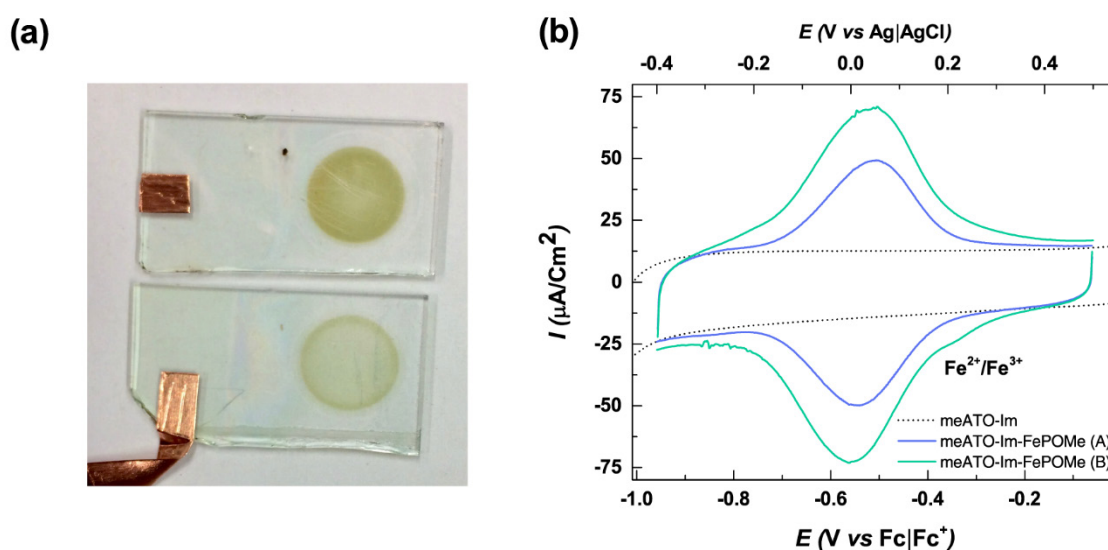


**Figure 52**

(a) Photograph of me-ATO coated pl-ITO electrodes after immobilisation of FePOMe using the ‘pre-coordination’ (top) or ‘post-coordination’ method (bottom) and (b) CVs in acetonitrile (0.1 M TBAP) of FePOMe immobilised on me-ATO electrografted using the ‘post-coordination’ method (labelled A, green trace) and the ‘pre-coordination’ method (labelled B, blue trace). Scan rate = 50 mV/s.

Both the ‘post-coordination’ and ‘pre-coordination’ methods for immobilising FePOMe on me-ATO result in a dark brown colouration of the films that is resistant to rinsing and soaking in acetonitrile and dichloromethane, with a darker colour achieved using the ‘pre-coordination’ approach (see photograph in Figure 52a and UV-Vis spectra in Figure 60). The darker colour and higher adsorption in the UV-Vis spectra indicate a higher loading of FePOMe using the ‘pre-coordination’ approach.

CVs in acetonitrile of me-ATO modified *via* ‘post-coordination’ (method A) and ‘pre-coordination’ (method B) are shown in Figure 52b. The CVs stabilise over several cycles and show reversible redox peaks close to 0.56 V vs.  $\text{Fc}/\text{Fc}^+$  for the  $\text{Fe}^{2+/3+}$  redox couple of the immobilised FePOMe. Peak currents ( $I_p$ ) increase linearly with applied scan rate for species immobilised *via* both the ‘post-coordination’ and ‘pre-coordination’ methods (Figure 53 a and b, respectively), as expected for electron transfer to and from a surface-bound redox species.

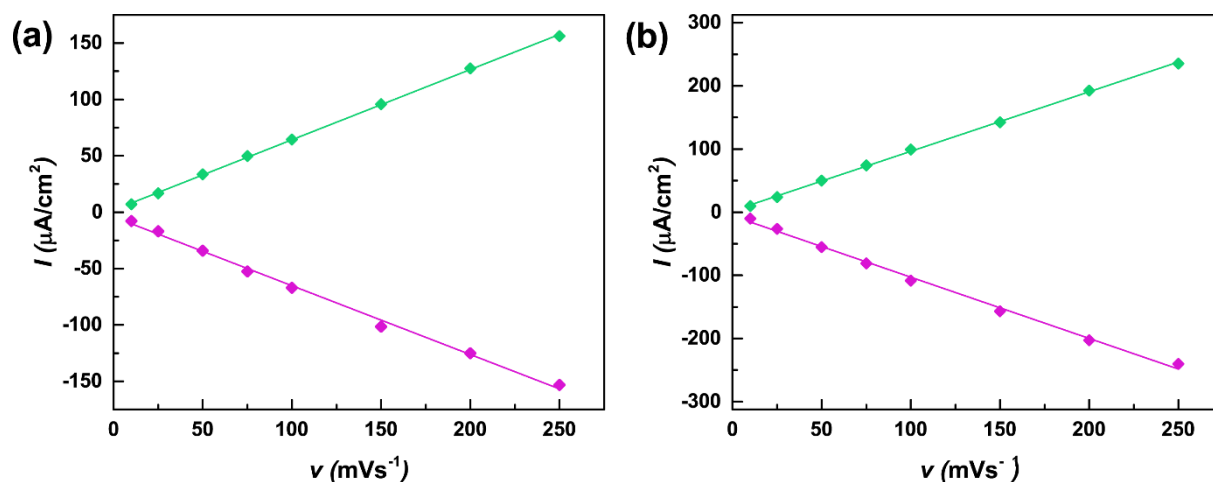


**Figure 53**

Plot of peak currents  $I_p$  vs scan rates  $v$  for FePOMe immobilised on me-ATO via (a) the 'post-coordination method' and (b) 'pre-coordination' method.

Surface coverages of electrochemically accessible FePOMe,  $\Gamma_{\text{FePOMe}}$ , were calculated from background subtracted CVs and found to be  $1.5$  and  $3.0 \times 10^{-9}$  mol.cm $^{-2}$  for 'post-coordination' method and 'pre-coordination' method, respectively. The electrochemically accessible coverage of FePOMe will henceforth be denoted by  $\Gamma_{\text{CV}}$  to distinguish it from the coverage measured using UV-Vis spectroscopy,  $\Gamma_{\text{UV}}$ . As previously stated, electron transfer (ET) through insulating organic interfaces proceeds *via* a tunnelling mechanism, in which the ET rate  $k_{\text{ET}}$  decays exponentially with the distance between the redox centre and the electrode surface.<sup>282</sup> It is well known that electrochemical reduction of diazonium salts often leads to thick and often insulating polymeric interfaces films on a broad range of materials<sup>45,55</sup>, as was observed on gold electrodes in chapter 4, and ITO electrodes in chapter 5. Phosphonates, however, bind selectively to surface oxide sites, meaning that interface formation is self-limiting and that multilayers of chemisorbed phosphonate species do not readily form. The values of  $\Gamma_{\text{CV}}$  obtained here for Im-diazo are in line with those reported in the literature for molecular catalysts immobilised on other porous oxide electrode materials using phosphonates, when taking into consideration differences in film thicknesses (catalyst loading increases linearly with the film thickness). A comparison between the values obtained here and those obtained in the literature (using electrochemical or spectroscopic means) are summarised in Table 10.

**Table 10**

A comparison between surface coverages  $\Gamma_{CV}$  of molecular catalysts and redox species on different porous oxide electrodes of different film thicknesses from the literature.

<b>Redox species</b>	<b>Electrode</b>	<b>Film thickness (<math>\mu\text{M}</math>)</b>	<b>Coverage (<math>\times 10^{-9} \text{ molcm}^{-2}</math>)</b>	<b>Volume coverage (<math>\times 10^5 \text{ molcm}^{-3}</math>)</b>	<b>Ref.</b>
<i>[Ru(bpy)<sub>2</sub>(4,4'-PO<sub>3</sub>H<sub>2</sub>-bpy)](PF<sub>6</sub>)<sub>2</sub></i> - Phosphonate	Porous ITO	0.55	5.5	~ 10	283
		2.5	25		
		15.7	160 (UV-Vis)		
<i>[Co<sup>III</sup>Br<sub>2</sub>{(DO)(DOH)pn}]</i> - Phosphonate	Porous ITO	13	~ 150 (UV-Vis)	~12	70
Various Co catalysts - Phosphonate	Porous ITO	13	22 – 28 (CV)	~ 2	247
<i>[Ru(Mebimpy)(4,4'-((HO)<sub>2</sub>-OPCH<sub>2</sub>)<sub>2</sub>bpy)(OH<sub>2</sub>)<sub>2</sub>]<sup>+</sup></i> - Phosphonate	Porous TiO <sub>2</sub>	~ 10	53 (UV-Vis)	~ 5.3	234
<i>Ni<sup>II</sup> bis(diphosphine) complex</i> - Phosphonate	Porous TiO <sub>2</sub>	4	146 (UV-Vis)	~ 37	227
<i>fac-[MnBr(4,4'-bis(PO<sub>3</sub>H<sub>2</sub>)-2,2'-bipyridine)(CO)<sub>3</sub>]</i> - Phosphonate	Porous TiO <sub>2</sub>	6	34 (UV-Vis)	~ 6	173
<i>[Ru<sup>II</sup>(Mebimpy)(4,4'-PO<sub>3</sub>H<sub>2</sub>)<sub>2</sub>bpy)(OH<sub>2</sub>)<sub>2</sub>]<sup>2+</sup></i> - Phosphonate	Mesoporous ATO	2	248 (UV-Vis)	~ 12	267
			1.58 (CV)	~ 8	
<i>Ferrocene carboxylic acid (via amide-coupling to 3-aminopropyltriethoxysilane)</i> - Silane	Mesoporous ATO	0.21	0.9 – 0.6 (CV)	~ 3	240
<i>FePOMe ('post-coordination')</i> - Diazonium	Mesoporous ATO	0.16	1.5 (UV-Vis)	~ 9.4	This work
			1.5 (CV)	~ 9.4	
<i>FePOMe ('pre-coordination')</i> - Diazonium	Mesoporous ATO	0.16	3.9 (UV-Vis)	~ 24	This work
			3.0 (CV)	~ 19	

Coverages ( $\Gamma_{UV}$ ) of FePOMe were also calculated for the same me-ATO electrodes using UV-Vis spectroscopy.  $\Gamma_{UV}$  of 1.2 and 3.2  $\times 10^{-9}$  molcm<sup>-2</sup> were determined for the 'post-coordination' and 'pre-coordination' methods, respectively. These values are in line with those calculated using CVs ( $\Gamma_{CV}$ ) and suggest that all of the immobilised species are electrochemically accessible using the 'post-coordination' method, while around 75% of the species immobilised using the 'pre-coordination' method are electroactive.

Full-widths at half maximum (FWHMs) of the oxidation and reduction waves,  $E_{a \text{ fwhm}}$  and  $E_{p \text{ fwhm}}$ , accounting for 199 and 197 mV for 'post-coordination' and 210 and 211 mV for 'pre-coordination', respectively, are found to be greater than the theoretical 90.6 mV<sup>17</sup> expected for a 1-electron transfer process. For increased coverages, broadening of the FWHMs of the oxidation and reduction wave are indicative of so-called surface charge effects, which are electrostatic

intermolecular interactions between charged species.<sup>284</sup> Such behaviour has previously been reported for immobilised porphyrins on silicon.<sup>285,286</sup> As can be seen in Figure 52b, the slightly broadened FWHMs observed in case of the ‘pre-coordination’ method are in line with the higher electroactive porphyrin loading  $\Gamma_{CV}$  and may as such indeed be related to enhanced crowding. In addition, broadening may also reflect a certain heterogeneity of the imidazole coordination sites.

Given the propensity for diazonium salts to form thick interfaces during electrochemical grafting of electrode surface, it is reasonable to expect that ‘pre-coordination’ with FePOMe would lead to high values of  $\Gamma_{CV}$  due to the electrografting of pre-coordinated species directly at the surface. This would lead to a more even distribution of FePOMe species through the interface, as well as reduce the distance between the FePOMe redox centres and the electrode surface compared to the ‘post-coordination’ method, in which FePOMe coordinate on top of the already electrografted Im-interface in a ‘monolayer-like’ fashion. If the Im-interface is too thick in the latter case, then the charge transfer resistance might become too great to and could lead to low values of  $\Gamma_{CV}$ . The similarity between the values of  $\Gamma_{CV}$  obtained on the me-ATO using both methods, which are also in line with values of  $\Gamma_{CV}$  obtained using phosphonates in the literature, suggest that thin interfaces are electrografted on me-ATO from Im-diazo (even in the absence of FePOMe). This compares to the thick, insulating interfaces previously electrografted on planar gold and ITO, and may result from diffusion limitation of Im-diazo inside the porous structure of the high-surface area me-ATO during the electrochemical modification step, thereby limiting the interface thickness formed.

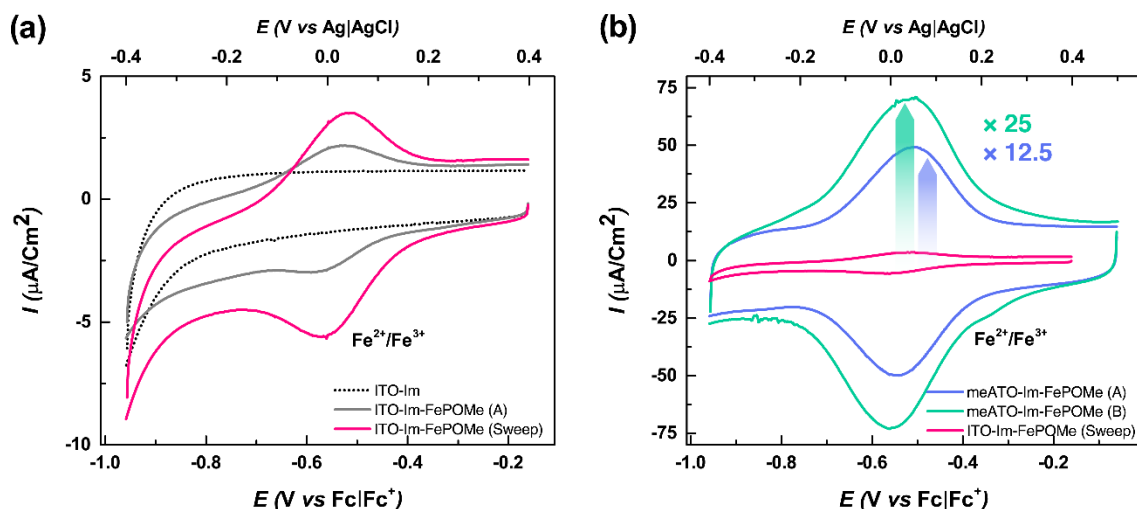


**Figure 54**

CVs in acetonitrile (0.1 M TBAP) of FePOMe immobilised on (a) pI-ITO using the ‘post-coordination’ method at constant potential (labelled A, grey trace) or with a linear sweep (labelled Sweep, pink trace). (b) CVs comparing the current densities obtained for FePOMe immobilised on pI-ITO and me-ATO (blue and green). Scan rate = 50 mV/s.

Applying the ‘post-coordination’ method on planar ITO (pI-ITO) results in a  $\Gamma_{CV}$  of  $0.5 \times 10^{-10}$  mol  $\text{cm}^{-2}$ , which is 12% of the value expected for a perfectly packed monolayer of hangman porphyrin species on a planar surface ( $4.2 \times 10^{-10}$  mol  $\text{cm}^{-2}$  – as calculated from dimensions<sup>129</sup> determined

using single crystal X-ray crystallography) and indeed indicates the electrografting of a thick, insulating interface (grey trace, Figure 54a). In the case of ITO, a potential of -0.56 V (vs Fc/Fc<sup>+</sup>) was applied due to the more negative reduction potential of Im-diazo on ITO (Appendix 9), which is approximately 0.14 V more negative than that observed on ATO. Applying instead a linear sweep from 0.04 V to -0.86 V (vs Fc/Fc<sup>+</sup>) at 50 mV/s in the same concentration of Im-diazo in acetonitrile results in a reproducible  $\Gamma_{CV}$  of  $1.2 \times 10^{-10}$  molcm<sup>-2</sup> (pink trace, Figure 54a), equivalent to 29% of a monolayer of FePOMe. This value is in line with coverages given in literature for molecular catalysts immobilised on planar ITO and FTO using phosphonate anchoring groups.<sup>234,267,283</sup> Values of  $\Gamma_{CV}$  on ITO may be especially limited by electrochemical ‘dead spots’.<sup>35,287</sup> As is the case for me-ATO,  $I_p$  increase linearly with scan rate (Figure 57 b), as expected for a surface-bound species.

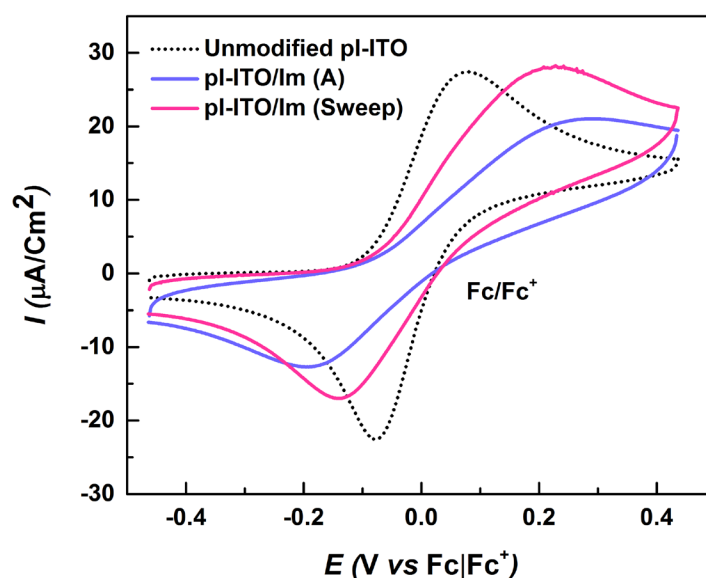


**Figure 55**

CVs of 0.1 mM ferrocene in acetonitrile (0.1 M TBAP) using unmodified pl-ITO and pl-ITO modified with Im-diazo after applying a constant potential of -0.56 (vs Fc/Fc<sup>+</sup>) for 120 s (violet trace) or linear sweep voltammetry from 0.04 V to -0.86 V (vs Fc/Fc<sup>+</sup>) (pink trace). Scan rate = 50 mV/s.

CVs of the ferrocene/ferrocenium (Fc/Fc<sup>+</sup>) redox probe before and after electrografting of pl-ITO with Im-diazo using either electrochemical reduction at constant potential (-0.56 V vs Fc/Fc<sup>+</sup>) or the application of a linear sweep from 0.04 V to -0.86 V (vs Fc/Fc<sup>+</sup>) show a decrease in the ferrocene oxidation current of 61% and 29%, respectively. The lower decrease in current for the sweep method indicates the electrografting of a thinner, less insulating interface. This, along with the results obtained on mesoporous ATO, strongly suggests that a slower interface formation is necessary to obtain high  $k_{ET}$  for immobilised species, whether it be a result of diffusion limitation in a porous material or applied potential.

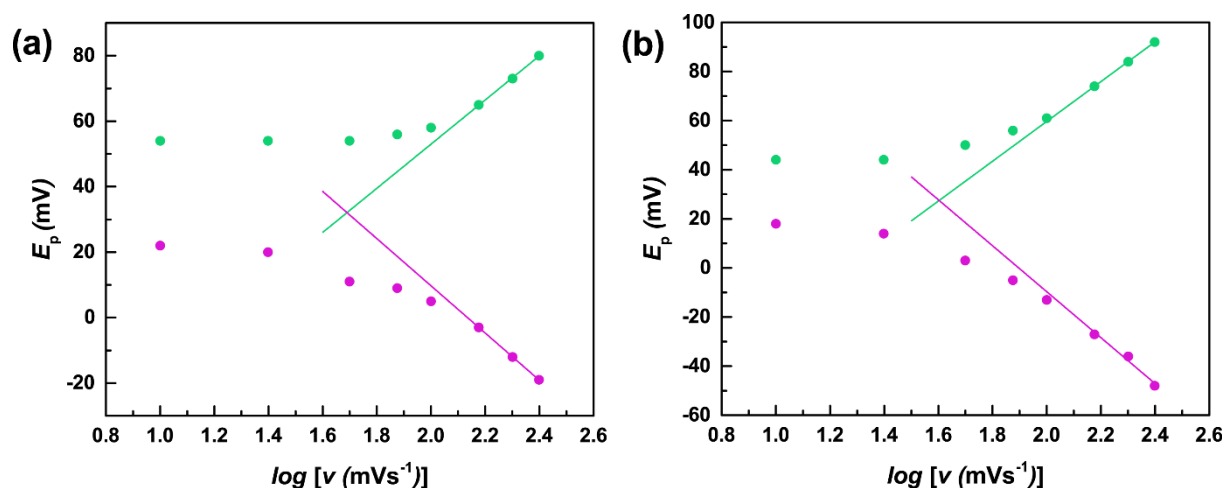


**Figure 56**

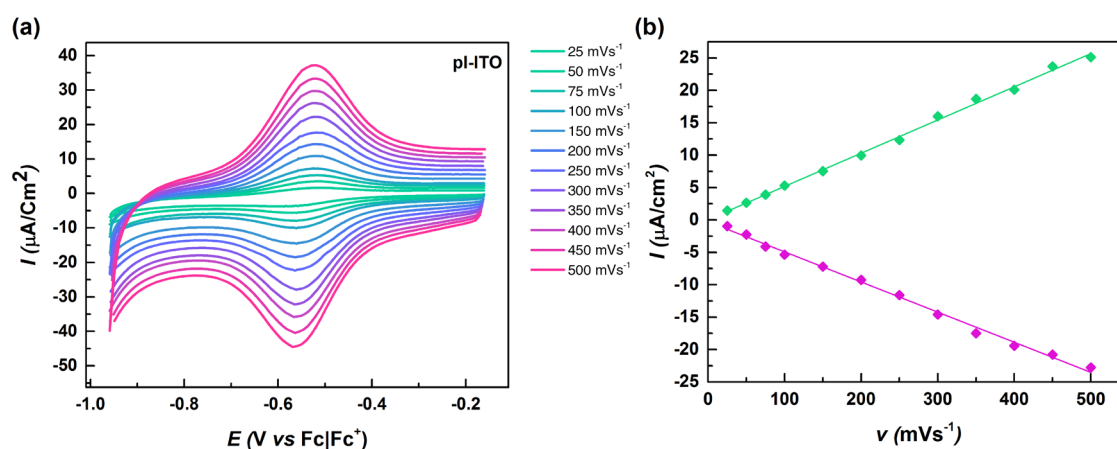
Plots of peak separation  $\Delta E_p$  vs the log of the scan rate  $\log(v)$  for the  $\text{Fe}^{(2+/3+)}$  redox couple of FePOMe immobilised on me-ATO modified *via* (a) 'post-coordination' and (b) 'pre-coordination'.

CVs of the FePOMe species immobilised on me-ATO were conducted at different scan rates (Appendix 10). Peak separations  $\Delta E_p$  for the  $\text{Fe}^{(2+/3+)}$  couple recorded at 10 mV/s for me-ATO modified using 'post-coordination' and 'pre-coordination' are small (26 mV and 32 mV, respectively), while at higher scan rates they deviate from a linear relationship (Figure 56a and b), indicating a kinetic limitation. Theoretically  $\Delta E_p$  should be zero for redox processes at low scan rates; however,  $\Delta E_p$  increases as the scan rate increases and the time taken to scan through the peak becomes comparable or faster than the electron transfer rate.<sup>284</sup> The apparent electron transfer rate constants  $k_c$  and  $k_a$  for the cathodic and anodic peaks, as well as the electron transfer coefficients  $\alpha_c$  and  $\alpha_a$ , were calculated using mathematical treatments devised by Laviron.<sup>288</sup> 'Post-coordination' results in  $k_c = 4.4 \pm 0.7 \text{ s}^{-1}$ ,  $\alpha_c = 0.62$ ,  $k_a = 2.9 \pm 0.1 \text{ s}^{-1}$  and  $\alpha_a = 0.28$ , while 'pre-coordination' results in  $k_c = 4.9 \pm 0.1 \text{ s}^{-1}$ ,  $\alpha_c = 0.81$ ,  $k_a = 2.8 \pm 0.1 \text{ s}^{-1}$  and  $\alpha_a = 0.14$ . The unsymmetrical energetic barrier for electron transfer, as indicated by  $\alpha$ , can be explained by structural changes to the porphyrin, e.g. the axial ligation, upon changes in the Fe-centre oxidation state. The electron transfer rates calculated here are in line with those obtained for other redox systems that are immobilised on nanostructured metal oxide electrodes (see comparisons to literature in Table 11), including Fe-porphyrin containing Fe-mimochrome ( $4 \text{ s}^{-1}$ ) or microperoxidase-11 ( $10 \text{ s}^{-1}$ ) immobilised on nanostructured ITO electrodes<sup>289,290</sup>, microperoxidase-11 ( $1.5 \text{ s}^{-1}$ ) immobilised on mesoporous ATO.<sup>291</sup> Attempts to compare the ET behaviour of FePOMe immobilised on me-ATO *via* the carboxylic acid anchoring group of the analogous, carboxylic acid-containing linker molecule 4-(1H-imidazol-1-yl)benzoic acid failed, presumably due to the instability of the anchoring group. A similar attempt in the literature to immobilise a ruthenium dye on me-ATO using a carboxylic acid failed for the same reason.<sup>292</sup>

**Table 11**

A comparison of the redox potentials  $E_0$  and electron transfer rates ( $k_{ET}$ ) for the  $Fe^{(2+/3+)}$  redox couple of the system presented here and different molecular/enzymatic redox species from literature immobilised on different porous oxide electrodes of different film thicknesses. Potentials are given versus RHE and were calculated using the Nernst equation.

Redox species	Electrode	Film thickness ( $\mu M$ )	$E^\circ(Fe^{2+/3+})$ (V vs RHE)	$k_{ET}$ ( $s^{-1}$ )	Ref.
Cytochrome C	Mesoporous ITO	0.17	0.425	1.2	202
Cytochrome C	Mesoporous ITO	2	0.670	12	204
Fe mimochrome	Mesoporous ITO	1	0.274	4	289
Microperoxidase-11	Mesoporous ITO	0.2	0.263	10	293
Cytochrome C	Mesoporous SnO <sub>2</sub>	4	0.673	1	201
Fe tetra(2,6-dihydroxyphenyl) porphyrin	Carbon nanotubes	-	0.330	-	152
Microperoxidase-11	Mesoporous ATO	0.42	0.274	1.5	291
FePOMe (A)	Mesoporous ATO	0.16	0.429	4.4	This work
FePOMe (B)	Mesoporous ATO	0.16	0.496	4.9	This work

**Figure 57**

(a) CVs in acetonitrile (0.1 M TBAP) of FePOMe immobilised on pl-ITO using the linear sweep voltammetry method and (b) a plot of peak separation  $E_p$  vs the log of the scan rate  $\log(v)$  for the  $Fe^{(2+/3+)}$  redox couple. Scan rate = 50 mV/s.

Peak separation  $\Delta E_p$  for FePOMe immobilised on pl-ITO remains approximately the same at 45 mV from a scan rate of 10 mV/s up to 500 mV/s (Fig. 7 SI), above which faster measurements could not be carried out, which meant that a kinetically limited  $k_{ET}$  could not be calculated. The difference between the redox behaviour of FePOMe on the more conductive pl-ITO and the me-ATO suggests that the ET rates calculated on me-ATO are limited by the resistivity of the porous ATO support<sup>240,241</sup> (aside from any possible difference in the intrinsic bulk conductivity of ATO over ITO, the small size of the ATO nanocrystals result in more grain boundaries when

assembled in thin films when compared to planar ITO films that are deposited using sputtering techniques) rather than the charge transfer resistance of the interface. This limitation may also explain why the values of  $k_c$  and  $k_a$  are the same for me-ATO modified using both the ‘pre-coordination’ and ‘post-coordination’ methods, within the given values of error. For comparison with another material, electron transfer rates of  $0.35 \text{ s}^{-1}$  were obtained for and Fe protoporphyrin XI immobilised on MWCNTs<sup>281</sup>, while a rate of  $2.9 \text{ s}^{-1}$  was obtained for hemin immobilised on MWCNTs in another study<sup>294</sup>. This compares to a transfer rate of  $4.9 \times 10^3 \text{ s}^{-1}$  obtained for hemin immobilised on a glassy carbon electrode<sup>295</sup> and highlights the limited conductivity in 3D structured electrodes compared to planar electrodes.

Comparing the  $\Gamma_{CV}$  obtained for 160 nm thick me-ATO films electrografted with the ‘pre-coordination’ and ‘post-coordination’ methods with planar ITO electrografted with linear sweep voltammetry, we see a 25 and 12.5-fold increase, respectively. Comparing the same values with those obtained for planar ITO electrografted with a constant potential, we see a 30 and 60-fold increase.

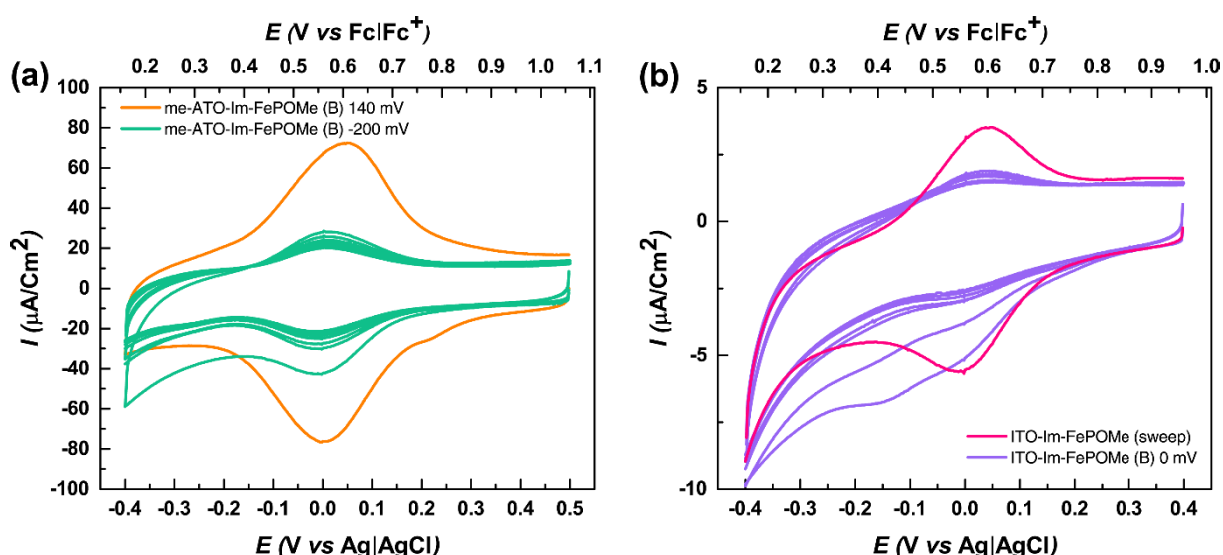
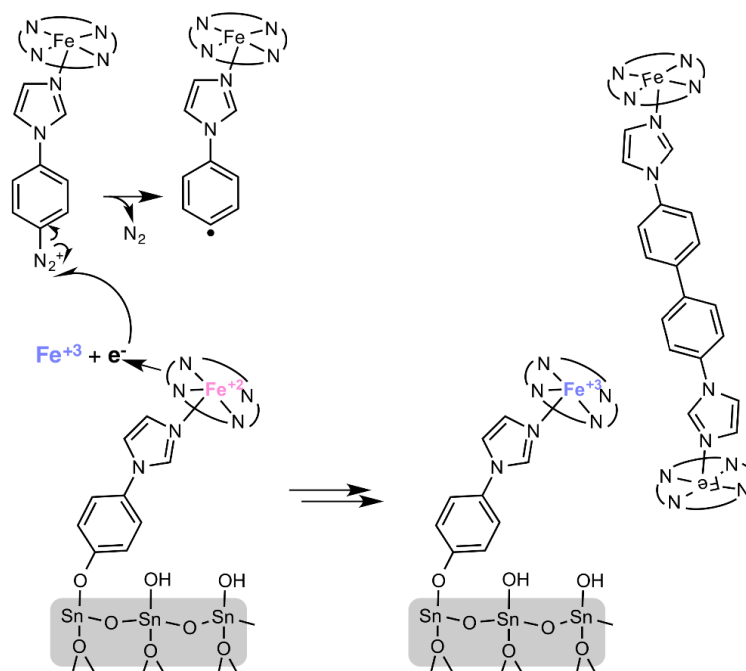


**Figure 58** CVs in acetonitrile (0.1 M TBAP) of FePOMe immobilised on (a) me-ATO electrografted using the ‘pre-coordination’ method B at -0.42 (vs Fc/Fc<sup>+</sup>) (orange trace) and -0.76 (vs Fc/Fc<sup>+</sup>) (green trace) and (b) pl-ITO electrografted using the ‘pre-coordination’ method at -0.56 V (vs Fc/Fc<sup>+</sup>) (labelled B, purple trace) or electrografted using linear sweep voltammetry (labelled Sweep, pink trace). Scan rate = 50 mV/s.

Electrografting of pl-ITO *via* the ‘pre-coordination’ method (i.e. in the presence of FePOMe) results in a brown surface film that is easily removed/dissolved upon rinsing in dichloromethane, and results in negligible redox current for the Fe(<sup>2+/3+</sup>) couple in acetonitrile (0.1 M TBAP, Figure 58b), indicating the deposition of weakly bound, physisorbed species. A similar behaviour is observed on me-ATO when a potential more negative (-0.42 V vs (vs Fc/Fc<sup>+</sup>) than the FePOMe Fe(<sup>2+/3+</sup>) couple is applied in the ‘pre-coordination’ method. Given that the applied reduction potential of Im-diazo on pl-ITO (-0.56 V vs vs Fc/Fc<sup>+</sup>) is *more* negative than the potential of the FePOMe Fe(<sup>2+/3+</sup>) couple (close to -0.56 V vs vs Fc/Fc<sup>+</sup>), these results suggest that the

application of potentials at or below the redox potential of the species being immobilised results in electron hopping through the Fe centres of already-grafted FePOMe species. This causes diazonium species to be reduced away from the electrode surface, which may in turn reduce other diazonium species or form oligomeric species that aren't chemisorbed at the surface (as illustrated in Scheme 55). Electron-hopping has previously been observed for diazonium-bearing osmium and ruthenium species on a range of electrode materials and resulted in thick, polymeric films.<sup>45,275</sup> The electron transport pathway may take three different routes: through the conjugated bonds of the macrocycle, *via* the metal atom, or a mixture of both of these pathways.<sup>284</sup> Picot et al. deposited films on glassy carbon (GC), pyrolised photoresist films (PPF) and ITO electrodes *via* the electrochemical reduction of a diazonium meso-substituted free-base porphyrin in aqueous solvent (0.1 M HCl) and observed the formation of thick, purple films (measured at 20 nm on PPF) that were insoluble in aqueous solvents but easily removed in organic solvents. The solute was identified as non-chemisorbed H<sub>2</sub>TPP monomers and it is suggested that these form as a result of the electrochemically generated radicals undergoing further reduction to carbanions and abstract a hydrogen from water.<sup>296</sup> While the presence of water in the acetonitrile used in the experiments presented here cannot be excluded and is indeed quite likely, it is not plausible that this mechanism takes place here as it was shown that an insulating interface was also deposited on pl-ITO under a potential of -0.56 V (vs vs Fc/Fc<sup>+</sup>) in the absence of FePOMe (i.e. the radicals formed are able to adsorb on the oxide surface and form covalent bonds). Identification of the soluble material should be possible using mass spectrometry techniques and may provide evidence for the type of mechanism taking place.



**Scheme 55**

Schematic representation of a possible mechanism for the formation of thick, weakly bound films on pl-ITO and me-ATO electrodes when applying potentials more negative than the FePOMe Fe<sup>(2+/3+)</sup> redox couple. Reduced FePOMe species (i.e. in oxidation state +2) at the electrode interface reduce Im-diazo or FePOMe species further away from the interface *via* an electron 'hopping' mechanism, which eventually leads to radicals forming in solution that react with other species in solution, rather than the oxide surface, finally leading to the formation of some kinds of oligomeric species.

The high loadings of FePOME that could be achieved on me-ATO result in very high resonance Raman (RR) scattering intensities, thus allowing to ascertain the spin, coordination and redox states of the porphyrin. For the RR investigation, FePOME was immobilised on a me-ATO electrode using the ‘post-functionalisation’ method. *In situ* RR measurements were performed under different applied potential steps (Figure 59 a) and a component fit analysis was carried out to decompose each potential-dependent spectrum into the different contributing ligation, spin and redox components (Figure 59).<sup>251</sup>k

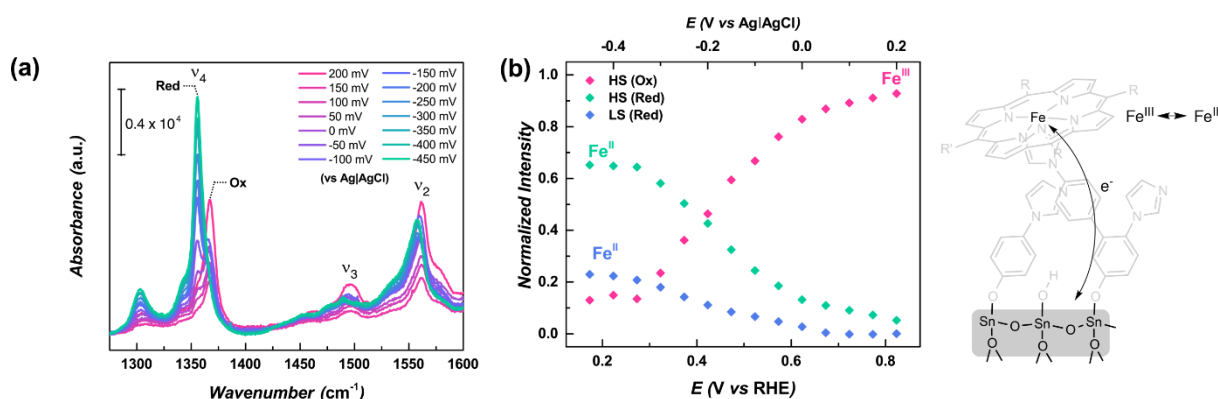


**Figure 59**

(a) Potential-dependent resonance Raman (RR) spectra recorded in pH 7 (0.1 M PB) of FePOME immobilised on me-ATO using the ‘post-coordination’ method and (b) the relative contributions from the different FePOME spectra components at different potentials.

The component fit analysis was conducted using the same methodology as that used by Ly et al. for the iron Hangman porphyrins immobilised on imidazole-terminated SAMs on silver electrodes.<sup>251</sup> At OCP (135 mV vs 3M Ag/AgCl) in pH 7 (0.1 M PB), intense marker bands appear around  $1367\text{ cm}^{-1}$  ( $\nu_4$ ) and  $1561\text{ cm}^{-1}$  ( $\nu_2$ ), and a lower intensity band appears around  $1495\text{ cm}^{-1}$  ( $\nu_3$ ). The main spectral contribution observed comes from the 5-coordinated high-spin (HS) state of the FePOME with a small contribution from the 6-coordinated low-spin (LS) state, as evidenced by a high-frequency shoulder in the  $\nu_3$  band at  $1502\text{ cm}^{-1}$ . This indicates that almost all of the immobilised FePOME species are axially coordinated to the surface of the functionalised me-ATO *via* the electrografted imidazole linker molecule with a 6<sup>th</sup> free coordination site, which is available for the binding of oxygen. 6-coordinated species were also overserved by Ly et al.<sup>251</sup> and their molecular origin is at present unknown. Plotting the different contributions versus applied potential allows us to follow the change in oxidation state of the Fe centre and hence evaluate the electrochemical accessibility of the immobilised species. As can be observed in Figure 59b, upon application of cathodic potentials there is an almost complete reduction in intensity of the 5-coordinated HS oxidised state, indicating that most of the immobilised species are indeed electrochemically accessible (i.e. electrochemically contacted), despite passivation of the me-ATO surface during electrografting. Application of spectroelectrochemical methods, such as that outlined here, provides information on the evolution of immobilised species under different potentials or reaction conditions, and potentially allows the identification of intermediate species in catalytic reactions. It further provides precise information on the electrochemical accessibility of

the immobilised species (at least in the case of porphyrin-containing species), which may be used to effectively evaluate different immobilisation strategies.

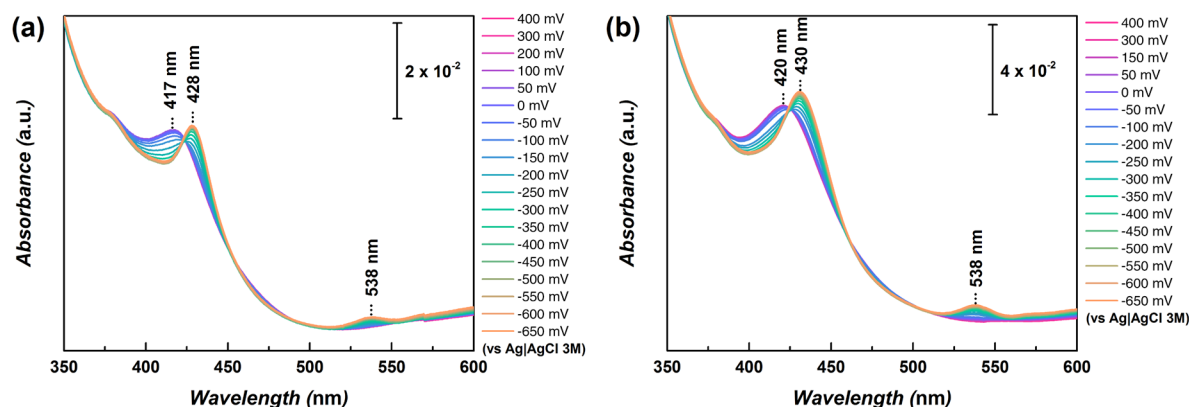


**Figure 60**  
Spectroelectrochemical UV-vis measurements of FePOMe immobilised on me-ATO using (a) 'post-coordination' and (b) 'pre-coordination' methods in pH 7 (0.1 M PBS).

UV-Vis spectroelectrochemistry may be used to measure redox changes of certain species, such as molecular catalysts, immobilised on TCO material surfaces; however, UV-Vis spectroscopy cannot be used to quantitatively measure the contributions from different redox states of immobilised porphyrin-type species in the same way as rR spectroscopy due to the broad overlap of the Soret bands (Figure 60 a, b).

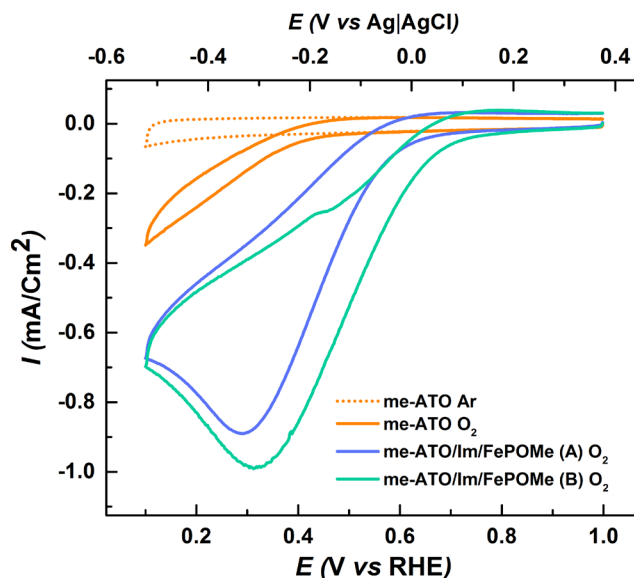


**Figure 61**  
CVs of unmodified me-ATO at pH 7 (0.1 M PB) under Ar and O<sub>2</sub> bubbling, as well as me-ATO with FePOMe immobilised using the 'post-coordination' (labelled A, blue trace) and 'pre-coordination' (labelled B, green trace) methods.

To evaluate the electrochemical performance of the modified thin film electrodes for ORR, CV's of unmodified and FePOMe-modified electrodes were recorded at pH 7 (0.1 M PB) in nitrogen and oxygen saturated electrolyte (Figure 61). While unmodified me-ATO shows some cathodic current in O<sub>2</sub> with an onset potential of around 0.4 V (vs RHE), the me-ATO electrodes

immobilised with FePOMe display diffusion limited reductive waves with onset potentials of 0.570 and 0.645 V (vs RHE) and maximum currents of 0.9 and 1 mA/cm<sup>2</sup> for the ‘post-coordination’ and ‘pre-coordination’ methods, indicating that the immobilised FePOMe-species is catalytically active for ORR.

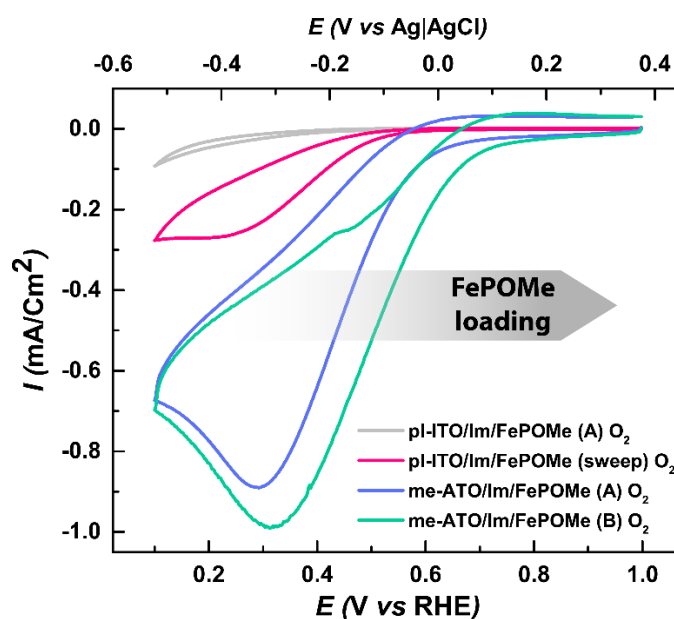


**Figure 62**

CVs of pl-ITO and me-ATO electrodes in pH 7 (0.1 M PB) electrolyte under O<sub>2</sub> bubbling with increasing loadings of immobilised FePOMe.

**Table 12**

A comparison of the onset potentials for the ORR for FePOMe immobilised on pl-ITO and me-ATO using different immobilisation methods and the corresponding coverages of FePOMe as determined using CV.

	<b>Coverage FePOMe <math>\Gamma_{CV}</math></b> <b>(<math>\times 10^{-9} \text{ molcm}^{-2}</math>)</b>	<b>Onset potential</b> <b>(mV) vs. RHE</b>
pl-ITO – ‘post-coordination’ method, constant potential	0.05	-
pl-ITO – ‘post-coordination’ method, linear sweep	0.12	500
me-ATO – ‘post-coordination’ method	1.5	570
me-ATO – ‘pre-coordination’ method	3.0	645

To determine the influence of the catalyst electrode loading on the catalytic performance, CVs were recorded for the pl-ITO electrodes modified with FePOMe using the ‘post-coordination’ and ‘sweep’ methods. CVs for both the me-ATO and pl-ITO electrodes are shown in Figure 62. The onset potentials for ORR and the corresponding coverages of FePOMe ( $\Gamma_{CV}$ ) for each electrode are shown in Table 12. FePOMe-modified electrodes show improved onset potentials for ORR with increasing coverages of electroactive FePOMe (i.e. catalyst loading) in the order me-ATO ‘pre-coordination’ > me-ATO ‘post-coordination’ > pl-ITO ‘post-coordination’, with onset potentials of around 645 mV, 570 mV and 500 mV (vs RHE), respectively. It has previously been shown that overpotentials for ORR reduce with the amount of metal complex present on the surface,

with ORR currents shown to be directly proportional to the amount of complex, indicating that the reaction is first order with respect to the surface concentration of the catalyst.<sup>116,297,298</sup> This is true for cases where multi-layers are not formed and all of the metal active centres are accessible and available for catalysis, as is the case shown here. pi-ITO modified using the ‘post-coordination’ method shows negligible ORR activity, presumably due to the very low loading of FePOMe.

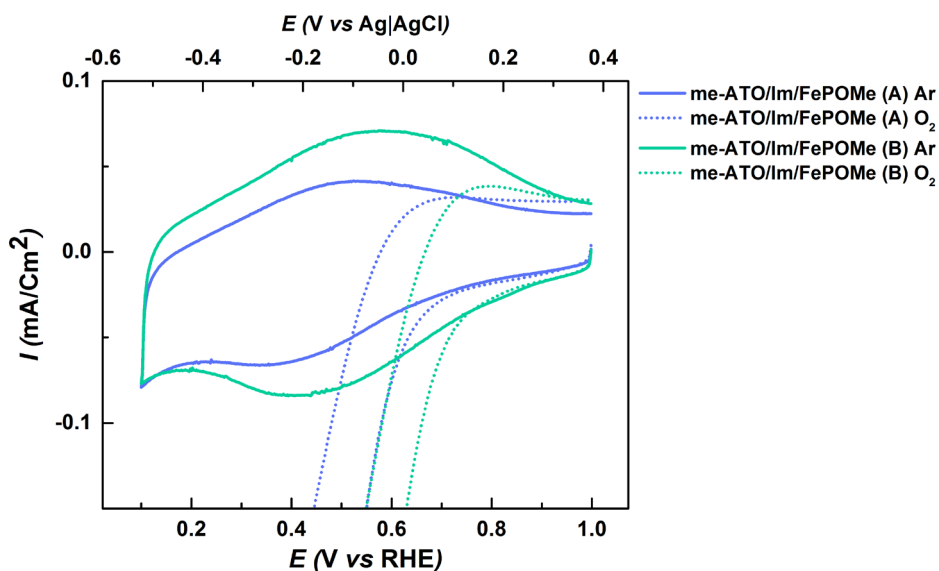


**Figure 63**

CVs of FePOMe immobilised on me-ATO using (a) ‘post-coordination’ method (labelled A, blue traces) and (b) ‘pre-coordination’ method (labelled B, green traces) in aqueous media pH 7 (0.1 M PB) under Ar and O<sub>2</sub>. Scan rate = 50 mV/s.

The redox peak potential of a process  $E_{1/2}$  can be shifted to more positive potentials when immobilised on a surface.<sup>284</sup> In the surface activity theory of Brown and Anson, the anodic and cathodic peak potentials are considered as equal and related to the surface coverage of redox species ( $\Gamma$ ) by:

$$E_{\text{peak}} = E^0 + \left(\frac{RT}{nF}\right)(r_{\text{R}} - r_{\text{O}})\Gamma \quad (45)$$

where  $r_{\text{R}}$  and  $r_{\text{O}}$  are interaction parameters that represent the intermolecular interactions between reduced and oxidised species, provided that the mixed interactions are the same, i.e. the oxidised-reduced and reduced-oxidised interactions.<sup>299,300</sup> As the anodic and cathodic peak potentials are not equal, the average formal potential  $E^0_{1/2}$  is used instead of  $E^0$ , and the theory predicts that the peak potential will shift depending on the relative magnitude of  $r_{\text{R}}$  and  $r_{\text{O}}$  as the coverage changes. Abruña and co-workers showed that for a SAM of  $[\text{Os}(\text{bpy})_2(\text{dipy})]^{1+}$  on platinum electrodes (with bpy = 2,2'-bipyridine and dipy = 4,4'-trimethylenedipyridine),  $E_{1/2}$  increases as a function of surface coverage in a range of solvents. Coupled with a broader than ideal (i.e. greater than 90.6 mV)  $\Delta E_{\text{FWHM}}$ , which implies negative interaction parameters, this indicates, as expected, that the repulsion between the +2 oxidised species is greater than between the reduced +1 species,<sup>300</sup> and indicates that the thermodynamic driving force for the

redox transition increases with coverage. Lindsey, Bocian and co-workers showed for porphyrins bound to metal and semiconductor surfaces *via meso*-substituents that  $\Delta E_{\text{FWHM}}$  and  $E_{1/2}$  also both increase as a function of surface coverage.<sup>301–303</sup> As shown previously in acetonitrile (with 0.1 M TBAP electrolyte),  $\Delta E_{\text{FWHM}}$  increases with the coverage of FePOMe on me-ATO, while  $E_{1/2}$  slightly decreases by 3 mV from 36 mV for a coverage of  $1.5 \times 10^{-9} \text{ molcm}^{-2}$  (for the ‘post-coordination’ method) to 33 mV for a coverage  $\Gamma_{\text{CV}}$  of  $3.0 \times 10^{-9} \text{ molcm}^{-2}$  (for the ‘pre-coordination’ method). However, as can be seen in Figure 63, in aqueous media (with 0.1 M PB electrolyte), there is an increase in  $\Delta E_{\text{FWHM}}$  and an increase in  $E_{1/2}$  of almost 70 mV with an increased coverage of FePOMe, as expected, and this explains why there is a shift in the onset potential (of 75 mV) for ORR with an increased loading of FePOMe. The insignificant decrease in  $E_{1/2}$  of 3 mV observed in acetonitrile with an increased loading of FePOMe may be a result of more complex structural differences, e.g. the presence of multi-layers.

The values of  $\Delta E_{\text{FWHM}}$  for CVs performed in aqueous media are much broader than those measured in acetonitrile at the same scan rates (see Appendix 10 and Appendix 11). This phenomenon may be explained by an increase in the strength of the ion pairing between the FePOMe and the TBAP perchlorate anion, or the intercalation of the less polar acetonitrile solvent molecules between the FePOMe species, both of which would minimise intermolecular repulsions between the FePOMe redox species and each other and lead to lower values of  $\Delta E_{\text{FWHM}}$ . Collman, Chidsey, Hal Van Ryswyk and co-workers showed for a ruthenium porphyrin with hydrophobic tolyl *meso*-substituents, axially coordinated to imidazole-terminated SAM coated gold electrodes, that an increase in the strength of the ion pairing between the redox species and the electrolyte anion can indeed minimise intermolecular repulsion, thereby reducing  $\Delta E_{\text{FWHM}}$  and leading to a decrease in  $E_{1/2}$ . In water in particular, hydrophilic electrolytes led to waves with broadened values of  $\Delta E_{\text{FWHM}}$  that are difficult to differentiate from the baseline.<sup>304</sup>

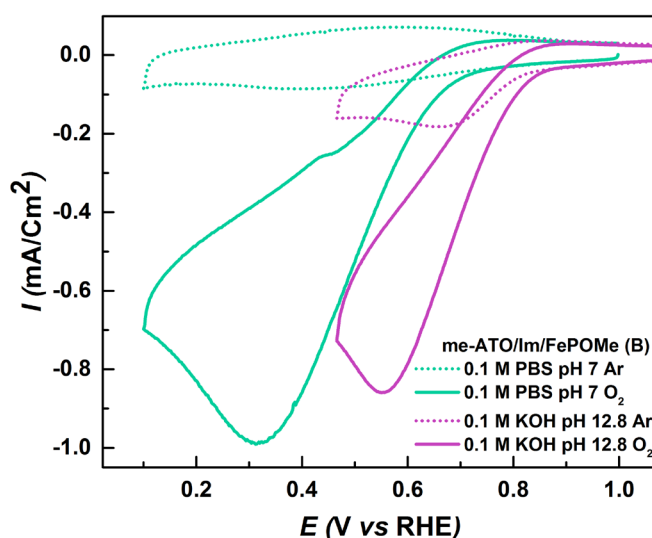


**Figure 64**

CVs of me-ATO in pH 7 (0.1 M PB) and pH 12.8 (0.1 M KOH) under  $\text{O}_2$  or Ar bubbling with FePOMe immobilised using the ‘pre-coordination’ method.

The highest onset potential for the me-ATO modified electrodes was obtained in 0.1 M KOH (pH 12.8) using the 'pre-coordination' method, yielding an onset potential of 810 mV (vs RHE), as shown in Figure 64. This compares well to previously reported onset potentials of 922 mV (vs RHE) measured in O<sub>2</sub> saturated 0.1 M KOH electrolytes for axial-pyridine coordinated iron phthalocyanine reported by Liu and co-workers<sup>150</sup>, or 913 mV for axial-imidazole coordinated iron porphyrin immobilised on carbon nanotubes by Cho and co-workers.<sup>151</sup> In both cases diazonium salts were used to chemically functionalise (i.e. not electrochemically, as is the case here) the carbon nanotubes during the catalyst ink preparation, which is possible for carbonaceous materials. Onset potentials in 0.1 M HClO<sub>4</sub> could not be measured for FePOMe immobilised on me-ATO due to the instability of the interface to hydrolysis at such an acidic pH. Aside from the activity of the porphyrin itself, a number of other factors may affect the activity of such species immobilised on nanostructured oxides, such as me-ATO, or CNTs. These include: different substrate conductivities and electronic coupling between the catalyst and the substrate, which may affect the electron transfer rate; completely different substrate geometries or different interface structures, potentially influencing intermolecular interactions between the immobilised catalytic species; and finally, different loadings of catalyst. The amount of catalyst present in the herein presented me-ATO system is up to 3.5 μg/cm<sup>2</sup> of FePOMe, which is an about two orders of magnitude less than the 318 μg/cm<sup>2</sup> loading found in the work of Cho and co-workers and the 1 mg/cm<sup>2</sup> loading found in the work of Liu and co-workers. Other studies have reported onset potentials of 820 mV<sup>305</sup> and 880 mV<sup>306</sup> for iron phthalocyanine supported on carbon electrodes with loadings of 800 and 200 μg/cm<sup>2</sup> of catalyst, respectively. Improved onset potentials and activities could potentially be achieved using thicker films of me-ATO, which can easily be accomplished using different coating conditions, or other nanostructured TCO films.

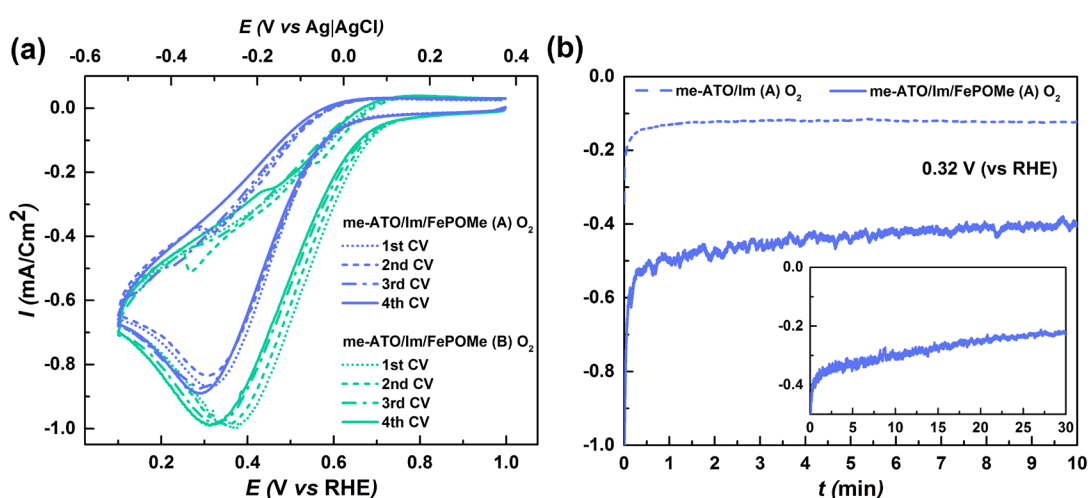


**Figure 65**

(a) CVs of me-ATO in pH 7 (0.1 M PB) electrolyte under O<sub>2</sub> bubbling with FePOMe immobilised using 'post-coordination' method (labelled A, blue trace) and 'pre-coordination' method (labelled B, green trace). (b) Chronoamperometry at -0.32 V (vs RHE) for 10 min under O<sub>2</sub> bubbling of me-ATO immobilised with FePOMe using 'post-coordination'. Inset shows second chronoamperometry applied for a second time to the same electrode for a further 30 min.

Figure 65a shows the first 4 CVs of the me-ATO electrodes immobilised with FePOMe using the 'pre-coordination' and 'post-coordination' methods. The onset potential for the me-ATO modified using 'post-coordination' method shows significantly better stability upon repeated cycling compared to the 'pre-coordination' method. While the reason for this behaviour currently remains unclear, it may be related to the previously discussed increased 'crowding' of FePOMe species in the interface deposited using the 'pre-coordination' method, which may lead to a re-structuring or displacement of electro-accessible and catalytically active species over repeated cycling. The stability of the catalytic species and interface were further investigated using chronoamperometry recorded at a potential of -323 mV (vs RHE) for the me-ATO electrodes modified using the 'post-coordination' method, with measurements recorded before and after incubation with the catalytically active FePOMe species (Figure 65b). The current density decreases over time, which may be a result of: (a) desorption of the interface linker molecules from the oxide surface, (b) disruption of the linker-catalyst axial coordination molecules (e.g. due to protonation of the imidazole<sup>250</sup> or a change in the orbital overlap resulting from the formation of intermediate Fe-oxo species during catalysis), or (c) deactivation of the catalytically active species (e.g. due to the formation of superoxides during catalysis). Imidazole protonation may be enhanced on hydrophilic substrates such as me-ATO when compared to hydrophobic substrates such as CNTs. Another reason for the loss of activity may be due to the formation of H<sub>2</sub>O<sub>2</sub> due to ORR taking place on the ATO (see Figure 61). It has been shown that ITO predominantly forms H<sub>2</sub>O<sub>2</sub> via a 2-electron process during ORR at highly cathodic potentials.<sup>307</sup> Further experiments would need to be carried out to determine the exact reason for this apparent deactivation and loss of catalytic activity.

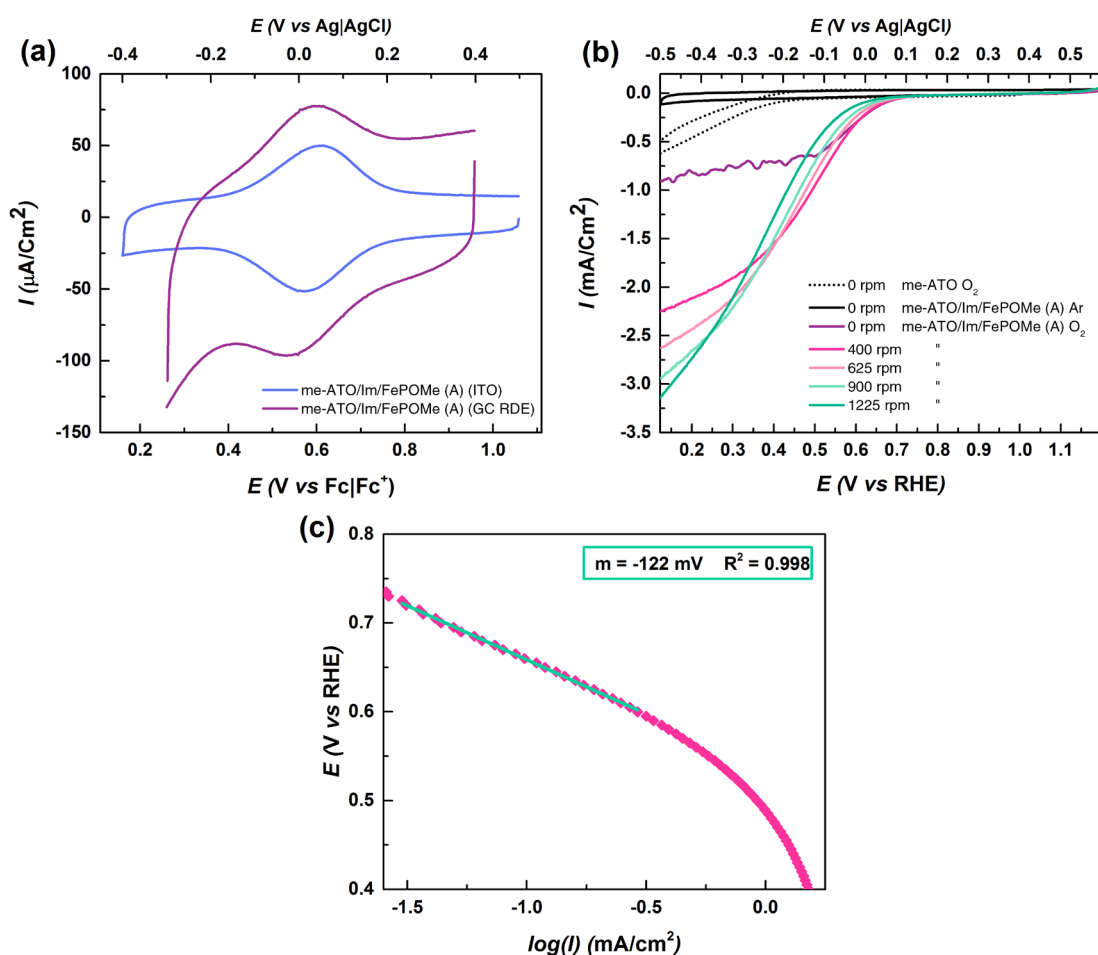


**Figure 66**

(a) CVs in acetonitrile (0.1 M TBAP) of FePOME immobilised on a me-ATO-coated ITO electrode (blue trace) and a me-ATO-coated GC RDE electrode (pink trace) using the ‘post-coordination’ method (labelled method A), scan rate = 50 mV/s. (b) LSVs in pH 7 (0.1 M PB) electrolyte under O<sub>2</sub> bubbling, and a CV under Ar bubbling, of the FePOME immobilised on me-ATO coated on the RDE electrode at different rotation rates, as well as a CV the unmodified me-ATO under O<sub>2</sub> bubbling. Scan rates = 10 mV/s. (c) Tafel plot of the applied potential against the logarithm of the current for the oxygen reduction reaction (ORR) using FePOME immobilised on me-ATO coated on the RDE electrode.

To study the ORR electrocatalytic behaviour and kinetics, a rotating disk electrode (RDE) was used. me-ATO was coated on the GC RDE electrode using spin-coating, and subsequently FePOME was immobilised on its surface using the ‘post-coordination’ method. It was possible to see by eye that the films were not even in thickness across the whole surface of the GC electrode and this was likely a result of the GC electrode surface not being completely flat, or due to the spin-coating procedure. Film thicknesses could not be determined for this electrode. Figure 66a shows a CV of FePOME immobilised on the me-ATO coated GC electrode using the ‘post-coordination’ method compared to a CV of FePOME immobilised on the me-ATO films on ITO using the same method. A higher  $\Gamma_{CV}$  of  $2.1 \times 10^{-9}$  molcm<sup>-2</sup> was calculated for this electrode using the geometrical surface area of the GC. Figure 66b shows the linear sweep voltammograms (LSVs) of the electrode in pH 7 (0.1 M PB) under O<sub>2</sub> at different rotation rates. At a rotation rate of 400 rpm, an onset potential of 730 mV for ORR was obtained, which is 160 mV greater than that obtained for me-ATO coated ITO electrodes. This difference is likely due to differences in the me-ATO structure or film thickness, as discussed previously. Slower scan rates of 10 mV/s were

used for the LSVs, so the increase in onset potential after each LSV is more pronounced. Due to this instability, it was not possible to carry out a Koutecký-Levich analysis to determine the mass transport parameters or the standard rate constant. Currents for ORR should plateau at higher overpotentials due to diffusion limitation to the catalyst; however, as can be seen in Figure 66b, the currents do not plateau. This can be attributed to ORR taking place on the ATO substrate itself at higher overpotentials. A CV of unmodified me-ATO in pH 7 under  $O_2$  in Figure 66 (dotted black trace) shows this behaviour more clearly. Tafel plots give a linear slope with no significant curvature at low overpotentials, which is similar to those given for other iron porphyrin or phthalocyanine species immobilised on carbon electrodes *via* coordination to imidazole or pyridine interfaces.<sup>150,151,250</sup> A slope of 122 mV per decade is obtained, which compares to around 27 mV per decade for iron phthalocyanine immobilised on CNTs *via* axial coordination to pyridine, 67 mV for an iron porphyrin immobilised on CNTs *via* axial coordination to imidazole and 100 mV for an iron porphyrin immobilised on Vulcan (a carbon material) *via* axial coordination to imidazole.<sup>150,151,250</sup> Axial coordination to imidazole was shown known to enhance activity for ORR and improve its selectivity towards water (as opposed to  $H_2O_2$ ) in the latter study.<sup>250</sup>

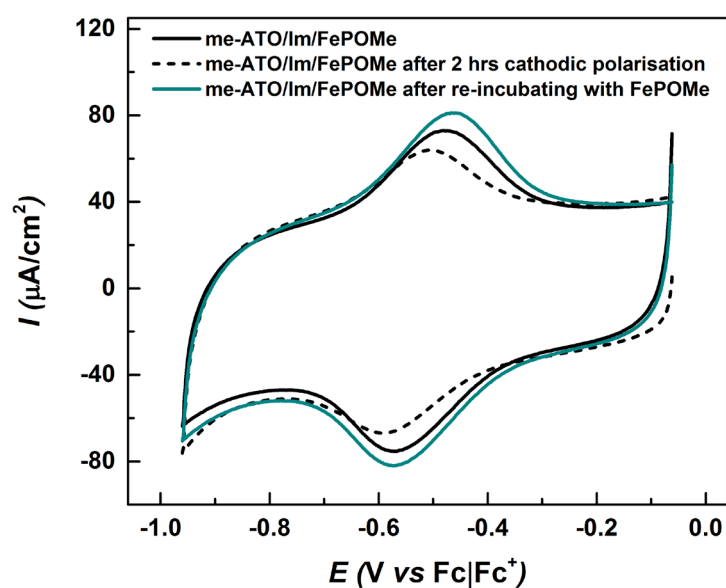


**Figure 67**

CVs in acetonitrile (0.1 M TBAP) of FePOMe immobilised on me-ATO using 'post-coordination' before and after cathodic polarisation in pH 7 (0.1 M PB) in air for ca. 2 hrs in pH 7, and then again after re-incubating with fresh FePOMe.

Despite the exact reason for the deactivation of the catalytic interface remaining unclear thus far, CVs of me-ATO electrodes modified using the 'post-coordination' method before and after cathodic polarisation for ca. 2 hours show that the lost current density for the  $Fe^{(2+/3+)}$  couple could be restored by re-incubating the electrode in 1 mM FePOMe in acetonitrile (0.1 M TBAP). This result therefore clearly emphasises the robustness of the grafted Im-diazo interface itself, as well as the strong bond between the electrografted linker and the metal oxide surface; a result which is in line with the ATR-IR spectroelectrochemical stability measurements performed previously (*vide supra*).



the me-ATO, therefore the sample was measured using resonance Raman using 413 nm excitation. As can be seen in Figure 68, the resonance Raman intensity is much greater for the me-ATO electrode that has been electrografted with the Im-linker molecules and incubated with CoPOH than for the drop-cast sample, indicating that the Im functionality is required to immobilise the CoPOH successfully in significant amounts. This suggests that the CoPOH is immobilised via axial ligation of Im to the porphyrin Co-centre.

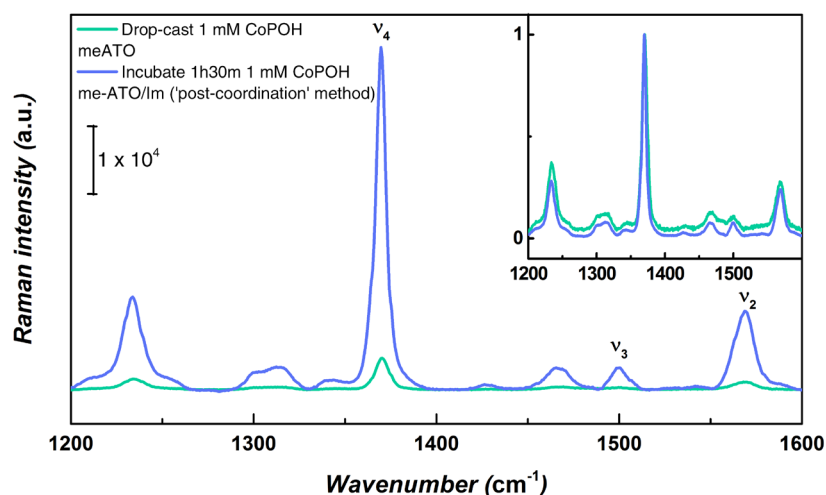


**Figure 68**

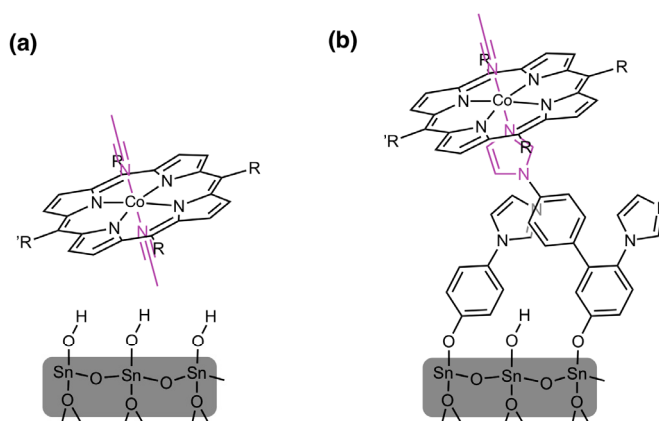
Resonance Raman spectra recorded in air of CoPOH immobilised on Im-functionalised me-ATO using the 'post-coordination method (blue), and CoPOH drop cast onto me-ATO (from a 1 mM solution of CoPOH in acetonitrile) and subsequently rinsed with acetonitrile (green). The inset shows both spectra normalised to the  $\nu_4$  vibrational band.

The inset shows the resonance Raman spectra with intensities normalised on the  $\nu$  vibrational band. Excluding a broad peak around  $1100\text{ cm}^{-1}$  due to the substrate, the peak positions and the peak intensity ratios are roughly the same in both spectra, indicating that both species are in the same oxidation state and have the same coordination number. Intense marker bands appear at  $1370\text{ cm}^{-1}$  ( $\nu_4$ ) and  $1569\text{ cm}^{-1}$  ( $\nu_2$ ), and a lower intensity band appears around  $1499\text{ cm}^{-1}$  ( $\nu_3$ ). The  $\nu_4$  vibrational mode, which is mostly composed of pyrrolic C-N stretching coordinates, is highly sensitive to the metal centre oxidation state, and the band observed at  $1370\text{ cm}^{-1}$  indicates an oxidation state of either  $\text{Co}^{2+}$  or  $\text{Co}^{3+}$ .<sup>313</sup> A  $E^0$  ( $\text{Co}^{2+/3+}$ ) of  $0.085\text{ V}$  (vs RHE) was measured by Kielb<sup>314</sup> for cobalt Hangman species with a methyl ester hanging group (CoPOMe), and therefore at the measured OCP of around  $0.93\text{ V}$  (vs RHE), the CoPOH species are expected to be in the  $\text{Co}^{3+}$  oxidation state.

The frequencies of the  $\nu_3$  and  $\nu_2$  vibrational modes, which are composed of pyrrolic C-C stretching coordinates, are sensitive to the coordination and spin state of the metal centre, and can be correlated to the core size, which is the distance from the centre of the porphyrin core to the pyrrole nitrogens ( $d_{\text{Ct-N}}$ ), according to:

$$v = K(A - d_{\text{Ct-N}}) \quad (46)$$

where  $A$  and  $K$  are mode-specific empirical constants.<sup>315</sup> A change in the metal d-orbital population, e.g. as a result of the substitution of a strong ligand for a weaker ligand, can induce a change in the spin state of the metal, resulting in a change in the ion radius and a change in the C<sub>1</sub>-N distance, and therefore a shift in frequency. The positions of the bands observed here indicate that the main spectral contribution is from species that are 6 coordinated low-spin (LS)<sup>316</sup>, indicating axial coordination by two solvent molecules. This suggests that, in the case of the drop-cast sample, the non-specifically adsorbed CoPOH species are coordinated by two acetonitrile solvent molecules, while in the case of the ‘post-coordination’ sample, the specifically adsorbed CoPOH species must be coordinated by a surface-grafted Im-linker molecule and an acetonitrile solvent molecule, as illustrated in Scheme 57. Imidazole and acetonitrile ligands have a similar ligand-field splitting parameter and are thus very likely to result in the same spin state. A coverage ( $\Gamma_{UV}$ ) of CoPOH on the me-ATO of  $1.2 \times 10^{-9}$  molcm<sup>-2</sup> was estimated with UV-Vis spectroscopy using the adsorption coefficient ( $\epsilon$ ) of  $1.69 \times 10^4$  M<sup>-1</sup>cm<sup>-1</sup> measured for FePOMe (see UV-vis spectra in Figure 76).



**Scheme 57**

Schematic illustration of CoPOH molecules (a) non-specifically adsorbed on me-ATO and coordinated by two acetonitrile solvent molecules, and (b) specifically adsorbed on me-ATO *via* coordination to a surface-grafted Im-linker molecule and an acetonitrile solvent molecule.

An attempt was made to conduct HER using the immobilised species in 0.1 M NaClO<sub>4</sub> (pH 5). CVs of the CoPOH immobilised on the me-ATO are shown in Figure 69. No substantial current for HER can be detected within the potential range probed. For HER to take place, cobalt must first be reduced to the oxidation state Co<sup>I</sup>.<sup>252</sup> A redox potential  $E^0$  (Co<sup>+1/2+</sup>) of -0.325 V (vs RHE) was measured by Kielb for CoPOMe.<sup>314</sup>

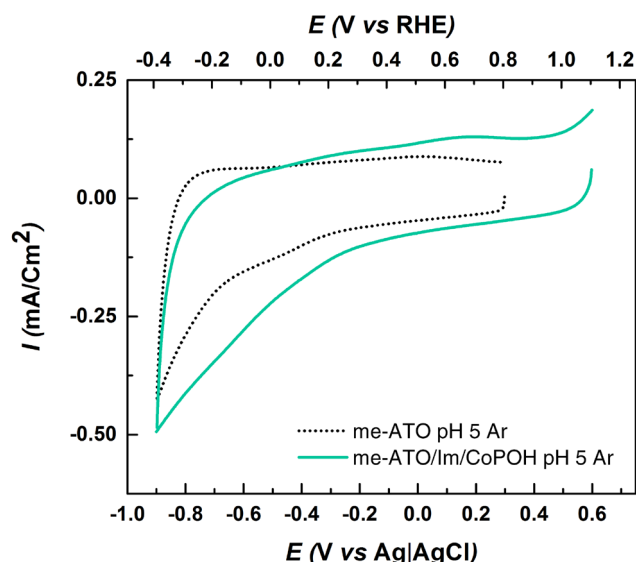


**Figure 69**

CVs in 0.1 M NaClO<sub>4</sub> (pH 5) under Ar bubbling of me-ATO with (green trace) or without (dotted black trace) CoPOH immobilised using the 'post coordination' method. Scan rate = 50 mV/s.

As previously mentioned, cobalt tetrapyrrole compounds have been shown to be good catalysts for OER, particularly under basic conditions. Resonance Raman spectra of the CoPOH species immobilised on the me-ATO *via* the post-coordination method were measured in 0.1 M NaOH, and, as shown in Figure 70, no substantial changes in the band positions or peak intensity ratios can be observed in comparison to a spectrum recorded in air. It should be noted that the spectroscopic pH titrations performed in section 9.3 indicated the desorption of the (metastable) electrografted Im-linker molecules in 0.1 M NaOH takes place with an apparent hydrolysis rate of  $k = 3.77 \times 10^{-5} \pm 0.34 \text{ s}^{-1}$  and thus a half-life of 5.5 hours, which is significantly longer than the timeframe of the experiments performed here.

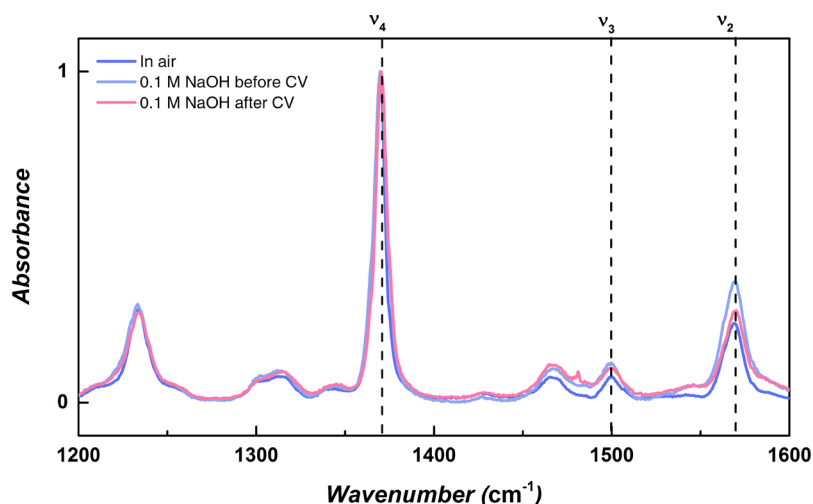


**Figure 70**

Resonance Raman spectra normalised to the  $\nu_4$  vibrational band of CoPOH immobilised on Im-functionalised me-ATO using the 'post-coordination' method in air and in 0.1 M NaOH, before and after applying a CV between 0.97 and 2.17 V (vs RHE).

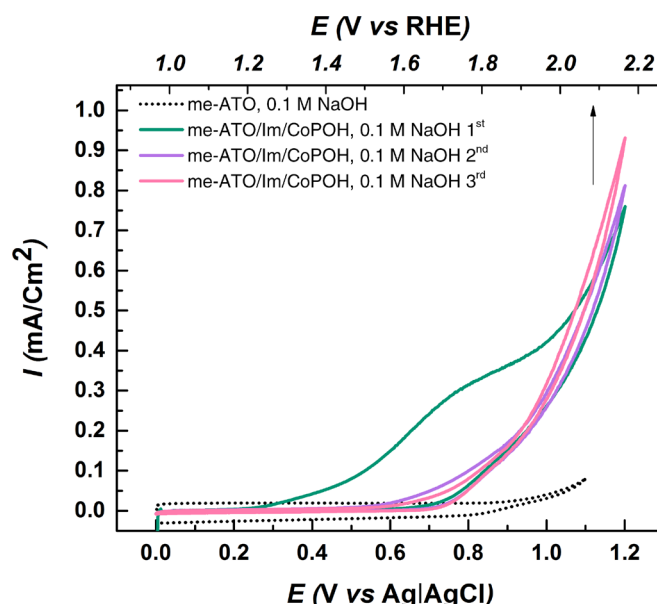


**Figure 71**  
CVs in 0.1 M NaOH of CoPOH immobilised on Im-functionalised me-ATO using the 'post-coordination' method.

Several CVs between 0.97 and 2.17 V (vs RHE) were applied to the sample (see Figure 71). In the first cycle, an irreversible anodic peak centred around 1.7 V (vs RHE) can be detected that is absent in the subsequent cycles. In these subsequent cycles, anodic current is observed for OER with an onset potential of ca. 1.7 V (vs RHE), with the current density increasing with the cycle number. This represents an overpotential of 0.47 V. The onset potential for OER is compared to those obtained for other cobalt tetrapyrrole compounds reported in literature in Table 13.

**Table 13**

A comparison of reported onset potentials for the oxygen evolution reaction (OER) catalysed by cobalt tetrapyrrole compounds. Potentials are given versus RHE and were calculated using the Nernst equation.

<b>Catalyst</b>	<b>System</b>	<b>Onset potential for OER (V vs RHE)</b>	<b>Ref.</b>
Co Hangman $\beta$ -octafluoro corrole (with carboxylic acid hanging group)	Heterogenous	1.7 (pH 14)	309
		1.75 (pH 10)	
	$3 \times 10^{-8}$ mol/cm <sup>2</sup> in nafion, coated on planar FTO	1.85 (pH 7)	
Soluble Co porphyrins (various)	Homogenous	1.8 (pH 7) <sup>a,b</sup>	253
	1 mM aqueous solution		
Perfluorinated Co phthalocyanine	Heterogeneous	1.7 (pH 7)	256
	Up to $1.5 \times 10^{-9}$ mol/cm <sup>2</sup> , drop-coated on planar FTO		
Co 5,10,15-tris(pentafluorophenyl)-corrole (with various axial ligands)	Heterogeneous	1.75 <sup>a</sup> (pH 7)	257
	$2.0 \times 10^{-9}$ mol/cm <sup>2</sup> , drop-coated on planar FTO		
Co Hangman porphyrin (with carboxylic acid hanging group)	Heterogeneous	1.7 (pH 12.6)	This work
	$1.2 \times 10^{-9}$ mol/cm <sup>2</sup> <sup>c</sup> , immobilised on <i>via</i> axial coordination to Im-functionalised me-ATO		

<sup>a</sup> best onset potential. <sup>b</sup> shown to be highly dependent on pKa of the buffer used. <sup>c</sup> calculated using UV-vis with the adsorption co-efficient ( $\epsilon$ ) of FePOMe in dichloromethane ( $1.69 \times 10^4$  M<sup>-1</sup>cm<sup>-1</sup>).

After the first CV, there is a slight shift in the  $\nu_4$  band in Figure 70 from 1370 to 1371  $\text{cm}^{-1}$  and the  $\nu_2$  band from 1569 to 1570  $\text{cm}^{-1}$ , suggesting no overall change in the oxidation state or coordination number of the immobilised CoPOH species (or the possible oxidation of some  $\text{Co}^{2+}$  species to  $\text{Co}^{3+}$ ). The origin of the anodic peak observed in the first CV will be discussed later.

Resonance Raman spectra of the sample were recorded under constant potential electrolysis (CPE) at different potentials in 0.1 M NaOH, as shown in Figure 72. The corresponding chronoamperometric data is shown in Figure 73. At a potential of 1.76 V (vs RHE), the current density for OER is stable and increases slightly as a function of time, while at 2.16 V (vs RHE) the current density is at its highest but decreases as a function of time. Raman spectra are only shown for two potentials. On moving from a potential of 1.16 V (vs RHE), i.e. where no OER occurs, to a potential of 2.16 V (vs RHE), i.e. where OER takes place, no change can be observed in the Raman spectra. This either suggests that the catalytically active species has a very short lifetime and can't be detected spectroscopically, or that the incident light is not resonant with an electronic transition in the catalytically active species (e.g. an oxide). It has been proposed in the literature that for Co tetrapyrrole species, Co is active for the OER in oxidation state  $\text{Co}^{\text{IV}}$  or  $\text{Co}^{\text{V}}$ .<sup>253,255,257</sup>

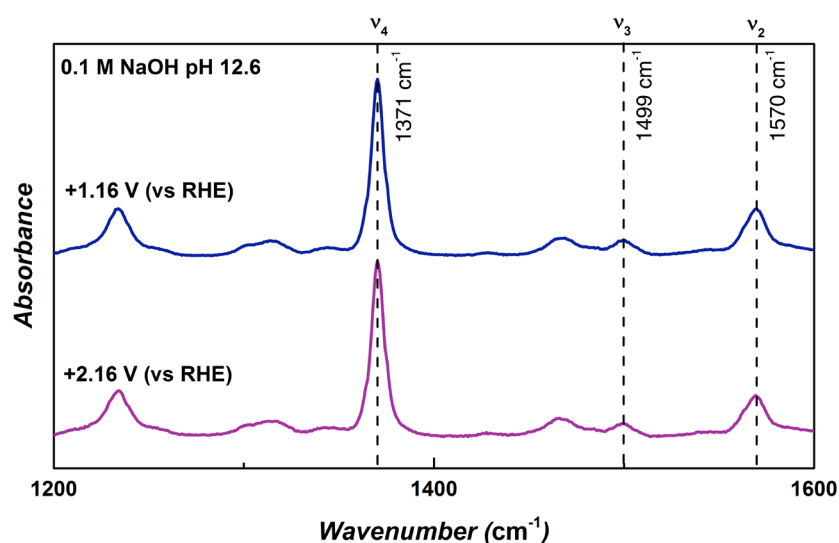


**Figure 72**

Resonance Raman spectra normalised to the  $\nu_4$  vibrational band of CoPOH immobilised on Im-functionalised m-ATO using the 'post-coordination method' in 0.1 M NaOH under constant potential electrolysis at +1.16 and + 2.16 V (vs RHE).

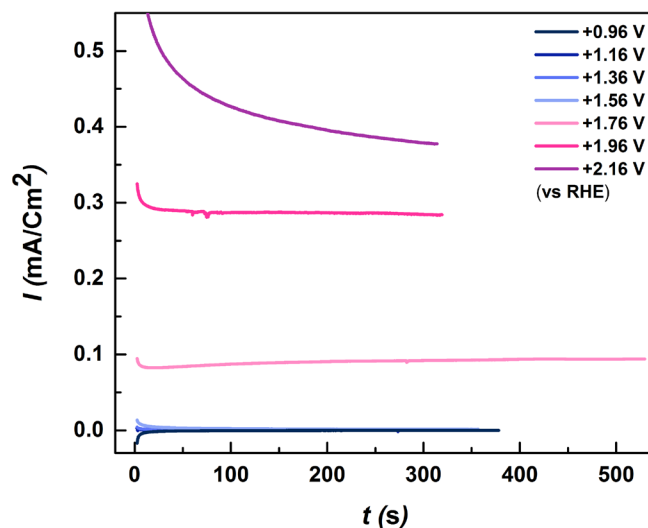
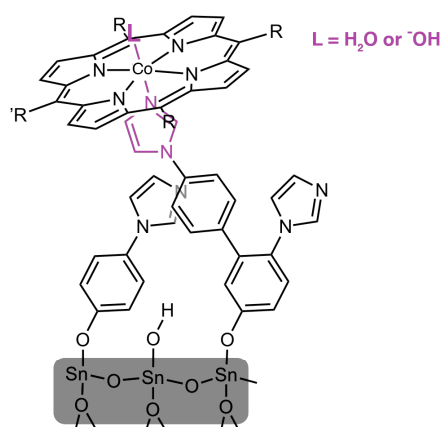


**Figure 73**

Constant potential electrolysis (CPE) at different potentials in 0.1 M NaOH for CoPOH immobilised on Im-functionalised me-ATO using the 'post-coordination' method.

For a species with a coordination number of 6, the loss of one or two of the axial ligands is a prerequisite for forming a species with a free coordination site capable of accepting a water molecule. Upon completing the OER catalytic cycle, the CoPOH species must either be 5-coordinated or once again form a 6-coordinated species with a water or hydroxide ligand (assuming the loss of the acetonitrile ligand). The resonance Raman spectra indicate that the resting species are 6-coordinated low spin. It is thus proposed that, for catalytically active species, these resting species are coordinated by an Im-linker molecule and a water or hydroxide ligand (as illustrated in Scheme 58). It is assumed that substitution of an acetonitrile ligand for a weaker ligand such as a water or a hydroxide ligand will not lower the energy difference between the  $e_g$ - and  $t_{2g}$ - orbitals so much such that a high spin configuration becomes energetically favourable.

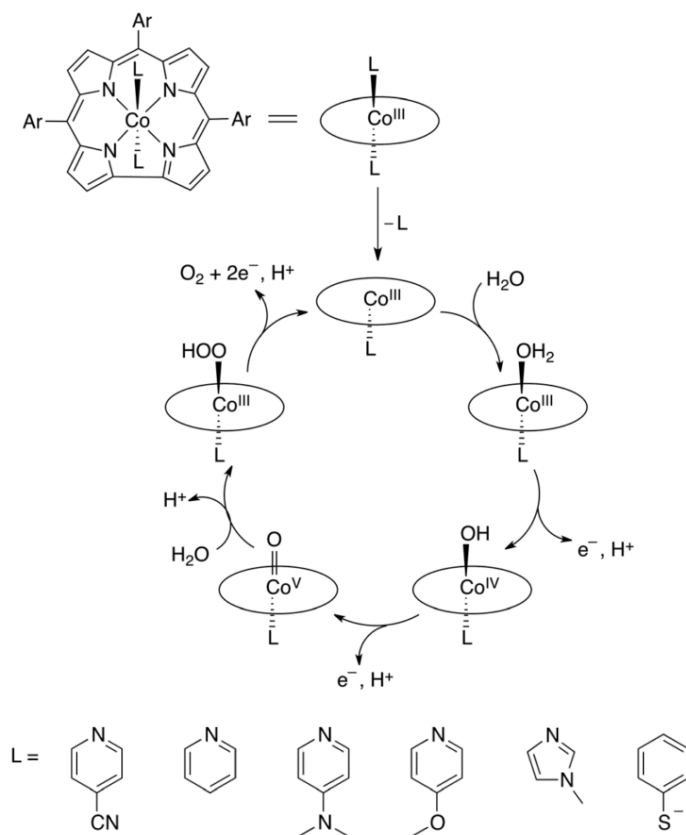


**Scheme 58**

Proposed structure of the resting species of catalytically active CoPOH molecules immobilised on me-ATO and coordinated by an Im-linker molecule and a water or hydroxide ligand.

A catalytic OER cycle mediated by axially-coordinated Co-corroles, as proposed by Cao and co-workers, is shown in Scheme 59. The nature of the axial ligands are shown to have a substantial

effect on the corroles activity for the OER, with electron-donating axial ligands leading to higher activity, which is likely the result of a strong *trans* effect weakening the  $\text{Co}^{\text{V}}$ -oxo bond and reducing the energy barrier for O-O bond formation *via* nucleophilic attack by water.<sup>257</sup>



**Scheme 59**

Catalytic oxygen evolution reaction (OER) cycle mediated by axially-coordinated Co corroles, as proposed by Cao and co-workers. Adapted from <sup>257</sup> with permission from the PCCP Owner Societies.

To determine whether or not the CoPOH species were immobilised in an electrochemically accessible manner, resonance Raman measurements were also conducted under the application of potentials lower than  $E^0(\text{Co}^{+/2+})$  ( $-0.325\text{ V}$  (vs RHE)<sup>314</sup>). Measurements were conducted in a sodium borate buffer at pH 10, the same conditions used by Kielb to measure CoPOH physisorbed on nanostructured Ag electrodes (immobilised by dip-coating) under reducing conditions using surface enhanced resonance Raman (SERR) spectroscopy.<sup>252</sup> As can be seen in Figure 74, at  $-0.7\text{ V}$  (vs RHE), there is a downward shift in the positions of the  $\nu_2$  and  $\nu_4$  bands by 2 and  $4\text{ cm}^{-1}$ , respectively. Such a downward shift in the position of the oxidation-state sensitive  $\nu_4$  band would be expected upon reduction of the initial oxidation state.<sup>315,316</sup> Furthermore, there is a significant increase in the  $\nu_2$  to  $\nu_4$  band ratio. The SERR spectra of Kielb also show such an increase in the  $\nu_2$  to  $\nu_4$  band ratio, as well as the appearance of a shoulder at  $1361\text{ cm}^{-1}$  next to the dominant peak at  $1369\text{ cm}^{-1}$  in the  $\nu_4$  band.<sup>252</sup> The downward shift in the broad  $\nu_4$  band observed in Figure 74 clearly indicates a greater contribution from a lower wavenumber component, and suggests that a greater proportion of the immobilised CoPOH species are reduced than in the work of Kielb. This observation is to be expected, given that it is highly likely that thick multilayers of CoPOH species are deposited on the Ag electrode surface by

dip-coating, whereas (close to) monolayer coverage is expected in the case of the Im-functionalised me-ATO. While the oxidation state of the Co Hangman species cannot be as easily resolved as for the Fe Hangman species, with a  $11\text{ cm}^{-1}$  difference in the  $\nu_4$  band positions of the  $\text{Fe}^{2+}$  and  $\text{Fe}^{3+}$  high spin states, it is clear that the immobilised CoPOH species are electrochemically accessible.

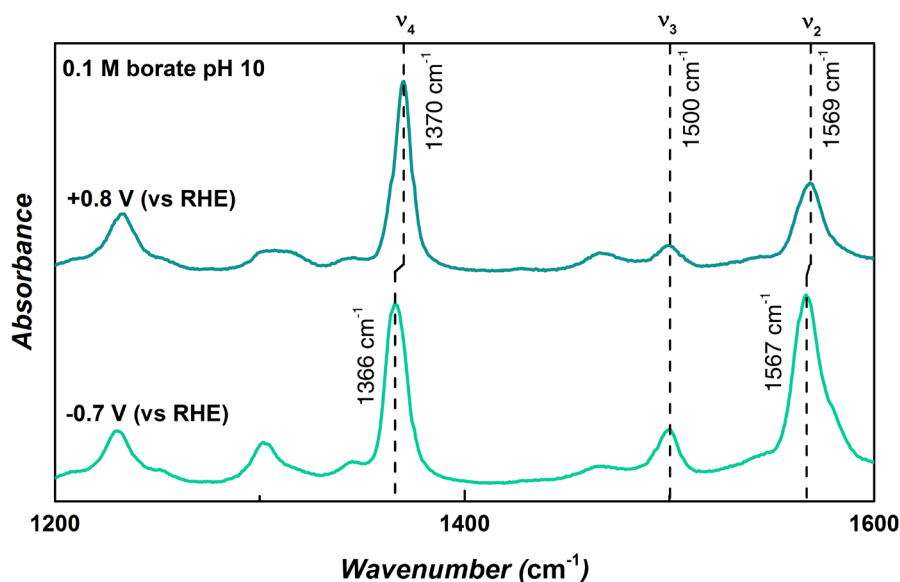


**Figure 74**

Resonance Raman spectra normalised to the  $\nu_4$  vibrational band of CoPOH immobilised on Im-functionalised me-ATO using the 'post-coordination' method in 0.1 M sodium borate buffer (pH 10) under the application of a constant potential of +0.8 and -0.7 V (vs RHE).

As shown in Figure 75, CVs were recorded of the CoPOH modified electrodes after CPE and reveal the appearance of a reversible redox peak centred at ca.  $E_{1/2} = 1.31\text{ V}$  (vs RHE) ( $\Delta E_p = 161\text{ mV}$ ). In a recent work by Sun and co-workers on the OER electrocatalytic activity of three different Co porphyrins spin-coated onto FTO substrates, an increase in OER current with an onset potential of ca.  $1.75\text{ V}$  (vs RHE) is observed upon repeated cycling in a borate buffer (pH 9.2), along with the concurrent growth of a reversible redox peak at ca.  $E_{1/2} = 1.35\text{ V}$  (vs RHE), irrespective of the porphyrin used.<sup>317</sup> The OER activity and the redox peaks remain after removing the immobilised porphyrin species by solvent rinsing. In fact, there is even a slight enhancement in the OER activity. The redox peaks were therefore assigned to the  $\text{Co}^{2+/3+}$  couple of cobalt oxide  $\text{CoO}_x$  that forms due to the decomposition of the cobalt porphyrins. Evidence for the formation of this highly active ultratrace oxide is made possible due to the use of low energy synchrotron-based XPS, which has a high surface sensitivity. While the CoPOH species immobilised on the me-ATO are not soluble in organic solvents due to axial coordination by surface-bound Im-linker molecules, and thus cannot be removed in the same way to check for activity due to oxide formation, any decomposition of bound CoPOH can be monitored using *in situ* spectroelectrochemistry.

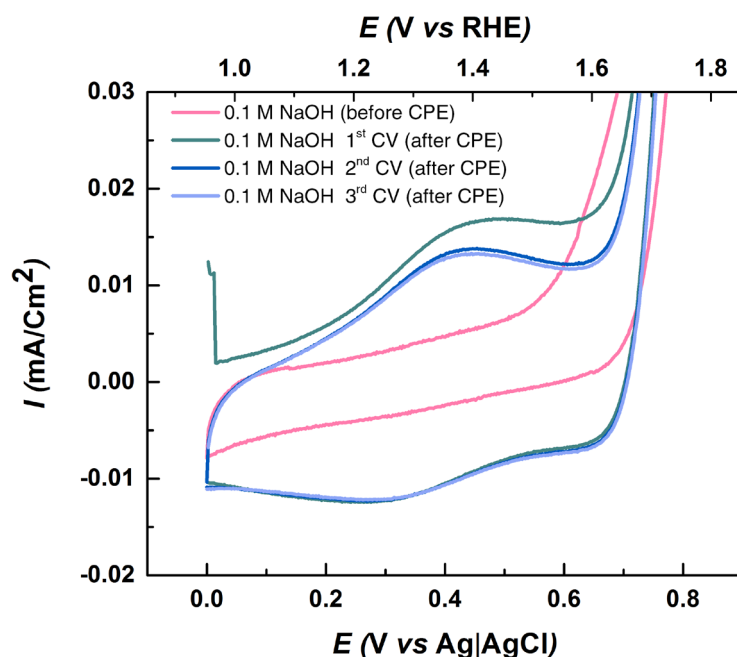


**Figure 75**

CVs in 0.1 M NaOH of the CoPOH immobilised on Im-functionalised me-ATO using the 'post-coordination' method before and after the application of constant potential electrolysis (CPE) steps in 0.1 M NaOH (see Figure 73) showing the appearance of a reversible redox peak at ca.  $E_{1/2} = 1.31$  V (vs RHE) ( $\Delta E_p = 161$  mV).

Quantitative measurements of the CoPOH species could not be made using resonance Raman spectroelectrochemistry due to fluctuating Raman intensities as a result of the movement of the rotating optical stage. As such, UV-vis spectroelectrochemistry was used instead. UV-Vis spectra were recorded in 0.1 M NaOH before and after the application of an increasing number of CVs between 0.95 and 2.15 V (vs RHE), as shown in Figure 76a and b. The UV-vis spectra show a Soret band with an absorbance maximum at 441 nm, which is similar to a maximum of 435 nm obtained for an aqueous solution of  $\text{Co}^{3+}\text{TMpyP}(4)$ , where TMpyP = tetrakis(*N*-methyl-4-pyridiniumyl).<sup>313</sup> The irreversible oxidation peak observed in the first CV can be decoupled from any substantial decomposition processes taking place at the immobilised CoPOH by virtue of the relatively insignificant change induced in the UV-Vis spectrum. The corresponding total charge passed is equivalent to  $0.8 \times 10^{-9}$  molcm<sup>-2</sup>, which compares to an estimated total coverage  $\Gamma_{\text{UV}}$  of CoPOH on the me-ATO of  $1.2 \times 10^{-9}$  molcm<sup>-2</sup>.

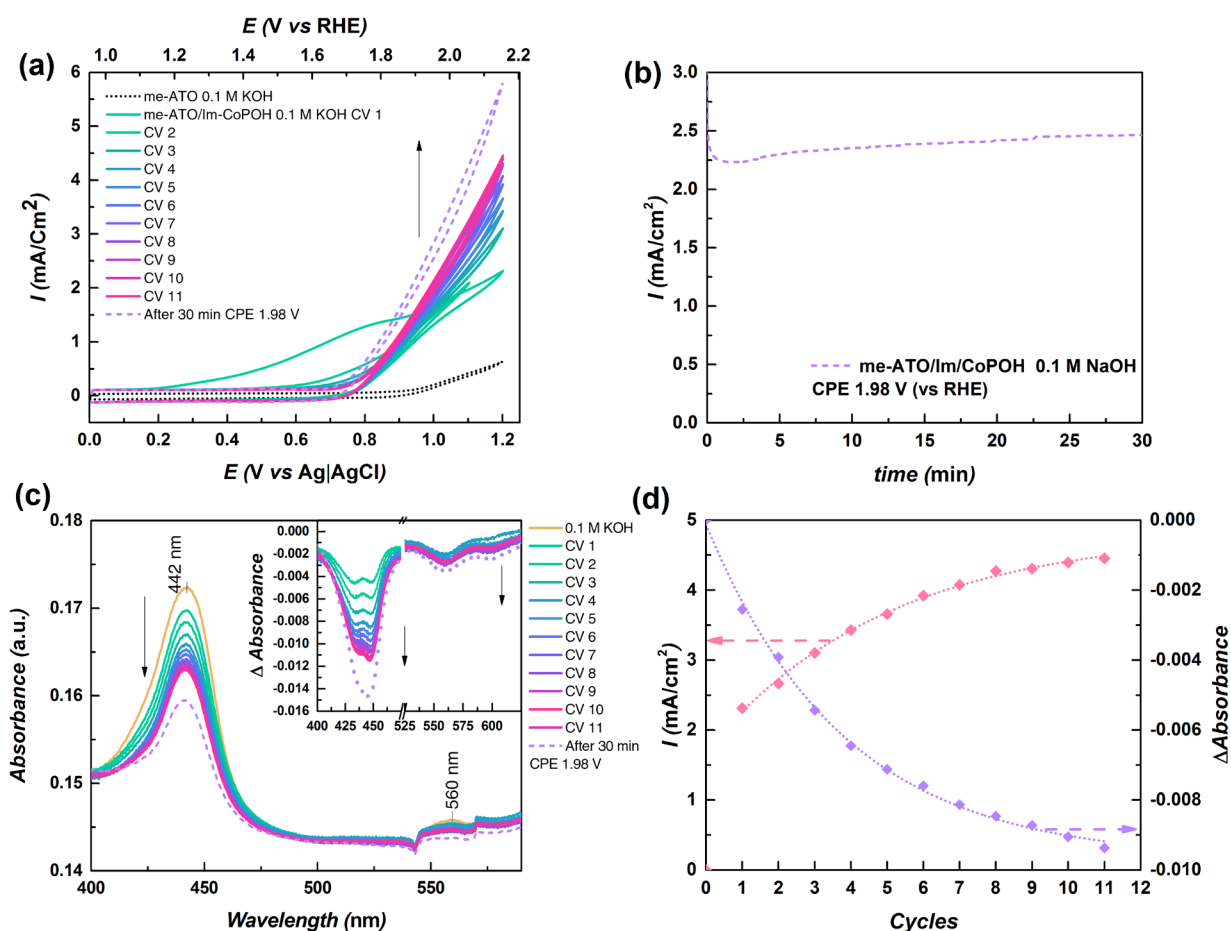


**Figure 76**

(a) 11 CVs in 0.1 M NaOH of the CoPOH immobilised on Im-functionalised me-ATO using the ‘post-coordination’ method before and after application of a 30 min CPE step at 1.98 V (vs RHE) (shown in (b)), as well as a blank CV of unmodified me-ATO. UV-Vis absorption spectra recorded before and after each CV are shown in (c), with difference spectra calculated using the first recorded spectrum shown in the inset. The maximum OER current density obtained (i.e. at 2.15 V vs RHE) during each CV is plotted in (d), alongside the corresponding change in the UV-Vis absorption intensity at 442 nm.

Both the maximum current densities for OER and the corresponding change in the UV-Vis absorption intensities at 442 nm are plotted as a function of the applied cycle number in Figure 76d. The steady increase in current density after the first CV can be correlated to a concurrent decrease in Soret band intensity, which strongly suggests that the electrochemically induced decomposition of the CoPOH leads to the formation of a new inorganic catalytic species, such as  $\text{CoO}_x$  species, as was observed by Sun and co-workers. Such species would exhibit comparatively weak UV-Vis d-d transition absorption bands and, furthermore, trace amounts of oxide would not be visible in Raman spectra without any resonance enhancement. The appearance of a single dominant Q-band at 560 nm in the UV-vis spectra in Figure 76c (and a weaker second band that is visible in the difference spectra that were calculated using the first spectrum recorded, shown in the inset) indicates the presence of a metalloporphyrin, rather than a free-base porphyrin that would display four Q-bands. There are no indications of the CoPOH transforming into the free-base porphyrin upon repeated cycling, and thus, it is likely that the porphyrin ring is oxidised upon removal of the cobalt.

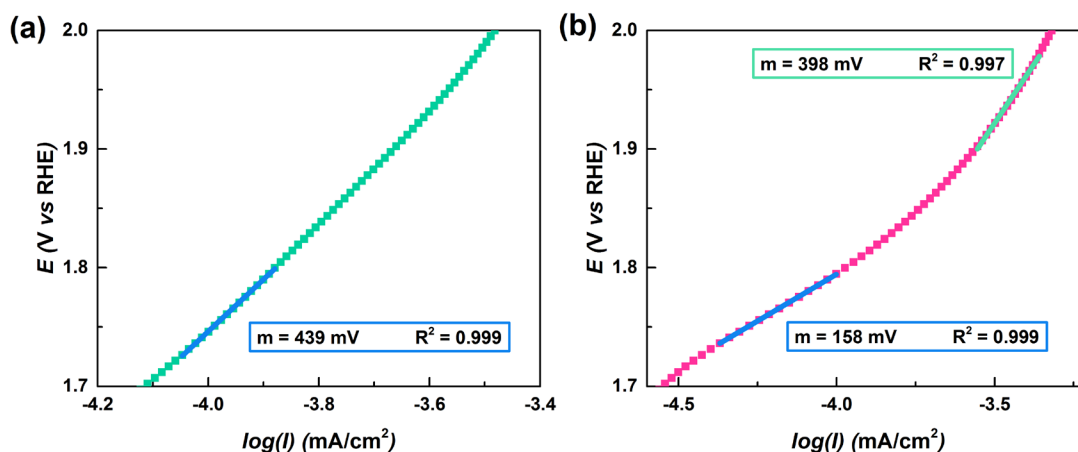


**Figure 77**

Tafel plots of the applied potential against the logarithm of the current for the oxygen evolution reaction (OER) using CoPOH immobilised on Im-functionalised me-ATO after (a) 1 CV, and after (b) 10 CVs.

It is unclear whether the initial OER catalytic current can be attributed to the immobilised CoPOH or to any trace amounts of  $\text{CoO}_x$  or other species formed during the first cycle. Tafel slope analysis was carried out after the first CV (and the disappearance of the first irreversible anodic peak), as well as after 10 CVs to determine whether or not there is a change in the OER kinetics that would be indicative of different contributions from different catalytic species. A Tafel slope of 439 mV per decade is obtained after the first CV, while after 10 CVs the Tafel slope decreases to 158 mV per decade at low overpotentials and 398 mV per decade at high overpotentials. This change clearly indicates a change in the rate determining step, and hence the OER mechanism after repeated cycling, and therefore it is proposed that most of the initial catalytic OER current is due to the immobilised CoPOH. Cobalt oxides typically exhibit Tafel slopes of between 40-60 mV per decade<sup>318–320</sup>, while single-site or molecular OER catalysts exhibit higher Tafel slopes. A Tafel slope of 118 mV per decade was obtained in pH 7 for single site Co OER catalysts immobilised directly on mesoporous ITO from a  $\text{Co}[\text{N}(\text{SiMe}_3)_2]_2$  precursor<sup>321</sup>, 183 mV per decade in pH 1 for a 3,5-bis(bipyridyl)pyrazolate-based diruthenium OER catalyst immobilised on mesoporous ITO *via* a carboxylate anchor<sup>268</sup>, ca. 120 mV in pH 7 for a perfluorinated Co phthalocyanine drop-coated on FTO<sup>256</sup>, and 120 mV in pH 7 for a Co Hangman  $\beta$ -octafluoro corrole (with carboxylic acid hanging group) in Nafion coated on FTO<sup>309</sup>. For  $[\text{Ir}(\text{pyalc})(\text{H}_2\text{O})_2(\mu\text{-O})]_2^{2+}$  (pylac = 2-(2'pyridyl)-2-propanolate) immobilised on mesoporous ITO *via* Ir-O- $\text{MO}_x$  bonds, the Tafel slope in pH 2.6 was shown to increase with the ITO film thickness, increasing from 66 mV per decade with a film thickness of 3  $\mu\text{m}$ , to 118 mV per decade for a film thickness of 11  $\mu\text{m}$ .<sup>235</sup> This increase is attributed to protons generated by the OER having to diffuse through the thicker film (at pH 2.6, the pH is less sensitive to proton production from the OER). While this may not pose as much of a problem at a pH of 12.6 and with a lower film thickness, the current densities obtained here are up to 5 times higher than those obtained with the Ir catalyst. Excluding such mass transport effects, the Tafel slope should be independent of the current magnitude. The large values obtained here for the Tafel slopes may also be the result of a higher

resistivity in the me-ATO electrode, as previously discussed in section 9.4. Again, the mesoporous ITO films in the aforementioned studies were composed of ITO nanocrystals of around 50 nm in size, and these films are expected to exhibit lower resistivities compared to the me-ATO films, which are composed of ATO nanocrystals 3-4 nm in size.

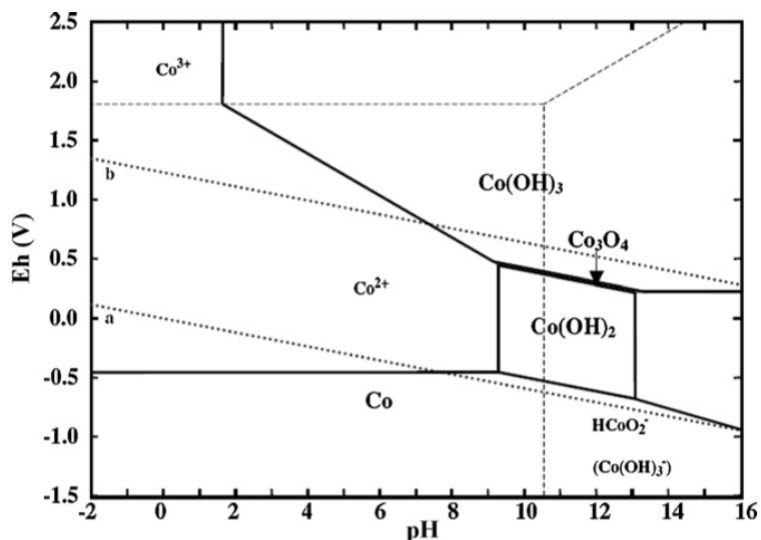


**Figure 78**

A Pourbaix diagram mapping out the possible equilibrium phases of cobalt species in an aqueous electrochemical system. Reproduced with permission from <sup>322</sup>, copyright 2008 Elsevier.

A Pourbaix diagram mapping out the possible equilibrium phases of cobalt species in an aqueous electrochemical system is shown in Figure 78. In basic pH's and at high potentials close to or greater than the thermodynamic potential for OER, cobalt is stable as an oxide or hydroxide, whereas at lower pH's or potentials it is stable as a free ion. It is proposed that the abstraction of Co ions from the porphyrin ring and the formation of Co oxides or hydroxides under anodic potentials is favoured in basic pH's, such as those used in this work and in the work of Sun and co-workers<sup>317</sup>. The decomposition of cobalt porphyrins leads to the formation of a highly active OER catalyst. Use of lower pH's is likely required in order to maintain the molecular character of cobalt porphyrin and other tetrapyrrole species under OER conditions. Fluorinated Co corroles and phthalocyanines both show higher OER activity than their non-fluorinated counterparts in the works of Rodionov and co-workers, and Nocera and co-workers. The lower overpotentials that can be obtained with these species can further stabilise their molecular character.<sup>256,309</sup>

## 6.6 Conclusions

me-ATO and p-I-ITO were used as model TCO materials and electrochemically grafted with diazonium salts in order to immobilise a range of molecular electrocatalysts on their surfaces. *In situ* potential-modulated IR measurements in the ATR mode were carried out and demonstrated that grafted diazonium interfaces on me-ATO are highly stable in a broad electrochemical stability window, encompassing the stability window of the ITO and FTO. Furthermore, these interfaces exhibit hydrolytic stability down to a pH of ca. 2.5 and good stability in highly basic pH's. This is

the first time such *in situ* IR methods have been applied with nanostructured TCO electrodes and that the stability of interfaces on TCO surfaces has been determined in such a way. *In situ* IR spectroscopy yields unprecedented information on interface formation, stability and structure that is simply not possible using conventional techniques, such as UV-vis spectroscopy or purely electrochemical methods.

A number of molecular catalysts were immobilised on pI-ITO and me-ATO, including a copper bipyridine catalyst that is active for the oxygen evolution reaction (OER), and iron and cobalt Hangman porphyrin catalysts, which are active for the oxygen reduction reaction (ORR) and the OER, respectively. As the electrografting of interfaces from diazonium salts can often result in thick, insulating layers on a range of electrode materials, strategies were developed to functionalise the oxide surfaces in a way that the immobilised molecular species are electrochemically accessible and able to take part in electrocatalysis. This is the first time that diazonium salts have been used to successfully immobilise molecular complexes on nanostructured TCO materials.

The copper-bipyridine catalyst was able to catalyse the OER with an onset potential of 1.73 V (vs RHE), which represents a lower overpotential than those reported for homogenous copper-bipyridine systems, most likely due to the electron-withdrawing substituent used to bind the complex to the ITO surface. While the catalytic currents for this system were unstable, presumably due to the loss of the copper active site, the diazonium-derived interface itself was stable under non-turnover conditions for 24 hours in 0.1 M KOH, which is highly significant given that most known anchoring groups would rapidly desorb under such basic pH's, including phosphonic acid derivatives, which are currently the most widely adopted anchoring groups used in electrocatalytic cells or photo-electrocatalytic cells. Using the iron Hangman species FePOMe, an onset potential of up to 0.81 V (vs RHE) could be obtained for the ORR for a relatively small loading of catalyst. The overpotential was shown to decrease with catalyst loading. The cobalt Hangman species CoPOH was shown to be active for the OER with an onset potential of 1.7 V (vs RHE). An increase in OER current density as a function of time/applied potential was shown to be related to the decomposition of CoPOH, which presumably forms a small amount of highly active cobalt oxide OER catalyst. It is proposed that this reaction is favoured in basic pH's.

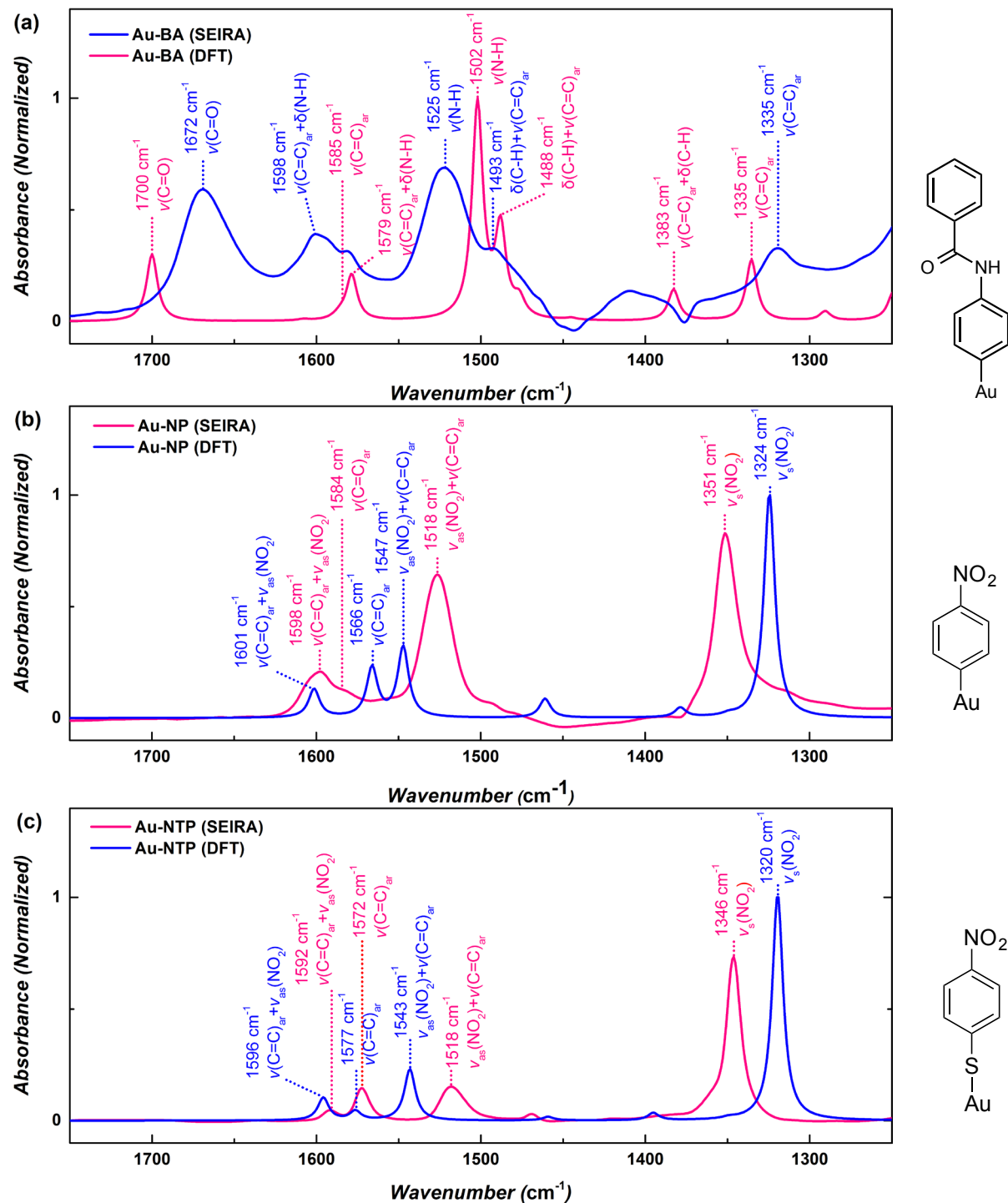
The electronic behaviour and high stabilities observed for the electrografted diazonium interfaces are likely the result of the binding motif formed with the oxide surfaces, which differs from other common anchoring groups, such as phosphonates and silanes or purely organic anchoring groups. Experimental and theoretical studies on TiO<sub>2</sub> have shown that organic carboxylate and hydroxamate anchoring groups exhibit faster interfacial electron transfer because of a better electronic coupling at the oxide interface compared to phosphonate anchoring groups.<sup>27,231,236</sup>

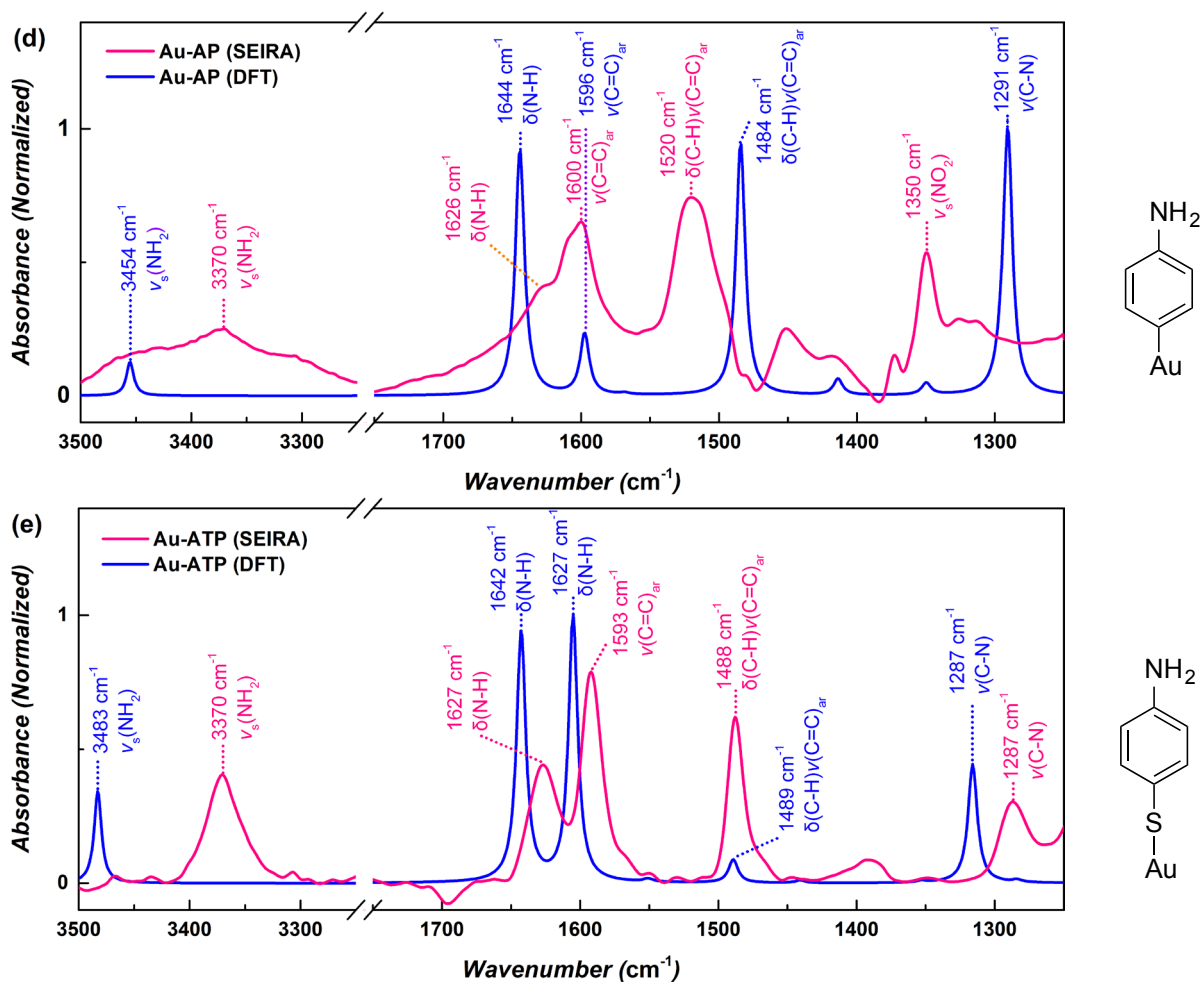
The poor coupling observed for phosphonate (and silane) anchoring groups may arise from the tetrahedral geometry of the phosphorous (or silicon) atom and the loss of conjugation through the oxide.<sup>323</sup> However, at the expense of better electronic behaviour, phosphonate and silane-derived anchoring groups exhibit greater stabilities, with phosphonate anchoring groups showing stabilities that are orders of magnitude greater than carboxylate anchoring groups.<sup>37,38</sup> That being said, phosphonates show poor stability in pH's above 5 or 6, which limits their applicability, while silanes result in bonds which are stronger and have been shown to be stable up to pH 11.<sup>25,36,38,39</sup> It is tentatively proposed that the strong M–O–C bond formed upon the electrochemical grafting of diazonium salts on oxide surfaces not only results in good electronic coupling with immobilised molecular redox species, but also provides high chemical and electrochemical stabilities. Such stabilities not attainable with other organic anchoring groups (or indeed phosphonates).

To conclude, the work here illustrates the potential for diazonium salts to be used as novel anchoring groups on metal oxides materials, e.g. for electrocatalytic applications, as well as potentially for other applications, e.g. in dye sensitised solar cells and optoelectronic devices.

# Appendices

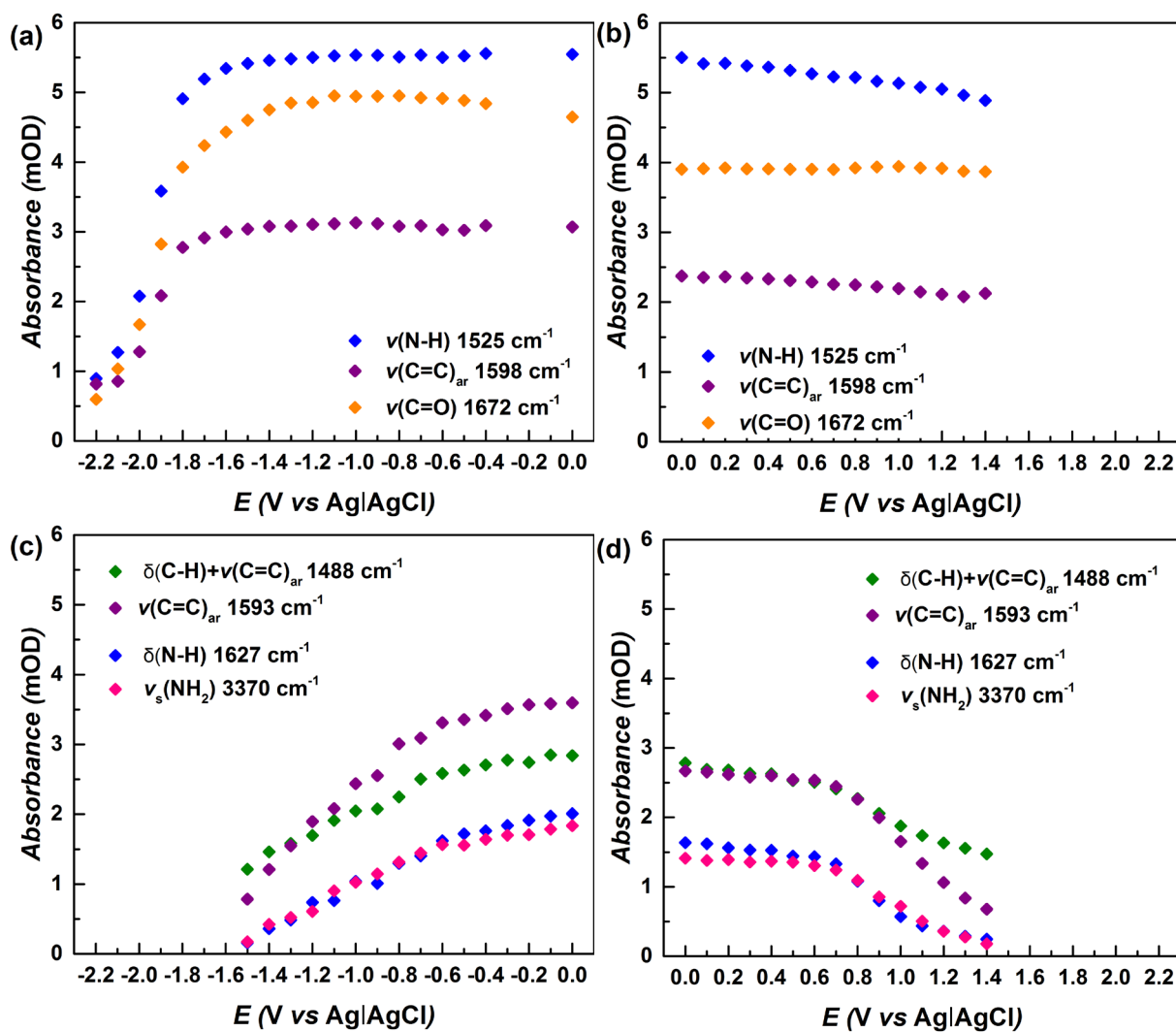
## 10.1 Appendix to chapter 4.1





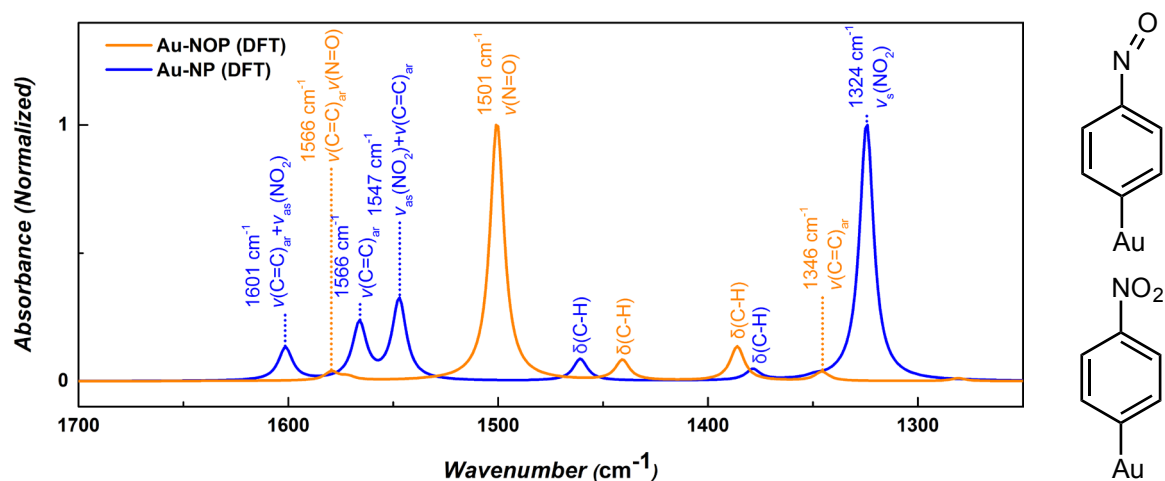
### Appendix 1

SEIRA spectra in acetonitrile and the corresponding spectra calculated using DFT of (a) interface deposited by electrochemical grafting of 1 mM 4-BABD, (b) interface deposited by electrochemical grafting of 1 mM 4-NBD, (c) SAM deposited by spontaneous grafting of 1 mM 4-NTP, (d) amino functionalised interfaces formed by the electrochemical grating of (b), (e) SAM deposited by spontaneous adsorption of 1 mM 4-ATP.



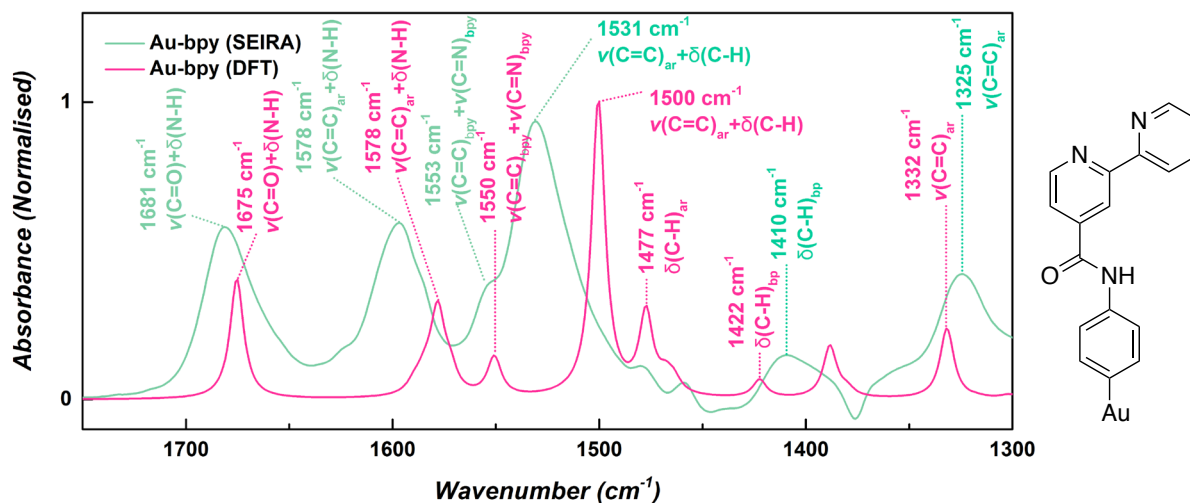
### Appendix 2

Absorption band intensity against polarisation potential during the desorption of electrografted 4-BABD diazonium interfaces in acetonitrile (0.1 M TBAP) under (a) cathodic and (b) anodic polarisation and desorption of 4-ATP SAM-derived interface under (c) cathodic and (d) anodic polarisation.



### Appendix 3

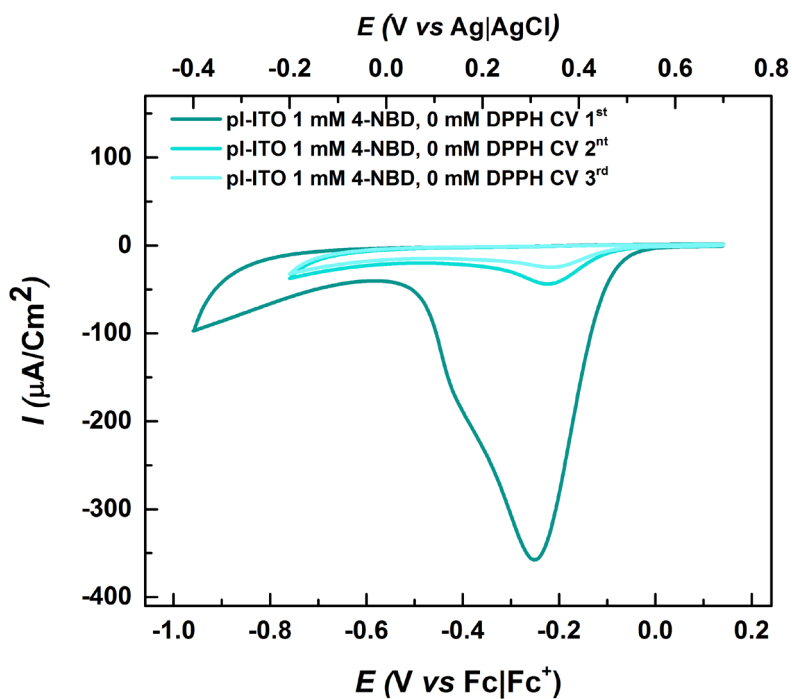
Spectra calculated using DFT of nitrobenzene-Au (Au-NP) and the partially reduced nitrosobenzene species (4-NOP).



#### Appendix 4

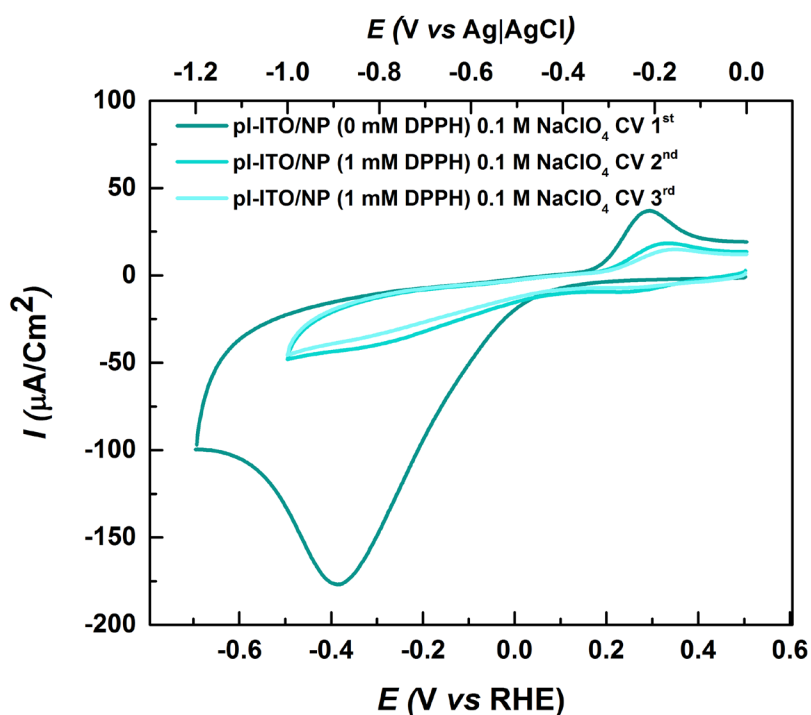
SEIRA spectrum in acetonitrile and the corresponding spectrum calculated using DFT of an interface deposited by electrochemical grafting of 1 mM bpy-diazo.

### 10.2 Appendix to chapter 4.2



#### Appendix 5

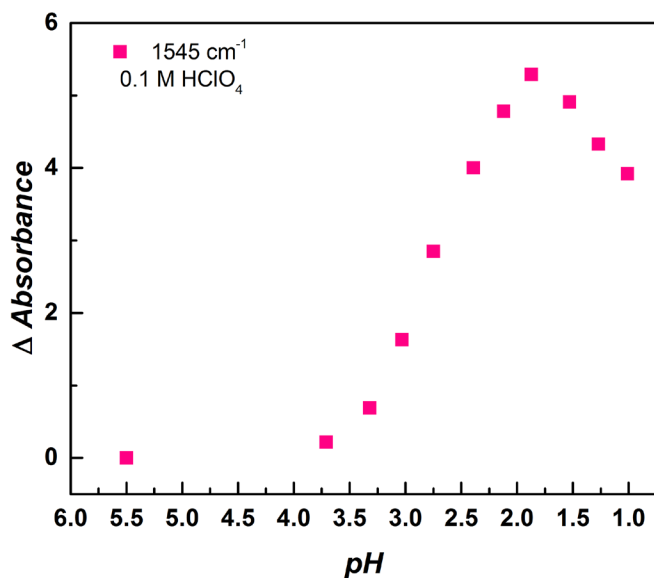
CVs of 1 mM solutions of 4-NBD in acetonitrile (0.1 M TBAP) using pl-ITO as a working electrode. Scan rate = 50 mV/s.



### Appendix 6

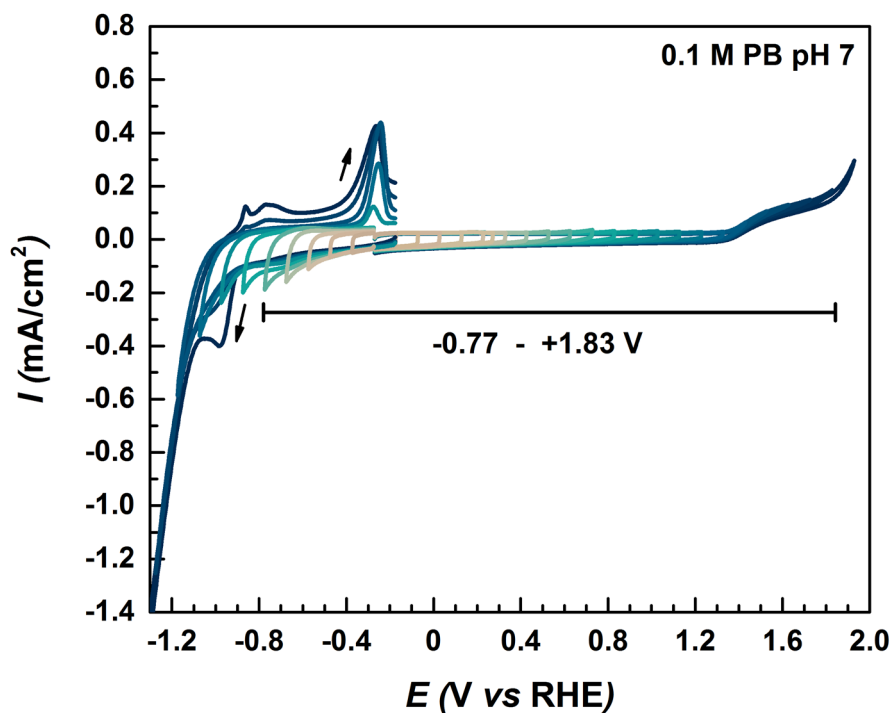
Electrochemical reduction of the nitrophenyl moieties of the interface electrografted on pI-ITO from a 1 mM solution 4-NBD with no added DPPH to aminophenyl/hydroxyaminophenyl moieties in a 0.1 M NaClO<sub>4</sub>, 1:9 ethanol:water solution.

### 10.3 Appendix to chapter 4.3



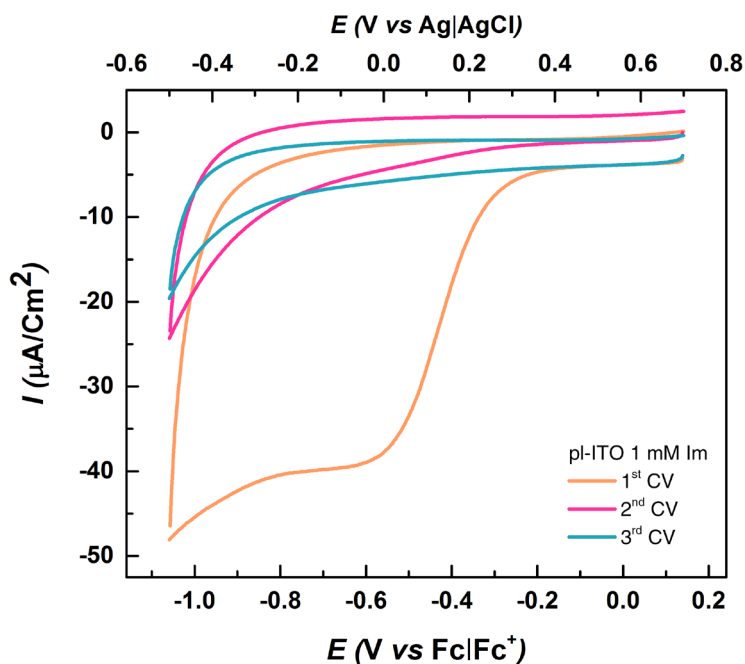
### Appendix 7

Plot of change in absorption intensity  $\Delta A$  with decreasing pH for the C-H bending mode  $\delta(\text{C-H})$  at  $1545 \text{ cm}^{-1}$ .



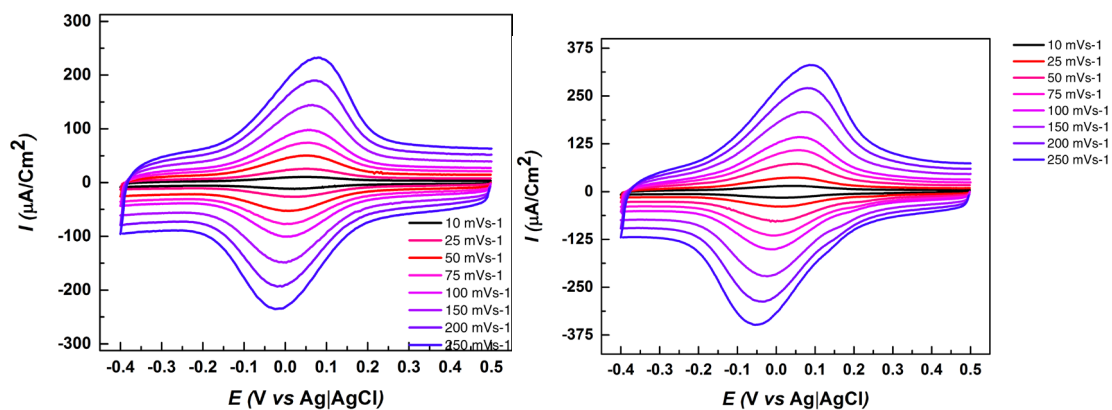
#### Appendix 8

CVs conducted in 0.1 M PB pH 7 using me-ATO as a working electrode in order to determine the stability range of the electrode. Progressive scans with increments of 0.1 V were applied in both cathodic and anodic directions originating from a potential of -0.35 V (vs RHE).



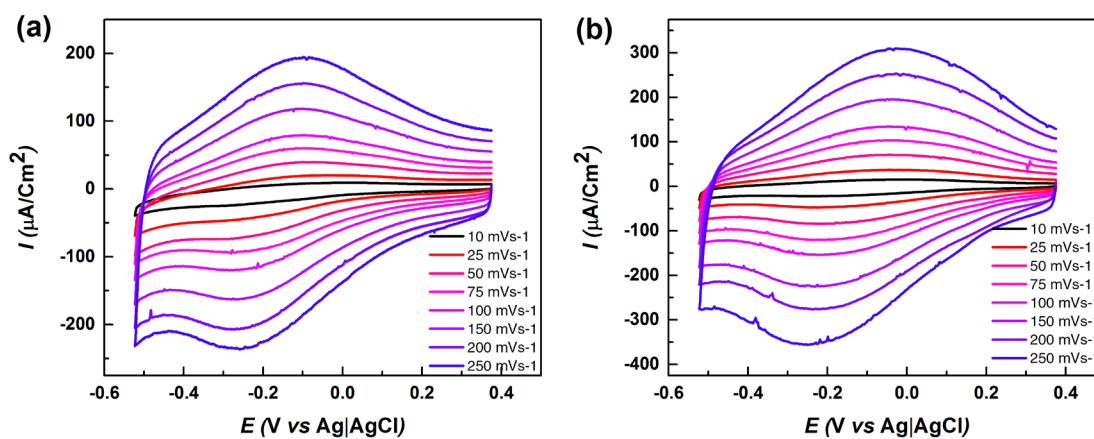
#### Appendix 9

CVs of 1 mM solutions of Im-diazo in acetonitrile (0.1 M TBAP) using pl-ITO as a working electrode. Scan rate = 50 mV/s.



### Appendix 10

CVs in acetonitrile (0.1 M TBAP) of FePOME immobilised on me-ATO modified using 'post-coordination' (method A) (left) and 'pre-coordination' (method B) (right) at different scan rates.



### Appendix 11

CVs in pH 7 (0.1 M PB) of FePOME immobilised on me-ATO modified using (a) 'post-coordination' (method A) and (b) 'pre-coordination' (method B) at different scan rates.

## Bibliography

1. Bleich, K. & Guimaraes, R. D. *Renewable Infrastructure Investment Handbook: A Guide for Institutional Investors*. (2016).
2. Tatin, A., Bonin, J. & Robert, M. A Case for Electrofuels. *ACS Energy Lett.* **1**, 1062–1064 (2016).
3. Misson, M., Zhang, H. & Jin, B. Nanobiocatalyst advancements and bioprocessing applications. *J. R. Soc. Interface* **12**, 20140891–20140891 (2014).
4. Oh, H. S., Nong, H. N. & Strasser, P. Preparation of mesoporous Sb-, F-, and in-doped SnO<sub>2</sub> bulk powder with high surface area for use as catalyst supports in electrolytic cells. *Adv. Funct. Mater.* **25**, 1074–1081 (2015).
5. Willkomm, J. *et al.* Dye-sensitized semiconductors modified with molecular catalysts for light-driven H<sub>2</sub> production. *Chem. Soc. Rev* **45**, 9–23 (2016).
6. Brennaman, M. K. *et al.* Finding the Way to Solar Fuels with Dye-Sensitized Photoelectrosynthesis Cells. *J. Am. Chem. Soc.* **138**, 13085–13102 (2016).
7. Materna, K. L., Crabtree, R. H. & Brudvig, G. W. Anchoring groups for photocatalytic water oxidation on metal oxide surfaces. *Chemical Society Reviews* **46**, 6099–6110 (2017).
8. Solymar, L. & Walsh, D. *Lectures on the electrical properties of materials*. (Oxford University Press, 1993).
9. Parker, G. *Introductory Semiconductor Device Physics*. (Institute of Physics Publishing, 2004).
10. Grahn, H. T. *Introduction to Semiconductor Physics*. (World Scientific, 1999).
11. Krol, R. in *Photoelectrochemical Hydrogen Production SE - 2* (eds. van de Krol, R. & Grätzel, M.) **102**, 13–67 (Springer US, 2012).
12. Gellings, P. J. & Bouwmeester, H. J. M. *The CRC Handbook of Solid State Electrochemistry*. (Taylor & Francis, 1997).
13. Kröger, F. A. & Vink, H. J. Relations between the Concentrations of Imperfections in Crystalline Solids. *Solid State Phys. - Adv. Res. Appl.* **3**, 307–435 (1956).
14. González, G. B. Investigating the Defect Structures in Transparent Conducting Oxides Using X-ray and Neutron Scattering Techniques. *Materials (Basel)*. **5**, 818–850 (2012).
15. Giménez, S. & Bisquert, J. *Photoelectrochemical solar fuel production: from basic principles to advanced devices*. (Springer, 2016).
16. Schmickler, W. & Santos, E. *Interfacial electrochemistry*. (Springer, 2010). doi:10.1007/978-3-642-04937-8
17. Bard, A. J. & Faulkner, L. R. *Electrochemical Methods: Fundamentals and Applications, 2nd Edition*. (John Wiley & Sons, 2001). doi:10.1016/j.aca.2010.06.020
18. Memming, R. *Semiconductor Electrochemistry. Semiconductor Electrochemistry* (Wiley-VCH Verlag GmbH & Co. KGaA, 2015). doi:10.1002/9783527688685
19. Zoski, C. G. *Handbook of electrochemistry. Handbook of Electrochemistry* (Elsevier, 2007). doi:10.1016/B978-0-444-51958-0.X5000-9
20. Shinagawa, T., Garcia-Esparza, A. T. & Takanabe, K. Insight on Tafel slopes from a microkinetic analysis of aqueous electrocatalysis for energy conversion. *Sci. Rep.* **5**, 13801 (2015).
21. Edwards, G. A., Bergren, A. J. & Porter, M. D. in *Handbook of Electrochemistry* 295–327 (2007). doi:10.1016/B978-044451958-0.50021-5
22. Scheres, L., Giesbers, M. & Zuilhof, H. Self-assembly of organic monolayers onto hydrogen-terminated silicon: 1-alkynes are better than 1-alkenes. *Langmuir* **26**, 10924–10929 (2010).
23. Li, Y. & Zuilhof, H. Photochemical grafting and patterning of organic monolayers on indium tin oxide substrates. *Langmuir* **28**, 5350–9 (2012).

24. Müller, V., Haase, F., Rathousky, J. & Fattakhova-Rohlfing, D. Surface functionalization of mesoporous antimony doped tin oxide by metalorganic reaction. *Mater. Chem. Phys.* **137**, 207–212 (2012).
25. Brennan, B. J. *et al.* Comparison of silatrane, phosphonic acid, and carboxylic acid functional groups for attachment of porphyrin sensitizers to TiO<sub>2</sub> in photoelectrochemical cells. *Phys. Chem. Chem. Phys.* **15**, 16605 (2013).
26. Zhang, L. & Cole, J. M. Anchoring groups for dye-sensitized solar cells. *ACS Applied Materials and Interfaces* **7**, 3427–3455 (2015).
27. Li, W. *et al.* What makes hydroxamate a promising anchoring group in dye-sensitized solar cells? Insights from theoretical investigation. *J. Phys. Chem. Lett.* **5**, 3992–3999 (2014).
28. McNamara, W. R. *et al.* Acetylacetonate anchors for robust functionalization of TiO<sub>2</sub> nanoparticles with Mn(II)-terpyridine complexes. *J. Am. Chem. Soc.* **130**, 14329–14338 (2008).
29. Takeshita, N., Okuno, M. & Ishibashi, T. Molecular conformation of DPPC phospholipid Langmuir and Langmuir–Blodgett monolayers studied by heterodyne-detected vibrational sum frequency generation spectroscopy. *Phys. Chem. Chem. Phys.* **19**, 2060–2066 (2017).
30. Love, J. C., Estroff, L. A., Kriebel, J. K., Nuzzo, R. G. & Whitesides, G. M. Self-assembled monolayers of thiolates on metals as a form of nanotechnology. *Chem. Rev.* **105**, 1103–1169 (2005).
31. Pujari, S. P., Scheres, L., Marcelis, A. T. M. & Zuilhof, H. Covalent surface modification of oxide surfaces. *Angew. Chemie - Int. Ed.* **53**, 6322–6356 (2014).
32. Zaba, T. *et al.* Formation of Highly Ordered Self-Assembled Monolayers of Alkynes on Au(111) Substrate. *J. Am. Chem. Soc.* **136**, 11918–11921 (2014).
33. Guerrero, G., Alauzun, J. G., Granier, M., Laurencin, D. & Mutin, P. H. Phosphonate coupling molecules for the control of surface/interface properties and the synthesis of nanomaterials. *Dalt. Trans.* **42**, 12569–12585 (2013).
34. Brumbach, M. & Armstrong, N. R. in *Encyclopedia of Electrochemistry* (Wiley-VCH Verlag GmbH & Co. KGaA, 2007). doi:10.1002/9783527610426.bard100101
35. Li, J. *et al.* Characterization of transparent conducting oxide surfaces using self-assembled electroactive monolayers. *Langmuir* **24**, 5755–65 (2008).
36. Materna, K. L., Brennan, B. J. & Brudvig, G. W. Silatranes for binding inorganic complexes to metal oxide surfaces. *Dalt. Trans.* **44**, 20312–20315 (2015).
37. Péchy, P. *et al.* Preparation of phosphonated polypyridyl ligands to anchor transition-metal complexes on oxide surfaces: application for the conversion of light to electricity with nanocrystalline TiO<sub>2</sub> films. *J. Chem. Soc., Chem. Commun.* **0**, 65–66 (1995).
38. Gillaizeau-Gauthier, I. *et al.* Phosphonate-based bipyridine dyes for stable photovoltaic devices. *Inorg. Chem.* **40**, 6073–6079 (2001).
39. Bae, E. *et al.* Effects of surface anchoring groups (Carboxylate vs Phosphonate) in ruthenium-complex-sensitized TiO<sub>2</sub> on visible light reactivity in aqueous suspensions. *J. Phys. Chem. B* **108**, 14093–14101 (2004).
40. Bélanger, D. & Pinson, J. Electrografting: a powerful method for surface modification. *Chem. Soc. Rev.* **40**, 3995–4048 (2011).
41. Adenier, A., Chehimi, M. M., Gallardo, I., Pinson, J. & Vilà, N. Electrochemical oxidation of aliphatic amines and their attachment to carbon and metal surfaces. *Langmuir* **20**, 8243–53 (2004).
42. Palacin, S. *et al.* Molecule-to-metal bonds: Electrografting polymers on conducting surfaces. *ChemPhysChem* **5**, 1468–1481 (2004).
43. Allongue, P. *et al.* Covalent modification of carbon surfaces by aryl radicals generated from the electrochemical reduction of diazonium salts. *J. Am. Chem. Soc.* **114**, 5883–5884 (1992).
44. Downard, A. J. Electrochemically assisted covalent modification of carbon electrodes. *Electroanalysis* **12**, 1085–1096 (2000).

45. Mahouche-Chergui, S., Gam-Derouich, S., Mangeney, C. & Chehimi, M. M. Aryl diazonium salts: a new class of coupling agents for bonding polymers, biomacromolecules and nanoparticles to surfaces. *Chem. Soc. Rev.* **40**, 4143–4166 (2011).
46. Tanaka, M., Sawaguchi, T., Sato, Y., Yoshioka, K. & Niwa, O. Surface modification of GC and HOPG with diazonium, amine, azide, and olefin derivatives. *Langmuir* **27**, 170–178 (2011).
47. Gross, A. J. *et al.* Nickel (II) tetraphenylporphyrin modified surfaces via electrografting of an aryldiazonium salt. *Electrochem. commun.* **13**, 1236–1239 (2011).
48. Li, Z., Yan, W. & Dai, S. Surface functionalization of ordered mesoporous carbons - A comparative study. *Langmuir* **21**, 11999–12006 (2005).
49. Griveau, S., Mercier, D., Vautrinul, C. & Chausse, a. Electrochemical grafting by reduction of 4-aminoethylbenzenediazonium salt: Application to the immobilization of (bio)molecules. *Electrochem. commun.* **9**, 2768–2773 (2007).
50. Ghilane, J. *et al.* Indirect reduction of aryldiazonium salts onto cathodically activated platinum surfaces: Formation of metal-organic structures. *Langmuir* **21**, 6422–6429 (2005).
51. Guselnikova, O. *et al.* Surface modification of Au and Ag plasmonic thin films via diazonium chemistry: Evaluation of structure and properties. *Colloids Surf., A* **516**, 274–285 (2017).
52. Mesnage, A., Lefèvre, X., Jégou, P., Deniau, G. & Palacin, S. Spontaneous grafting of diazonium salts: chemical mechanism on metallic surfaces. *Langmuir* **28**, 11767–78 (2012).
53. Chen, M., Kobashi, K., Chen, B., Lu, M. & Tour, J. M. Functionalized self-assembled InAs/CaAs quantum-dot structures hybridized with organic molecules. *Adv. Funct. Mater.* **20**, 469–475 (2010).
54. Agnès, C. *et al.* XPS study of ruthenium tris-bipyridine electrografted from diazonium salt derivative on microcrystalline boron doped diamond. *Phys. Chem. Chem. Phys.* **11**, 11647 (2009).
55. Maldonado, S. *et al.* Surface modification of indium tin oxide via electrochemical reduction of aryldiazonium cations. *Langmuir* **22**, 2884–91 (2006).
56. Adenier, A. *et al.* Study of the spontaneous formation of organic layers on carbon and metal surfaces from diazonium salts. *Surf. Sci.* **600**, 4801–4812 (2006).
57. Lamberti, F. *et al.* Surface functionalization of fluorine-doped tin oxide samples through electrochemical grafting. *ACS Appl. Mater. Interfaces* **5**, 12887–94 (2013).
58. Lund, T., Nguyen, P. T. & Ruhland, T. Electrochemical grafting of TiO<sub>2</sub>-based photo-anodes and its effect in dye-sensitized solar cells. *J. Electroanal. Chem.* **758**, 85–92 (2015).
59. Bureau, C. & Pinson, J. Method for modifying insulating or semi-conductive surfaces, and resulting products. *European Patent Application 1948720* (2006).
60. Combellas, C. *et al.* Surface modification of halogenated polymers. 4. Functionalisation of poly(tetrafluoroethylene) surfaces by diazonium salts. *Polymer (Guildf)*. **44**, 19–24 (2003).
61. Chehimi, M. M. Aryl diazonium salts: new coupling agents in polymer and surface science. (2012).
62. Laforgue, A., Addou, T. & Bélanger, D. Characterization of the Deposition of Organic Molecules at the Surface of Gold by the Electrochemical Reduction of Aryldiazonium Cations. *Langmuir* **21**, 6855–65 (2005).
63. McKone, J. R., Lewis, N. S. & Gray, H. B. Will solar-driven water-splitting devices see the light of day? *Chemistry of Materials* **26**, 407–414 (2014).
64. McKone, J. R., Marinescu, S. C., Brunschwig, B. S., Winkler, J. R. & Gray, H. B. Earth-abundant hydrogen evolution electrocatalysts. *Chem. Sci.* **5**, 865–878 (2014).
65. Reisner, E., Windle, C. D. & Reisner, E. Heterogenised Molecular Catalysts for the Reduction of CO<sub>2</sub> to Fuels. *Chimia (Aarau)*. **69**, 435–441 (2015).
66. Blakemore, J. D., Crabtree, R. H. & Brudvig, G. W. Molecular Catalysts for Water Oxidation. *Chemical Reviews* **115**, 12974–13005 (2015).

67. Haddad, A. Z., Garabato, B. D., Kozlowski, P. M., Buchanan, R. M. & Grapperhaus, C. A. Beyond metal-hydrides: Non-transition-metal and metal-free ligand-centered electrocatalytic hydrogen evolution and hydrogen oxidation. *J. Am. Chem. Soc.* **138**, 7844–7847 (2016).
68. V. Dolganov, A. Metal-free Electrocatalyst for Hydrogen Production from Water. *Int. J. Electrochem. Sci.* **1111**, 9559–9565 (2016).
69. Reuillard, B. *et al.* Tuning Product Selectivity for Aqueous CO<sub>2</sub> Reduction with a Mn(bipyridine)-pyrene Catalyst Immobilized on a Carbon Nanotube Electrode. *J. Am. Chem. Soc.* **139**, 14425–14435 (2017).
70. Muresan, N. M., Willkomm, J., Mersch, D., Vaynzof, Y. & Reisner, E. Immobilization of a molecular cobaloxime catalyst for hydrogen evolution on a mesoporous metal oxide electrode. *Angew. Chemie - Int. Ed.* **51**, 12749–12753 (2012).
71. DeKrafft, K. E. *et al.* Electrochemical water oxidation with carbon-grafted iridium complexes. *ACS Appl. Mater. Interfaces* **4**, 608–613 (2012).
72. Goff, A. Le *et al.* From hydrogenases to noble metal-free catalytic nanomaterials for H<sub>2</sub> production and uptake. *Science* **326**, 1384–1387 (2009).
73. Tong, L., Göthelid, M. & Sun, L. Oxygen evolution at functionalized carbon surfaces: a strategy for immobilization of molecular water oxidation catalysts. *Chem. Commun.* **48**, 10025 (2012).
74. Gentil, S. *et al.* Electrocatalytic O<sub>2</sub> Reduction at a Bio-inspired Mononuclear Copper Phenolato Complex Immobilized on a Carbon Nanotube Electrode. *Angew. Chemie - Int. Ed.* **55**, 2517–2520 (2016).
75. Elgrishi, N., Griveau, S., Chambers, M. B., Bedioui, F. & Fontecave, M. Versatile functionalization of carbon electrodes with a polypyridine ligand: metallation and electrocatalytic H(+) and CO<sub>2</sub> reduction. *Chem. Commun.* **51**, 2995–8 (2015).
76. Polsky, R. *et al.* Diazonium-functionalized horseradish peroxidase immobilized via addressable electrodeposition: Direct electron transfer and electrochemical detection. *Langmuir* **23**, 364–366 (2007).
77. Barbosa, O. *et al.* Glutaraldehyde in bio-catalysts design: a useful crosslinker and a versatile tool in enzyme immobilization. *RSC Adv.* **4**, 1583–1600 (2014).
78. Liu, F., Tao, G. & Zhuo, R. Synthesis of thermal phase separating reactive polymers and their applications in immobilized enzymes. *Polym. J. (Tokyo, Japan)* **25**, 561–567 (1993).
79. Putzbach, W. & Ronkainen, N. J. Immobilization techniques in the fabrication of nanomaterial-based electrochemical biosensors: A review. *Sensors* **13**, 4811–4840 (2013).
80. Guisan, J. M. *Immobilization of Enzymes and Cells 3rd Edition.* (Humana Press, 2013). doi:10.1007/978-1-62703-550-7
81. Secundo, F. Conformational changes of enzymes upon immobilisation. *Chem. Soc. Rev.* **42**, 6250 (2013).
82. Pace, C. N., Grimsley, G. R. & Scholtz, J. M. Protein ionizable groups: pK values and their contribution to protein stability and solubility. *Journal of Biological Chemistry* **284**, 13285–13289 (2009).
83. Talasaz, A. H. *et al.* Prediction of protein orientation upon immobilization on biological and nonbiological surfaces. *Proc. Natl. Acad. Sci. U. S. A.* **103**, 14773–8 (2006).
84. Heidary, N. IR spectro-electrochemistry of an adsorbed oxygen-tolerant [NiFe] hydrogenase on conductive surfaces. (2016).
85. Heidary, N. *et al.* Orientation-Controlled Electrocatalytic Efficiency of an Adsorbed Oxygen-Tolerant Hydrogenase. *PLoS One* **10**, e0143101 (2015).
86. Petek, M., Neal, T. E. & Murray, R. W. Spectroelectrochemistry. Application of Optically Transparent Minigrad Electrodes under Semi-Infinite Diffusion Conditions. *Anal. Chem.* **43**, 1069–1074 (1971).
87. Lindon, J. C., Tranter, G. E. & Koppenaal, D. W. Encyclopedia of spectroscopy and spectrometry. (2016).

88. Valeur, B. & Service), W. I. (Online. *Molecular fluorescence: principles and applications*. (Wiley-VCH, 2001).
89. Li, H. H. Refractive index of silicon and germanium and its wavelength and temperature derivatives. *J. Phys. Chem. Ref. Data* **9**, 561–658 (1980).
90. Li, H. H. Refractive Index of ZnS, ZnSe, and ZnTe and Its Wavelength and Temperature Derivatives. *J. Phys. Chem. Ref. Data* **13**, 103–150 (1984).
91. König, T. A. F. *et al.* Electrically tunable plasmonic behavior of nanocube-polymer nanomaterials induced by a redox-active electrochromic polymer. *ACS Nano* **8**, 6182–6192 (2014).
92. Mohamed, H. A. Properties of pure and light antimony-doped tin oxide thin films prepared by e-beam technique. *Optoelectron. Adv. Mater. Rapid Commun.* **3**, 936–941 (2009).
93. McQuillan, A. J. The discovery of surface-enhanced Raman scattering. *Notes Rec. R. Soc.* **63**, 105–109 (2009).
94. Osawa, M. in *Near-Field Optics and Surface Plasmon Polaritons* (ed. Kawata, S.) 163–187 (Springer, 2001). doi:10.1007/3-540-44552-8\_9
95. Chalmers, J. & Griffiths, P. R. *Handbook of vibrational spectroscopy*. (Wiley, 2002).
96. Vincent, K. A., Parkin, A. & Armstrong, F. A. Investigating and exploiting the electrocatalytic properties of hydrogenases. *Chemical Reviews* **107**, 4366–4413 (2007).
97. Mazurenko, I., Wang, X., de Poulpique, A. & Lojou, E. H<sub>2</sub>/O<sub>2</sub> enzymatic fuel cells: from proof-of-concept to powerful devices. *Sustain. Energy Fuels* **1**, 1475–1501 (2017).
98. Wait, A. F., Parkin, A., Morley, G. M., Dos Santos, L. & Armstrong, F. A. Characteristics of enzyme-based hydrogen fuel cells using an oxygen-tolerant hydrogenase as the anodic catalyst. *J. Phys. Chem. C* **114**, 12003–12009 (2010).
99. Kim, D.-H. & Kim, M.-S. Hydrogenases for biological hydrogen production. *Bioresour. Technol.* **102**, 8423–8431 (2011).
100. Reisner, E. Solar hydrogen evolution with hydrogenases: From natural to hybrid systems. *European Journal of Inorganic Chemistry* **2011**, 1005–1016 (2011).
101. Sakai, T., Mersch, D. & Reisner, E. Photocatalytic hydrogen evolution with a hydrogenase in a mediator-free system under high levels of oxygen. *Angew. Chemie - Int. Ed.* **52**, 12313–12316 (2013).
102. Mersch, D. *et al.* Wiring of Photosystem II to Hydrogenase for Photoelectrochemical Water Splitting. *J. Am. Chem. Soc.* **137**, 8541–8549 (2015).
103. Lubitz, W., Ogata, H., Rüdiger, O. & Reijerse, E. Hydrogenases. *Chemical Reviews* **114**, 4081–4148 (2014).
104. Murphy, B. J., Sargent, F. & Armstrong, F. A. Transforming an oxygen-tolerant [NiFe] uptake hydrogenase into a proficient, reversible hydrogen producer. *Energy Environ. Sci.* **7**, 1426–1433 (2014).
105. Fritsch, J. *et al.* The crystal structure of an oxygen-tolerant hydrogenase uncovers a novel iron-sulphur centre. *Nature* **479**, 249–52 (2011).
106. Lenz, O. *et al.* H<sub>2</sub> conversion in the presence of O<sub>2</sub> as performed by the membrane-bound [NiFe]-Hydrogenase of *Ralstonia eutropha*. *ChemPhysChem* **11**, 1107–1119 (2010).
107. Evans, R. M. & Armstrong, F. A. in *Methods in molecular biology (Clifton, N.J.)* **1122**, 73–94 (2014).
108. Cracknell, J. A., Wait, A. F., Lenz, O., Friedrich, B. & Armstrong, F. A. A kinetic and thermodynamic understanding of O<sub>2</sub> tolerance in [NiFe]-hydrogenases. *Proc. Natl. Acad. Sci. U. S. A.* **106**, 20681–20686 (2009).
109. Goris, T. *et al.* A unique iron-sulfur cluster is crucial for oxygen tolerance of a [NiFe]-hydrogenase. *Nat. Chem. Biol.* **7**, 310–318 (2011).
110. Frielingsdorf, S. *et al.* Reversible [4Fe-3S] cluster morphing in an O<sub>2</sub>-tolerant [NiFe]

- hydrogenase. *Nat. Chem. Biol.* **10**, 378–385 (2014).
111. Eckermann, A. L., Feld, D. J., Shaw, J. A. & Meade, T. J. Electrochemistry of redox-active self-assembled monolayers. *Coord. Chem. Rev.* **254**, 1769–1802 (2010).
  112. Sezer, M., Millo, D., Weidinger, I. M., Zebger, I. & Hildebrandt, P. Analyzing the catalytic processes of immobilized redox enzymes by vibrational spectroscopies. *IUBMB Life* **64**, 455–464 (2012).
  113. Cracknell, J. a, Vincent, K. a & Armstrong, F. a. Enzymes as working or inspirational electrocatalysts for fuel cells and electrolysis. *Chem. Rev.* **108**, 2439–61 (2008).
  114. Patil, S. A., Hasan, K., Leech, D., Hägerhäll, C. & Gorton, L. Improved microbial electrocatalysis with osmium polymer modified electrodes. *Chem. Commun.* **48**, 10183 (2012).
  115. Plumeré, N. *et al.* A redox hydrogel protects hydrogenase from high-potential deactivation and oxygen damage. *Nat. Chem.* **6**, 822–827 (2014).
  116. Zagal, J. H., Bedioui, F. & Dodelet, J.-P. *N4-macrocyclic metal complexes*. (Springer Science & Business Media, 2006).
  117. Zagal, J. H. Metallophthalocyanines as catalysts in electrochemical reactions. *Coord. Chem. Rev.* **119**, 89–136 (1992).
  118. Shao, M. *Electrocatalysis in fuel cells: A non- and low- Platinum approach*. **9**, (Springer-Verlag, 2013).
  119. Blakemore, J. D., Crabtree, R. H. & Brudvig, G. W. Molecular Catalysts for Water Oxidation. *Chem. Rev.* (2015). doi:10.1021/acs.chemrev.5b00122
  120. Gersten, S. W., Samuels, G. J. & Meyer, T. J. Catalytic Oxidation of Water by an Oxo-Bridged Ruthenium Dimer. *J. Am. Chem. Soc.* **104**, 4029–4030 (1982).
  121. Thomsen, J. M., Huang, D. L., Crabtree, R. H. & Brudvig, G. W. Iridium-based complexes for water oxidation. *Dalt. Trans.* **44**, 12452–12472 (2015).
  122. Miyake, H., Ye, S. & Osawa, M. Electroless deposition of gold thin films on silicon for surface-enhanced infrared spectroelectrochemistry. *Electrochem. commun.* **4**, 973–977 (2002).
  123. Angerstein-Kozłowska, H., Conway, B. E., Hamelin, A. & Stoicoviciu, L. Elementary steps of electrochemical oxidation of single-crystal planes of Au Part II. A chemical and structural basis of oxidation of the (111) plane. *J. Electroanal. Chem. Interfacial Electrochem.* **228**, 429–453 (1987).
  124. Chen, Z. *et al.* Fabrication of highly transparent and conductive indium-tin oxide thin films with a high figure of merit via solution processing. *Langmuir* **29**, 13836–42 (2013).
  125. Kosynkin, D. V & Tour, J. M. Phenylene ethynylene diazonium salts as potential self-assembling molecular devices. *Org. Lett.* **3**, 993–995 (2001).
  126. Broxton, T. J., Colton, R. & Traeger, J. C. Electrospray mass spectral studies of aromatic diazonium salts and diazotates. *J. Mass Spectrom.* **30**, 319–323 (1995).
  127. Dogutan, D. K., Kwabena Bediako, D., Teets, T. S., Schwalbe, M. & Nocera, D. G. Efficient synthesis of hangman porphyrins. *Org. Lett.* **12**, 1036–1039 (2010).
  128. Chang, C. J., Chng, L. L. & Nocera, D. G. Proton-coupled O-O activation on a redox platform bearing a hydrogen-bonding scaffold. *J. Am. Chem. Soc.* **125**, 1866–1876 (2003).
  129. Yeh, C. Y., Chang, C. J. & Nocera, D. G. ‘Hangman’ porphyrins for the assembly of a model heme water channel. *J. Am. Chem. Soc.* **123**, 1513–1514 (2001).
  130. Wisitruangsakul, N. *et al.* Monitoring catalysis of the membrane-bound hydrogenase from *Ralstonia eutropha* H16 by surface-enhanced IR absorption spectroscopy. *Angew. Chemie - Int. Ed.* **48**, 611–613 (2009).
  131. Becke, A. D. Density-functional exchange-energy approximation with correct asymptotic behavior. *Phys. Rev. A* **38**, 3098–3100 (1988).
  132. Perdew, J. P. Density-functional approximation for the correlation energy of the inhomogeneous electron gas. *Phys. Rev. B* **33**, 8822–8824 (1986).

133. Frisch, M. J. *et al.* *Gaussian 09, Revision D.01*. (Gaussian, Inc., 2013).
134. Weigend, F. & Ahlrichs, R. Balanced basis sets of split valence, triple zeta valence and quadruple zeta valence quality for H to Rn: design and assessment of accuracy. *Phys. Chem. Chem. Phys.* **7**, 3297–3305 (2005).
135. Rippers, Y., Utesch, T., Hildebrandt, P., Zebger, I. & Mroginski, M. A. Insights into the structure of the active site of the O<sub>2</sub>-tolerant membrane bound [NiFe] hydrogenase of *R. eutropha* H16 by molecular modelling. *Phys. Chem. Chem. Phys.* **13**, 16146–16149 (2011).
136. Kozuch, J. *et al.* Voltage-dependent structural changes of the membrane-bound anion channel hVDAC1 probed by SEIRA and electrochemical impedance spectroscopy. *Phys. Chem. Chem. Phys.* **16**, 9546–9555 (2014).
137. Rüdiger, O. *et al.* Enzymatic anodes for hydrogen fuel cells based on covalent attachment of Ni-Fe hydrogenases and direct electron transfer to SAM-modified gold electrodes. *Electroanalysis* **22**, 776–783 (2010).
138. Liu, G., Böcking, T. & Gooding, J. J. Diazonium salts: Stable monolayers on gold electrodes for sensing applications. *J. Electroanal. Chem.* **600**, 335–344 (2007).
139. Shewchuk, D. M. & McDermott, M. T. Comparison of diazonium salt derived and thiol derived nitrobenzene layers on gold. *Langmuir* **25**, 4556–63 (2009).
140. D'Amours, M. & Belanger, D. Stability of Substituted Phenyl Groups Electrochemically Grafted at Carbon Electrode Surface. *J. Phys. Chem. B* **107**, 4811–4817 (2003).
141. Blankespoor, R., Limoges, B., Schöllhorn, B., Syssa-Magalé, J. L. & Yazidi, D. Dense monolayers of metal-chelating ligands covalently attached to carbon electrodes electrochemically and their useful application in affinity binding of histidine-tagged proteins. *Langmuir* **21**, 3362–3375 (2005).
142. Vaz-Dominguez, C. *et al.* Laccase electrode for direct electrocatalytic reduction of O<sub>2</sub> to H<sub>2</sub>O with high-operational stability and resistance to chloride inhibition. *Biosens. Bioelectron.* **24**, 531–537 (2008).
143. Liu, G., Paddon-Row, M. N. & Justin Gooding, J. A molecular wire modified glassy carbon electrode for achieving direct electron transfer to native glucose oxidase. *Electrochem. commun.* **9**, 2218–2223 (2007).
144. Rüdiger, O., Abad, J. M., Hatchikian, E. C., Fernandez, V. M. & De Lacey, A. L. Oriented immobilization of *Desulfovibrio gigas* hydrogenase onto carbon electrodes by covalent bonds for nonmediated oxidation of H<sub>2</sub>. *J. Am. Chem. Soc.* **127**, 16008–16009 (2005).
145. Radi, A. E., Munoz-Berbel, X., Cortina-Puig, M. & Marty, J. L. Novel protocol for covalent immobilization of horseradish peroxidase on gold electrode surface. *Electroanalysis* **21**, 696–700 (2009).
146. Pita, M. *et al.* High Redox Potential Cathode Based on Laccase Covalently Attached to Gold Electrode. *J. Phys. Chem. C* **115**, 13420–13428 (2011).
147. Vaz-Dominguez, C., Pita, M., De Lacey, A. L., Shleev, S. & Cuesta, A. Combined ATR-SEIRAS and EC-STM study of the immobilization of laccase on chemically modified Au electrodes. *J. Phys. Chem. C* **116**, 16532–16540 (2012).
148. Yeşildağ, A. & Ekinçi, D. Covalent attachment of pyridine-type molecules to glassy carbon surfaces by electrochemical reduction of in situ generated diazonium salts. Formation of ruthenium complexes on ligand-modified surfaces. *Electrochim. Acta* **55**, 7000–7009 (2010).
149. Tsukahara, Y., Wada, T. & Tanaka, K. Redox Behavior of Ruthenium(Bipyridine)(Terpyridine)(Carbonyl) Complex-modified Carbon Electrode and Reactivity toward Electrochemical Reduction of CO<sub>2</sub>. *Chem. Lett.* **39**, 1134–1135 (2010).
150. Cao, R. *et al.* Promotion of oxygen reduction by a bio-inspired tethered iron phthalocyanine carbon nanotube-based catalyst. *Nat. Commun.* **4**, 2076 (2013).
151. Wei, P. J., Yu, G. Q., Naruta, Y. & Liu, J. G. Covalent grafting of carbon nanotubes with a biomimetic heme model compound to enhance oxygen reduction reactions. *Angew. Chemie - Int. Ed.* **53**, 6659–6663 (2014).

152. Maurin, A. & Robert, M. Catalytic CO<sub>2</sub>-to-CO conversion in water by covalently functionalized carbon nanotubes with a molecular iron catalyst. *Chem. Commun.* **52**, 12084–12087 (2016).
153. Harper, J. C., Polsky, R., Dirk, S. M., Wheeler, D. R. & Brozik, S. M. Electroaddressable selective functionalization of electrode arrays: Catalytic NADH detection using aryl diazonium modified gold electrodes. *Electroanalysis* **19**, 1268–1274 (2007).
154. Gutierrez-Sanchez, C. *et al.* Efficiency of Enzymatic O<sub>2</sub> Reduction by *Myrothecium verrucaria* Bilirubin Oxidase Probed by Surface Plasmon Resonance, PMIRRAS, and Electrochemistry. *ACS Catal.* **6**, 5482–5492 (2016).
155. Vincent, K. A. *et al.* Electrocatalytic hydrogen oxidation by an enzyme at high carbon monoxide or oxygen levels. *Proc. Natl. Acad. Sci. U. S. A.* **102**, 16951–16954 (2005).
156. Sensi, M., Del Barrio, M., Baffert, C., Fourmond, V. & Léger, C. New perspectives in hydrogenase direct electrochemistry. *Curr. Opin. Electrochem.* **5**, 135–145 (2017).
157. Menanteau, T., Levillain, E. & Breton, T. Electrografting via Diazonium Chemistry: From Multilayer to Monolayer Using Radical Scavenger. *Chem. Mater.* **25**, 2905–2909 (2013).
158. Hidalgo, R., Ash, P. A., Healy, A. J. & Vincent, K. A. Infrared spectroscopy during electrocatalytic turnover reveals the Ni-L active site state during H<sub>2</sub> oxidation by a NiFe hydrogenase. *Angew. Chemie - Int. Ed.* **54**, 7110–7113 (2015).
159. Reuillard, B. *et al.* Tuning Product Selectivity for Aqueous CO<sub>2</sub> Reduction with a Mn(bipyridine)-pyrene Catalyst Immobilized on a Carbon Nanotube Electrode. *J. Am. Chem. Soc.* **139**, 14425–14435 (2017).
160. Imabayashi, S.-I., Hobara, D., Kakiuchi, T., Knoll, W. & Plank-institut, M. Selective replacement of adsorbed alkanethiols in phase-separated binary self-assembled monolayers by electrochemical partial desorption. *Langmuir* **7463**, 4502–4504 (1997).
161. Sumi, T. & Uosaki, K. Electrochemical Oxidative Formation and Reductive Desorption of a Self-Assembled Monolayer of Decanethiol on a Au(111) Surface in KOH Ethanol Solution. *J. Phys. Chem. B* **108**, 6422–6428 (2004).
162. Chen, Y., Yang, C. & Wang, F. Bin. Electrochemical assessment of electrochemical oxidation stability of self-assembled monolayers on gold and preparation of binary self-assembled monolayers on gold. *Electrochim. Acta* **55**, 3951–3956 (2010).
163. Hawecker, J., Lehn, J.-M. & Ziessel, R. Electrocatalytic reduction of carbon dioxide mediated by Re (bipy)(CO)<sub>3</sub>Cl (bipy= 2, 2'-bipyridine). *Chem. Commun.* 328–330 (1984).
164. Ishida, H., Tanaka, K. & Tanaka, T. Electrochemical CO<sub>2</sub> reduction catalyzed by ruthenium complexes [Ru(bpy)<sub>2</sub>(CO)<sub>2</sub>]<sup>2+</sup> and [Ru(bpy)<sub>2</sub>(CO)Cl]<sup>+</sup>. Effect of pH on the formation of CO and HCOO<sup>-</sup>. *Organometallics* **6**, 181–186 (1987).
165. Bourrez, M., Molton, F., Chardon-Noblat, S. & Deronzier, A. [Mn(bipyridyl)(CO)<sub>3</sub>Br]: An abundant metal carbonyl complex as efficient electrocatalyst for CO<sub>2</sub> reduction. *Angew. Chemie - Int. Ed.* **50**, 9903–9906 (2011).
166. Smieja, J. M. *et al.* Manganese as a substitute for rhenium in CO<sub>2</sub> reduction catalysts: The importance of acids. *Inorg. Chem.* **52**, 2484–2491 (2013).
167. Walsh, J. J., Neri, G., Smith, C. L. & Cowan, A. J. Electrocatalytic CO<sub>2</sub> reduction with a membrane supported manganese catalyst in aqueous solution. *Chem. Commun. (Camb)*. **50**, 12698–701 (2014).
168. Sampson, M. D. & Kubiak, C. P. Electrocatalytic Dihydrogen Production by an Earth-Abundant Manganese Bipyridine Catalyst. *Inorg. Chem.* **54**, 6674–6676 (2015).
169. Sampson, M. D. *et al.* Manganese catalysts with bulky bipyridine ligands for the electrocatalytic reduction of carbon dioxide: eliminating dimerization and altering catalysis. *J. Am. Chem. Soc.* **136**, 5460–71 (2014).
170. Riplinger, C. & Carter, E. a. Influence of Weak Brønsted Acids on Electrocatalytic CO<sub>2</sub> Reduction by Manganese and Rhenium Bipyridine Catalysts. *ACS Catal.* **5**, 900–908 (2015).
171. Sampson, M. D. & Kubiak, C. P. Manganese Electrocatalysts with Bulky Bipyridine Ligands: Utilizing Lewis Acids to Promote Carbon Dioxide Reduction at Low Overpotentials. *J. Am.*

- Chem. Soc.* **138**, 1386–1393 (2016).
172. Walsh, J. J. *et al.* Improving the efficiency of electrochemical CO<sub>2</sub> reduction using immobilized manganese complexes. *Faraday Discuss.* **0**, 1–14 (2015).
  173. Rosser, T. E., Windle, C. D. & Reisner, E. Electrocatalytic and Solar-Driven CO<sub>2</sub> Reduction to CO with a Molecular Manganese Catalyst Immobilized on Mesoporous TiO<sub>2</sub>. *Angew. Chem. Int. Ed. Engl.* **55**, 7388–7392 (2016).
  174. Lukkari, J., Kleemola, K., Meretoja, M., Ollonqvist, T. & Kankare, J. Electrochemical post-self-assembly transformation of 4-aminothiophenol monolayers on gold electrodes. *Langmuir* **14**, 1705–1715 (1998).
  175. Jiang, C., Elliott, J. M., Cardin, D. J. & Tsang, S. C. An electrochemical study of 4-aminothiophenol/Pt nanoparticle multilayers on gold electrodes. *Langmuir* **25**, 534–541 (2009).
  176. Batz, V. *et al.* Electrochemistry and structure of the isomers of aminothiophenol adsorbed on gold. *J. Electroanal. Chem.* **491**, 55–68 (2000).
  177. Jiang, D., Sumpter, B. G. & Dai, S. Structure and bonding between an aryl group and metal surfaces. *J. Am. Chem. Soc.* **128**, 6030–1 (2006).
  178. Jiang, D. E., Sumpter, B. G. & Dai, S. How do aryl groups attach to a graphene sheet? *J. Phys. Chem. B* **110**, 23628–23632 (2006).
  179. Le Floch, F., Simonato, J. P. & Bidan, G. Electrochemical signature of the grafting of diazonium salts: A probing parameter for monitoring the electro-addressed functionalization of devices. *Electrochim. Acta* **54**, 3078–3085 (2009).
  180. Menanteau, T., Levillain, E. & Breton, T. Spontaneous grafting of nitrophenyl groups on carbon: Effect of radical scavenger on organic layer formation. *Langmuir* **30**, 7913–7918 (2014).
  181. Menanteau, T., Dias, M., Levillain, E., Downard, A. J. & Breton, T. Electrografting via Diazonium Chemistry: The Key Role of the Aryl Substituent in the Layer Growth Mechanism. *J. Phys. Chem. C* **120**, 4423–4429 (2016).
  182. Lehr, J., Williamson, B. E., Flavel, B. S. & Downard, A. J. Reaction of gold substrates with diazonium salts in acidic solution at open-circuit potential. *Langmuir* **25**, 13503–13509 (2009).
  183. Jayasundara, D. R., Cullen, R. J., Soldi, L. & Colavita, P. E. In situ studies of the adsorption kinetics of 4-nitrobenzenediazonium salt on gold. *Langmuir* **27**, 13029–36 (2011).
  184. Ricci, A. M., Méndez De Leo, L. P., Williams, F. J. & Calvo, E. J. Some evidence for the formation of an azo bond during the electroreduction of diazonium salts on Au substrates. *ChemPhysChem* **13**, 2119–2127 (2012).
  185. Yu, S. S. C., Tan, E. S. Q., Jane, R. T. & Downard, A. J. An electrochemical and XPS study of reduction of nitrophenyl films covalently grafted to planar carbon surfaces. *Langmuir* **23**, 11074–11082 (2007).
  186. Gui, A. L. *et al.* A comparative study of electrochemical reduction of 4-nitrophenyl covalently grafted on gold and carbon. *Electroanalysis* **22**, 1824–1830 (2010).
  187. Millo, D., Hildebrandt, P., Pandelia, M. E., Lubitz, W. & Zebger, I. SEIRA spectroscopy of the electrochemical activation of an immobilized [NiFe] hydrogenase under turnover and non-turnover conditions. *Angew. Chemie - Int. Ed.* **50**, 2632–2634 (2011).
  188. Saggi, M. *et al.* Spectroscopic insights into the oxygen-tolerant membrane-associated [NiFe] hydrogenase of *Ralstonia eutropha* H16. *J. Biol. Chem.* **284**, 16264–16276 (2009).
  189. De Lacey, A. L., Fernández, V. M., Rousset, M. & Cammack, R. Activation and inactivation of hydrogenase function and the catalytic cycle: Spectroelectrochemical studies. *Chem. Rev.* **107**, 4304–4330 (2007).
  190. Utesch, T. *et al.* Effect of the protonation degree of a self-assembled monolayer on the immobilization dynamics of a [NiFe] hydrogenase. *Langmuir* **29**, 673–682 (2013).
  191. Breton, T. & Bélanger, D. Modification of carbon electrode with aryl groups having an aliphatic amine by electrochemical reduction of in situ generated diazonium cations. *Langmuir* **24**,

- 8711–8718 (2008).
192. Bryant, M. A. & Crooks, R. M. Determination of Surface pKa Values of Surface-Confined Molecules Derivatized with pH-Sensitive Pendant Groups. *Langmuir* **9**, 385–387 (1993).
  193. Ludwig, M., Cracknell, J. A., Vincent, K. A., Armstrong, F. A. & Lenz, O. Oxygen-tolerant H<sub>2</sub> oxidation by membrane-bound [NiFe] hydrogenases of *Ralstonia* species coping with low level H<sub>2</sub> in air. *J. Biol. Chem.* **284**, 465–477 (2009).
  194. Murgida, D. H. & Hildebrandt, P. Electron-transfer processes of cytochrome c at interfaces. New insights by surface-enhanced resonance Raman spectroscopy. *Acc. Chem. Res.* **37**, 854–861 (2004).
  195. Winkler, J. R. & Gray, H. B. Long-range electron tunneling. *J. Am. Chem. Soc.* **136**, 2930–2939 (2014).
  196. Nakamoto, K. in *Infrared and Raman Spectra of Inorganic and Coordination Compounds* 1–273 (John Wiley & Sons, Inc., 2008). doi:10.1002/9780470405888.ch1
  197. Barton, S. C., Gallaway, J. & Atanassov, P. Enzymatic Biofuel Cells for Implantable and Microscale Devices. *Chem. Rev.* **104**, 4867–4886 (2004).
  198. Grieshaber, D., MacKenzie, R., Vörös, J. & Reimhult, E. Electrochemical Biosensors - Sensor Principles and Architectures. *Sensors* **8**, 1400–1458 (2008).
  199. Zebda, A. *et al.* Single glucose biofuel cells implanted in rats power electronic devices. *Sci. Rep.* **3**, (2013).
  200. Mazurenko, I., De Poulpiquet, A. & Lojou, E. Recent developments in high surface area bioelectrodes for enzymatic fuel cells. *Curr. Opin. Electrochem.* (2017). doi:10.1016/j.coelec.2017.07.001
  201. Topoglidis, E., Astuti, Y., Duriaux, F., Grätzel, M. & Durrant, J. R. Direct electrochemistry and nitric oxide interaction of heme proteins adsorbed on nanocrystalline tin oxide electrodes. *Langmuir* **19**, 6894–6900 (2003).
  202. Frasca, S. *et al.* Mesoporous Indium Tin Oxide as a Novel Platform for Bioelectronics. *ChemCatChem* **2**, 839–845 (2010).
  203. Kwan, P. *et al.* Spectroelectrochemistry of cytochrome c and azurin immobilized in nanoporous antimony-doped tin oxide. *Chem. Commun.* **47**, 12367 (2011).
  204. Schaming, D. *et al.* Spectroelectrochemical characterization of small hemoproteins adsorbed within nanostructured mesoporous ITO electrodes. *Langmuir* **28**, 14065–14072 (2012).
  205. Frasca, S. *et al.* Bioelectrocatalysis at mesoporous antimony doped tin oxide electrodes—Electrochemical characterization and direct enzyme communication. *Electrochim. Acta* **110**, 172–180 (2013).
  206. Müller, V., Rathousky, J. & Fattakhova-Rohlfing, D. Covalent immobilization of redox protein within the mesopores of transparent conducting electrodes. *Electrochim. Acta* **116**, 1–8 (2014).
  207. Mersch, D. *et al.* Wiring of Photosystem II to Hydrogenase for Photoelectrochemical Water-splitting. *J. Am. Chem. Soc.* 150605124103001 (2015). doi:10.1021/jacs.5b03737
  208. Reuillard, B. *et al.* High Performance Reduction of H<sub>2</sub>O<sub>2</sub> with an Electron Transport Decaheme Cytochrome on a Porous ITO Electrode. *J. Am. Chem. Soc.* **139**, 3324–3327 (2017).
  209. González-Arribas, E. *et al.* Transparent, mediator- and membrane-free enzymatic fuel cell based on nanostructured chemically modified indium tin oxide electrodes. *Biosens. Bioelectron.* **97**, 46–52 (2017).
  210. Lund, T., Nguyen, P. T. & Ruhland, T. Electrochemical grafting of TiO<sub>2</sub>-based photo-anodes and its effect in dye-sensitized solar cells. *J. Electroanal. Chem.* **758**, 85–92 (2015).
  211. Chen, X. *et al.* A Molecule with Dual Functionality 4-Aminophenylmethylphosphonic Acid: A Comparison Between Layers Formed on Indium Tin Oxide by In Situ Generation of an Aryl Diazonium Salt or by Self-Assembly of the Phosphonic Acid. *Electroanalysis* **23**, 2633–2642 (2011).
  212. Hebié, S., Devillers, C. H., Fournier, S. & Lucas, D. Direct Grafting of Free-Base meso-

- Triarylporphyrins on Electrode Materials through Diazonium Reduction: Reversible Zinc(II) Metallation of the Resulting Materials. *ChemElectroChem* **3**, 45–50 (2016).
213. Rawson, F. J., Yeung, C. L., Jackson, S. K. & Mendes, P. M. Tailoring 3D single-walled carbon nanotubes anchored to indium tin oxide for natural cellular uptake and intracellular sensing. *Nano Lett.* **13**, 1–8 (2013).
  214. Lamberti, F. *et al.* Optoelectrochemical Biorecognition by Optically Transparent Highly Conductive Graphene-Modified Fluorine-Doped Tin Oxide Substrates. *ACS Appl. Mater. Interfaces* **6**, 22769–77 (2014).
  215. Charlton, M. R., Suhr, K. J., Holliday, B. J. & Stevenson, K. J. Electrochemical Modification of Indium Tin Oxide Using Di(4-nitrophenyl) Iodonium Tetrafluoroborate. *Langmuir* **31**, 695–702 (2015).
  216. Finklea, H. O. *et al.* Characterisation of octadecanethiol-coated gold electrodes as microarray electrodes by cyclic voltammetry and AC-impedance spectroscopy. *Langmuir* **9**, 3660–3667 (1993).
  217. Allongue, P. *et al.* Covalent modification of carbon surfaces by aryl radicals generated from the electrochemical reduction of diazonium salts. *J. Am. Chem. Soc.* **119**, 201–207 (1997).
  218. Brooksby, P. A., Shields, J. D., Farquhar, A. K. & Downard, A. J. Reduction of Nitrophenyl Films in Aqueous Solutions: How Many Electrons? *ChemElectroChem* **3**, 2021–2026 (2016).
  219. Brooksby, P. a & Downard, A. J. Multilayer nitroazobenzene films covalently attached to carbon. An AFM and electrochemical study. *J. Phys. Chem. B* **109**, 8791–8 (2005).
  220. Ceccato, M. *et al.* Nitrophenyl groups in diazonium-generated multilayered films: which are electrochemically responsive? *Langmuir* **26**, 10812–21 (2010).
  221. Menanteau, T., Levillain, E., Downard, A. J. & Breton, T. Evidence of monolayer formation via diazonium grafting with a radical scavenger: electrochemical, AFM and XPS monitoring. *Phys. Chem. Chem. Phys.* **17**, 13137–13142 (2015).
  222. Siebert, E. *et al.* Resonance Raman Spectroscopic Analysis of the [NiFe] Active Site and the Proximal [4Fe-3S] Cluster of an O<sub>2</sub>-Tolerant Membrane-Bound Hydrogenase in the Crystalline State. *J. Phys. Chem. B* **119**, 13785–13796 (2015).
  223. Liu, B. & Liu, J. DNA adsorption by indium tin oxide nanoparticles. *Langmuir* **31**, 371–377 (2015).
  224. Young, K. J. *et al.* Light-driven water oxidation for solar fuels. *Coord. Chem. Rev.* **256**, 2503–2520 (2012).
  225. Bullock, R. M., Das, A. K. & Appel, A. M. Surface Immobilization of Molecular Electrocatalysts for Energy Conversion. *Chem. - A Eur. J.* **23**, 7626–7641 (2017).
  226. Benck, J. D., Pinaud, B. A., Gorlin, Y. & Jaramillo, T. F. Substrate Selection for fundamental studies of electrocatalysts and photoelectrodes: inert potential windows in acidic, neutral, and basic electrolyte. *PLoS One* **9**, e107942 (2014).
  227. Rosser, T. E., Gross, M. A., Lai, Y.-H. & Reisner, E. Precious-metal free photoelectrochemical water splitting with immobilised molecular Ni and Fe redox catalysts. *Chem. Sci.* **7**, 4024–4035 (2016).
  228. Hoertz, P. G., Chen, Z., Kent, C. A. & Meyer, T. J. Application of high surface area tin-doped indium oxide nanoparticle films as transparent conducting electrodes. *Inorg. Chem.* **49**, 8179–8181 (2010).
  229. Odrobina, J. *et al.* Backbone Immobilization of the Bis(bipyridyl)pyrazolate Diruthenium Catalyst for Electrochemical Water Oxidation. *ACS Catal.* **7**, 2116–2125 (2017).
  230. Moore, G. F. *et al.* A visible light water-splitting cell with a photoanode formed by codeposition of a high-potential porphyrin and an iridium water-oxidation catalyst. *Energy Environ. Sci.* **4**, 2389 (2011).
  231. Martini, L. A. *et al.* Modular assembly of high-potential zinc porphyrin photosensitizers attached to TiO<sub>2</sub> with a series of anchoring groups. *J. Phys. Chem. C* **117**, 14526–14533 (2013).

232. Materna, K. L. *et al.* Heterogenized Iridium Water-Oxidation Catalyst from a Silatrane Precursor. *ACS Catal.* **6**, 5371–5377 (2016).
233. Li, F. *et al.* Organic Dye-Sensitized Tandem Photoelectrochemical Cell for Light Driven Total Water Splitting. *J. Am. Chem. Soc.* **137**, 9153–9159 (2015).
234. Chen, Z., Concepcion, J. J., Jurss, J. W. & Meyer, T. J. Single-site, catalytic water oxidation on oxide surfaces. *J. Am. Chem. Soc.* **131**, 15580–15581 (2009).
235. Sheehan, S. W. *et al.* A molecular catalyst for water oxidation that binds to metal oxide surfaces. *Nat. Commun.* **6**, 6469 (2015).
236. Negre, C. F. A. *et al.* Efficiency of interfacial electron transfer from Zn-porphyrin dyes into TiO<sub>2</sub> correlated to the linker single molecule conductance. *J. Phys. Chem. C* **117**, 24462–24470 (2013).
237. Berisha, A., Chehimi, M., Pinson, J. & Podvorica, F. in *Electroanalytical Chemistry* 115–224 (CRC Press, 2015). doi:doi:10.1201/b19196-4
238. Bard, A. J. & Zoski, C. G. *Electroanalytical Chemistry A Series of Advances: Volume 26*. (CRC Press, 2015).
239. Müller, V. *et al.* Highly Conducting Nanosized Monodispersed Antimony-Doped Tin Oxide Particles Synthesized via Nonaqueous Sol–Gel Procedure. *Chem. Mater.* **21**, 5229–5236 (2009).
240. Müller, V. *et al.* Transparent conducting films of antimony-doped tin oxide with uniform mesostructure assembled from preformed nanocrystals. *Small* **6**, 633–7 (2010).
241. Luo, L., Bozyigit, D., Wood, V. & Niederberger, M. High-Quality Transparent Electrodes Spin-Cast from Preformed Antimony-Doped Tin Oxide Nanocrystals for Thin Film Optoelectronics. *Chem. Mater.* **25**, 4901–4907 (2013).
242. Oh, H.-S., Nong, H. N., Reier, T., Gliech, M. & Strasser, P. Oxide-supported Ir nanodendrites with high activity and durability for the oxygen evolution reaction in acid PEM water electrolyzers. *Chem. Sci.* **6**, 3321–3328 (2015).
243. Ostermann, R., Zieba, R., Rudolph, M., Schlettwein, D. & Smarsly, B. M. Electrospun antimony doped tin oxide (ATO) nanofibers as a versatile conducting matrix. *Chem. Commun.* **47**, 12119 (2011).
244. Correa Baena, J. P. & Agrios, A. G. Antimony-doped tin oxide aerogels as porous electron collectors for dye-sensitized solar cells. *J. Phys. Chem. C* **118**, 17028–17035 (2014).
245. Auwärter, W., Écija, D., Klappenberger, F. & Barth, J. V. Porphyrins at interfaces. *Nat. Chem.* **7**, 105–120 (2015).
246. Brumbach, M. T., Boal, A. K. & Wheeler, D. R. Metalloporphyrin assemblies on pyridine-functionalized titanium dioxide. *Langmuir* **25**, 10685–10690 (2009).
247. Willkomm, J., Muresan, N. M. & Reisner, E. Enhancing H<sub>2</sub> evolution performance of an immobilised cobalt catalyst by rational ligand design. *Chem. Sci.* **6**, 2727–2736 (2015).
248. Subbaiyan, N. K., Wijesinghe, C. A. & D'Souza, F. Supramolecular solar cells: Surface modification of nanocrystalline TiO<sub>2</sub> with coordinating ligands to immobilize sensitizers and dyads via metal-ligand coordination for enhanced photocurrent generation. *J. Am. Chem. Soc.* **131**, 14645–14647 (2009).
249. Panagiotopoulos, A., Ladomenou, K., Sun, D., Artero, V. & Coutsolelos, A. G. Photochemical hydrogen production and cobaloximes: the influence of the cobalt axial N-ligand on the system stability. *Dalt. Trans.* **45**, 6732–6738 (2016).
250. Chlistunoff, J. & Sansiñena, J. M. Effects of axial coordination of the metal center on the activity of iron tetraphenylporphyrin as a nonprecious catalyst for oxygen reduction. *J. Phys. Chem. C* **118**, 19139–19149 (2014).
251. Ly, H. K. *et al.* 2<sup>nd</sup> coordination sphere controlled electron transfer of iron heme complexes on electrodes probed by surface enhanced vibrational spectroscopy. *Chem. Sci.* **6**, 6999–7007 (2015).

252. Kielb, P. Redox processes of heme proteins and metalloporphyrins studied by vibrational spectroelectrochemistry. (Technische Universität Berlin, 2017).
253. Wang, D. & Groves, J. T. Efficient water oxidation catalyzed by homogeneous cationic cobalt porphyrins with critical roles for the buffer base. *Proc. Natl. Acad. Sci. U. S. A.* **110**, 15579–84 (2013).
254. Nakazono, T., Parent, A. R. & Sakai, K. Cobalt porphyrins as homogeneous catalysts for water oxidation. *Chem. Commun. Chem. Commun* **49**, 6325–6327 (2013).
255. Nakazono, T., Parent, A. R. & Sakai, K. Improving Singlet Oxygen Resistance during Photochemical Water Oxidation by Cobalt Porphyrin Catalysts. *Chem. - A Eur. J.* **21**, 6723–6726 (2015).
256. Morlanés, N., Joya, K. S., Takanabe, K. & Rodionov, V. Perfluorinated cobalt phthalocyanine effectively catalyzes water electrooxidation. *Eur. J. Inorg. Chem.* **2015**, 49–52 (2015).
257. Cao, S. R. *et al.* Showcasing research from the laboratory of Professor Rui Cao at the As featured in: The effect of the trans axial ligand of cobalt corroles on water oxidation activity in neutral aqueous solutions. *Phys. Chem. Chem. Phys.* **19**, 9755–9761 (2017).
258. Jia, H., Sun, Z., Jiang, D. & Du, P. Covalent Cobalt Porphyrin Framework on Multiwalled Carbon Nanotubes for Efficient Water Oxidation at Low Overpotential. *Chem. Mater.* **27**, 4586–4593 (2015).
259. Joya, K. S., Morlanés, N., Maloney, E., Rodionov, V. & Takanabe, K. Immobilization of a molecular cobalt electrocatalyst by hydrophobic interaction with a hematite photoanode for highly stable oxygen evolution. *Chem. Commun.* **51**, 13481–13484 (2015).
260. Barnett, S. M., Goldberg, K. I. & Mayer, J. M. A soluble copper–bipyridine water-oxidation electrocatalyst. *Nat. Chem.* **4**, 498–502 (2012).
261. Zhang, T., Wang, C., Liu, S., Wang, J. L. & Lin, W. A biomimetic copper water oxidation catalyst with low overpotential. *J. Am. Chem. Soc.* **136**, 273–281 (2014).
262. Zhang, T., Wang, C., Liu, S., Wang, J. L. & Lin, W. A biomimetic copper water oxidation catalyst with low overpotential. *J. Am. Chem. Soc.* **136**, 273–281 (2014).
263. Koepke, S. J., Light, K. M., VanNatta, P. E., Wiley, K. M. & Kieber-Emmons, M. T. Electrocatalytic Water Oxidation by a Homogeneous Copper Catalyst Disfavors Single-Site Mechanisms. *J. Am. Chem. Soc.* **139**, 8586–8600 (2017).
264. Zhang, M. T., Chen, Z., Kang, P. & Meyer, T. J. Electrocatalytic water oxidation with a copper(II) polypeptide complex. *J. Am. Chem. Soc.* **135**, 2048–2051 (2013).
265. Shen, J., Wang, M., Zhang, P., Jiang, J. & Sun, L. Electrocatalytic water oxidation by copper(ii) complexes containing a tetra- or pentadentate amine-pyridine ligand. *Chem. Commun.* **53**, 4374–4377 (2017).
266. Fisher, K. J., Materna, K. L., Mercado, B. Q., Crabtree, R. H. & Brudvig, G. W. Electrocatalytic Water Oxidation by a Copper(II) Complex of an Oxidation-Resistant Ligand. *ACS Catal.* **7**, 3384–3387 (2017).
267. Luo, H. *et al.* High Surface Area Antimony-Doped Tin Oxide Electrodes Templated by Graft Copolymerization. Applications in Electrochemical and Photoelectrochemical Catalysis. *ACS Appl. Mater. Interfaces* **7**, 25121–25128 (2015).
268. Odrobina, J. *et al.* Backbone Immobilization of the Bis(bipyridyl)pyrazolate Diruthenium Catalyst for Electrochemical Water Oxidation. *ACS Catal.* **7**, 2116–2125 (2017).
269. Chen, Z. & Meyer, T. J. Copper(II) catalysis of water oxidation. *Angew. Chemie - Int. Ed.* **52**, 700–703 (2013).
270. Liu, C., Dubois, K. D., Louis, M. E., Vorushilov, A. S. & Li, G. Photocatalytic CO<sub>2</sub> reduction and surface immobilization of a tricarbonyl Re(I) compound modified with amide groups. *ACS Catal.* **3**, 655–662 (2013).
271. Schreier, M. *et al.* Covalent Immobilization of a Molecular Catalyst on Cu<sub>2</sub>O Photocathodes for CO<sub>2</sub> Reduction. *J. Am. Chem. Soc.* **138**, 1938–1946 (2016).

272. Brushett, F. R. *et al.* A carbon-supported copper complex of 3,5-diamino-1,2,4-triazole as a cathode catalyst for alkaline fuel cell applications. *J. Am. Chem. Soc.* **132**, 12185–12187 (2010).
273. McCrory, C. C. L. *et al.* Electrocatalytic O<sub>2</sub> reduction by covalently immobilized mononuclear copper(I) complexes: Evidence for a binuclear Cu<sub>2</sub>O<sub>2</sub> intermediate. *J. Am. Chem. Soc.* **133**, 3696–3699 (2011).
274. Kakuda, S., Peterson, R. L., Ohkubo, K., Karlin, K. D. & Fukuzumi, S. Enhanced catalytic four-electron dioxygen (O<sub>2</sub>) and two-electron hydrogen peroxide (H<sub>2</sub>O<sub>2</sub>) reduction with a copper(II) complex possessing a pendant ligand pivalamido group. *J. Am. Chem. Soc.* **135**, 6513–6522 (2013).
275. Garrett, D. J. *et al.* Diazonium salt derivatives of osmium bipyridine complexes: Electrochemical grafting and characterisation of modified surfaces. *Electrochim. Acta* **56**, 2213–2220 (2011).
276. Müller, V. Mesoporous Transparent Conducting Films of Antimony Doped Tin Oxide as Nanostructured Electrodes. (Ludwig-Maximilians-Universität München, 2013).
277. Tian, R. *et al.* The effect of annealing on a 3D SnO<sub>2</sub>/graphene foam as an advanced lithium-ion battery anode. *Sci. Rep.* **6**, 1–9 (2016).
278. Brinker, C. J. Hydrolysis and Condensation of Silicates: Effects on Structure. *Journal of Non-Crystalline Solids* **100**, 31–50 (1988).
279. Hanson, K. *et al.* Photostability of phosphonate-derivatized, Ru II polypyridyl complexes on metal oxide surfaces. *ACS Appl. Mater. Interfaces* **4**, 1462–1469 (2012).
280. Hyde, J. T. *et al.* Electrochemical instability of phosphonate-derivatized, ruthenium(III) polypyridyl complexes on metal oxide surfaces. *ACS Appl. Mater. Interfaces* **7**, 9554–9562 (2015).
281. Reuillard, B., Gentil, S., Carrière, M., Le Goff, A. & Cosnier, S. Biomimetic versus enzymatic high-potential electrocatalytic reduction of hydrogen peroxide on a functionalized carbon nanotube electrode. *Chem. Sci.* **6**, 5139–5143 (2015).
282. Eckermann, A. L., Feld, D. J., Shaw, J. A. & Meade, T. J. Electrochemistry of redox-active self-assembled monolayers. *Coord. Chem. Rev.* **254**, 1769–1802 (2010).
283. Hoertz, P. G., Chen, Z., Kent, C. A. & Meyer, T. J. Application of high surface area tin-doped indium oxide nanoparticle films as transparent conducting electrodes. *Inorg. Chem.* **49**, 8179–8181 (2010).
284. Galloni, P. *et al.* in *Handbook of Porphyrin Science* **33**, 225–415 (World Scientific Publishing Company, 2012).
285. Roth, K. M. *et al.* Measurements of electron-transfer rates of charge-storage molecular monolayers on Si(100). Toward hybrid molecular/semiconductor information storage devices. *J. Am. Chem. Soc.* **125**, 505–517 (2003).
286. Laviron, E. The use of linear potential sweep voltammetry and of a.c. voltammetry for the study of the surface electrochemical reaction of strongly adsorbed systems and of redox modified electrodes. *J. Electroanal. Chem.* **100**, 263–270 (1979).
287. Liao, Y.-H., Scherer, N. F. & Rhodes, K. Nanoscale Electrical Conductivity and Surface Spectroscopic Studies of Indium–Tin Oxide. *J. Phys. Chem. B* **105**, 3282–3288 (2001).
288. Laviron, E. General expression of the linear potential sweep voltammogram in the case of diffusionless electrochemical systems. *J. Electroanal. Chem. Interfacial Electrochem.* **101**, 19–28 (1979).
289. Vitale, R. *et al.* Spectroelectrochemistry of Fe<sup>III</sup>- and Co<sup>III</sup>-mimochrome VI artificial enzymes immobilized on mesoporous ITO electrodes. *Chem. Commun.* **50**, 1894–1896 (2014).
290. Renault, C. *et al.* Unraveling the mechanism of catalytic reduction of O<sub>2</sub> by microperoxidase-11 adsorbed within a transparent 3D-nanoporous ITO film. *J. Am. Chem. Soc.* **134**, 6834–6845 (2012).
291. Neumann, B. *et al.* Bioelectrocatalytic Reduction of Hydrogen Peroxide by Microperoxidase-11

- Immobilized on Mesoporous Antimony-Doped Tin Oxide. *ChemElectroChem* **4**, 913–919 (2017).
292. Hou, K. *et al.* Dye-anchored mesoporous antimony-doped tin oxide electrochemiluminescence cell. *Adv. Mater.* **21**, 2492–2496 (2009).
293. Renault, C., Harris, K. D., Brett, M. J., Balland, V. & Limoges, B. Time-resolved UV-visible spectroelectrochemistry using transparent 3D-mesoporous nanocrystalline ITO electrodes. *Chem. Commun.* **47**, 1863–1865 (2011).
294. Ye, J. S. *et al.* Application of multi-walled carbon nanotubes functionalized with hemin for oxygen detection in neutral solution. *J. Electroanal. Chem.* **562**, 241–246 (2004).
295. Feng, Z., Sagara, T. & Niki, K. Application of potential-modulated UV-visible reflectance spectroscopy to electron transfer rate measurements for adsorbed species on electrode surfaces. *Anal. Chem.* **67**, 3564–3570 (1995).
296. Picot, M., Nicolas, I., Poriel, C., Rault-Berthelot, J. & Barrière, F. On the nature of the electrode surface modification by cathodic reduction of tetraarylporphyrin diazonium salts in aqueous media. *Electrochem. commun.* **20**, 167–170 (2012).
297. Elzing, A., van der Putten, A., Visscher, W. & Barendrecht, E. The cathodic reduction of oxygen at cobalt phthalocyanine. *J. Electroanal. Chem. Interfacial Electrochem.* **200**, 313–322 (1986).
298. Elzing, A., van der Putten, A., Visscher, W. & Barendrecht, E. The cathodic reduction of oxygen at cobalt phthalocyanine. Influence of electrode preparation on electrocatalysis. *J. Electroanal. Chem.* **200**, 313–322 (1986).
299. Brown, A. P. & Anson, F. C. Cyclic and Differential Pulse Voltammetric Behavior of Reactants Confined to the Electrode Surface. *Anal. Chem.* **49**, 1589–1595 (1977).
300. Acevedo, D. & Abruña, H. D. Electron-transfer study and solvent effects on the formal potential of a redox-active self-assembling monolayer. *J. Phys. Chem.* **95**, 9590–9594 (1991).
301. Roth, K. M. *et al.* Comparison of electron-transfer and charge-retention characteristics of porphyrin-containing self-assembled monolayers designed for molecular information storage. *J. Phys. Chem. B* **106**, 8639–8648 (2002).
302. Yasserli, A. A. *et al.* Structural and Electron-Transfer Characteristics of O-, S-, and Se-Tethered Porphyrin Monolayers on Si(100). *Journal of the American Chemical Society* **127**, 15603–15612 (2005).
303. Jiao, J., Nordlund, E., Lindsey, J. S. & Bocian, D. F. Effects of counterion mobility, surface morphology, and charge screening on the electron-transfer rates of porphyrin monolayers. *J. Phys. Chem. C* **112**, 6173–6180 (2008).
304. Eberspacher, T. A., Collman, J. P., Chidsey, C. E. D., Donohue, D. L. & Ryswyk, H. Van. Modular Assembly and Air-Stable Electrochemistry of Ruthenium Porphyrin Monolayers. *Langmuir* **19**, 3814–3821 (2003).
305. Thorum, M. S., Hankett, J. M. & Gewirth, A. A. Poisoning the Oxygen Reduction Reaction on Carbon-Supported Fe and Cu Electrocatalysts: Evidence for Metal-Centered Activity. *J. Phys. Chem. Lett.* **2**, 295–298 (2011).
306. Chen, R., Li, H., Chu, D. & Wang, G. Unraveling oxygen reduction reaction mechanisms on carbon-supported Fe-phthalocyanine and Co-phthalocyanine catalysts in alkaline solutions. *J. Phys. Chem. C* **113**, 20689–20697 (2009).
307. Wang, N. *et al.* Oxygen electroreduction promoted by quasi oxygen vacancies in metal oxide nanoparticles prepared by photoinduced chlorine doping. *Chem. Commun.* **51**, 10620–10623 (2015).
308. Liu, B. *et al.* Improved Photoelectrocatalytic Performance for Water Oxidation by Earth-Abundant Cobalt Molecular Porphyrin Complex-Integrated BiVO<sub>4</sub> Photoanode. *ACS Appl. Mater. Interfaces* **8**, 18577–18583 (2016).
309. Dogutan, D. K., McGuire, R. & Nocera, D. G. Electrocatalytic water oxidation by cobalt(III) hangman  $\beta$ -octafluoro corroles. *J. Am. Chem. Soc.* **133**, 9178–80 (2011).

310. Lee, C. H., Dogutan, D. K. & Nocera, D. G. Hydrogen generation by hangman metalloporphyrins. *J. Am. Chem. Soc.* **133**, 8775–8777 (2011).
311. Roubelakis, M. M., Bediako, D. K., Dogutan, D. K. & Nocera, D. G. Proton-coupled electron transfer kinetics for the hydrogen evolution reaction of hangman porphyrins. *Energy Environ. Sci.* **5**, 7737 (2012).
312. Solis, B. H. *et al.* Theoretical analysis of cobalt hangman porphyrins: Ligand dearomatization and mechanistic implications for hydrogen evolution. *ACS Catal.* **4**, 4516–4526 (2014).
313. Terekhov, S. N., Galievsky, V. A., Chirvony, V. S. & Turpin, P. Y. Resonance Raman and absorption characterization of cationic Co(II)-porphyrin in its complexes with nucleic acids: Binding modes, nucleic base specificity and role of water in Co(II) oxidation processes. *J. Raman Spectrosc.* **36**, 962–973 (2005).
314. Kielb, P. *et al.* Spectroelectrochemistry of biomimetic cobalt hangman complexes during electrocatalytic hydrogen formation and relevance of –COOH hanging group. in *16th European Conference on the Spectroscopy of Biological Molecules* (2015).
315. Siebert, F. & Hildebrandt, P. *Vibrational spectroscopy in life science*. (Wiley-VCH, 2008).
316. Parthasarathi, N., Hansen, C., Yamaguchi, S. & Spiro, T. G. Metalloporphyrin Core Size Resonance Raman Marker Bands Revisited: Implications for the Interpretation of Hemoglobin Photoproduct Raman Frequencies. *J. Am. Chem. Soc.* **109**, 3865–3871 (1987).
317. Daniel, Q. *et al.* Re-Investigation of Cobalt Porphyrin for Electrochemical Water Oxidation on FTO Surface: Formation of CoOx as Active Species. *ACS Catal.* **7**, 1143–1149 (2017).
318. Surendranath, Y., Kanan, M. W. & Nocera, D. G. Mechanistic studies of the oxygen evolution reaction by a cobalt-phosphate catalyst at neutral pH. *J. Am. Chem. Soc.* **132**, 16501–16509 (2010).
319. Gerken, J. B. *et al.* Electrochemical Water Oxidation with Cobalt-Based Electrocatalysts from pH 0–14: The Thermodynamic Basis for Catalyst Structure, Stability, and Activity. *J. Am. Chem. Soc.* **133**, 14431–14442 (2011).
320. Chen, W. *et al.* In situ electrochemical oxidation tuning of transition metal disulfides to oxides for enhanced water oxidation. *ACS Cent. Sci.* **1**, 244–251 (2015).
321. Swierk, J. R. & Tilley, T. D. Electrocatalytic Water Oxidation by Single Site and Small Nuclearity Clusters of Cobalt. *J. Electrochem. Soc.* **165**, H3028–H3033 (2018).
322. Garcia, E. M., Santos, J. S., Pereira, E. C. & Freitas, M. B. J. G. Electrodeposition of cobalt from spent Li-ion battery cathodes by the electrochemistry quartz crystal microbalance technique. *J. Power Sources* **185**, 549–553 (2008).
323. Guerrero, G., Alauzun, J. G., Granier, M., Laurencin, D. & Mutin, P. H. Phosphonate coupling molecules for the control of surface/interface properties and the synthesis of nanomaterials. *Dalt. Trans.* **42**, 12569–12585 (2013).

